BRNO UNIVERSITY OF TECHNOLOGY

VYSOKÉ UČENÍ TECHNICKÉ V BRNĚ

FACULTY OF ELECTRICAL ENGINEERING AND COMMUNICATION

FAKULTA ELEKTROTECHNIKY
A KOMUNIKAČNÍCH TECHNOLOGIÍ

DEPARTMENT OF CONTROL AND INSTRUMENTATION

ÚSTAV AUTOMATIZACE A MĚŘICÍ TECHNIKY

HIGH POWER-EFFICIENT SENSORLESS CONTROL OF SYNCHRONOUS RELUCTANCE MOTOR

BEZSNÍMAČOVÉ ŘÍZENÍ SYNCHRONNÍHO RELUKTANČNÍHO MOTORU SE ZAMĚŘENÍM NA VYSOKOU ÚČINNOST

DOCTORAL THESIS

DIZERTAČNÍ PRÁCE

AUTHOR   Ing. Zbyněk Mynář

AUTOR PRÁCE

SUPERVISOR   prof. Ing. Pavel Václavek, Ph.D.

ŠKOLITEL

BRNO 2022

ABSTRACT

Synchronous reluctance motors are becoming a more and more popular alternative to the AC induction machine for their relatively high power efficiency, low cost, and high robustness. Full utilization of benefits of sensorless control and high power efficiency are being complicated by non-linearities of the motor, especially magnetic saturation. The beginning of this work is dedicated to an inference of the mathematical-physical model of SynRM and an overview of existing state-of-the-art sensorless power-optimal algorithms. The core of this work is then the introduction of the SynRM state and parameter estimator, which is based on a new approach to measurement and utilization of phase reluctances. The key elements of the algorithm are a new methodology for measuring phase reluctances, a PWM switching scheme that allows to reduce switching losses and to measure phase reluctances from zero speed, and finally the integration of these measurements with the SynRM mathematical model using extended Kalman filter. The experimental part of the thesis then discusses the real measurement results obtained with the proposed algorithms and several selected state-of-the-art algorithms.

KEYWORDS

Synchronous, SynRM, Reluctance, FOC, Power optimization, MTPA, ME, EKF

ABSTRAKT

Synchronní reluktanční motory se pro svou relativně vysokou účinnost, robustnost a nízkou cenu stávají stále populárnější alternativou velmi rozšířených asynchronních motorů. Snaha o využití výhodných vlastností bezsnímačového řízení, a dosažení co nejvyšší účinnost jejich provozu, je však komplikována jejich výraznou nelinearitou způsobenou saturací magnetického obvodu. Úvod této práce je věnován popisu matematicko-fyzikálního modelu SynRM a přehledu existujících moderních algoritmů výkonově-optimálního bezsnímačového řízení. Jádrem práce je pak představení estimátoru stavů a parameterů SynRM postaveného na novém přístupu k měření a využití fázových reluktancí. Klíčovými prvky algoritmu jsou nová metodologie měření fázových reluktancí, spínací PWM schéma jež umožňuje snížit spínací ztráty a měřit fázové reluktance od nulových otáček, a nakonec integrace těchto měření s matematickým modelem SynRM s pomocí rozšířeného Kalmánova filtru. Experimentální část práce pak diskutuje výsledky reálných měření s navrženým algoritmem a vybranými současnými algoritmy.

KLÍČOVÁ SLOVA

Synchronní, SynRM, Reluktance, FOC, Optimalizace výkonu, MTPA, ME, EKF

PROHLÁŠENÍ

Prohlašuji, že disertační práci na téma „Bezsnímačové řízení synchronního reluktančního motoru se zaměřením na vysokou účinnost" jsem vypracoval samostatně pod vedením vedoucího disertační práce a s použitím odborné literatury a dalších informačních zdrojů, které jsou všechny citovány v práci a uvedeny v seznamu literatury na konci práce.

Jako autor uvedené diplomové práce dále prohlašuji, že v souvislosti s vytvořením tohoto pojednání jsem neporušil autorská práva třetích osob, zejména jsem nezasáhl nedovoleným způsobem do cizích autorských práv osobnostních a/nebo majetkových a jsem si plně vědom následků porušení ustanovení § 11 a následujících autorského zákona č. 121/2000 Sb., o právu autorském, o právech souvisejících s právem autorským a o změně některých zákonů (autorský zákon), ve znění pozdějších předpisů, včetně možných trestněprávních důsledků vyplývajících z ustanovení části druhé, hlavy VI. díl 4 Trestního zákoníku č. 40/2009 Sb.

Místo . . . .

                                                              (podpis autora)

PODĚKOVÁNÍ

Místo . . . .

                                                     (podpis autora)

Contents

Conclusions   135

Publication History and Bibliography   137

List of Figures

9

List of Tables

List of Symbols and Abbreviations

List of Symbols

Symbol	Description	Unit
$\mathbf{A}$	Feedback matrix in system state description	-
B	Viscous friction coefficient	[Nm·s/rad]
$\mathbf{B}$	Input matrix in system state description	-
c_{INF}	Complex vector obtained by INFORM method	[1]
$\mathbf{C}$	Output matrix in system state description	-
$\mathbf{D}$	Input-output system state matrix	-
E_{on}	IGBT transistor switch-on energy	[J]
E_{off}	IGBT transistor switch-off energy	[J]
E_{doff}	Diode reverse recovery loss energy	[J]
$\mathbf{F}$	Non-linear system state function matrix	-
$F_{PI}(p)$	Differential function of PI controller	-
$\vec{e}_{\alpha\beta}, \vec{e}_{dq}, \vec{e}_{\gamma\delta}$	Back electromotive force voltage vector in $\alpha\beta$, dq, and $\gamma\delta$ coordinate systems	[V]
$\mathbf{H}$	Non-linear system output function matrix	-
$\vec{i}_{abc}$	Three-phase stator current vector in abc coordinate system	[A]
$\vec{i}_{\alpha\beta}, \vec{i}_{dq}, \vec{i}_{\gamma\delta}$	Two-phase stator current vector in $\alpha\beta$, dq, and $\gamma\delta$ coordinate systems	[A]
$\vec{i}_{dq0}$	Torque-producing stator current vector in dq coordinate system	[A]
$\vec{i}_{dqc}$	Core-loss stator current vector in dq coordinate system	[A]
$\mathbf{I}$	Unit matrix	[1]
I_{dc}	Average DC-bus current i_{dc}	[A]
I_d^{thr}	Direct axis current saturation threshold	[A]
I_m	Amplitude of stator current	[A]
I_{m0}	Amplitude of the torque-producing stator current vector $\vec{i}_{dq0}$	[A]
I_{nom}	Nominal stator current	[A$_{\text{rms}}$]
I_q^{thr}	Quadrature axis current saturation threshold	[A]
J	Moment of inertia	[kg·m^2]
k	Discrete sample number	[1]
k_t	Torque constant	[Nm/A]
$\mathbf{K}$	Gain matrix	-
K_I	Integral gain	[1]
K_P	Proportional gain	[1]

L	Matrix of dq axis inductances	[H]
L_0	Average stator inductance	[H]
L_1	Stator inductance difference	[H]
L_a	Inductance of phase A	[H]
L_b	Inductance of phase B	[H]
L_c	Inductance of phase C	[H]
L_d	Static inductance in d-axis	[H]
$L_d^{'}$	Dynamic inductance in d-axis	[H]
L_{d0}	Initial L_d estimate	[H]
L_{pha}	Inductance between phase A and shorted phases B and C	[H]
L_{phb}	Inductance between phase B and shorted phases A and C	[H]
L_{phc}	Inductance between phase C and shorted phases A and B	[H]
L_q	Static inductance in q-axis	[H]
$L_q^{'}$	Dynamic inductance in q-axis	[H]
L_{q0}	Initial L_q estimate	[H]
M	Number of turns	[1]
N_m	Mechanical rotor speed	[rpm]
N_{ADC}	Resolution of ADC in the number of bits	[bit]
N_{nom}	Nominal mechanical rotor speed	[rpm]
N_{smpl}	Number of acquired i_{dc} samples	[1]
N_{vM}	Number of i_{dc} samples valid for inverter voltage vector	[1]
p	Differential operator with respect to time $\mathrm{d}/\mathrm{d}t$	-
P	Covariance matrix	-
$\mathbf{P}_0$	Initial covariance matrix	-
P_{con}	Conductive semiconductor power losses	[W]
P_{Cu}	Joule losses in stator	[W]
P_e	Total mechanical power applied to the rotor shaft	[W]
P_{Fe}	Core loss power	[W]
P_{in}	Electrical input power	[W]
P_m	Mechanical output power	[W]
P_{nom}	Nominal output power	[W]
P_p	Number of pole pairs	[1]
P_ω	Mechanical power losses	[W]
P_{sw}	Semiconductor switching losses	[W]
$\mathcal{P}$	Permeance $1/\mathcal{R}$	[H]

$\mathbf{Q}$	State noise covariance matrix	-
$\mathbf{R}$	Measurement noise covariance matrix	-
R_c	Resistance modelling core losses	[Ω]
R_s	Stator resistance	[Ω]
R_{sh}	Shunt resistor for $\vec{i}_{abc}$ measurement	[Ω]
R_{shc}	Common shunt resistor for i_{dc} measurement	[Ω]
$\mathcal{R}'_{pha}$	Normalized reluctance in phase A	[1/H]
$\mathcal{R}'_{phb}$	Normalized reluctance in phase B	[1/H]
$\mathcal{R}'_{phc}$	Normalized reluctance in phase C	[1/H]
$\mathcal{R}'_d$	Normalized reluctance in d axis	[1/H]
$\mathcal{R}'_q$	Normalized reluctance in q axis	[1/H]
$\mathbf{T}^{abc}_{\alpha\beta}$	Clarke transformation matrix	-
$\mathbf{T}^{\alpha\beta}_{abc}$	Inverse Clarke transformation matrix	-
$\mathbf{T}^{\alpha\beta}_{dq}(\theta)$	Park transformation matrix by angle θ	-
$\mathbf{T}^{dq}_{\alpha\beta}(\theta)$	Inverse Park transformation matrix by angle θ	-
T_e	Torque generated by motor	[Nm]
T_l	Loading torque	[Nm]
T_s	Discrete sampling period	[s]
T_{sidc}	Discrete sampling period of the i_{dc} current	[s]
$\boldsymbol{T}_{vM}$	Set of voltage vector $\boldsymbol{v}_M$ time durations	[s]
$\vec{u}_{abc}$	Three-phase stator voltage vector in abc coordinate system	[V]
$\vec{u}_{\alpha\beta}, \vec{u}_{dq}, \vec{u}_{\gamma\delta}$	Two-phase stator voltage vector in $\alpha\beta$, dq, or $\gamma\delta$ coordinate systems	[V]
u_{DD}	Circuit supply voltage	[V]
u_{idc}	Output voltage of the MC IDC circuit leading to ADC	[V]
u_{off}	Offset voltage for the MC IDC circuit generated by DAC	[V]
U_{dc}	DC-bus voltage	[V]
U_{nom}	Nominal stator voltage	[V$_{\mathrm{rms}}$]
$\boldsymbol{v}_M$	Set of inverter voltage vectors	-
$\vec{x}$	System state vector	-
$\vec{x}_0$	Initial system state vector	-
$\vec{y}$	System output vector	-
$\mathbf{Z}$	Matrix of rotation by $\pi/2$	[1]
δ_x	Relative error of measured quantity x	[%]
θ_e	Rotor electrical position	[rad]

θ_I	Angle between rotor position and the stator current vector	[rad]
θ_{I0}	Angle of the torque-producing stator current vector $\vec{i}_{dq0}$	[rad]
θ_m	Mechanical rotor angle	[rad]
θ_{ui}	Angle between stator voltage and current vectors	[rad]
$\boldsymbol{\Theta}$	Matrix of unknown parameters	-
λ	Forgetting factor	[1]
σ_x	Standard deviation of quantity x	-
ϑ	Temperature	[°C]
τ	Time constant	[s]
ω_e	Electric angular speed	[rad/s]
ω_m	Mechanical angular speed	[rad/s]
ω_{hf}	Angular frequency of injected signal	[rad/s]
ε	Control error signal	-
$\vec{\Psi}_{\alpha\beta}, \vec{\Psi}_{dq}, \vec{\Psi}_{\gamma\delta}$	Stator magnetic flux vector in $\alpha\beta$, dq, or $\gamma\delta$ coordinate systems	[Wb]
Ψ_m	Stator magnetic flux amplitude	[Wb]
Ψ_{PM}	PMSM permanent magnet flux	[Wb]

List of Indexes and Notations

Index	Description
$.^{\mathrm{err}}$	Error value
$.^{\mathrm{max}}$	Maximal value
$.^{\mathrm{min}}$	Minimal value
$.^{\mathrm{nom}}$	Nominal value
$.^{\mathrm{opt}}$	Optimal value
$.^{\mathrm{req}}$	Required value
$.^{\mathrm{thr}}$	Threshold value
$\lvert . \rvert$	Absolute value
$\hat{.}$	Estimated value
$\bar{.}$	Mean value
$\vec{.}$	Vector
$._\alpha, ._\beta, ._{\alpha\beta}$	Vector components in stator reference system
$._\gamma, ._\delta, ._{\gamma\delta}$	Vector components in general rotating system
$._d, ._q, ._{dq}$	Vector components in rotor reference frame
$._a, ._b, ._c, ._{abc}$	Vector components in motor phases

List of Abbreviations

Abbrv.	Description
ASPWM	Alignment-Swap PWM
ACIM	AC Induction Machine
BEMF	Back Electromotive Force
BPF	Band-pass Filter
CAPWM	Centre-aligned PWM
DMA	Direct Memory Access
DTC	Direct Torque Control
EEMF	Extended EMF
EIN	Equivalent Input Noise
EKF	Extended Kalman Filter
EKF-BASIC	Extended Kalman Filter - proposed basic algorithm version
EKF-RS	Extended Kalman Filter - proposed version with $\hat{R}_s$ estimation
EM	Expectation-Maximization
FOC	Field Oriented Control
HFI	High Frequency Injection
HVAC	Heating, Ventilation, and Air Conditioning
IGBT	Insulated Gate Bipolar Transistors
INFORM	Indirect Flux detection by Online Reactance Measurement
IPMSM	Interior PMSM
KF	Kalman Filter
LMC	Loss Model Controller
LPF	Low-pass Filter
LUT	Look-up Table
LSB	Least Significant Bit
MC IABC	Measurement circuit for phase currents
MC IDC	Measurement circuit for DC-bus current
MCU	Micro-controller Unit
ME	Maximum Efficiency
MLR	Multi-Linear Regression
MPFC	Maximal Power Factor Control

MRAS	Model Reference Adaptive System
MSB	Most Significant Bit
MTPA	Max Torque Per Ampere
PI	Proportional Integral controller
PID	Proportional Integral Derivative controller
PMSM	Permanent Magnet Synchronous Machine
PRBS	Pseudo-Random Binary Sequence
PWM	Pulse Width Modulation
RLS	Recursive Least Squares
RMS	Root Mean Square
SC	Search Controller
SVM	Space vector Modulation
SynRM	Synchronous Reluctance Motor
THD	Total Harmonic Distortion
TO	Tracking Observer
VFC	Voltage-to-Frequency Converter
VSI	Voltage Source Inverter

Introduction

Synchronous reluctance motor (SynRM) is known since the first half of 20th century [Kos23]. This type of electrical motor was initially considered to be inferior in comparison with other types of motors, mostly because of relatively low output torque and efficiency. Thanks to technological advances in the design of SynRM rotors, which greatly enhanced machine performance, more and more attention is being paid to SynRM. The most notable advantages of this technology are:

- SynRM can achieve around 10% to 15% larger rated torque for a given frame size in comparison to an AC induction machine (ACIM) [BP08].

- Very low production cost because the assembly of laminated rotor topology is quite simple and requires no costly permanent magnets [MDD+22].

- There are no Joule losses in the rotor of SynRM. Resulting lower operation temperature has many benefits, like, for example, longer life of ball-bearings and reduced thermal requirements for lubricants [RFC10].

- There is no risk of permanent magnet demagnetization due to heat like in the case of permanent magnet synchronous machine (PMSM).

- Constant power region during field weakening can be theoretically extended to infinite speed because there is no permanent magnet flux to suppress.

A comprehensive comparison of SynRM technology with ACIM and PMSM technologies is available in Table 1. It should be also noted that permanent magnet assisted synchronous reluctance motors are not within scope of this thesis and only purely magnet-less machines are considered.

Despite several SynRM disadvantages, it can be expected, that the low maintenance, production, and operation cost of SynRM will make it popular mainly in cost-sensitive inverter-based applications like pumps, fans, or HVACs. That being said, other major applications, like the automotive, are being considered as well [BP08, MDD+22]. To fully exploit this potential, great attention is currently being paid to the development of power-optimal sensorless control algorithms for SynRM, which would minimize necessary operation input power and remove the need for expensive rotor position and speed sensor. Such power-optimal control is also the topic of this thesis, or more precisely, a proposal of sensorless state and parameter observer necessary to build such an application.

The first section of this thesis introduces SynRM mathematical model. Attention is paid especially to the magnetic saturation phenomenon and the core losses, which are the major non-linearities of SynRM, complicating its power-efficient sensorless control.

The second chapter summarizes the existing sensorless SynRM state and parameter estimation algorithms, which can be integrated within the well-known field-oriented vector control (FOC) algorithm. The rotor position and speed estimation algorithms can be generally divided into groups based on exploitation of extended back-electromotive-force (EEMF), rotor saliency, or both. An overview of the currently used state-of-the-art sensorless algorithms from each group is provided. Some

Table 1: Comparison of SynRM with PMSM and ACIM technologies [MDD$^+$22]

SynRM advantages over PMSM	SynRM advantages over ACIM

• No permanent magnets:
  - Significantly reduced cost
  - Reduced embedded carbon
  - Easier manufacturing
  - Reduced risk of over-voltage
  - Reduced risk in the supply chain
• No demagnetization risk
• Wider operating speed range
• No need for clutch in case of
  short-circuit fault
	• Synchronous operation (no slip)
	• No conductors in rotor:
	  - Improved robustness
	  - Manufacturing cost
	  - Lower rotor losses (cold rotor)
	  - Lower maintenance requirements
	• Higher efficiency
	• Higher power density for same size
	• Lower rotor inertia
	• Longer bearing life

SynRM disadvantages over PMSM	**SynRM disadvantages over ACIM**

• Lower power and torque density
• Lower power factor
• Not yet widely accepted
  by industry
• Complex control due
  to non-linearity
• Lower efficiency
	• No line-startup capability
	  without rotor modifications
	• Lower power factor
	• Not yet widely accepted
	  by industry
	• Complex control due
	  to non-linearity

of these algorithms, especially the EEMF-based ones, then require accurate machine parameters for their operation. Several notable parameter estimation algorithms are, therefore, also described in that chapter.

The third chapter deals with SynRM power-loss modelling, optimization criteria, and with the existing power optimization algorithms. Several algorithms belonging either to active search or to power-loss-based algorithm groups are shown and discussed. One of the presented algorithms is the DC-current injection optimization search algorithm, which was proposed during research for this thesis.

The fourth chapter analyses the sensitivity of selected parameter estimation and power optimization algorithms to the inaccuracy of provided machine parameters. As an example, the optimal model-based power-optimization and the well-known EEMF observer algorithm in combination with both the inductance look-up table and the online least square estimation method were simulated. This analysis aimed mainly to determine the necessary parameter observer performance requirements, which aware then taken as goals for the algorithms proposed in this thesis.

The fifth section presents the core of the conducted research. It describes the proposed observer, which is based on the extended Kalman filter, novel low-cost current derivative measurement method, and pulse-width modulation technique. Besides the theory and discussion, this chapter also introduces simulation results. As will be shown, the algorithm has several attractive features, like full-speed operation range, improved efficiency, and the machine rotor and position information redundancy, which can be used to estimate additional machine states and parameters (this thesis shows an example with stator resistance estimation).

The final chapter then describes and discusses the experimental setup and results. Beside the proposed methods, selected existing state-of-the-art algorithms were implemented and analysed as well. The basic function of rotor position and speed tracking was investigated but the main focus was paid to steady-state parameter estimation accuracy and impact to achievable power efficiency.

1. SynRM Model and Properties

The goal of this chapter is to introduce the SynRM non-linear system model and properties to show challenges related to its optimal control and to serve as a foundation for later chapters of this thesis. The first part of this section is focused on the mathematical modelling of SynRM including magnetic saturation and core power loss phenomenons. Section 1.2 then shows offline-identified parameters of the real, commercially-available SynRM machine, in order to highlight the extent of non-linearity of a typical machine and to serve as a reference for the rest of this thesis.

1.1. Mathematical Model

The stator of SynRM is identical to a standard AC induction machine, which means typically a three-phase stator with harmonically distributed windings so a sinusoidal rotating magnetic field is created when powered by AC power. The rotor construction is, however, different, because it contains no windings or permanent magnets. Instead, the rotor is constructed so the highest possible difference in magnetic reluctance (and thus stator inductance as well) is achieved between the rotor axes. The rotor and stator always have the same number of pole pairs. When such a rotor is exposed to a rotating magnetic field, a torque is produced, because the most magnetically conductive rotor axis tries to align itself with the vector of the stator magnetic field. This is because an aligned configuration achieves the minimal magnetic flux density in the air gap and so the minimal energy state of the magnetic field is reached. The rule is that the higher the rotor anisotropy, the higher torque can be achieved.

Figure 1.1 depicts the typical construction topologies of the four-pole SynRM rotor. The construction with pronounced poles in Figure 1.1a offers relatively low maximal achievable torque, however, due to its simple and robust construction it is often found in very-high-speed applications. The highest rotor anisotropy can be currently achieved using the axially-laminated construction as shown in Figure 1.1b. Due to increased eddy current power losses and higher manufacturing costs due to its complicated design, it is, however, used marginally. The most widespread rotor topology today is the transversally-laminated rotor as shown in Figure 1.1c. These rotors offer a relatively good balance between production cost and the maximal achievable torque [Kol10, ODM15].

As the first step, Clarke's transformation will be used to obtain a sufficiently simple SynRM mathematical model. This transformation converts quantities from the three-phase abc to two-phase $\alpha\beta$ stationary coordinate system as shown in Figure 1.2. The stator phase voltage vector $\vec{u}_{abc} = [u_a, u_b, u_c]^{\mathrm{T}}$ can be written as

$$\vec{u}_{\alpha\beta} = \begin{bmatrix} u_\alpha \\ u_\beta \end{bmatrix} = \frac{2}{3} \begin{bmatrix} 1 & -\frac{1}{2} & -\frac{1}{2} \\ 0 & \frac{\sqrt{3}}{2} & -\frac{\sqrt{3}}{2} \end{bmatrix} \begin{bmatrix} u_a \\ u_b \\ u_c \end{bmatrix} = \mathbf{T}_{\alpha\beta}^{abc} \vec{u}_{abc}, \tag{1.1}$$
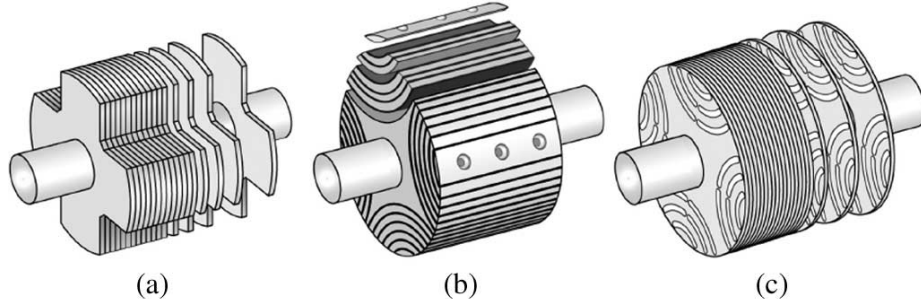
Figure 1.1: Rotor construction (a) with pronounced poles, (b) axially-laminated, and (c) transversally-laminated [Kol10]

where $\vec{u}_{\alpha\beta}$ is the stator voltage vector in $\alpha\beta$ coordinate system and $\mathbf{T}_{\alpha\beta}^{abc}$ is Clarke's transformation matrix. The $\frac{2}{3}$ coefficient in equation (1.1) was added to normalize amplitudes of quantities in $\alpha\beta$ coordinate system to values in three-phase system abc. The inverse transformation can be done as

$$\vec{u}_{abc} = \mathbf{T}_{abc}^{\alpha\beta}\vec{u}_{\alpha\beta} = \begin{bmatrix} 1 & 0 \\ -\frac{1}{2} & \frac{\sqrt{3}}{2} \\ -\frac{1}{2} & -\frac{\sqrt{3}}{2} \end{bmatrix} \vec{u}_{\alpha\beta}, \tag{1.2}$$

where $\mathbf{T}_{abc}^{\alpha\beta}$ is the inverse Clarke's transformation matrix [CČerný10].
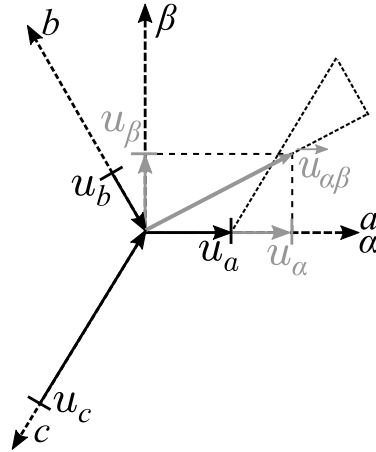
Figure 1.2: Principle of Clarke's transformation

Further model simplification can be achieved using Park's transformation. This transformation converts quantities from the two-phase stationary $\alpha\beta$ to the two-phase rotating dq coordinate system as shown in Figure 1.3. The d axis is usually referred to as the direct axis and the q axis as the quadrature axis. The SynRM stator voltage vector can be written as

$$\vec{u}_{dq} = \begin{bmatrix} u_d \\ u_q \end{bmatrix} = \mathbf{T}_{dq}^{\alpha\beta}(\theta_e) \begin{bmatrix} u_\alpha \\ u_\beta \end{bmatrix} = \begin{bmatrix} \cos\theta_e & \sin\theta_e \\ -\sin\theta_e & \cos\theta_e \end{bmatrix} \vec{u}_{\alpha\beta}, \tag{1.3}$$

where $\vec{u}_{dq}$ is the stator voltage vector in dq coordinate system, θ_e is the rotation angle, and $\mathbf{T}_{dq}^{\alpha\beta}(\theta_e)$ is the Park's transformation matrix. The inverse transformation can be done as

$$\vec{u}_{\alpha\beta} = \mathbf{T}_{\alpha\beta}^{dq}(\theta_e)\vec{u}_{dq} = \begin{bmatrix} \cos\theta_e & \text{-}\sin\theta_e \\ \sin\theta_e & \cos\theta_e \end{bmatrix} \vec{u}_{dq}, \tag{1.4}$$

where $\mathbf{T}_{\alpha\beta}^{dq}(\theta_e)$ is the inverse Parks's transformation matrix.
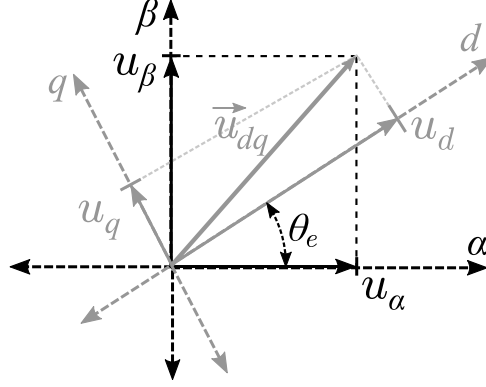
Figure 1.3: Principle of Park's transformation

The electrical angle θ_e is chosen with regard to the simplicity of the resulting mathematical model. In the case of permanent magnet synchronous motor (PMSM), the angle is chosen identical to the rotation angle of the permanent magnet north pole. In the case of SynRM, however, the choice is ambiguous. The direct d-axis can be aligned with the maximal or the minimal inductance axis. The SynRM model is non-linear and the alignment choice does not necessarily lead to identical results in the case of some algorithms. In this work, similarly to the great majority of literature, the alignment with the maximal inductance axis will be used, as shown in Figure 1.4 [CČerný10, ITDO06].
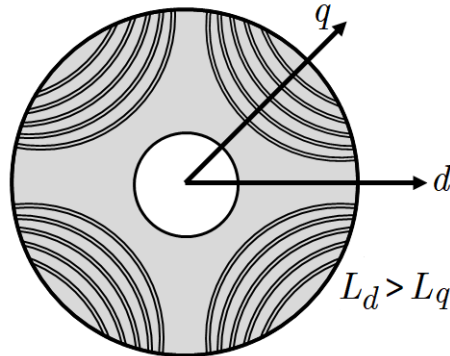
Figure 1.4: Four-pole rotor with highlighted dq-axes

The stator voltage in stationary reference frame can be described by equation

$$\vec{u}_{\alpha\beta} = R_s\vec{i}_{\alpha\beta} + \frac{\mathrm{d}}{\mathrm{d}t}\vec{\Psi}_{\alpha\beta}, \tag{1.5}$$

where R_s is stator winding resistance, $\vec{i}_{\alpha\beta} = [i_\alpha, i_\beta]^{\mathrm{T}}$ is stator current vector, and $\vec{\Psi}_{\alpha\beta} = [\Psi_\alpha, \Psi_\beta]^{\mathrm{T}}$ is stator magnetic flux vector in $\alpha\beta$ reference frame. Equation (1.5) can be expressed in rotating reference frame as

$$
\begin{aligned}
\vec{u}_{dq} = \mathbf{T}_{dq}^{\alpha\beta}(\theta_e)\vec{u}_{\alpha\beta} &= \\
&= R_s\mathbf{T}_{dq}^{\alpha\beta}(\theta_e)\vec{i}_{\alpha\beta} + \mathbf{T}_{dq}^{\alpha\beta}(\theta_e)\frac{\mathrm{d}}{\mathrm{d}t}\vec{\Psi}_{\alpha\beta} = \\
&= R_s\vec{i}_{dq} + \mathbf{T}_{dq}^{\alpha\beta}(\theta_e)\frac{\mathrm{d}}{\mathrm{d}t}\left[\mathbf{T}_{\alpha\beta}^{dq}(\theta_e)\vec{\Psi}_{dq}\right] = \\
&= R_s\vec{i}_{dq} + \mathbf{T}_{dq}^{\alpha\beta}(\theta_e)\left[\frac{\mathrm{d}}{\mathrm{d}t}\mathbf{T}_{\alpha\beta}^{dq}(\theta_e)\right]\vec{\Psi}_{dq} + \mathbf{T}_{dq}^{\alpha\beta}(\theta_e)\mathbf{T}_{\alpha\beta}^{dq}(\theta_e)\left[\frac{\mathrm{d}}{\mathrm{d}t}\vec{\Psi}_{dq}\right] = \\
&= R_s\vec{i}_{dq} + \omega_e\begin{bmatrix} 0 & -1 \\ 1 & 0 \end{bmatrix}\vec{\Psi}_{dq} + \frac{\mathrm{d}}{\mathrm{d}t}\vec{\Psi}_{dq} = R_s\vec{i}_{dq} + \omega_e\mathbf{Z}\vec{\Psi}_{dq} + \frac{\mathrm{d}}{\mathrm{d}t}\vec{\Psi}_{dq},
\end{aligned}
\tag{1.6}
$$

where $\omega_e = \mathrm{d}\theta_e/\mathrm{d}t$ is synchronous electrical speed, $\mathbf{Z}$ is $\pi/2$ rotation angle matrix, $\vec{i}_{dq} = [i_d, i_q]^{\mathrm{T}}$ is stator current vector, and $\vec{\Psi}_{dq} = [\Psi_d, \Psi_q]^{\mathrm{T}}$ is stator magnetic flux vector in dq reference frame. The stator current vector can also be expressed using it's amplitude I_m and the rotor position relative angle θ_I as

$$
\vec{i}_{dq} = I_m\begin{bmatrix} \cos\theta_I \\ \sin\theta_I \end{bmatrix}.
\tag{1.7}
$$

One of the SynRM disadvantages, which complicate its control, is the nonlinearity of the magnetic circuit, which saturates at higher currents. The SynRM machines are being operated under magnetic saturation commonly because relatively high magnetic flux is needed to reach the necessary torque. The stator inductances are therefore becoming functions of stator currents in both direct and perpendicular axis (also called cross-saturation). To simplify further SynRM model inferring, the cross-saturation is, however, going to be neglected. The ideal non-saturating situation for the direct axis is depicted in Figure 1.5a and the real saturating relation is shown in Figure 1.5b.
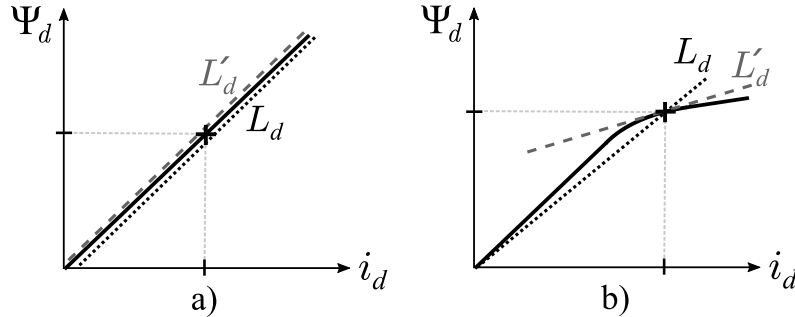
Figure 1.5: The current dependency of the stator magnetic flux a) with and b) without magnetic saturation [ITDO06]

The stator magnetic flux considering the saturation effect can be described as

$$
\vec{\Psi}_{dq} = \begin{bmatrix} L_d(i_d) & 0 \\ 0 & L_q(i_q) \end{bmatrix}\vec{i}_{dq} = \mathbf{L}\vec{i}_{dq},
\tag{1.8}
$$

where $\mathbf{L}$ is the static inductance matrix, $L_d(i_d)$ is the static inductance in the direct axis, and $L_q(i_q)$ is the static inductance in the quadrature axis. The static inductances are given by the ratio between the magnetic flux and the current amplitudes. To describe dynamic events, however, the dynamic inductances have to be introduced as

$$L_d^{'}(i_d) = \frac{\mathrm{d}\Psi_d}{\mathrm{d}i_d} \quad \text{and} \quad L_q^{'}(i_q) = \frac{\mathrm{d}\Psi_q}{\mathrm{d}i_q}, \tag{1.9}$$

where $L_d^{'}(i_d)$ is dynamic inductance in the direct axis and $L_q^{'}(i_q)$ is dynamic inductance in the quadrature axis. Figure 1.5 shows that dynamic inductance has a character of the tangent to the operating point. In the ideal case with no saturation in Figure 1.5a, the dynamic and static inductances are equal.

Introducing the relation (1.8) into (1.6), the stator voltages can be described as

$$u_d = R_s i_d + i_d \left(\frac{\mathrm{d}L_d(i_d)}{\mathrm{d}t} \right) + L_d(i_d) \frac{\mathrm{d}i_d}{\mathrm{d}t} - L_q(i_q)\omega_e i_q =$$

$$= R_s i_d + \left(i_d \frac{\mathrm{d}L_d(i_d)}{\mathrm{d}i_d} + L_d(i_d) \right) \frac{\mathrm{d}i_d}{\mathrm{d}t} - L_q(i_q)\omega_e i_q = \tag{1.10}$$

$$= R_s i_d + L_d^{'}(i_d) \frac{\mathrm{d}i_d}{\mathrm{d}t} - L_q(i_q)\omega_e i_q,$$

$$u_q = R_s i_q + \left(i_q \frac{\mathrm{d}L_q(i_q)}{\mathrm{d}i_q} + L_q(i_q) \right) \frac{\mathrm{d}i_q}{\mathrm{d}t} + L_d(i_d)\omega_e i_d =$$

$$= R_s i_q + L_q^{'}(i_q) \frac{\mathrm{d}i_q}{\mathrm{d}t} + L_d(i_d)\omega_e i_d. \tag{1.11}$$

These relations show that the difference between dynamic and static inductance has no effect when in steady-state [ITDO06, XXLN91]. Note, that from now on, both the static and dynamic inductances will be stated without their explicit current dependency to simplify the following text.

The SynRM machine core-losses P_{Fe} were neglected up until this moment. These losses are created during magnetization as hysteresis losses and represent the second most significant losses after the Joule losses. In the ideal case, the core losses are only present in the stator, thanks to the synchronous operation of the machine. In practice, however, there is also a flux change when the rotor crosses near the stator teeth, which leads to the formation of core losses in the rotor as well. The rotor losses are, however, negligible in comparison to stator losses and will not be considered. The core losses are usually modelled using the resistance R_c, which is the same for d and q axis. The resulting SynRM model is shown in Figure 1.6.

It can be noticed that the measured current $\vec{i}_{dq}$ is now divided into loss current $\vec{i}_{dqc} = [i_{dc}, i_{qc}]^{\mathrm{T}}$ and flux-producing current $\vec{i}_{dq0} = [i_{d0}, i_{q0}]^{\mathrm{T}}$. The core loss modelling for dynamic events would significantly complicate the model, so only the steady-state will be considered. This can be afforded if the SynRM machine is used in
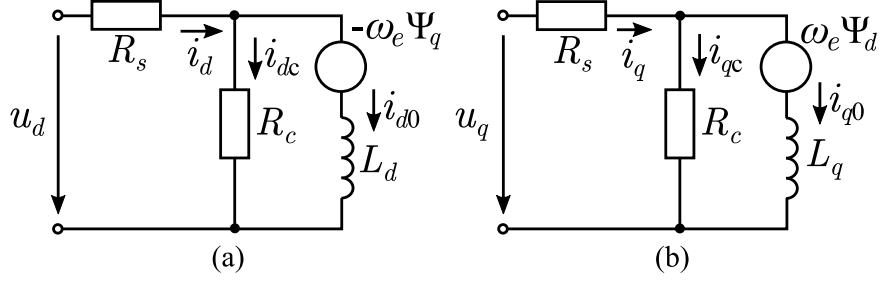
Figure 1.6: The SynRM model including core losses in a) direct and b) quadratic axis

low-dynamic applications, which is often the case [DTCB22]. The R_c resistance can be calculated as

$$R_c = \frac{3}{2} \frac{\omega_e^2(\Psi_d^2 + \Psi_q^2)}{P_{Fe}} \tag{1.12}$$

and is, therefore, dependent on both the size of the stator flux and the rotor speed. Alternatively, the core losses are often being described using the core loss coefficient

$$K_m = \frac{\omega_e L_d L_q}{R_c}, \tag{1.13}$$

which is used for its less variable nature when compared to resistance R_c. The relation between measured and flux-producing current can be expressed as

$$i_d = i_{d0} - \frac{\omega_e L_q i_{q0}}{R_c}, \tag{1.14}$$

$$i_q = i_{q0} + \frac{\omega_e L_d i_{d0}}{R_c}, \tag{1.15}$$

$$i_{d0} = \frac{R_c^2 i_d + R_c \omega_e L_q i_q}{R_c^2 + \omega_e^2 L_d L_q}, \tag{1.16}$$

$$i_{q0} = \frac{R_c^2 i_q - R_c \omega_e L_d i_d}{R_c^2 + \omega_e^2 L_d L_q}. \tag{1.17}$$

When expressing the flux-producing current using its amplitude I_{m0} and angle θ_{I0}, where $\vec{i}_{dq0} = I_{m0}[\cos\theta_{I0}, \sin\theta_{I0}]^{\mathrm{T}}$, it can be noticed that the relation $\theta_I > \theta_{I0}$ will always be true in motoring region, The situation is depicted in Figure 1.7. The inclusion of core loss resistance R_c into the model might, therefore, benefit the accuracy of found solution. The voltage equations (1.10) and (1.11) can be rewritten using the current expressions (1.16) and (1.17) as

$$\vec{u}_{dq} = R_s \vec{i}_{dq0} + \begin{bmatrix} L_d' & 0 \\ 0 & L_q' \end{bmatrix} \frac{\mathrm{d}}{\mathrm{d}t} \vec{i}_{dq0} + \omega_e \left(1 + \frac{R_s}{R_c}\right) \begin{bmatrix} L_d & 0 \\ 0 & L_q \end{bmatrix} \mathbf{Z} \vec{i}_{dq0} =$$
$$= R_s \vec{i}_{dq0} + \mathbf{L}' \frac{\mathrm{d}}{\mathrm{d}t} \vec{i}_{dq0} + \omega_e \left(1 + \frac{R_s}{R_c}\right) \mathbf{L} \mathbf{Z} \vec{i}_{dq0}, \tag{1.18}$$

where $\mathbf{L}'$ is the dynamic inductance matrix [IKK$^+$09, KS96b, YTA05, XXLN91].
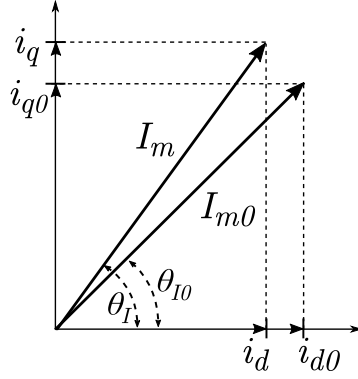
Figure 1.7: Stator current vector comparison with core loses included

Generated electrical torque applied to the machine shaft can be calculated as

$$
\begin{aligned}
T_e &= \frac{3}{2}P_p(\vec{\Psi}_{dq} \times \vec{i}_{dq0}) = \frac{3}{2}P_p\left(\Psi_d i_{q0} - \Psi_q i_{d0}\right) = \\
&= \frac{3}{2}P_p(L_d - L_q)i_{d0}i_{q0} = \frac{3}{4}P_p(L_d - L_q)I_{m0}\sin 2\theta_{I0},
\end{aligned}
\tag{1.19}
$$

where P_p is the number of pole pairs. It can be seen that the size of the difference between d and q axis inductances caused by rotor anisotropy is critical for achieving high output torque.

To make the mathematical model complete, the mechanical equation

$$
\frac{\mathrm{d}\omega_m}{\mathrm{d}t} = \frac{1}{J}\left[T_e - T_l - B_1\omega_m - \mathrm{sign}(\omega_m)B_2\omega_m^2\right]
\tag{1.20}
$$

is introduced, where $\omega_m = \omega_e/P_p$ is mechanical rotor speed, J is the moment of inertia, T_l is the loading torque, B_1 is internal machine viscous friction coefficient and B_2 is a ventilator mechanical loss coefficient. The rotor electrical position is then

$$
\theta_e = \int \omega_e \mathrm{d}t.
\tag{1.21}
$$

In summary, the final mathematical model of SynRM, including magnetic saturation and core losses, is formed by equations (1.18), (1.20), and (1.21) [CČerný10].

1.2. Parameters of Real SynRM Machine

This section will be discussing the offline-measured parameters of real SynRM. The goal is to highlight the extent of machine parameter non-linearities on a real example. The investigated machine is commercially-available four-pole 550 W SynRM with transversally-laminated rotor (as shown in Figure 1.1c) from the KSB manufacturer. It is also used as a reference for all simulations and measurements in this thesis. Its nominal plate values and other basic parameters are listed in Table 1.1. Further details provided by the manufacturer can be read from the machine label in Figure 1.8. The stator resistance R_s was measured using the RLC meter and the

mechanical parameters J and B were acquired from step dynamic response using the least square method approximation for the first order mechanical system (1.20).

Table 1.1: Basic parameters of 0.55 kW KSB SynRM machine

Quantity	Value	Unit
P_{nom}	550	W
N_{nom}	1500	rpm
U_{nom}	350	$\mathrm{V_{rms}}$
I_{nom}	1.6	$\mathrm{A_{rms}}$
P_p	2	-
R_s	9.68	Ω
J	$1.64 \cdot 10^{-3}$	$\mathrm{kg \cdot m^2}$
B	$1.96 \cdot 10^{-3}$	$\mathrm{Nm \cdot s/rad}$

Figure 1.8: Reference SynRM label

Measurement of the stator inductances is not as straightforward. As was explained in Section 1.1, magnetic saturation occurs when high stator currents are present. To obtain a sufficiently precise description of stator flux non-linearity, the combination of linear and inverse functions

$$
\begin{aligned}
\Psi_d &= L_{d0} i_d & \text{for} \quad |i_d| &< I_d^{\mathrm{thr}}, \\
\Psi_q &= L_{q0} i_q & \text{for} \quad |i_q| &< I_q^{\mathrm{thr}}, \\
\Psi_d &= \operatorname{sign}(i_d) \, \Psi_{d0} + L_{d1} i_d + \frac{\beta_d}{i_d} & \text{for} \quad |i_d| &> I_d^{\mathrm{thr}}, \\
\Psi_q &= \operatorname{sign}(i_q) \, \Psi_{q0} + L_{q1} i_q + \frac{\beta_q}{i_q} & \text{for} \quad |i_q| &> I_q^{\mathrm{thr}}
\end{aligned}
\tag{1.22}
$$

is used as models, where $L_{d0} = L_d = L_d'$ and $L_{q0} = L_q = L_q'$ are used in the linear region, I_d^{thr} and I_q^{thr} are currents for which the saturation starts to occur, and Ψ_{d0}, Ψ_{q0}, L_{d1}, L_{q1}, β_d, and β_q are parameters describing the current dependency of flux in non-linear saturating region.

Compared to the commonly used polynomial approximation, this approach requires fewer parameters to be identified and allows the option to simply express static and dynamic inductances in the linear and saturation regions as

$$L_d = \frac{\Psi_d}{i_d} = \frac{\Psi_{d0}}{i_d} + L_{d1} + \frac{\beta_d}{i_d^2}, \tag{1.23}$$

$$L_q = \frac{\Psi_q}{i_q} = \frac{\Psi_{q0}}{i_q} + L_{q1} + \frac{\beta_q}{i_q^2}, \tag{1.24}$$

$$L_d^{'} = \frac{\mathrm{d}\Psi_d}{\mathrm{d}i_d} = L_{d1} - \frac{\beta_d}{i_d^2}, \tag{1.25}$$

$$L_q^{'} = \frac{\mathrm{d}\Psi_q}{\mathrm{d}i_q} = L_{q1} - \frac{\beta_q}{i_q^2}. \tag{1.26}$$

The parameter needed for approximation (1.22) were acquired using the simple stator flux model (1.5) and multi-linear regression method (MLR) [BCP16]. The results are summarized in Table 1.2.

Table 1.2: Stator flux characteristics approximation parameters

Axis	I_x^{thr} [A]	L_{x0} [mH]	Ψ_{x0} [Wb]	L_{x1} [mH]	β_x [Wb·A]
Direct	0.99	670	1.30	26	$-647 \cdot 10^{-3}$
Quadrature	0.15	382	0.11	81	$-8.5 \cdot 10^{-3}$

The resulting stator flux current dependency maps are shown in Figure 1.9 and Figure 1.10. The corresponding static and dynamic inductances are then in Figure 1.11 to Figure 1.14. The direct axis inductance is not only several times higher than in the quadrature axis, but it also saturates at much higher currents. This result was expected because the direct rotor axis is by majority formed by iron, while the quadrature axis is air-dominant. The quadrature axis path, however, does contain a small amount of iron due to construction reasons, which is quickly saturated even with a small current. This effect can be seen in Figure 1.12 and Figure 1.14, where the L_q drops to 25 % of its original value when $|i_q| > 0.5$ A. Some SynRM control algorithms proposed in the literature are considering L_q to be constant in the full current range for simplicity [HKS99, KSG$^+$14]. The measurement, however, shows that this simplification can be afforded only when maintaining sufficiently high stator current amplitude (e.g. by operating loaded machine). Figure 1.11 shows that the direct axis inductance drops by one-third at nominal stator current I_{nom}. This effect cannot be neglected for efficiency-optimal sensorless SynRM control. On the other hand, the cross-saturation is relatively negligible, and is often neglected in the literature [AR15].

Comparison of static and dynamic inductance maps shows that dynamic inductances drop faster with the increasing current than static inductances. Neglecting the difference between static and dynamic inductance in the algorithm is going to have more negative impact during dynamic events at higher currents. Such simplification can be afforded if a low-dynamic target application is considered.
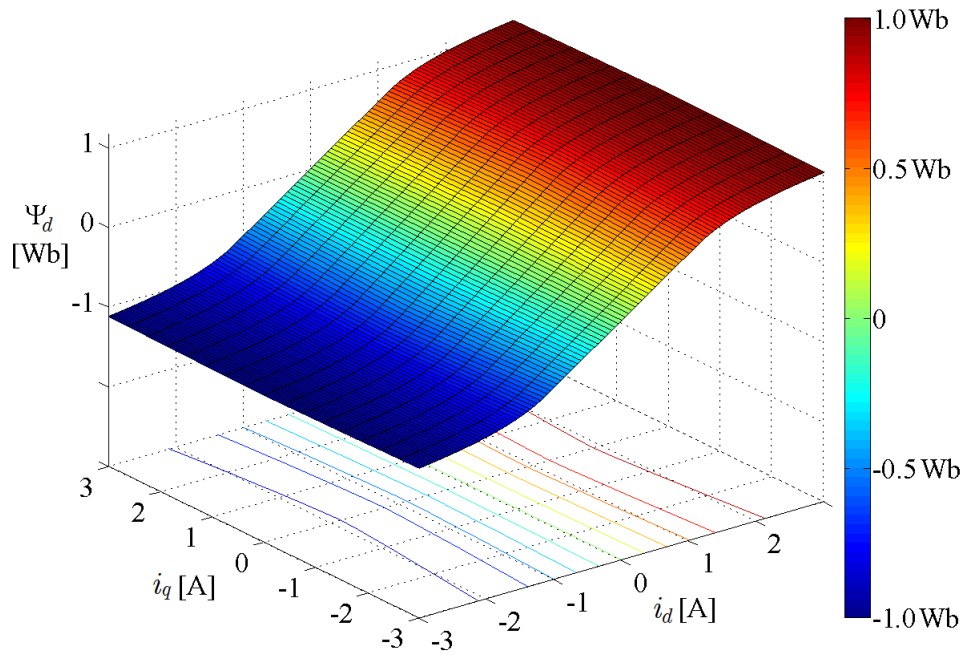
Figure 1.9: Direct axis stator flux Ψ_d dependency on stator current $\vec{i}_{dq}$
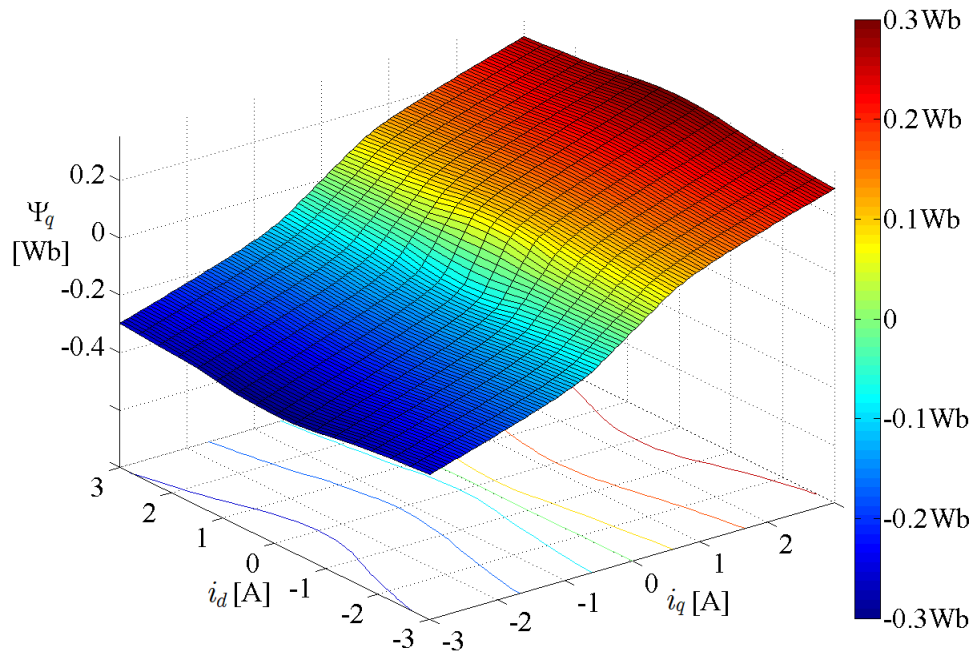
Figure 1.10: Quadrature axis stator flux Ψ_q dependency on stator current $\vec{i}_{dq}$
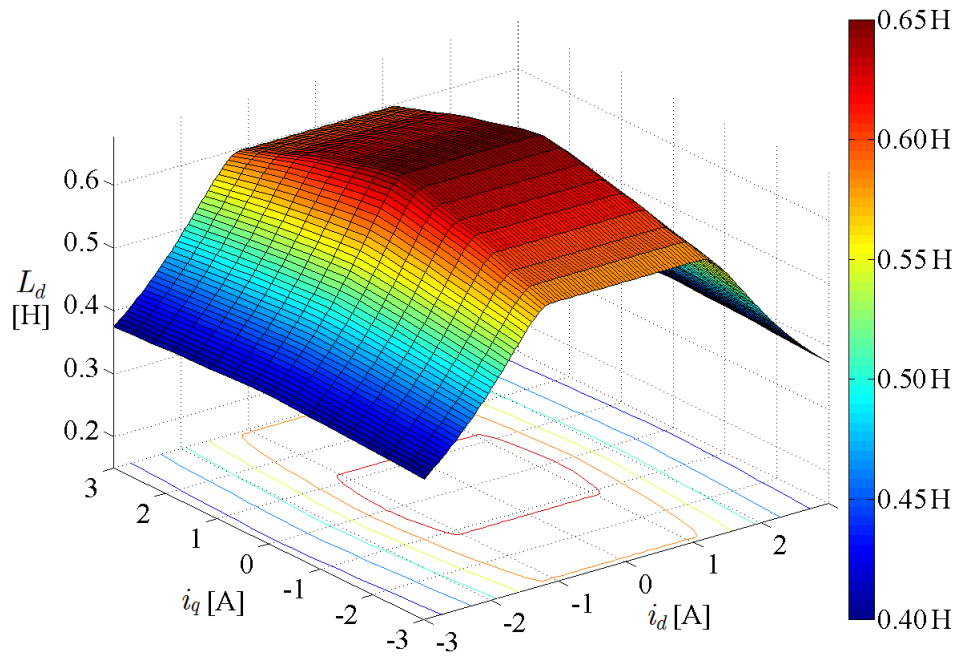
Figure 1.11: Direct axis static inductance L_d dependency on stator current $\vec{i}_{dq}$
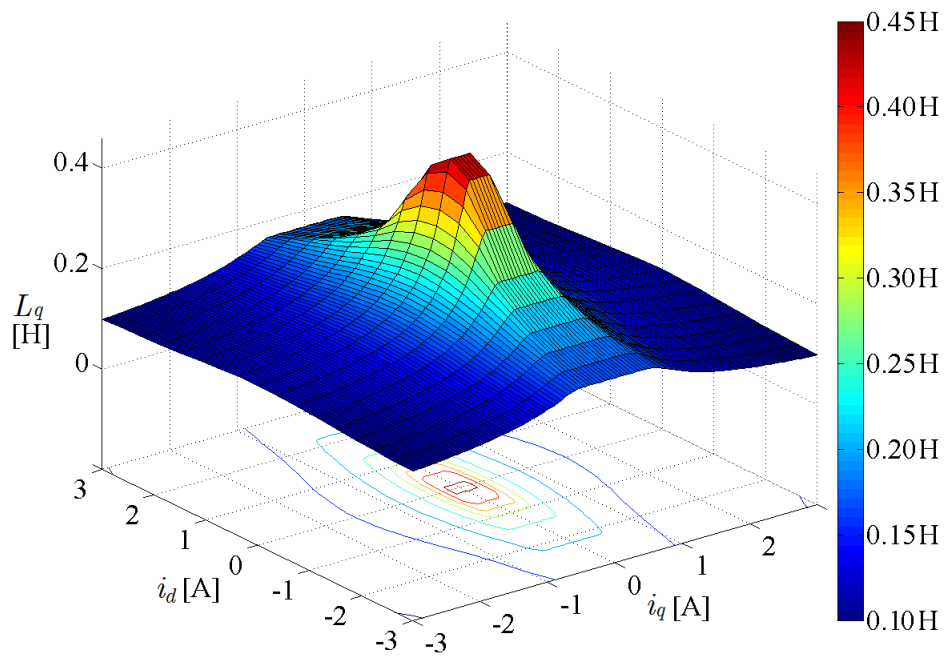
Figure 1.12: Quadrature axis static inductance L_q dependency on stator current $\vec{i}_{dq}$
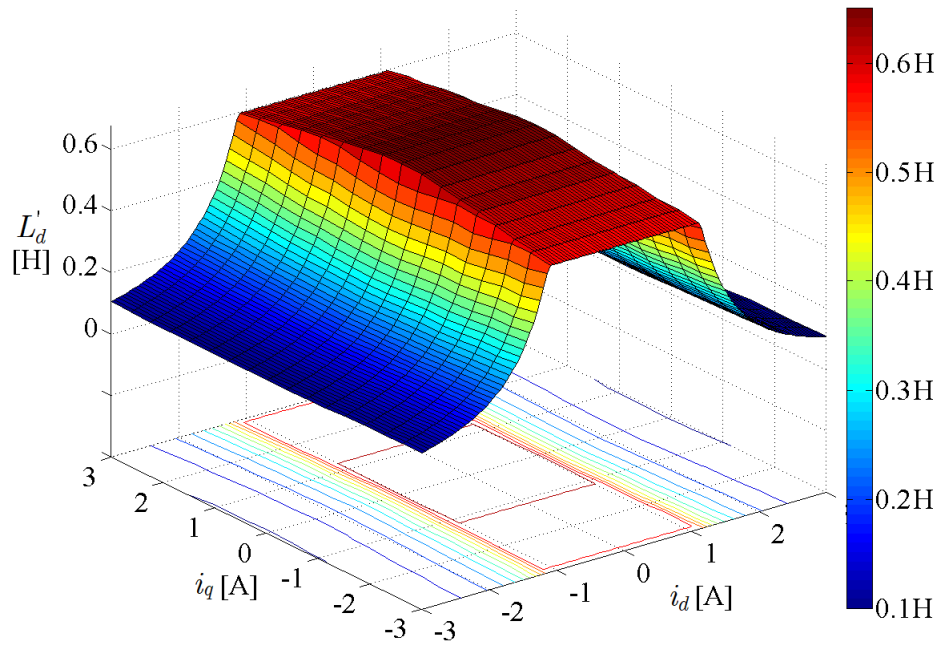
Figure 1.13: Direct axis dynamic inductance L'_d dependency on stator current $\vec{i}_{dq}$
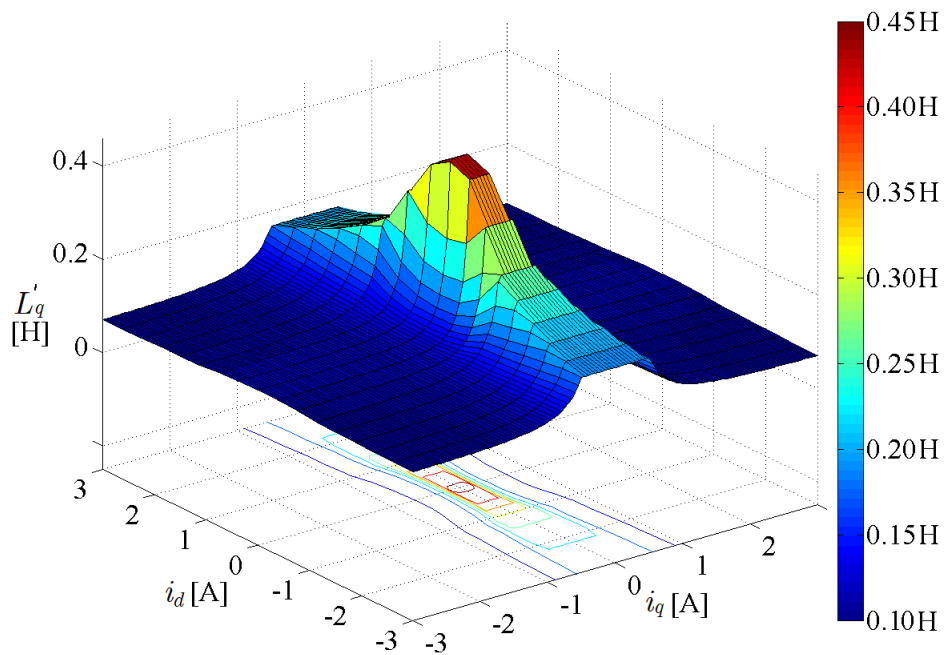
Figure 1.14: Quadrature axis dynamic inductance L'_q dependency on current $\vec{i}_{dq}$

The core-loss modelling resistance R_c was expressed by equation (1.12). Unlike for PMSM motors, where the permanent magnet flux is dominant when compared to generated stator flux, the simplification of assuming the stator flux amplitude to be

constant cannot be used. Hence, the R_c parameter has to be measured for both the rotor speed N_m and stator flux amplitude $|\vec{\Psi}_{dq}|$. The core-loss resistance R_c speed and flux characteristic is shown in Figure 1.12 and, similarly, the flux and speed dependency of core-loss coefficient K_m is shown in Figure 1.16. Both characteristics were acquired from core power loss estimation, which was determined as a difference between the measured machine input electrical power, output mechanical power, estimated Joule losses, and internal mechanical stator losses. Note that the missing map area for high speed and flux products could not be measured due to stator voltage limitation.

The SynRM model equation (1.18) is impacted by the ratio between R_c and R_s. It can be noticed that R_c can differ significantly based on the actual operating point, however, in general, the R_c is several hundred times higher than stator resistance R_s for all measured operation points. It can, therefore, be assumed, that accurate modelling of the non-linearity caused by saturation is going to have a higher impact on SynRM model accuracy than core losses. It can be also seen that coefficient K_m varies less than the resistance R_c, which makes it more suitable for online adaptation.
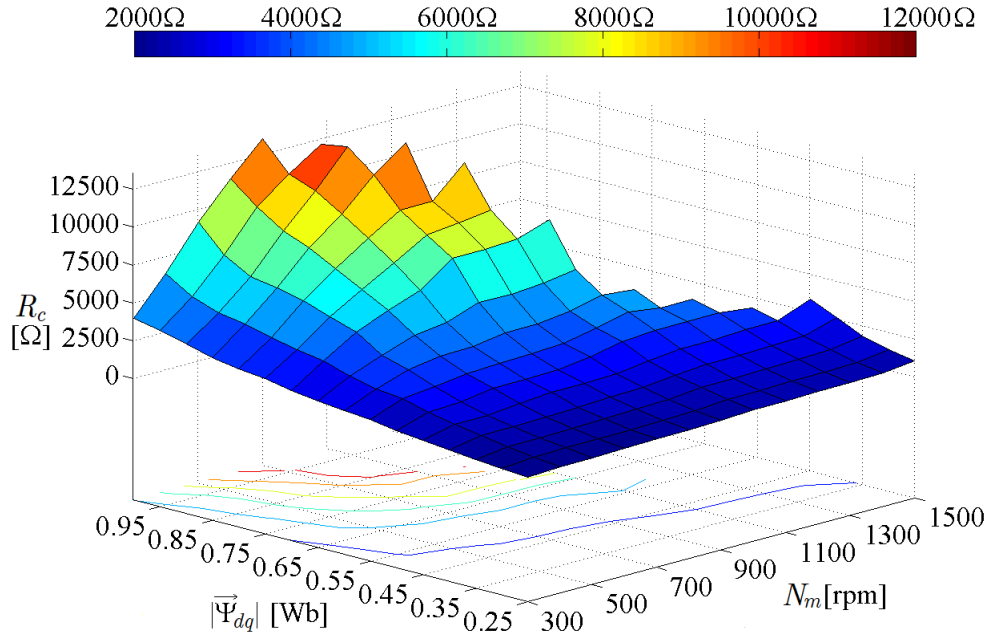
Figure 1.15: Core loss resistance R_c dependency on the amplitude of the stator flux $|\vec{\Psi}_{dq}|$ and the mechanical speed N_m
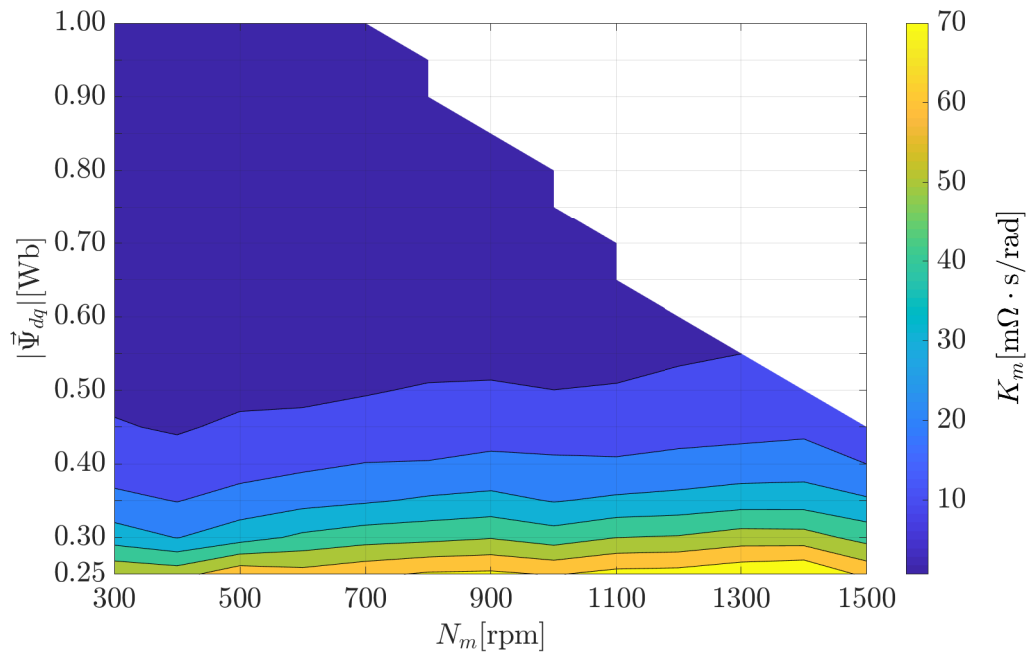
Figure 1.16: Core loss coefficient K_m dependency on the amplitude of the stator flux $|\vec{\Psi}_{dq}|$ and the mechanical speed N_m

2. SynRM Sensorless Control

Synchronous reluctance motors cannot be run from mains voltage, without special modifications like additional rotor cage winding [MDD+22]. The scalar or Volt per Hertz control, which is otherwise commonly used for AC induction machines, is not suitable as well. The reason is the problematic control stability leading to significant vibrations or even loss of synchronicity. The most commonly used classes of control algorithms are then the field-oriented control (FOC) and direct torque control (DTC). Classic DTC has several advantages compared to FOC, like the ability to achieve lower inverter switching losses, faster torque dynamic response, and relatively lower computational requirements. On the other hand, the DTC algorithms exhibit higher torque ripple at low speed and often lack the ability to directly control the stator current [CPST02, LBM94, WD15, XXLN91]. This thesis will, therefore, focus only on field-oriented control algorithms.

The SynRM sensorless vector control is very similar to the FOC of other motor types, especially the interior permanent magnet synchronous motor. Harmonic voltages, currents, and fluxes within the rotor-aligned dq-axis frame are turned into DC quantities, which allows the FOC to effectively control the machine stator flux and rotor torque by controlling dq-axis stator currents $\vec{i}_{dq}$ to track reference

$$\vec{i}_{dq}^{\text{req}} = \begin{bmatrix} i_d^{\text{req}} \\ i_q^{\text{req}} \end{bmatrix} = I_m^{\text{req}} \begin{bmatrix} \cos\theta_I^{\text{req}} \\ \sin\theta_I^{\text{req}} \end{bmatrix}, \tag{2.1}$$

where I_m^{req} is the amplitude and θ_I^{req} is the angle of stator current reference. As will be discussed later, the θ_I^{req} angle directly affects the SynRM efficiency and is the main focus of the efficiency optimizing algorithms.

High-level block diagram of the most common form of the FOC algorithm is shown in Figure 2.1. Stator current control loops are often based on direct and quadrature axis current PID-type controllers. Their control outputs might sometimes be compensated for the influence of the non-linear flux and speed products in (1.18) using a decoupling algorithm. This is, however, not critical because the integrators within the PID-type controller can handle the compensation as well. The stator current references $\vec{i}_{dq}^{\text{req}}$ are then set by the outer control loop or loops, which reflect the type of targeted application (e.g. whether the goal is the speed, position, or torque control).
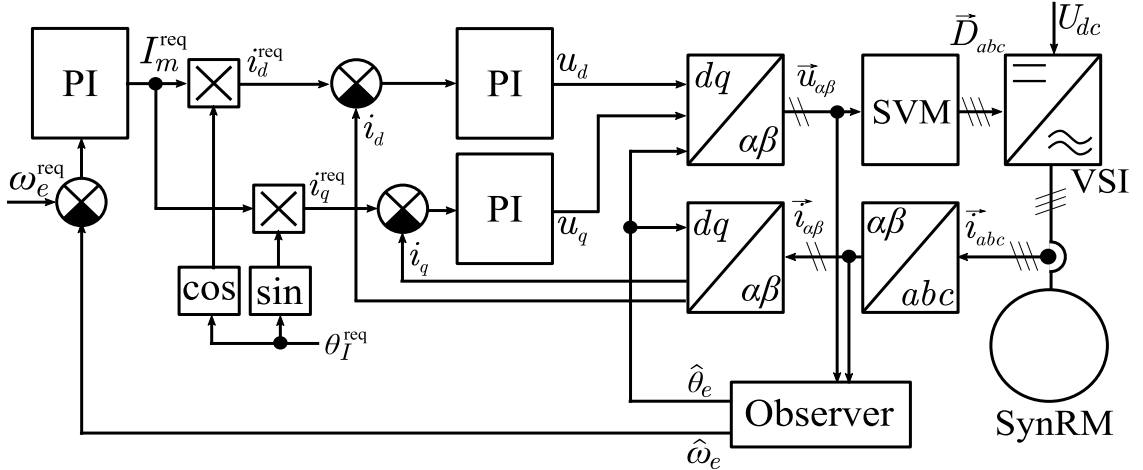
Figure 2.1: Generic block diagram of SynRM sensorless vector control

Such a PID-based cascaded control structure allows to build a high-performing drive system. That being said, alternatives are being proposed to bring further improvements. For example, the topic of model-based predictive control has been gaining attention in recent years, mainly because it allows straightforward and easy-to-understand tuning and constraint handling [Myn15,MVV16,VM17]. These methods are being adopted slowly by industry mainly because of the increased computational demands.

No matter the controller type, the resulting stator voltages $\vec{u}_{\alpha\beta}$ are translated to phase duty-cycle control signals $\vec{D}_{abc}$ and then applied to the machine using the Voltage Source Inverter (VSI) power stage. A generic block diagram of three-phase VSI is shown in Figure 2.2. There are many methods for obtaining the phase duty-cycles $\vec{D}_{abc}$ and the inverter control signals AT, AB, BT, BB, CT, and CB, with different properties like switching losses or a total harmonic distortion [KC17]. A very common is the use of the standard Space Vector Modulation (SVM), which principle is depicted in Figure 2.3. The two-state VSI can generate six active voltage vectors $\boldsymbol{v}_1$, $\boldsymbol{v}_2$, $\boldsymbol{v}_3$, $\boldsymbol{v}_4$, $\boldsymbol{v}_5$, and $\boldsymbol{v}_6$ and two zero voltage vectors $\boldsymbol{v}_0$ and $\boldsymbol{v}_7$. What voltage vectors are going to be applied and their durations $T_{\boldsymbol{v}_0}$ up to $T_{\boldsymbol{v}_7}$ during the PWM period T_{PWM} depends on the voltage vector $\vec{u}_{\alpha\beta}$ and SVM sector in which it resides. An example of the centre-aligned PWM (CAPWM) scheme for $\vec{u}_{\alpha\beta}$ residing in the first SVM sector is shown in Figure 2.4. Note that due to the finite switching time of the inverter transistor, the rising edges of the control signals must be delayed by the so-called dead-time T_{DT}. Its length depends on the type and technology of the used transistors and usually leads to distortion of the actually applied stator voltage vector and, therefore, must be compensated using suitable algorithm [LK97].

The rotor speed ω_e and especially the rotor position θ_e are critical for FOC. Both could be measured using a sensor. The drive realization without speed and position sensor, however, leads to lower cost and improvement in reliability. This, together with increasing capabilities of computation technology, lead to the development of sensorless control algorithms, which can estimate these quantities. The sensorless estimation algorithms can be classified based on the utilized physical principle.

The first class of algorithms utilizes the extended back-electromotive force (EEMF). These algorithms are using the machine model and require knowledge of actual ma-
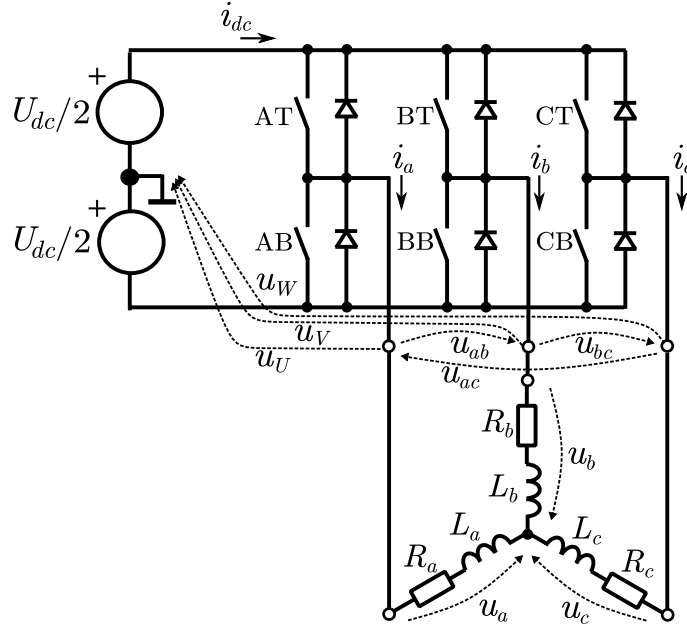
Figure 2.2: Block diagram of generic three-phase Voltage Source Inverter

	AT	AB	BT	BB	CT	CB
$\boldsymbol{v}_0$	0	1	0	1	0	1
$\boldsymbol{v}_1$	1	0	0	1	0	1
$\boldsymbol{v}_2$	1	0	1	0	0	1
$\boldsymbol{v}_3$	0	1	1	0	0	1
$\boldsymbol{v}_4$	0	1	1	0	1	0
$\boldsymbol{v}_5$	0	1	0	1	1	0
$\boldsymbol{v}_6$	1	0	0	1	1	0
$\boldsymbol{v}_7$	1	0	1	0	1	0

Inverter control signals
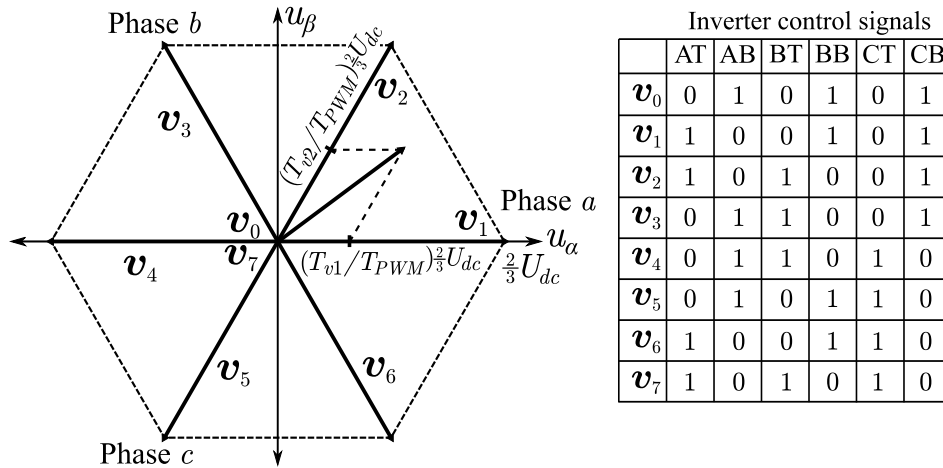
Figure 2.3: Standard space vector modulation voltage generation [MVB21]

chine parameters. The amplitude of EEMF voltage is increasing with the rotor speed and, therefore, these algorithms are suited for medium- to high-speed regions. Their use in low-speed region and standstill is, therefore, usually not possible due to high measurement noise [VPF96]. A short survey of several of the existing methods is then presented in Section 2.1.

The second class covers the rotor saliency-based algorithms. Some algorithms rely on high-frequency signal injection (HFI) into the fundamental control voltage or current. Demodulation of machine response signals then provides the rotor position information. The injected signal frequency upper limit is the inverter carrier PWM frequency and the bottom limit is given by the fundamental control algorithm frequency bandwidth. This usually means frequency in a range from hundreds of Hertz to units of kHz. Other saliency-based algorithms (e.g. the well known IN-FORM method) rely on excitation of stator currents by the phase PWM waveforms. Due to worse signal-to-noise ratio, it is often necessary to employ special current
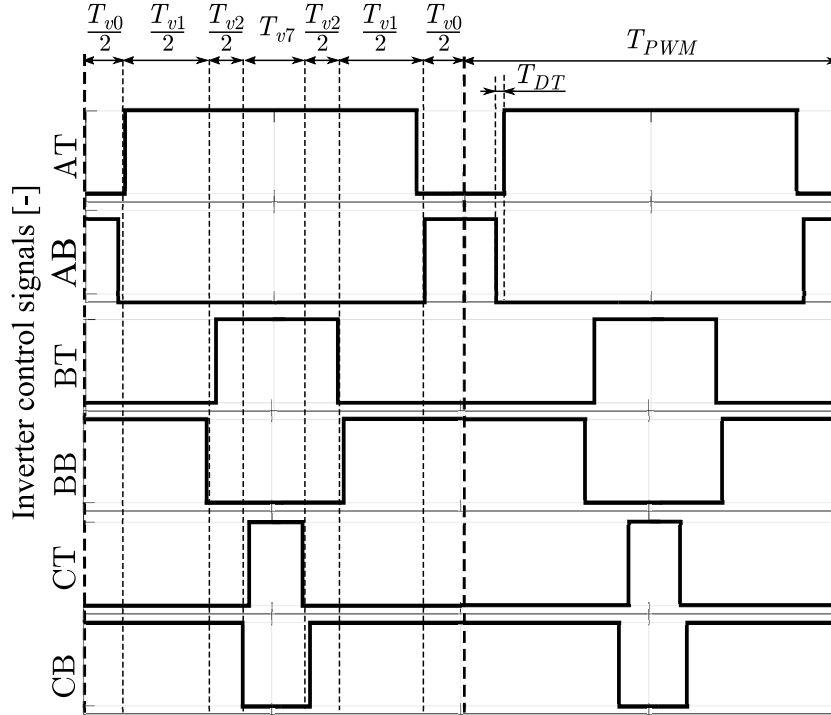
Figure 2.4: Example of the centre-aligned PWM waveform

derivative measurement sensors. General advantage of all saliency-based algorithms are their ability to operate from standstill and usually no need for exact knowledge of machine parameters. Some of these algorithms are then discussed in Section 2.2.

To exploit the advantages of both sensorless algorithm classes, hybrid algorithms were developed. The saliency-based principle is then used at standstill and low speed and with the increasing speed, the rotor speed and position estimation is transitioned to the EEMF-based algorithm. Selected algorithms from this class are going to be described further in Section 2.3.

As was shown in the previous Chapter 1, the SynRM is a highly non-linear system. In combination with machine parameter spread from manufacturing or changes caused by effects like the machine heating or wear an tear, the performance or even stability of the sensorless algorithms is going to be affected. The last section of this chapter is, therefore, going to deal with algorithms for online parameter estimation and adaptive sensorless SynRM control.

2.1. Algorithms Based on Back Electromotive Force

One of the more simple algorithms is the direct rotor position estimation method. It does not require a complicated observer algorithm, instead, the position is determined directly as

$$\widehat{\theta'_e} = \frac{1}{2} \arctan\left(\frac{u_\beta \sin\theta_I - u_\alpha \cos\theta_I + R_s I_m \cos 2\theta_I - L_0 I_m \frac{\mathrm{d}\theta_I}{\mathrm{d}t} \sin 2\theta_I}{u_\alpha \sin\theta_I + u_\beta \cos\theta_I - R_s I_m \sin 2\theta_I - L_0 I_m \frac{\mathrm{d}\theta_I}{\mathrm{d}t} \cos 2\theta_I} \right), \quad (2.2)$$

where $L_0 = \frac{1}{2}(L_d + L_q)$ is the average inductance. The acquired position is in range $\widehat{\theta}'_e \in \left(-\frac{\pi}{4}, \frac{\pi}{4}\right)$ and the resulting information is therefore ambiguous. To solve this problem, the position information (2.2) can be filtered as

$$\frac{\mathrm{d}\widehat{\theta}_e}{\mathrm{d}t} = -\tau \left[\left(\widehat{\theta}_e \bmod \pi \right) - \widehat{\theta}'_e \right], \tag{2.3}$$

where τ is the filter time constant. An advantage of the method is its simplicity and the fact that the average inductance L_0 information is used instead of the direct L_d and quadrature L_q inductances. On the other hand, the method neglects the magnetic saturation, which limits its usability at higher current and load [PSLK11].

Another simple but more commonly used rotor position estimation method is based on the simple stator flux estimator. Its principle lies in the integration of the equation (1.5), or

$$\widehat{\vec{\Psi}}_{\alpha\beta} = \begin{bmatrix} \widehat{\Psi}_\alpha \\ \widehat{\Psi}_\beta \end{bmatrix} = \int \left(\vec{u}_{\alpha\beta} - R_s \vec{i}_{\alpha\beta} \right) \mathrm{d}t, \tag{2.4}$$

where $\widehat{\vec{\Psi}}_{\alpha\beta}$ is the estimated stator flux vector. The rotor position can then be acquired as

$$\widehat{\theta}_e = \arctan \frac{\widehat{\Psi}_\beta}{\widehat{\Psi}_\alpha} - \sin^{-1} \sqrt{\frac{\frac{L_q^2 I_m^2}{\widehat{\Psi}_m^2} - \frac{L_q^2}{L_d^2}}{1 - \frac{L_q^2}{L_d^2}}}, \tag{2.5}$$

where $\widehat{\Psi}_m = \sqrt{\widehat{\Psi}_\alpha^2 + \widehat{\Psi}_\beta^2}$ is the stator flux amplitude. The algorithm implemented in this form is relatively simple. The pure integration in the relation (2.4), however, tends to drift due to noise presence and the R_s parameter inaccuracy. This issue is especially significant at lower speeds. To improve the situation, the pure integration is usually replaced with a low-pass first-order filter [LBM94, ATTM05].

The stator flux model in rotating dq-reference frame can be combined with the identical Luenberger-type observer. When neglecting the core losses, the following equations

$$\frac{\mathrm{d}\widehat{\vec{\Psi}}_{dq}}{\mathrm{d}t} = \vec{u}_{dq} - R_s \widehat{\vec{i}}_{dq} - \hat{\omega}_e \mathbf{Z} \widehat{\vec{\Psi}}_{dq} + \mathbf{K} \vec{i}_{dq}^{\,\mathrm{err}}, \tag{2.6}$$

$$\widehat{\vec{i}}_{dq} = \begin{bmatrix} \widehat{i}_d \\ \widehat{i}_q \end{bmatrix} = \begin{bmatrix} L_d & 0 \\ 0 & L_q \end{bmatrix}^{-1} \widehat{\vec{\Psi}}_{dq} = \mathbf{L}^{-1} \widehat{\vec{\Psi}}_{dq}, \tag{2.7}$$

can be obtained, where $\widehat{\vec{i}}_{dq}$ is the stator current estimate, $\vec{i}_{dq}^{\,\mathrm{err}} = \widehat{\vec{i}}_{dq} - \vec{i}_{dq} = \left[i_d^{\mathrm{err}}, i_q^{\mathrm{err}} \right]^{\mathrm{T}}$ is the stator current estimate error, $\mathbf{L}$ is the inductance matrix, and $\mathbf{K}$ is the gain matrix defined as

$$\mathbf{K} = \begin{bmatrix} k_{11} & k_{12} \\ k_{21} & k_{22} \end{bmatrix}. \tag{2.8}$$

The rotor speed is then obtained by observer adaptation so error i_q^{err} is driven to zero, which can be achieved by implementing controller

$$\frac{\mathrm{d}\hat{\theta}_e}{\mathrm{d}t} = \widehat{\omega}_e = \left(K_P + \frac{1}{p}K_I\right) i_q^{\mathrm{err}} = F_{PI}\left(p\right) i_q^{\mathrm{err}}, \tag{2.9}$$

where K_P and K_I are proportional and integral gains, p is differential operator $\mathrm{d}/\mathrm{d}t$, and $F_{PI}(p)$ is a differential function of PI controller. A disadvantage of this approach is the necessity of knowledge of static inductance matrix $\mathbf{L}$ in dq reference frame. It will be shown later in this chapter that this matrix can be estimated to achieve adaptive operation [TH14].

Similarly, the reduced observer estimating only the stator flux in the direct axis can be used. This leads to differential equations

$$\frac{\mathrm{d}\hat{\Psi}_d}{\mathrm{d}t} = u_d - R_s i_d + \hat{\omega}_e L_q i_q + k_1\left(\hat{\Psi}_d - L_d i_d\right), \tag{2.10}$$

$$\frac{\mathrm{d}\hat{\theta}_e}{\mathrm{d}t} = \frac{u_q - R_s i_q - L_q \frac{\mathrm{d}i_q}{\mathrm{d}t} + k_2\left(\hat{\Psi}_d - L_d i_d\right)}{\hat{\Psi}_d} = \hat{\omega}_e, \tag{2.11}$$

where k_1 and k_2 are the observer gains. The benefits of this approach are lower computational requirements than in the case of the previously shown full observer. On the other hand, it shows higher sensitivity to the presence of the measurement noise and the parameter inaccuracy [THHL10].

Likely the most widely used position and speed estimation algorithm is based on tracking of the extended electromotive force vector, which is generated as a result of rotor asymmetry. The voltage equations (1.10) and (1.11) can be rewritten as

$$\begin{aligned}
\begin{bmatrix} u_d \\ u_q \end{bmatrix} &= \begin{bmatrix} R_s + L_d'p & -\omega_e L_q \\ \omega_e L_q & R_s + L_d'p \end{bmatrix} \begin{bmatrix} i_d \\ i_q \end{bmatrix} + \left\{\left(L_d - L_q\right)\omega_e i_d - \left(L_d' - L_q'\right)p i_q\right\} \begin{bmatrix} 0 \\ 1 \end{bmatrix} = \\
&= \begin{bmatrix} R_s + L_d'p & -\omega_e L_q \\ \omega_e L_q & R_s + L_d'p \end{bmatrix} \vec{i}_{dq} + \begin{bmatrix} e_d \\ e_q \end{bmatrix},
\end{aligned} \tag{2.12}$$

where $\vec{e}_{dq} = [e_d, e_q]^{\mathrm{T}}$ is the EEMF vector, which can be acquired as shown in Figure 2.5. The synchronous rotor speed can then be acquired as

$$\widehat{\omega}_e = F_{PI}\left(p\right)\arctan\frac{-\hat{e}_d}{\hat{e}_q}. \tag{2.13}$$

The rotor position then can be obtained using a simple integration of speed (1.21). This algorithm is sometimes called tracking observer as it closes the phase-locked loop. An advantage of overall EEMF algorithm is that, although it is based on the model including the magnetic saturation, the $\vec{e}_{dq}$ vector calculation is dependent only on two parameters L_d' and L_q [ITDO06]. Note that it is also possible to imple-

ment the algorithm in the stator reference frame, where the rotor position can be
determined as

$$\hat{\theta}_e = \arctan\left(\frac{-\hat{e}_\alpha}{\hat{e}_\beta}\right). \tag{2.14}$$
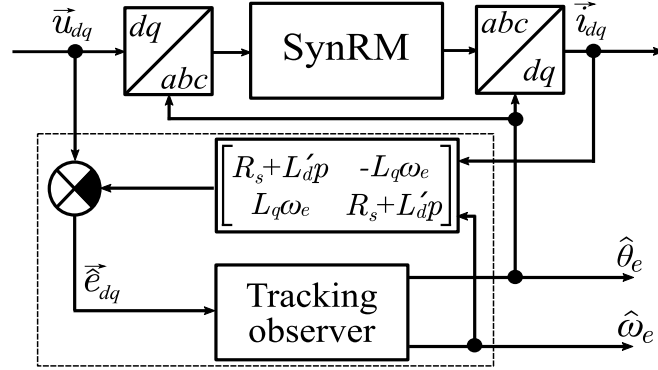
Figure 2.5: Simplified block diagram of the extended EMF and tracking observer

2.2. Saliency-Based Algorithms

Principle of the most well-known and basic high-frequency injection method can be
inferred from the SynRM model, where saturation and core losses are neglected,
the low-speed $\omega_e \to 0$ rad/s, and stator resistance voltage drop $R_s \vec{i}_{dq} \to 0$ V are
considered [JSH$^+$02]. The last mentioned condition can be afforded because in-
jected currents are of high frequency, and the stator reactance is much higher than
resistance or $\omega_{hf}^2 L_0 \gg R_s^2$. This leads to the simplified high-frequency model

$$\vec{u}_{dq} = \begin{bmatrix} pL_d & 0 \\ 0 & pL_q \end{bmatrix} \vec{i}_{dq}. \tag{2.15}$$

The dq reference frame position is unknown, therefore, the estimated rotating $\gamma\delta$
reference frame, shifted by error angle $\theta_e^{\mathrm{err}} = \hat{\theta}_e - \theta_e$, where $\hat{\theta}_e$ is the estimated angle,
will be introduced. Using the Park's transformation, the following voltage equation

$$\vec{u}_{\gamma\delta} = \begin{bmatrix} u_\gamma \\ u_\delta \end{bmatrix} = \begin{bmatrix} \cos\theta_e^{\mathrm{err}} & \sin\theta_e^{\mathrm{err}} \\ -\sin\theta_e^{\mathrm{err}} & \cos\theta_e^{\mathrm{err}} \end{bmatrix} \vec{u}_{dq} = \mathbf{T}_{\gamma\delta}^{dq}\left(\theta_e^{\mathrm{err}}\right) \vec{u}_{dq} \tag{2.16}$$

and current equation

$$\vec{i}_{dq} = \begin{bmatrix} \cos\theta_e^{\mathrm{err}} & -\sin\theta_e^{\mathrm{err}} \\ \sin\theta_e^{\mathrm{err}} & \cos\theta_e^{\mathrm{err}} \end{bmatrix} \begin{bmatrix} i_\gamma \\ i_\delta \end{bmatrix} = \mathbf{T}_{dq}^{\gamma\delta}\left(\theta_e^{\mathrm{err}}\right) \vec{i}_{\gamma\delta}, \tag{2.17}$$

can be obtained, where $\mathbf{T}_{\gamma\delta}^{dq}(\theta_e^{\mathrm{err}})$ and $\mathbf{T}_{dq}^{\gamma\delta}(\theta_e^{\mathrm{err}})$ are forward and inverse Park's transformation matrices. Including the above relations into equation (2.15) leads to model

$$
\begin{aligned}
\vec{u}_{\gamma\delta} &= \mathbf{T}_{\gamma\delta}^{dq}(\theta_e^{\mathrm{err}}) \begin{bmatrix} pL_d & 0 \\ 0 & pL_q \end{bmatrix} \mathbf{T}_{dq}^{\gamma\delta}(\theta_e^{\mathrm{err}}) \vec{i}_{\gamma\delta} = \\
&= \begin{bmatrix} L_0 + L_1 \cos 2\theta_e^{\mathrm{err}} & -L_1 \sin 2\theta_e^{\mathrm{err}} \\ -L_1 \sin 2\theta_e^{\mathrm{err}} & L_0 - L_1 \cos 2\theta_e^{\mathrm{err}} \end{bmatrix} p\vec{i}_{\gamma\delta},
\end{aligned}
\tag{2.18}
$$

where $L_1 = \frac{1}{2}(L_d - L_q)$ is the inductance difference and $L_0 = \frac{1}{2}(L_d + L_q)$ is the average inductance. The stator current vector can be expressed as

$$
\vec{i}_{\gamma\delta} = \frac{1}{L_d L_q} \begin{bmatrix} L_0 - L_1 \cos 2\theta_e^{\mathrm{err}} & L_1 \sin 2\theta_e^{\mathrm{err}} \\ L_1 \sin 2\theta_e^{\mathrm{err}} & L_0 + L_1 \cos 2\theta_e^{\mathrm{err}} \end{bmatrix} \frac{1}{p}\vec{u}_{\gamma\delta}.
\tag{2.19}
$$

The estimated position can be extracted using different types of injected voltage or current signal. Some methods rely on the injection of the voltage vector rotating with high frequency, however, use of harmonic or square signal injected into d or q axis can lead to smaller torque ripple. For example, using the injected signal $\vec{u}_{\gamma\delta} = [U_m \cos \omega_{hf}, 0 \text{ V}]^{\mathrm{T}}$ in the model (2.19) leads to

$$
\vec{i}_{\gamma\delta} = -\frac{U_m \cos \omega_{hf}}{L_d L_q \omega_{hf}} \begin{bmatrix} L_0 - L_1 \cos 2\theta_e^{\mathrm{err}} \\ L_1 \sin 2\theta_e^{\mathrm{err}} \end{bmatrix}.
\tag{2.20}
$$

Using the amplitude demodulation principle for current in the δ axis yields the error signal

$$
\varepsilon_{hfq} = \mathrm{LPF}\left\{ i_\delta \cos \omega_{hf} \right\} \cong \frac{U_m L_1}{2 L_d L_q \omega_{hf}} \sin 2\theta_e^{\mathrm{err}},
\tag{2.21}
$$

where LPF stands for low-pass filter. The final estimated rotor position and speed can be for example acquired using the phase-locked loop

$$
\frac{\mathrm{d}\hat{\theta}_e}{\mathrm{d}t} = \hat{\omega}_e = F_{PI}(p) \varepsilon_{hfq}.
\tag{2.22}
$$

As was already mentioned, there are many variations of this method, usually employing different types of injected voltage or current signals, more advanced demodulation methods, or phase-locked loop algorithms. To give an example, higher robustness can be achieved with a phase-locked loop, which includes the full mechanical machine model [WL00]. It is also possible to shift the $\gamma\delta$ reference frame by angle $\pi/4$ before demodulation and calculate the error θ_e^{err} as the difference of demodulation results in individual axes. This approach thus utilizes information from both axes, improving robustness [JSH$^+$02].

It can be noticed from equation (2.21) that the acquired position estimation is ambiguous. Thanks to the 180-degree rotor symmetry it, however, does not represent an issue because the produced torque will be the same (unlike in the case of PMSM machines, where the HFI algorithm also must provide correct permanent magnet polarity orientation).

It can also be noticed that the size of the error (2.21) is directly proportional to difference between axis inductances, which is significant in the case of the SynRM machine. On the other hand, the stator inductances of SynRM tend to be relatively large in the first place, which means that higher amplitude or lower frequency of injected voltage has to be applied to yield usable error signal θ_e^{err} level.

The signal injection leads to additional power losses, torque ripple, and audible noise. Some algorithms are, therefore, utilizing the inverter carrier PWM frequency as an excitation signal. When considering a centre-aligned PWM sequence generated using standard SVM as shown in Figure 2.4, the stator currents $\vec{i}_{abc}$ would be affected by the presence of voltage vectors as depicted in the example in Figure 2.6. The stator current slopes would differ for each phase due to the machine inductances. For example, the overall machine phase inductance L_{pha} measured between machine phase A and shorted phases B and C during $T_{v\mathbf{1}}$ would be

$$ L_{pha} = L_a + \frac{L_b L_c}{L_b + L_c}, \tag{2.23} $$

where

$$
\begin{aligned}
L_a &= \tfrac{L_d+L_q}{2} + (L_d - L_q)\cos\left(2\theta_e\right), \\
L_b &= \tfrac{L_d+L_q}{2} + (L_d - L_q)\cos\left[2(\theta_e - \tfrac{2\pi}{3})\right], \\
L_b &= \tfrac{L_d+L_q}{2} + (L_d - L_q)\cos\left[2(\theta_e + \tfrac{2\pi}{3})\right],
\end{aligned}
\tag{2.24}
$$

are position-dependent inductances. The measurement of stator current change during PWM cycle can, therefore, be used to extract the rotor position θ_e.
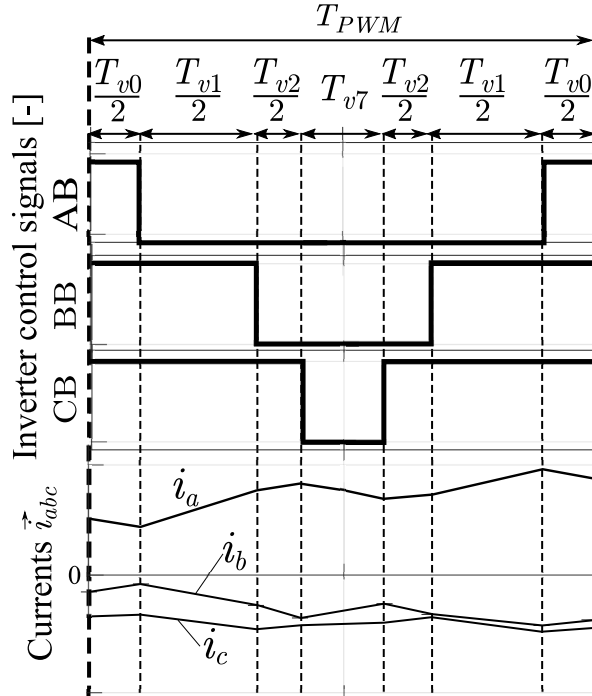
Figure 2.6: Example of stator current change during a single PWM period

A well-known example of algorithm using this principle is the Indirect Flux detection by Online Reactance Measurement (INFORM) method [HNS17]. Current

changes $\Delta \vec{i}_{abc} = [\Delta i_a, \Delta i_b, \Delta i_c]^{\mathrm{T}}$ are obtained during each PWM period to receive complex vector

$$c_{INF} = \frac{\Delta i_a}{\Delta T_a} + \frac{\Delta i_b}{\Delta T_b} e^{j\frac{4\pi}{3}} + \frac{\Delta i_c}{\Delta T_c} e^{j\frac{2\pi}{3}}, \quad (2.25)$$

where ΔT_a, ΔT_b, and ΔT_c are periods during which the current changes $\Delta \vec{i}_{abc}$ were measured. The resulting rotor position is obtained as

$$2\hat{\theta}_e = \arg(c_{INF}). \quad (2.26)$$

Fractions $\frac{\Delta i_a}{\Delta T_a}$, $\frac{\Delta i_b}{\Delta T_b}$, and $\frac{\Delta i_c}{\Delta T_c}$ in equation (2.25) are proportional to the phase reluctances, which brings a very interesting opportunity to measure the machine inductances at runtime as well [RSW18, RSW19].

When compared to HFI algorithms with explicit injection, the excitation by fundamental PWM causes only a small usable change in measured signals. Care then must be taken when implementing the stator current change measurement circuit. A special sensor (e.g. a current transformer) or PWM scheme must be often employed [NSS20, RSW18].

2.3. Hybrid Sensorless Algorithms

In order to achieve sensorless control in the full speed range, it is necessary to utilize a hybrid algorithm, which combines saliency-based principle at the low-speed region and EEMF-based principle at medium- to high-speed region. This section provides an overview of several such algorithms.

Probably the most commonly used approach is to operate low-speed and high-speed algorithms in parallel and combine the position estimates via a simple fuzzy transition function

$$\hat{\theta}_e = \alpha \hat{\theta}_e^{\mathrm{HFI}} + (1 - \alpha) \hat{\theta}_e^{\mathrm{EMF}}, \quad (2.27)$$

$$\alpha = \begin{cases} 1 & |\hat{\omega}_e| < \omega_{eLO}^{\mathrm{thr}} \\ 0...1 & |\hat{\omega}_e| \in \left\langle \omega_{eLO}^{\mathrm{thr}}, \omega_{eHI}^{\mathrm{thr}} \right\rangle, \\ 0 & |\hat{\omega}_e| > \omega_{eHI}^{\mathrm{thr}} \end{cases} \quad (2.28)$$

where θ_e^{HFI} and θ_e^{EMF} are position information obtained using the HFI and EEMF algorithm and $\omega_{eLO}^{\mathrm{thr}}$ and $\omega_{eHI}^{\mathrm{thr}}$ are speed transition thresholds between these two algorithms. Although this approach is very common, it can be expected, that higher robustness and smoother low- to high-speed region transition can be achieved via a single hybrid algorithm [HKS99].

Example of such approach is based on the EEMF observer algorithm (2.12), where the injection of the rotating stator current vector causes oscillation of the vector $\vec{e}_{\alpha\beta}$. Following amplitude demodulation of the vector $\vec{e}_{\alpha\beta}$ can provide the position information at low speeds. At higher speeds, where the position can be reliably acquired from EEMF, the injection stops. The algorithm, as it was pub-

lished, however, does not consider the magnetic saturation and cannot run with a full load [KSG$^+$14].

A different proposed hybrid algorithm is based on a modification of the observer (2.6). The estimated speed information $\hat{\omega}_e^{\mathrm{EMF}}$ is corrected at low speeds as

$$\frac{\mathrm{d}\widehat{\vec{\Psi}}_{dq}}{\mathrm{d}t} = \vec{u}_{dq} - R_s\widehat{\vec{i}}_{dq} - \left(\hat{\omega}_e^{\mathrm{EMF}} + \hat{\omega}_e^{\mathrm{HFI}}\right)\mathbf{Z}\widehat{\vec{\Psi}}_{dq} + \mathbf{K}\vec{i}_{dq}^{\,\mathrm{err}}, \tag{2.29}$$

where $\hat{\omega}_e^{\mathrm{HFI}}$ estimate is acquired from the HFI algorithm (2.22). It is usually necessary to limit the $\hat{\omega}_e^{\mathrm{HFI}}$ estimate and carefully chose the observer setup, otherwise, stability problems may occur [TH14].

2.4. SynRM Parameter Estimation

As it was shown in Chapter 1, the SynRM is significantly non-linear system, especially in thanks to magnetic saturation effect. The change of system parameters must be reflected in the control algorithm, otherwise, undesired effects might occur, like non-optimal power operation, deteriorated dynamic performance, or even loss of control stability. This leads to the topic of adaptive control.

A common approach is to identify parameter dependencies offline and store them into look-up tables. The suitability of such offline approach for mass production is, however, limited because of motor parameter spread during manufacturing and the time needed to conduct necessary measurements. This section will, therefore, further focus on online algorithms, which can provide machine parameter estimates during runtime, with only a rough previous parameter knowledge. A focus will be placed on commonly used and more computationally simple algorithms.

A well-known online parameter estimation method is the recursive least square algorithm with exponential forgetting (RLS), which is described generally calculated as

$$\mathbf{P}_k = \frac{1}{\lambda}\left(\mathbf{P}_{k-1} - \frac{\mathbf{P}_{k-1}\vec{\varphi}_k\vec{\varphi}_k^{\mathrm{T}}\mathbf{P}_{k-1}}{\lambda + \vec{\varphi}_k^{\mathrm{T}}\mathbf{P}_{k-1}\vec{\varphi}_k}\right), \tag{2.30}$$

$$\mathbf{\Theta}_k = \mathbf{\Theta}_{k-1} + \left(\vec{y}_k - \mathbf{\Theta}_{k-1}\vec{\varphi}_k\right)\vec{\varphi}_k^{\mathrm{T}}\mathbf{P}_k, \tag{2.31}$$

where $\mathbf{P}$ is the covariance matrix, $\vec{\varphi}$ is the vector of system inputs and outputs, $\mathbf{\Theta}$ is the matrix of unknown parameters, and $\vec{y} = \mathbf{\Theta}\vec{\varphi}$ is the vector of system outputs. The RLS implementation for SynRM with saturation, can be based on system

$$\begin{bmatrix} i_{\gamma,k} - i_{\gamma,k-1} \\ i_{\delta,k} - i_{\delta,k-1} \end{bmatrix} = \begin{bmatrix} a_{11} & a_{12} \\ a_{21} & a_{22} \end{bmatrix}\begin{bmatrix} i_{\gamma,k-1} \\ i_{\delta,k-1} \end{bmatrix} + \begin{bmatrix} b_{11} & b_{12} \\ b_{21} & b_{22} \end{bmatrix}\begin{bmatrix} u_{\gamma,k-1} \\ u_{\delta,k-1} \end{bmatrix} =$$
$$= \mathbf{A}\vec{i}_{\gamma\delta,k-1} + \mathbf{B}\vec{u}_{\gamma\delta,k-1}, \tag{2.32}$$

where $\mathbf{A}$ is the feedback matrix and $\mathbf{B}$ is the input matrix of the system state description. Relating to (2.30) and (2.31) then yields

$$\mathbf{\Theta}(k) = \begin{bmatrix} a_{11} & a_{12} & b_{11} & b_{12} \\ a_{21} & a_{22} & b_{21} & b_{22} \end{bmatrix}, \tag{2.33}$$

$$\vec{y} = [i_{\gamma,k} - i_{\gamma,k-1}, \; i_{\delta,k} - i_{\delta,k-1}]^{\mathrm{T}}, \tag{2.34}$$

$$\vec{\varphi} = \begin{bmatrix} i_{\gamma,k-1}, & i_{\delta,k-1}, & u_{\gamma,k-1}, & u_{\delta,k-1} \end{bmatrix}^{\mathrm{T}}. \tag{2.35}$$

The final estimated parameters then can be obtained as

$$\hat{R}_s = \frac{a_{11} + a_{22}}{b_{11} + b_{22}}, \tag{2.36}$$

$$\hat{L}'_d = \frac{2T_s}{b_{11} + b_{22} + C}, \tag{2.37}$$

$$\hat{L}_q = \frac{\hat{L}'_d}{2T_s\hat{\omega}_e} \left[a_{12} - a_{21} + \frac{C\left(\frac{2b_{12}(a_{11}+a_{22})}{b_{11}+b_{22}} + a_{12} + a_{21}\right)}{b_{11} - b_{12}} \right], \tag{2.38}$$

$$C = \sqrt{(b_{11} - b_{22})^2 + 4b_{12}b_{21}}, \tag{2.39}$$

where T_s is the discrete sampling period. To avoid the algorithm estimate divergence, it is necessary to continuously stimulate the system with a sufficiently rich signal. A common choice is, for example, the pseudo-random binary sequence (PRBS). The model in equation (2.32) and the following parameter calculation using (2.36) to (2.39) does not cover all the phenomenons occurring in the SynRM, such as the core-losses. The parameter estimates can, therefore, be biased. If such parameters are used for adaptation of position estimation and efficiency optimization algorithms, the resulting performance might suffer [ITDO06].

More simple adaptation method is based on the observer (2.6) and (2.7). The speed estimate is adapted based on the q-axis current error, as shown in equation (2.9). The d-axis current error then can be used for adaptation of one of the machine inductances as

$$\hat{L}_d = \int K_I \hat{L}_d i_d^{\mathrm{err}} \mathrm{d}t \quad \text{or} \quad \hat{L}_q = \int K_I \hat{L}_d i_d^{\mathrm{err}} \mathrm{d}t, \tag{2.40}$$

where K_I is the integral gain. The stator resistance adaptation for this algorithm was devised as well, which employs the HFI algorithm output as

$$\hat{R}_s = F_{PI}(p)\,\varepsilon_{hfq}. \tag{2.41}$$

In contrast to the hybrid algorithm (2.29), the stator resistance is being corrected here instead of the rotor speed estimate [Tuo14].

Similarly-simple adaptation approach was developed for the observer (2.4), which output is the estimated stator flux vector $[\widehat{\Psi}_\alpha, \widehat{\Psi}_\beta]^{\mathrm{T}}$. The stator inductance estimations can be acquired after the stator flux vector transformation into a rotating reference frame and a simple division as $\widehat{L}_d = \widehat{\Psi}_d/i_d$, and $\widehat{L}_q = \widehat{\Psi}_q/i_q$ [YAA09].

3. Efficiency Optimization

The potential to achieve high power efficiency is a key attribute of SynRM, which makes it a suitable replacement for the AC induction machine. The SynRM mathematical model was inferred in Chapter 1. As was shown, the SynRM is a non-linear system, which significantly complicates the exploitation of the possibility of high-efficient operation. Section 3.1, therefore, first presents the power loss model of the SynRM machine itself and definitions of optimal power loss operation. The power loss model of an inverter is briefly discussed in Section 3.2 because the inverter is a part of the overall drive system and its power losses are affected by the control algorithm as well.

Finally, the rest of this chapter presents an overview of algorithms designed to track the power-optimal operation point of SynRM. The power-loss optimization algorithms in the literature can be classified into two groups. The first class is for the loss-model controller algorithms or LMC, which are based on an accurate knowledge of the machine parameters and power loss model. The second class is for the search controllers (SC), which involve an active search of the optimal operating point based on the measured input power or related quantities. While the SC algorithms do not require previous knowledge of machine parameters, as the LMC algorithms do, their convergence time is usually slower and their operation requires a signal injection or operating point sweep, causing torque ripple and related small efficiency drops [QH13].

3.1. SynRM Power Loss Model and Optimization Strategies

The steady-state power balance in SynRM can be described by equation

$$P_{in} = P_{Cu} + P_{Fe} + P_{\omega} + P_m, \tag{3.1}$$

where P_{in} is the input electrical power, P_{Cu} is Joule power loss in the stator winding, P_{Fe} is the core power loss, P_{ω} is the internal mechanical power loss caused by viscous friction and ventilator, and $P_m = T_m \omega_m$ is the mechanical output power applied to the shaft. The total machine losses P_{loss} can be described as

$$
\begin{aligned}
P_{loss} =& P_{Cu} + P_{Fe} + P_{\omega} = R_s I_m^2 + R_c \left(i_{dc}^2 + i_{qc}^2 \right) + B_1 \omega_m^2 + B_2 \omega_m^3 = \\
=& R_s \left[\left(i_{d0} - \frac{\omega_e L_q i_{q0}}{R_c} \right)^2 + \left(i_{q0} + \frac{\omega_e L_d i_{d0}}{R_c} \right)^2 \right] + \\
& + \frac{\omega_e^2}{R_c} \left[(L_d i_{d0})^2 + (L_q i_{q0})^2 \right] + B_1 \omega_m^2 + B_2 \omega_m^3,
\end{aligned}
\tag{3.2}
$$

where B_1 is viscous friction coefficient and B_2 is a ventilator mechanical loss coefficient. This power-loss equation is graphically represented in Figure 3.1. The power-loss balance in a typical SynRM is often being compared with the induction machine in the current literature. When compared with a similar typical IE4 induc-

tion machine, the overall Joule losses are comparable in size but are all focused in the stator. The remaining P_{Fe} core and P_ω mechanical losses are usually similar in size as well. To give an idea of a typical SynRM machine nominal loss distribution, it was reported that for a four-pole 2.2 kW SynRM with 90 % nominal efficiency, the Joule losses contributed by 7.8 %, core losses by 1.7 %, and mechanical power losses by 0.5 % [JZL$^+$19].

$$P_{Cu} = R_s I_m^2$$
$$P_{Fe} = R_c\left(i_{dc}^2 + i_{qc}^2\right)$$
$$P_\omega = B_1\omega_m^2 + B_2\omega_m^3$$

P_{in}

$P_e = T_e\omega_e$

P_m
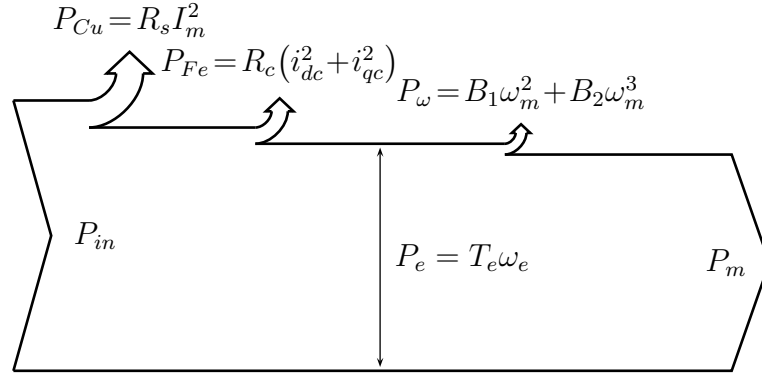
Figure 3.1: A general power diagram of SynRM

The internal mechanical losses P_ω are given by machine physical design and application, hence, their optimization is outside of the scope of this thesis. The power efficiency optimization is, therefore, considered to lie in the minimization of total electrical losses and achieving maximal electrical output power P_e at a given operating point. A SynRM power loss minimization problem is solved via optimization of the current angle θ_I^{req} (see the FOC block diagram in Figure 2.1). The fact, that there is always one power loss global minimum can be seen in Figure 3.3, which shows the simulated Joule loss P_{Cu} and core loss P_{Fe} dependency on the current angle θ_I and load torque T_l at nominal speed for the SynRM machine analysed in Section 1.2. Joule losses P_{Cu} in SynRM are clearly dominant in size, so their minimization will be a priority. Equation (3.2) shows that core losses P_{Fe} are dependent on the second power of the electrical speed ω_e and it is, therefore, beneficial to consider them when operating at medium- to the high-speed range. Several well-known criteria of SynRM power optimality, differing in considered loss model, will be introduced in the following text. Note that only the motoring region will be considered (i.e. the current angle will always be in range $\theta_I \in \left(0, \frac{\pi}{2}\right)$ rad).
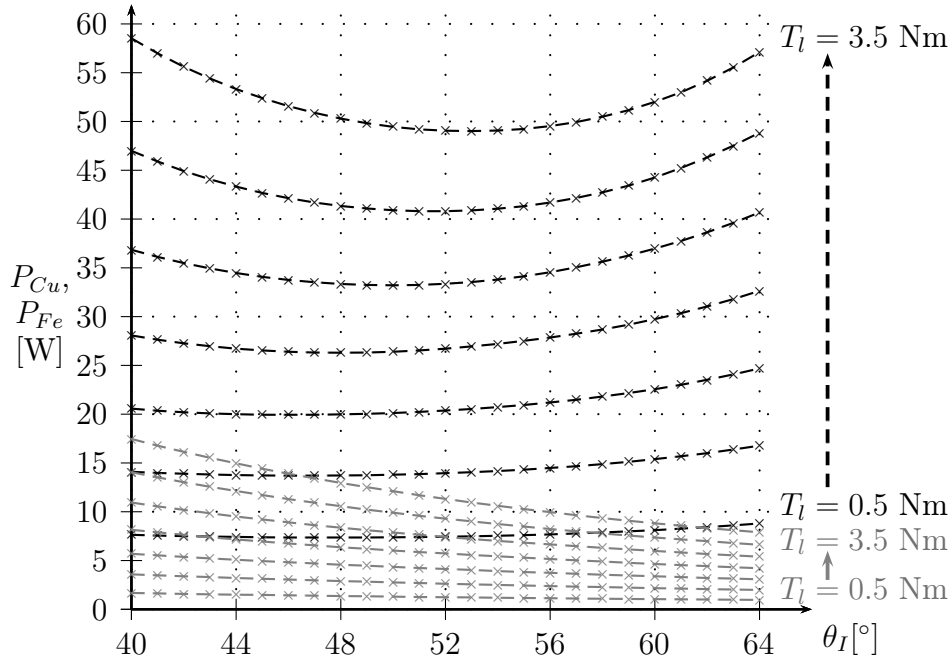
Figure 3.2: Simulated Joule losses P_{Cu} (black) and core losses P_{Fe} (grey) dependency on current angle θ_I and load T_l

The first well-known strategy is the *Maximal Power Factor Control* (MPFC). One of the disadvantages of SynRM is its poor power factor $\cos\theta_{ui}$, where θ_{ui} is the angle between stator current and voltage vectors [MDD+22]. The need to deliver relatively high reactive power leads to an increase in the current dimensioning of inverter, which is not desirable. To reach the optimal power factor, the

$$\frac{\mathrm{d}\cos\theta_{ui}}{\mathrm{d}\theta_I} = 0 \text{ rad}^{-1} \tag{3.3}$$

condition shall be maintained. When neglecting stator resistance, core losses, and saturation effect, the solution

$$\theta_I = \tan^{-1}\sqrt{\frac{L_d}{L_q}} \tag{3.4}$$

can be obtained [RFC10]. It was reported that the saturation effect has only a minor impact on the resulting MPFC-optimal angle θ_I and the stator resistance voltage drop is minor when compared to the drop on reactances, hence, the solution is relatively robust and often used in practical applications [FSM+22]. The MPFC, however, also sacrifices the achieved torque, therefore, it cannot be seen as optimal from electrical power efficiency point of view (i.e. it reduces acquisition cost rather than operation cost). Thus, the MPFC rule will not be considered further in this thesis.

The second criterion is the *Max Torque Per Ampere* (MTPA), which, as the name suggests, lies in the minimization of the stator current for a given torque, thus

effectively leading to minimization of Joule losses P_{Cu}. This can be alternatively expressed from torque equation (1.19) as

$$\frac{\mathrm{d}T_e}{\mathrm{d}\theta_I} = \frac{3}{4}P_p I_m^2 (L_d - L_q)\cos 2\theta_I = 0 \text{ Nm/rad,} \qquad (3.5)$$

where the MTPA-optimal operating point θ_I corresponds to minimal current I_m. The simulated stator current I_m dependency on current angle θ_I and load torque T_l at nominal speed for the SynRM machine shown in Section 1.2 is in Figure 3.3. The MTPA trajectory, which always crosses the stator current global minimum for given load torque, is marked by a thick line. Equation (3.5) would suggest a simple solution $\theta_I = \pi/4$, however, thanks to the saturation effect, the optimal trajectory is non-linear. The reason can be very well seen in the matching direct and quadrature inductance dependency in Figure 3.4 and Figure 3.5. Because the torque is proportional to $L_d - L_q$ difference, it is beneficial to saturate the q-axis even for small load torque and avoid d-axis saturation at higher load torques. Both effects result in the increase of the optimal current angle $\theta_I > \pi/4$ for low and high loads, while at medium load, the current angle drops toward the theoretical $\pi/4$ value.
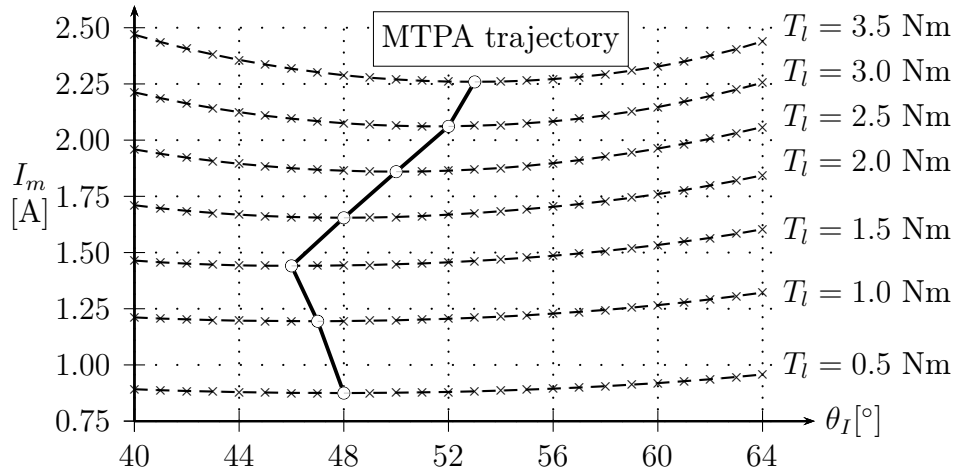
Figure 3.3: Simulated stator current I_m dependency on current angle θ_I

50
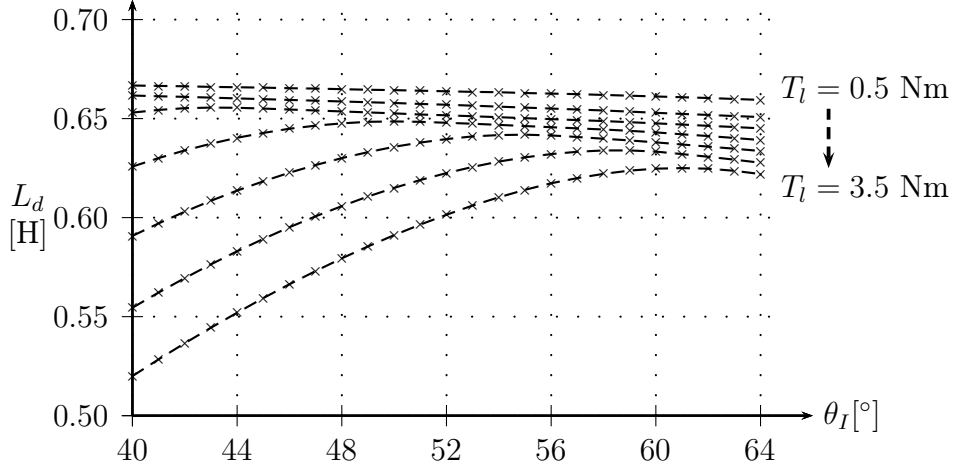
Figure 3.4: Simulated direct-axis inductance L_d dependency on current angle θ_I
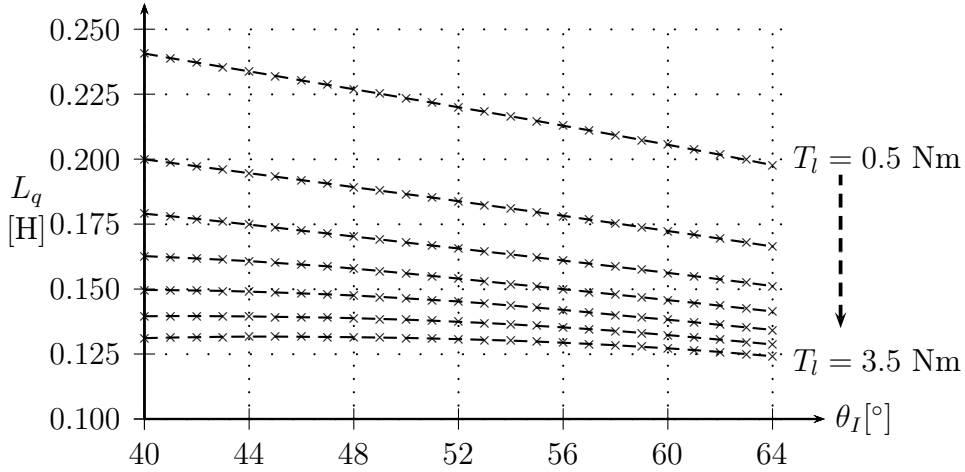
Figure 3.5: Simulated quadrature-axis inductance L_q dependency on angle θ_I

The third criterion is called the *Maximum Efficiency* (ME) operation and it minimizes both Joule losses P_{Cu} and core losses P_{Fe}. The simulated dependency of input power P_{in} and efficiency $\eta = P_e/P_{in}$ on current angle θ_I and load torque T_l at nominal speed for the SynRM machine shown in Section 1.2 is in Figure 3.6 and Figure 3.7. The ME trajectory was marked by a thick line. The saturation, which was affecting MTPA trajectory, is still visible, however, because the core losses are now being taken into account as well, the optimal current angle is generally increased. This is tied to the fact that the core losses P_{Fe} are decreasing with the higher current angle θ_I, as can be seen in Figure 3.2. The root cause is the decrease of stator flux vector amplitude $|\vec{\Psi}_{dq}|^2 = \Psi_d^2 + \Psi_q^2 = L_d^2 i_d^2 + L_q^2 i_q^2$, where $L_d \gg L_q$ and i_d drops with higher current angle θ_I.
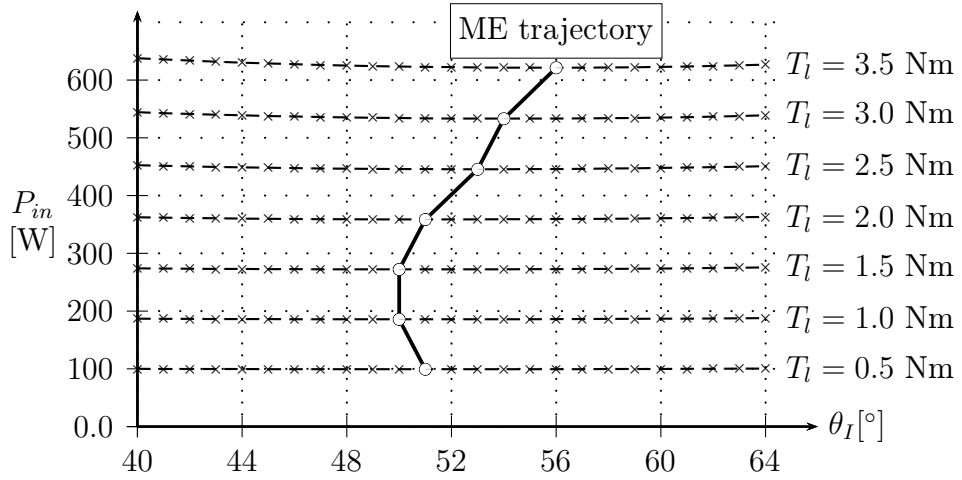
Figure 3.6: Simulated input power P_{in} dependency on current angle θ_I
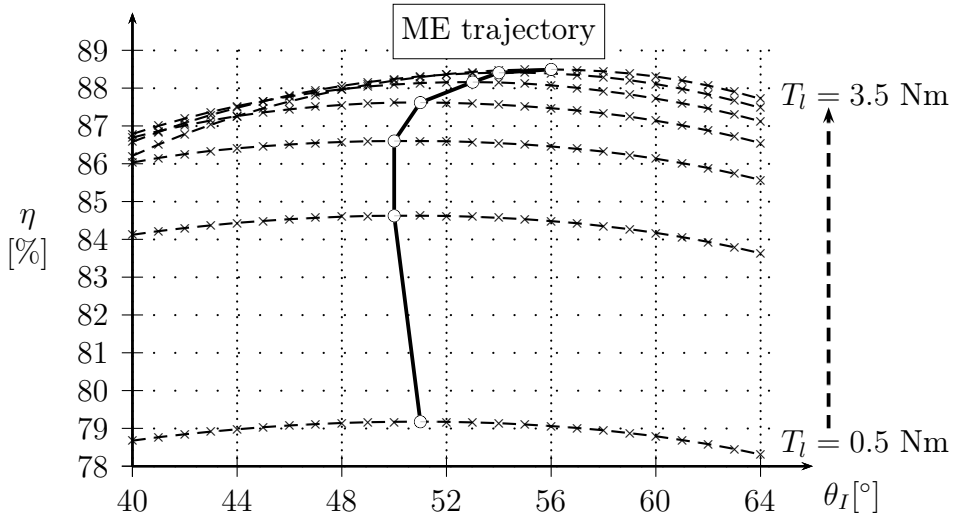
Figure 3.7: Simulated maximum efficiency curve

The simulated comparison of the MTPA and the ME criteria current angle θ_I trajectories is shown in Figure 3.8. The ME trajectory is several degrees higher than the MTPA trajectory, however, the shape of both trajectories is similar. This confirms that the saturation is a dominating non-linear phenomenon when it comes to the SynRM efficiency optimization.
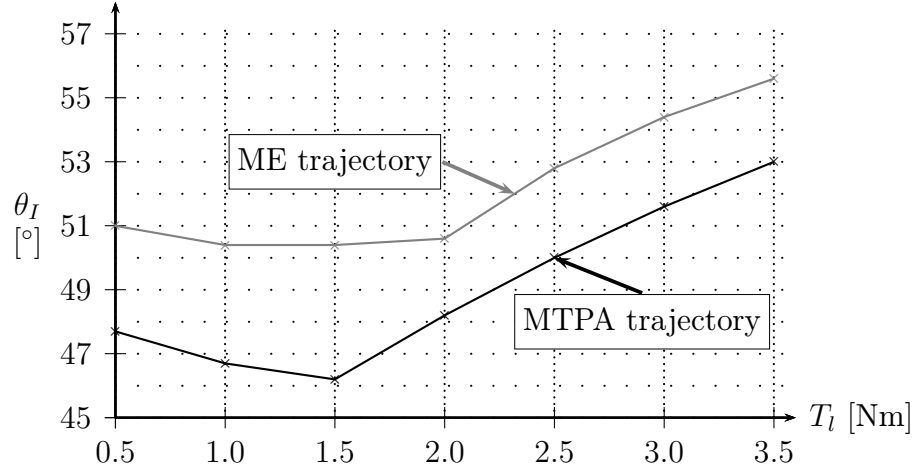
Figure 3.8: Simulated MTPA and ME optimal criterion comparison load torque T_l dependency

3.2. Inverter Power Losses

This section discusses a power loss model of a two-state three-phase voltage source inverter as shown in Figure 2.2 and its impact on ME and MTPA criteria defined in the previous section. The inverter power losses P_{inv} are not trivial to model due to a number of non-linear dependencies and dynamic phenomenons taking an effect. In general, the losses in inverter semiconductor elements can be described as a sum of conductive power losses P_{con}, switching power losses P_{sw}, and blocking losses. The latter one will be neglected in further discussion due to very low magnitude. To be able to model the resulting losses and evaluate their magnitude, the Insulated Gate Bipolar Transistors (IGBT) semiconductor technology represented by power module FNB41560 will be assumed in the following text as a reference [Sem12,Sem14,RK20]. This IGBT technology was chosen for its popularity and the FNB41560 platform for its use in experimental verification described in Chapter 6.3.

Conductive losses are occurring in both the transistor and the freewheeling diode of the inverter in each of its $N \in \{a, b, c\}$ phases. The conductive losses of the IGBT transistor are caused by finite collector-emitter saturation voltage $U_{CE(SAT)}$ of the fully open transistor. Similarly, the conducting freewheeling diode exhibits voltage drop U_{DF}. The exact values of both voltages vary with phase current i_N and the transistor temperature ϑ. Such characteristics are usually provided by the semiconductor manufacturer. For example, these characteristics for FNB41560 are shown in Figure 3.9. Conductive losses P_{conN} for phase N during single PWM period $T_s = T_{PWM}$ can be modelled as

$$
\begin{aligned}
P_{conN,k} &= D_{N,k}|i_{N,k}|U_{CE(SAT),k} + (1 - D_{N,k})|i_{N,k}|U_{DF,k} \text{ for } i_{N,k} > 0 \text{ A}, \\
P_{conN,k} &= (1 - D_{N,k})|i_{N,k}|U_{CE(SAT),k} + D_{N,k}|i_{N,k}|U_{DF,k} \text{ for } i_{N,k} < 0 \text{ A},
\end{aligned}
\tag{3.6}
$$

where $i_N \in \{i_a, i_b, i_c\}$ is a phase current and $D_N \in \{D_a, D_b, D_c\}$ is phase duty cycle at discrete time k.

53
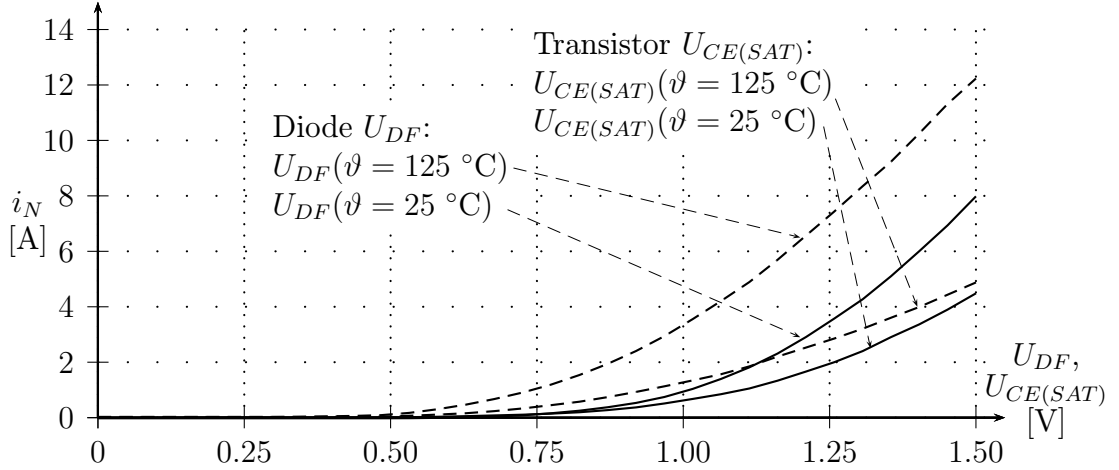
Figure 3.9: Typical voltage drop dependency of FNB14560 transistors and diodes on collector current or diode current i_N and temperature ϑ [Sem12]

The switching losses occur as a result of energy loss during the transistor and diode close-open transition and are a function of the operating frequency $1/T_{PWM}$, inverter supply voltage U_{dc}, temperature of semiconductor ϑ, and inverter load type (i.e. inductive, capacitive, or pure real). Usually, the switching losses are modelled as transistor switch-on, switch-off, and freewheeling diode recovery energy losses. Again, such characteristics are usually provided by the semiconductor manufacturer and the example for FNB41560 is shown in Figure 3.9. Note that energies in Figure 3.10 were linearly scaled for DC-bus voltage of $U_{dc} = 400$ V. The immediate discrete inverter switching power-loss at the discrete time k for phase N can be modelled as

$$P_{swN,k} = \frac{K_{sw}}{T_{PWM}}[E_{on,k} + E_{doff,k} + E_{off,k}], \tag{3.7}$$

where $E_{on,k}$ is switch-on, $E_{off,k}$ is switch-off, and $E_{doff,k}$ is diode reverse recovery loss energy at the discrete time k. The K_{sw} is a number of switch-on and switch-off events per PWM period T_{PWM}. For commonly used PWM switching schemes, like the centre-aligned PWM shown in Figure 2.4, the K_{sw} coefficient is equal to two. There can, however, be schemes with a different number of events (e.g. discontinuous PWM or schemes for single-shunt phase current measurement).

54
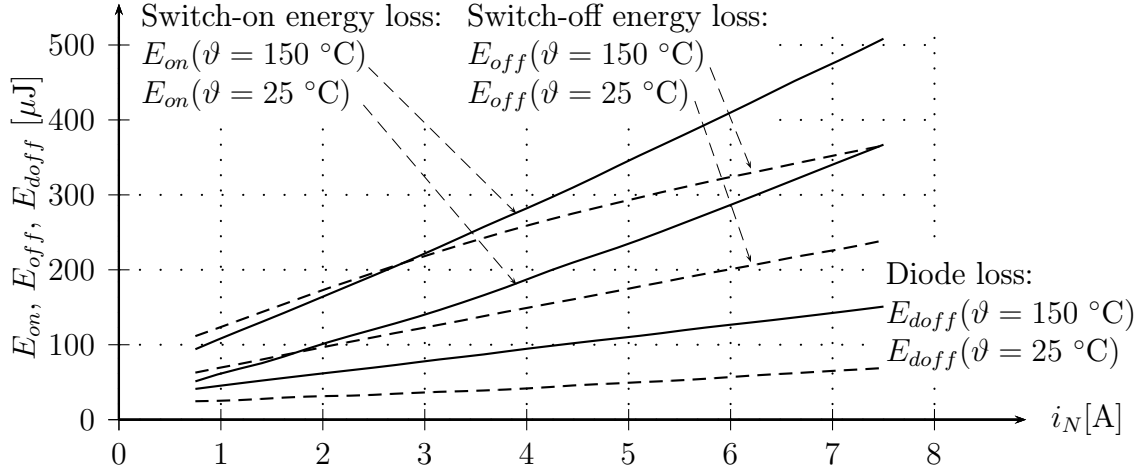
Figure 3.10: Dependency of energy losses of FNB14560 IGBT inverter module on collector and diode current i_N and temperature ϑ for inductive load at $U_{dc} = 400$ V [Sem14]

To establish an idea of inverter losses magnitude in comparison to SynRM losses, both the conductive power losses P_{con} and the switching power losses P_{sw} were simulated for the reference IGBT power module FNB14560. Note that the simulation was done for $1/T_{PWM} = 10$ kHz, $\vartheta = 75$ °C, and the $\vec{D}_{abc}$ duty cycles were obtained using Standard Vector Modulation, as depicted in Figure 2.3. Based on the model (3.6), the conductive power losses P_{con} are dependent on amplitudes of the phase current vector $\vec{i}_{dq}$ and the phase voltage vector $\vec{u}_{dq}$, as well as the angle between them $\arg(\vec{u}_{dq}) - \arg(\vec{i}_{dq})$. As the simulation results in Figure 3.11 show, the conductive losses are relatively insensitive to voltage vector $\vec{u}_{dq}$ and can be considered to be linearly growing with amplitude of stator current $I_m = |\vec{i}_{dq}|$. The result of modelling of switching losses P_{sw} is in Figure 3.12. Again, a clear linear dependency on the amplitude of stator current I_m is visible, although a higher power loss magnitude is reached when compared to conductive losses.

While it is understood, that different semiconductors will yield different power loss levels, the linear dependency on the stator current amplitude I_m is generally applicable. Minimization of semiconductor power losses is, therefore, aligned with the MTPA criterion. If the ME criterion is changed to take the semiconductor losses into account, it will increase an influence of I_m amplitude minimization to ME trajectory, moving the θ_I angle closer to the MTPA trajectory. This is also confirmed by simulation, as shown in Figure 3.13. The shift of the optimal ME trajectory is, however, only minor for the simulated SynRM and inverter, making the inverter power losses less significant for θ_I selection.
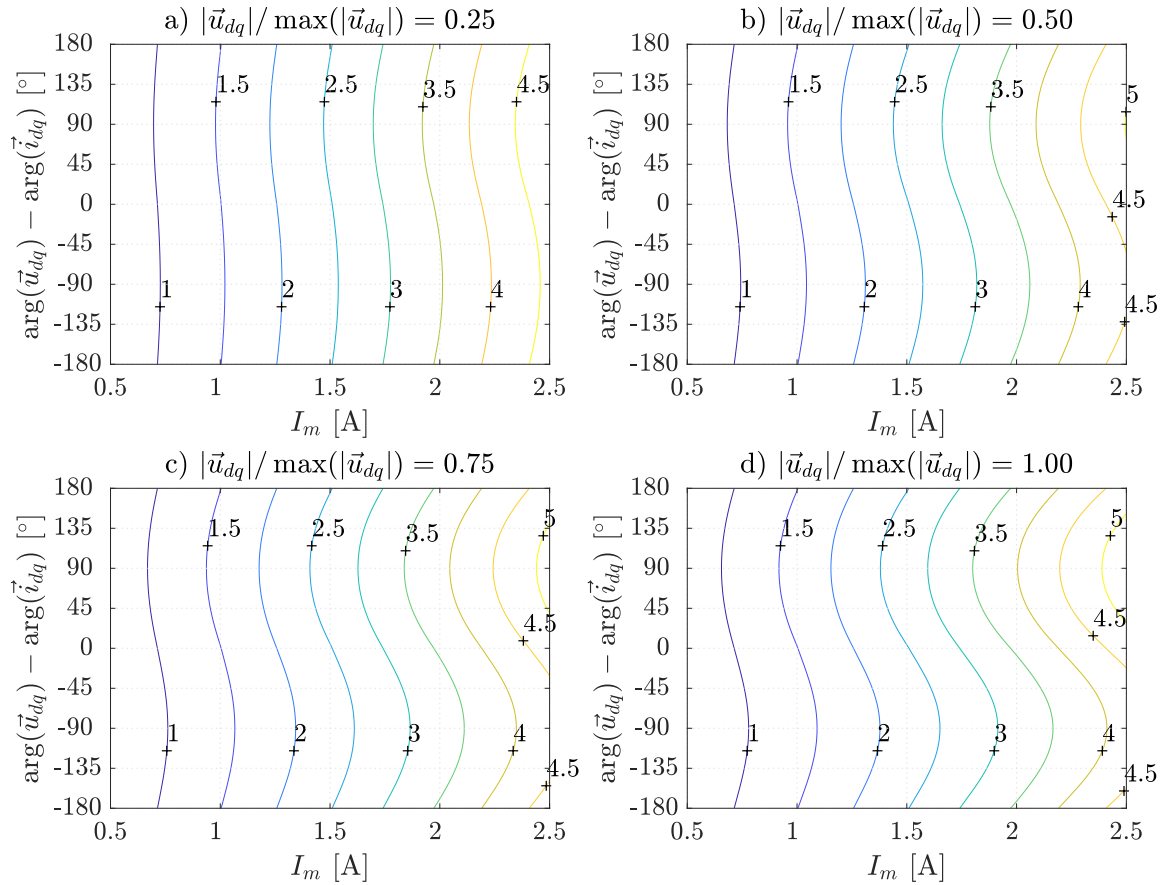
Figure 3.11: Simulated conductive losses P_{con} of IGBT FNB14560 three-phase power module in Watts
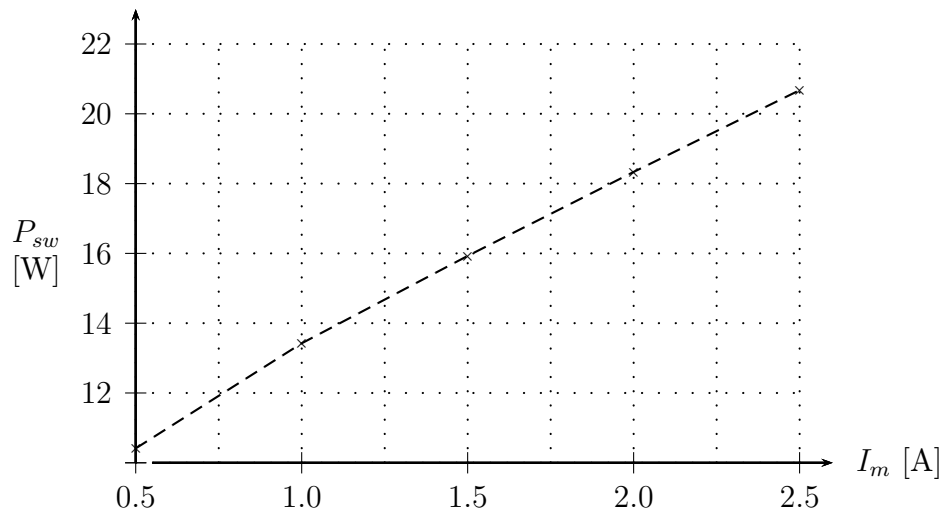
Figure 3.12: Simulated switching losses P_{sw} of FNB14560 IGBT three-phase power module at 10 kHz
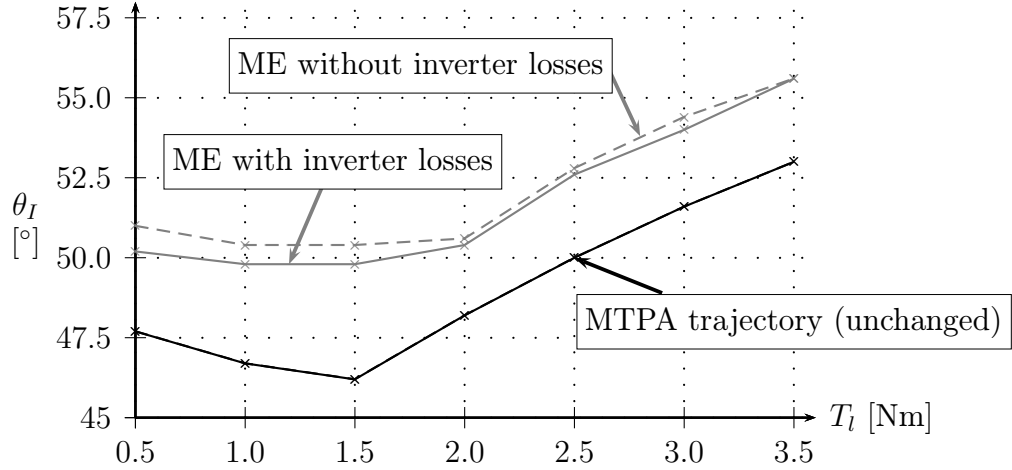
Figure 3.13: Simulated MTPA and ME trajectories with semiconductor losses in reference FNB14560 IGBT module taken into account

3.3. Loss-model Controller Optimization Algorithms

Probably the most well-known Loss-model Controller (LMC) optimization algorithm is the constant $\theta_I = \pi/4$ angle setup, following the ideal MTPA rule. As it was already discussed in Section 3, the same torque can be achieved with a different amplitude of the stator current, which is also shown in Figure 3.3. When neglecting the core losses and magnetic saturation, the MTPA criterion can be acquired from equation (3.5), where the optimal current angle is $\theta_I^{\mathrm{opt}} = \pi/4$. This algorithm is very simple and common, however, omitting both the core losses and the saturation results in a sub-optimal solution and the ME optimal angle is always going to be higher than 45°.

Another option is the ME optimal current angle calculation based on model (3.2). For example, if the saturation is neglected and the core loss modelling resistance R_c is considered to be constant, the optimal angle can be obtained as

$$\theta_I^{\mathrm{opt}} = \arctan \sqrt{\frac{R_s R_c^2 + (R_s + R_s)\omega_m^2 L_d^2}{R_s R_c^2 + (R_s + R_s)\omega_m^2 L_q^2}}. \tag{3.8}$$

Because the assumption $L_d > L_q$ is always true, the solution is always $\theta_I > \pi/4$ [KS96a].

There are various LMC algorithms (Kalman filtration, neuron networks, fuzzy logic systems, and more), which provide sub-optimal current angle solutions by omitting the saturation. This is a notable simplification because the analytical description of saturation dependency is non-trivial. On the other hand, the sub-optimal solution might diverge from the optimal value significantly, especially for higher loads, where the saturation is more significant [QH13].

A relatively simple analytical solution, which takes saturation into account, can be acquired when only the direct axis saturation is considered using a simple model

$$L_d = \begin{cases} L_{d0} & \text{for} \quad |i_d| < I_d^{\text{thr}}, \\ L_{d0} - \beta(i_q - I_d^{\text{thr}}) & \text{for} \quad |i_d| > I_d^{\text{thr}}, \end{cases} \tag{3.9}$$

where L_{d0} is non-saturated inductance and β is the slope of decrease of the inductance L_d once the d-axis stator current raises above saturation threshold I_d^{thr}. The sub-optimal stator current angle can then be acquired as

$$i_d^{\text{opt}} = -\frac{G_d i_q^2}{2(1 - G_d i_d)} + \sqrt{\left[\frac{G_d i_q^2}{2(1 - G_d i_d)}\right]^2 + i_q^2}, \tag{3.10}$$

where

$$G_d = \frac{\beta}{L_{d0} - L_q + \beta i_d} \tag{3.11}$$

is a help function [Mad03].

When trying to include saturation in both the direct and quadrature axis as well as the core loss non-linearity, there is no simple analytical solution and numerical approaches are often employed instead. The experimental results for some of the published non-adaptive LMC algorithms show a relatively fast convergence. An example of such algorithm involved repeated calls of a mathematical function, which output converges to the optimal current value in the direct axis i_d^{opt}. Thanks to inclusion of core losses into the model, the solution could be considered to be close to the actual ME criterion [YAA09]. Other algorithm example utilized a finite-element model of the machine to get accurate inductance maps and derived MTPA online tracking law afterwards [WJPK22].

The inductance current-dependency maps (like, for example, in Figure 1.10 and Figure 1.11) must be available for the saturation-modelling LMC algorithms to find the optimal current angle. This usually requires offline measurement. It also naturally complicates the use of these algorithms in adaptive systems (e.g. a need to compensate for inductance changes caused by machine temperature deviations). To obtain such inductance characteristics online, the parameter estimation algorithms described in Section 2.4 might be required to be operated in multiple operation points (e.g. to temporarily operate machine at sub-optimal current angles as well). Such an adaptive LMC algorithm would be then gain some of the negative properties of search algorithms like a longer convergence time, the need to change the optimized quantity, and usually a need to achieve a steady-state (see more details in Section 3.4).

Last but not least is the current angle trajectory tracking via look-up table (LUT) defining the non-linear $\theta_I^{\text{opt}} = f(I_m)$ relation (similar to the trajectory in Figure 3.8). Although this method does not rely on the machine model and, thus, does not entirely fit the LMC algorithm definition, its practical properties (i.e. convergence time, and no injections are involved) are matching the LMC-type algorithms and will be classified as such in this thesis. The current angle LUT is often employed in

the industry, because of its low computational demands, a relatively simple offline acquisition, and an instant convergence time [FZYJ20]. Use in adaptive systems, however, requires special considerations as well, like, for example, having multiple look-up tables for different temperature ranges or online table updates using search algorithms.

3.4. Search Controller Optimization Algorithms

In general, these algorithms rely on the measurement of the SynRM input power or stator current amplitude (depending on the selection of MTPA or ME tracking strategy), where the optimized quantity (usually the current angle θ_I or the direct axis current i_d) is being swept so the direction towards the optimal operation point can be determined. The benefits of these algorithms are usually low computational effort, the fact that the optimal operating point is found without previous machine parameter knowledge (i.e. natural adaptivity), or a need for accurate rotor position information. On the other hand, these algorithms might require a steady-state load, a relatively long convergence time, and a prolonged time spent outside of the power-optimal operation point, which reduces achieved efficiency [DTCB22, QH13].

The search controller algorithms can be divided into three categories:

1. *Algorithms with a discrete search step*, which gradually increase or decrease the current angle by a discrete value. The size of the step and the ability to find the optimal operating point with continual oscillations around it depends on the selected algorithm. The most simple and also the least effective approach involves an increase of the reference value by n steps and consequent decrease by $2n$ steps. The input power measurement then provides the location of the optimal operating point or at least direction towards it. The number of necessary iterations, which must be taken to find the optimal point, can be reduced, for example, using the Fibonacci search algorithms or fuzzy-logic-based algorithms [DTCB22, QH13].

2. *Continuous search* or *low-frequency injection algorithms*, which change the optimized variable as a smooth function, which, compared to discrete step algorithms, reduces undesired torque ripple. The optimized current angle can be swept, for example, using a ramp function. This will again provide the location of the optimal operating point or at least a direction towards it. There are also algorithms, which can acquire this information based on transition after change of the required speed or load [DTCB22, QH13].

3. *High-frequency injection algorithms*, which rely on the superposition of the high-frequency signal in a range of several hundred Hertz to the optimized variable. The following post-processing using amplitude demodulation is very similar to the HFI position estimation algorithm described in Section 2.2. The optimal operating point can be found for both the ME and MTPA criteria by either searching for $\mathrm{d}P_{in}/\mathrm{d}\theta_I = 0$ W/rad or $\mathrm{d}I_m/\mathrm{d}\theta_I = 0$ A/rad conditions during steady-state [DTCB22, BPPS10, KSIM10].

3.4.1. Proposed MTPA Search Algorithm

A variant of the MTPA search controller algorithm was published as part of the research of the power-optimal control of SynRM for this thesis. Instead of using a high-frequency injection, the DC current injection in the stator reference frame was employed. The injected current vector then rotated with the synchronous speed from perspective of dq reference frame and was injected into the stator current reference $\vec{i}_{dq}^{\text{req}}$. The amplitude demodulation then provided the error signal

$$\varepsilon_{\theta I} = \frac{1}{4}\left(L_d - L_q\right)^2 \omega_e^2 I_{DC}^2 \cos 2\theta_I \simeq K_P \frac{3}{4} P_p I_m^2 (L_d - L_q) \cos 2\theta_I, \qquad (3.12)$$

where K_P is a general proportional gain. This near-MTPA condition is then satisfied when zero error value is maintained using PI controller.

The most notable advantage of this algorithm, when compared to the other existing low-frequency search controllers, is its relatively low computational complexity. This is because it can utilize sine and cosine values of the rotor position already calculated for Park's transformation as necessary part FOC and does not require an extra calculation of any other goniometric function.

The proposed algorithm was tested on the machine analysed in Section 1.2. The MTPA tracking ability was measured and is shown in Figure 3.14. It did not find the true MTPA position in the measured example, however, the resulting stator current amplitude I_m was always smaller than in the case of the standard $\theta_I^{\text{opt}} = \pi/4$ control. The improved power efficiency is shown in more details in Figure 3.15, where current angle difference $\Delta\theta_I$ and stator current amplitude increase ΔI_m are compared with the true MTPA trajectory [Myn16].
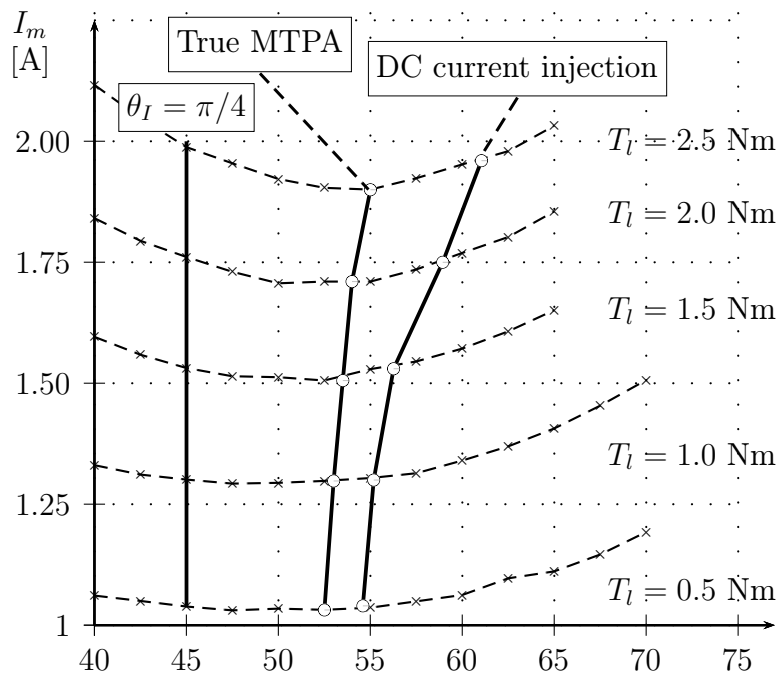
Figure 3.14: The MTPA trajectory tracking using proposed algorithm [Myn16]
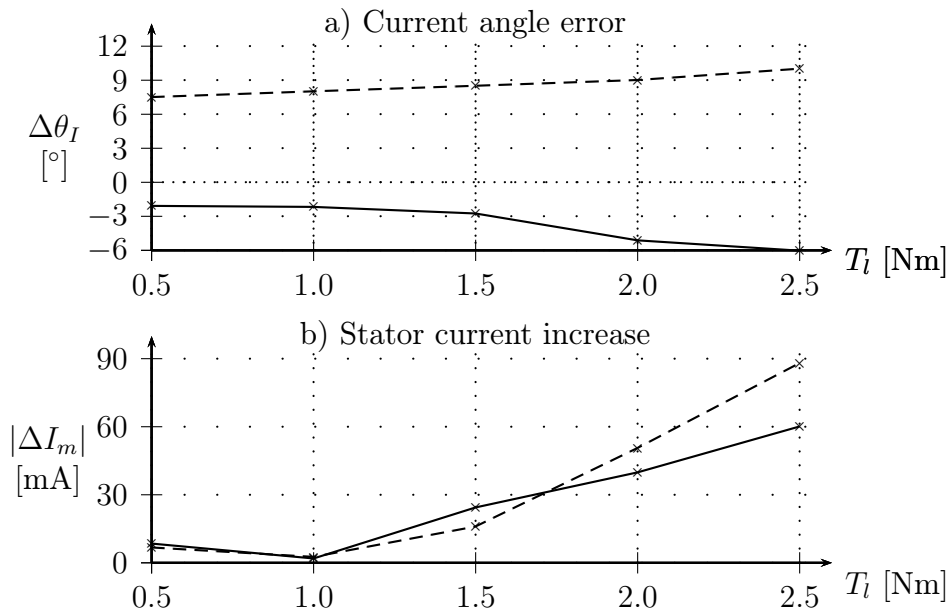
Figure 3.15: Comparison of a) current angle error and b) current amplitude increase for proposed search algorithm (solid line) and $\theta_I = \pi/4$ strategy (dashed line) with the true optimal MTPA trajectory

4. Evaluation of Current State of SynRM Power-optimal Control

The SynRM machine, its model, properties, and an overview of the existing applicable sensorless algorithms were discussed in the previous sections. In this chapter, the still-existing challenges of the state-of-the-art approaches will be formulated and the conclusions will be supported via simulation of the selected algorithms. The ultimate goal of this chapter is to define and justify specific goals of research for this thesis.

Because the main focus of this thesis are the power-optimal sensorless control algorithms, the status of power-optimization algorithms listed in Section 3 will be discussed first. The SC algorithms shown in Section 3.4 are working very well in applications where the impact of change of current angle on the optimized quantity (i.e. stator current for MTPA or input power for ME criterion) can be evaluated without interference. This is not a problem for systems where load changes very slowly, often reaches prolonged states of steady-state, or follows defined cycles. An example could be pumps or fans for systems of constant or slow-changing properties. The performance of these algorithms was also briefly investigated during an early stage of research for this thesis when a very simple MTPA search algorithm was proposed (see Section 3.4.1). Taking into account relatively low computational demands and a natural adaptivity, which reduces performance requirements for the position and speed tracking algorithms, the search-type algorithms were found to be quite mature and likely to be preferred in any suitable power-optimal application. Search algorithms were, thus, not investigated further in this thesis.

The LMC algorithms, which were surveyed in Section 3.3, can be used in a wider range of applications as they converge quickly and without a need of detecting feedback to signal injection to stator currents. The accuracy of found θ_I solution varies for each algorithm type, but since the LUT algorithm is considered to be LMC within this thesis as well, very high accuracy is generally achievable, hence a new design of LMC algorithms was also not pursued in this thesis. Based on the principle of the LMC algorithms, it is, however, presumable that such high performance has two conditions:

- Accurate machine parameters must be provided to the LMC algorithms, otherwise, the found solution $\hat{\theta}_I$ might not be optimal. To give an example, Figure 4.1 shows sensitivity of current angle error $\theta_I^{\mathrm{err}} = \theta_I^{\mathrm{opt}} - \hat{\theta}_I$ of LMC algorithm (3.8) to stator inductance inaccuracy. A more detailed analysis of sensitivity of LMC algorithms to machine parameter inaccuracy is in Section 4.1. To compensate for machine parameter change due to temperature, manufacturing deviations, wear and tear, or even a minor machine fault, an online parameter estimation would be required to allow for LMC adaptivity.

- The machine control algorithm is operated with an accurate rotor position estimate $\hat{\theta}_e$. As shown in Figure 4.2, the position estimation error θ_e^{err} offsets the solution $\hat{\theta}_I$ found by the LMC algorithm so the true current angle θ_I is no longer optimal. This increases performance requirements for algorithms like

those described in Section 2.1, Section 2.2, and Section 2.3. Also, similarly to LMC algorithms, the model-based position estimators are dependent on the accuracy of the known machine parameters, which again raises the need for online parameter estimation and adaptivity.

The two above-mentioned needs of accurate rotor position estimate and online machine parameter estimation were chosen as the main focus of this thesis. To give evidence and a rough idea of necessary performance, the following Section 4.1 provides simulation-based analysis of the sensitivity of ideal LMC to position and parameter inaccuracy. Section 4.2 then provides some simulation results of the existing position and parameter estimators. This is to evaluate and understand rough limitations of the currently-available solutions. All simulations within Section 4.1 and Section 4.2 were done for the 550 W SynRM machine described in Section 1.2, using the model from Section 1.1 and the simulation environment Matlab R2018a. Finally, the exact goals of the thesis are summarized in Section 4.3.
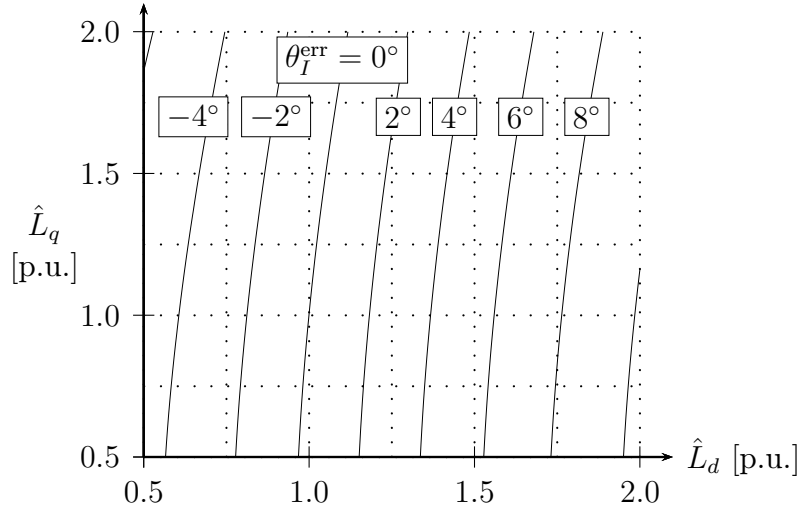
Figure 4.1: Optimal current angle error dependency on the dq-axis inductance estimation error for LMC algorithm (3.8)
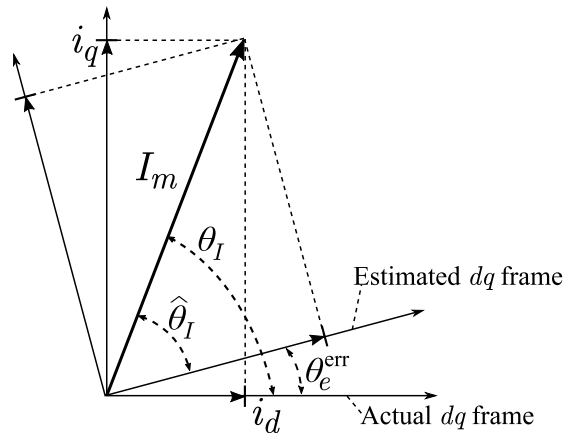
Figure 4.2: Relation between the optimal current vector error θ_I^{err} and the position estimate error θ_e^{err}

63

4.1. Analysis of LMC Sensitivity to Machine Parameter and Position Errors

The goal of this section is to evaluate the sensitivity of the LMC-based power optimization to error in assumed machine parameters and the position estimated by the sensorless algorithm.

First, the sensitivity of machine power losses to position error $\theta_I^{\mathrm{err}} = \theta_e^{\mathrm{err}}$ was investigated. This was done by taking the machine ME trajectory, like the one shown in Figure 3.8, and considering it as $\theta_I^{\mathrm{err}} = \theta_e^{\mathrm{err}} = 0$ degree axis. The Joule and iron power-losses increase $\Delta(P_{Cu} + P_{Fe})$ was then calculated using models described in Section 3 and related to this axis. Note that the mechanical losses P_m were neglected and the simulation was done only for nominal rotor speed $N_m = 1500$ rpm. The results are in Figure 4.3. As expected, the power losses increase with position error, but the important outcome is that rate is non-linear and almost exponential. The exact required performance is, of course, a matter of the specific application, but it is reasonably safe to assume that maximal steady-state $|\theta_e^{\mathrm{err}}|$ up to 7.5 degrees, which results in roughly a one percent efficiency loss, would be considered acceptable in most cases, hence, within this thesis as well.
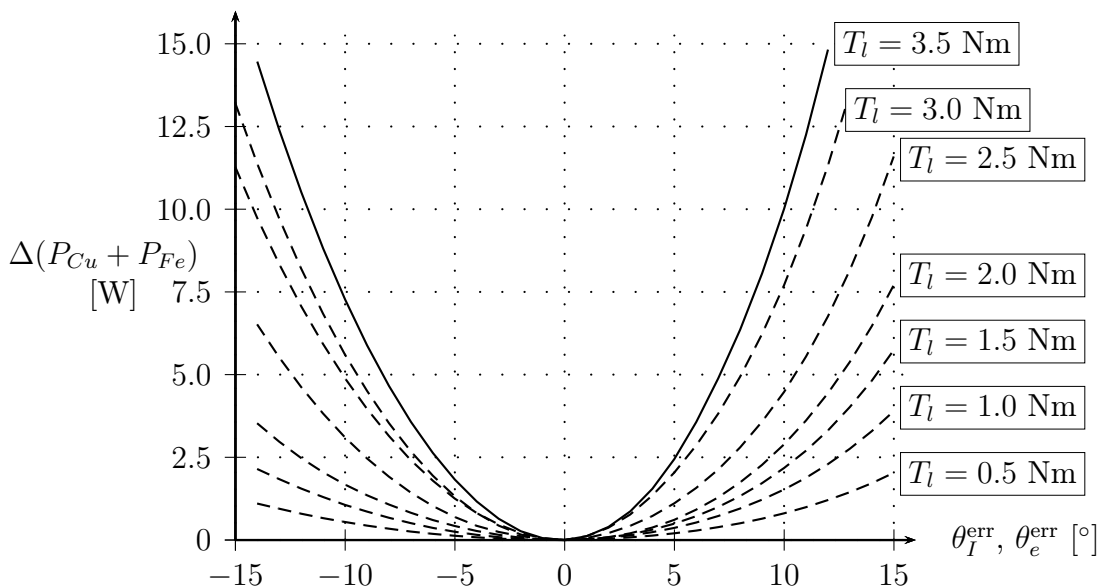
Figure 4.3: Simulated increase in SynRM power losses $\Delta(P_{Cu} + P_{Fe})$ versus the position estimate error θ_e^{err} at nominal speed

The second analysis investigated the sensitivity of the optimal LMC algorithm to error in the provided parameter of stator resistance $\hat{R}_s$ and characteristics $\hat{L}_d = f_d(i_d, i_q)$ and $\hat{L}_q = f_q(i_d, i_q)$. The optimal LMC is an algorithm, which is capable to find a true ME trajectory. Because the stator inductance characteristics f_d and f_q are non-linear and can be described by a non-trivial model (see model (1.22) in Section 2) a numerical search was used during simulation. Inaccuracy of the induc-

tance characteristics can be modelled in many different ways, but for the purpose of the following analysis we will assume deformation

$$\hat{L}_d = k_d f_d(i_d/k_d, i_q/k_q), \tag{4.1}$$

$$\hat{L}_q = k_q f_q(i_d/k_d, i_q/k_q), \tag{4.2}$$

where k_d and k_q are dimensionless coefficients. The resulting inaccurate inductance estimates $\hat{L}_d$ and $\hat{L}_q$ used during simulation are shown in Figure 4.4. The cases where condition $\hat{L}_q > \hat{L}_d$ occurred were not considered as valid deformations during the simulation.

The results of simulation for reference SynRM running at nominal rotor speed $N_m = 1500$ rpm and a nominal rotor load $T_l = 3.5$ Nm for 75 %, 100 %, and 125 % stator resistance $\hat{R}_s$ are in Figure 4.5. When comparing the current angle error θ_I^{err} to reference point $k_d = 1$, $k_q = 1$, and $\hat{R}_s = R_s$, it can be seen that even for relative errors of parameters around ± 30 %, the resulting change is well below five degrees. This, as Figure 4.3 shows, causes only a minimal power loss increase. Thus, in general, this thesis will consider that the LMC algorithms produce acceptable solutions even for parameter deviations up to ± 30 %.
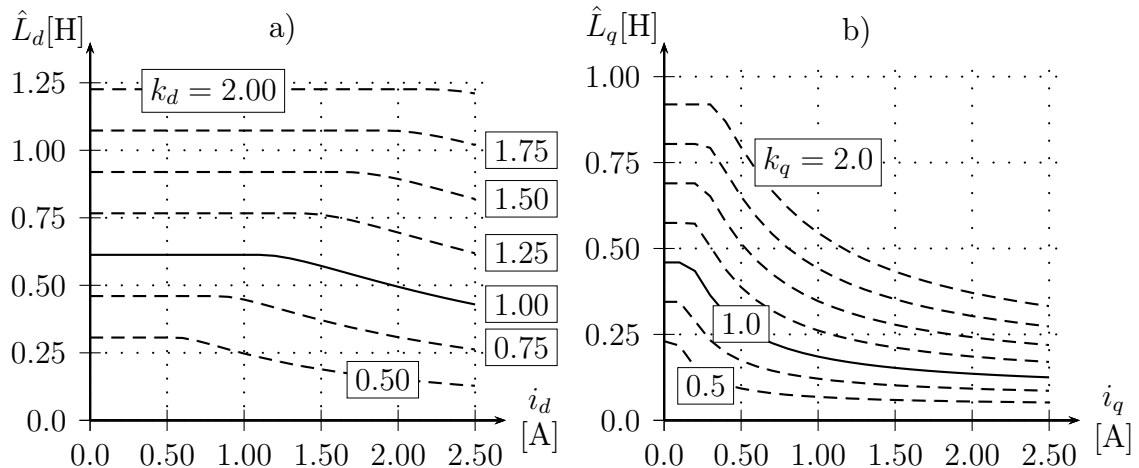
Figure 4.4: Simulated inaccuracies of a) $\hat{L}_d$ and b) $\hat{L}_q$ characteristics provided to optimal LMC algorithm during sensitivity analysis

Note that LMC algorithms described in Section 3.3 are usually only approximating the optimal solution. This is because of various simplifications, which achieve lower computational complexity. Their sensitivity to parameter inaccuracy could, therefore, differ from the previously simulated optimal LMC algorithm. Still, this approach is seen as valid to create a general idea of necessary parameter accuracy. For example, the inductance error sensitivity of the LMC algorithm (3.8) in Figure 4.1 is generally comparable to results obtained for the optimal LMC algorithm.
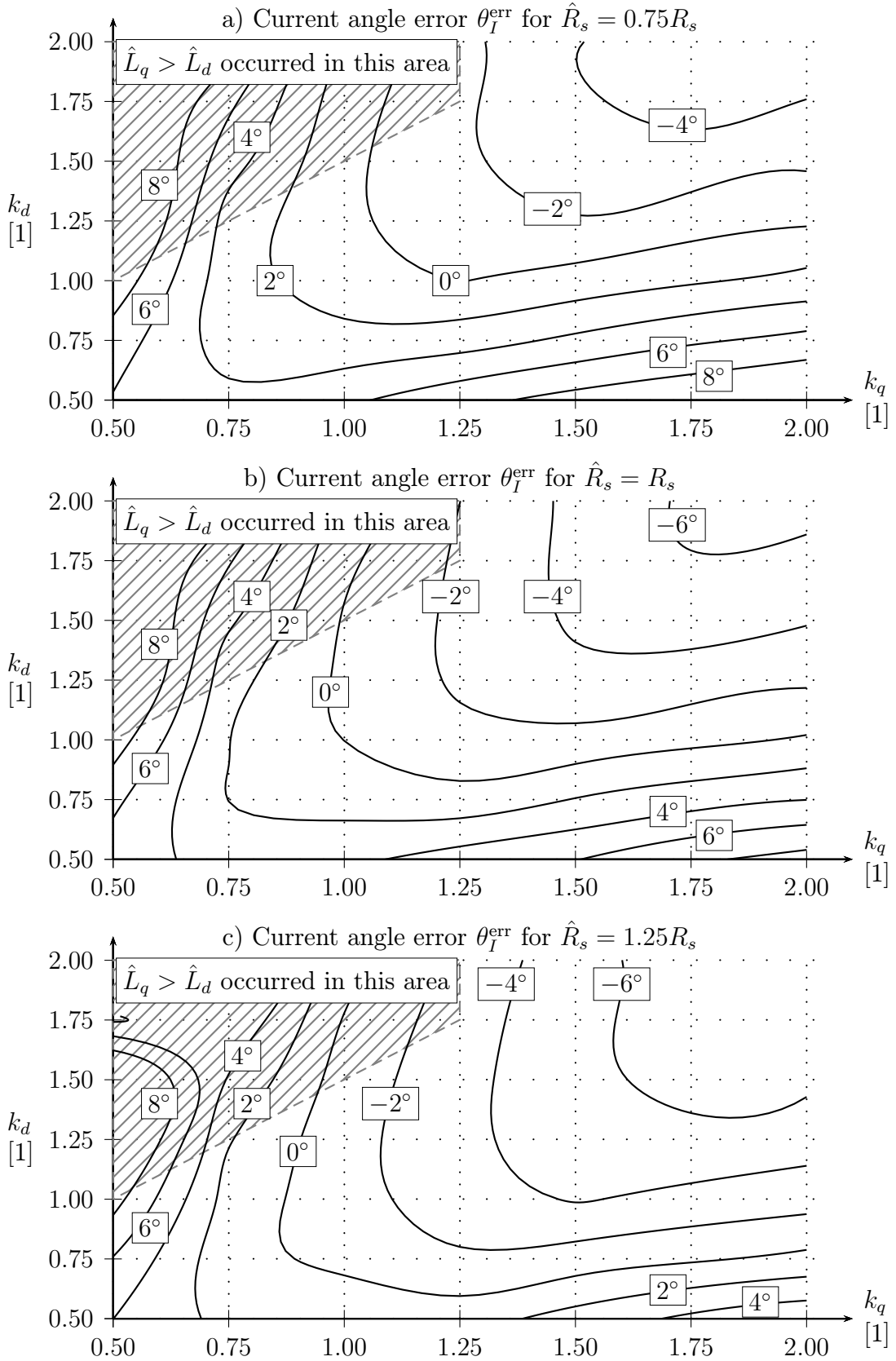
Figure 4.5: Simulated sensitivity of current angle θ_I^{err} of optimal LMC algorithm to inaccuracy of stator resistance $\hat{R}_s$ and inductance $\hat{L}_d$ and $\hat{L}_q$ parameters

4.2. Evaluation of Position Estimator Sensitivity to Machine Parameter Error

The goal of this section is to investigate selected well-known rotor position estimation algorithms from Section 2.1 and Section 2.3 to gain a general idea of their machine parameter sensitivity. The position and speed extended EMF observer (2.12) and the identical observer (2.6) were selected for implementation. The second part of this section also presents experimental results of selected SynRM parameter estimators from Section 2.4, to establish a general idea of performance in relation to the needs of the position estimators.

The identical observer represents an interesting alternative to the extended EMF observer due to its low computational demands and the possibility of inductance adaptation. Its disadvantages seem to be its sensitivity to the setup of gains (2.8) and (2.9) and also the fact that only one of the inductances can be adapted. If the second, non-adapted, inductance is not accurate, it will affect the adapted inductance as well. The situation where one of the inductances is adapted while the second one is burdened with error is depicted in Figure 4.6a. It can be seen that the increase of the pre-set inductance $\hat{L}_q$ by ten percent will propagate to the estimated inductance $\hat{L}_d$ by a similar amount. This will, unfortunately, also impact the accuracy of the estimated position θ_e^{err}, which is also shown in Figure 4.6b. The ±30 % inductance parameter deviation would lead to position error θ_e^{err} over ten degrees, which indicates higher parameter sensitivity of position error than in the case of the LMC algorithms, as established in Section 4.1.
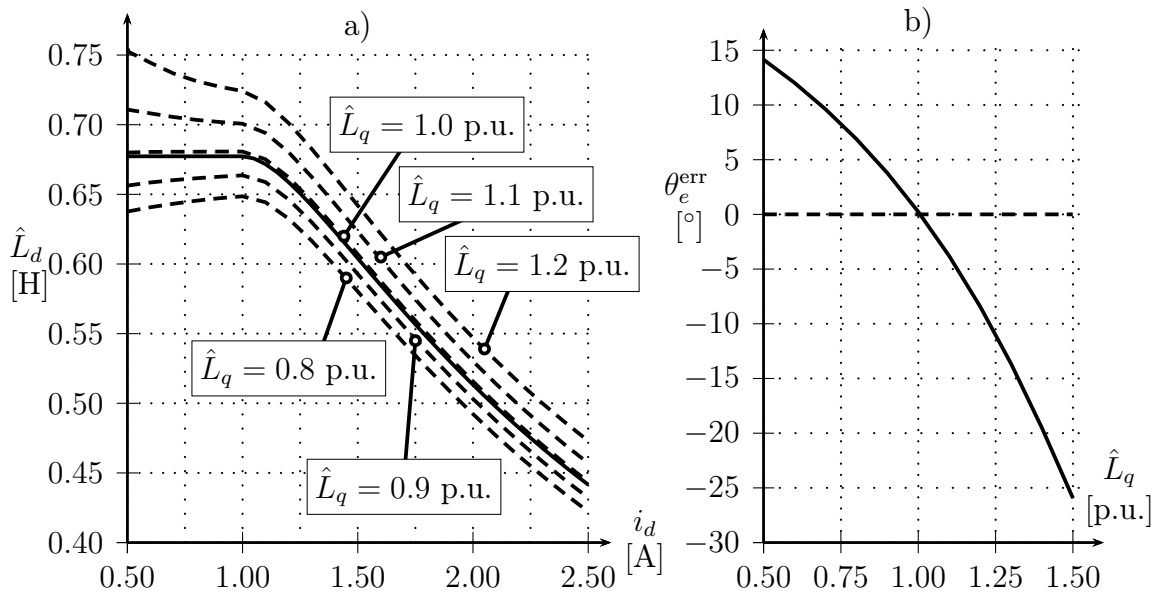
Figure 4.6: The impact of an error of inductance $\hat{L}_q$ on a) inductance estimate $\hat{L}_d$ and b) position estimation error of the identical observer

The second simulated position estimation algorithm, the extended EMF observer, is mainly dependent on the $\hat{R}_s$, $\hat{L}_q$, and $\hat{L}_d'$ machine parameters, where the $\hat{L}_d'$ does not affect the steady-state performance [ITDO06]. The simulated parameter sensitivity of the position error is shown in Figure 4.7. As expected from equation

(2.12), the sensitivity of the EEMF observer to $\hat{R}_s$ is lower than to $\hat{L}_q$ because the stator winding voltage drop is usually much smaller than the EMF voltage. In general, however, it can be seen that the sensitivity is lower than in the case of the identical observers, but roughly twice higher than in the case of the ideal LMC algorithm sensitivity estimated in Section 4.1.
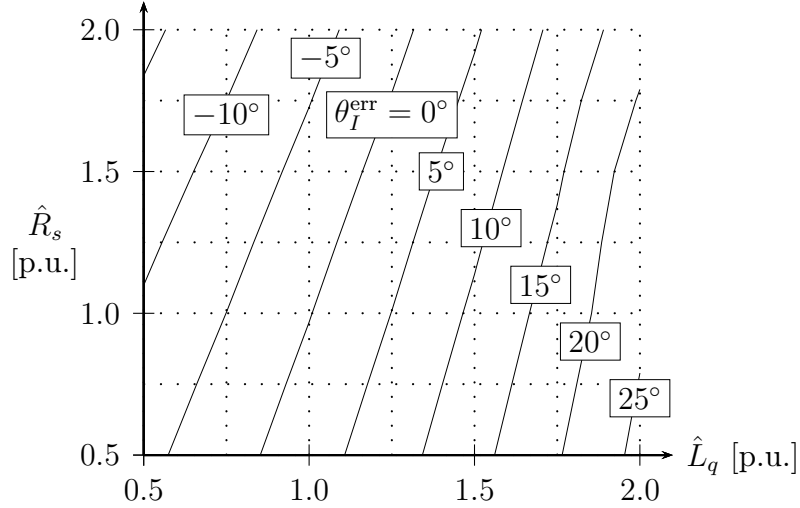
Figure 4.7: Sensitivity of the position estimate error $\hat{\theta}_e^{\mathrm{err}}$ of EEMF observer to error of inductance $\hat{L}_q$ and resistance $\hat{R}_s$

The adaptivity of the simulated EEMF observer could be achieved using the recursive online least square estimation method (2.30) and (2.31) and for the identical observer (2.40) using its self-adaptation capability. Both methods were run on a real SynRM machine at the speed $N_m = 750$ rpm, $\theta_I = \pi/4$, and various loads to gain more realistic data. The RLS method was utilized to obtain an online estimate of $\hat{R}_s$, $\hat{L}_q$ and $\hat{L}_d'$ inductances. The forgetting coefficient of the RLS method was chosen as $\lambda = 0.99$ and the 6-bit PRBS excitation signal with 10 V amplitude and 3 ms sampling period was superimposed to the voltage $\vec{u}_{dq}$. The experimental results are shown in Figure 4.8 to Figure 4.10. In the case of the identical observer, only one inductance was being adapted, while the inductance in the perpendicular axis was obtained from the look-up table, achieving only partial adaptivity.
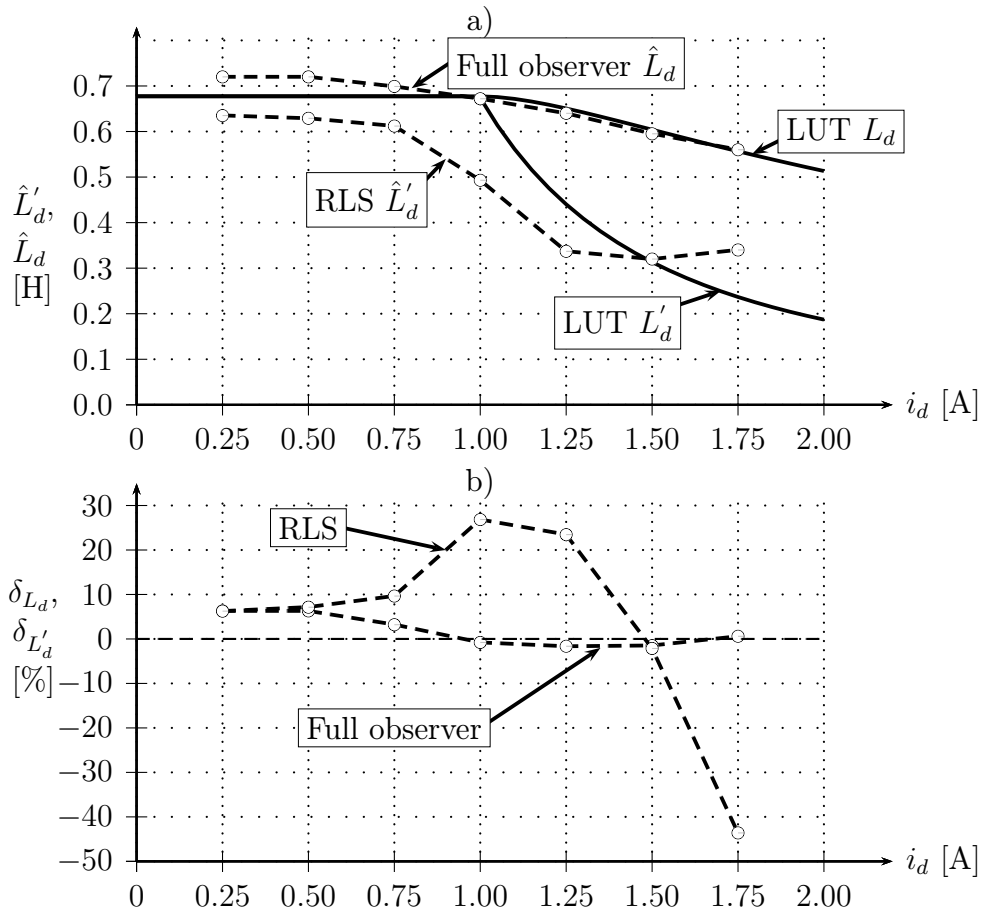
Figure 4.8: Estimated inductance $\hat{L}_d'$ and $\hat{L}_d$ in a) absolute and b) relative values
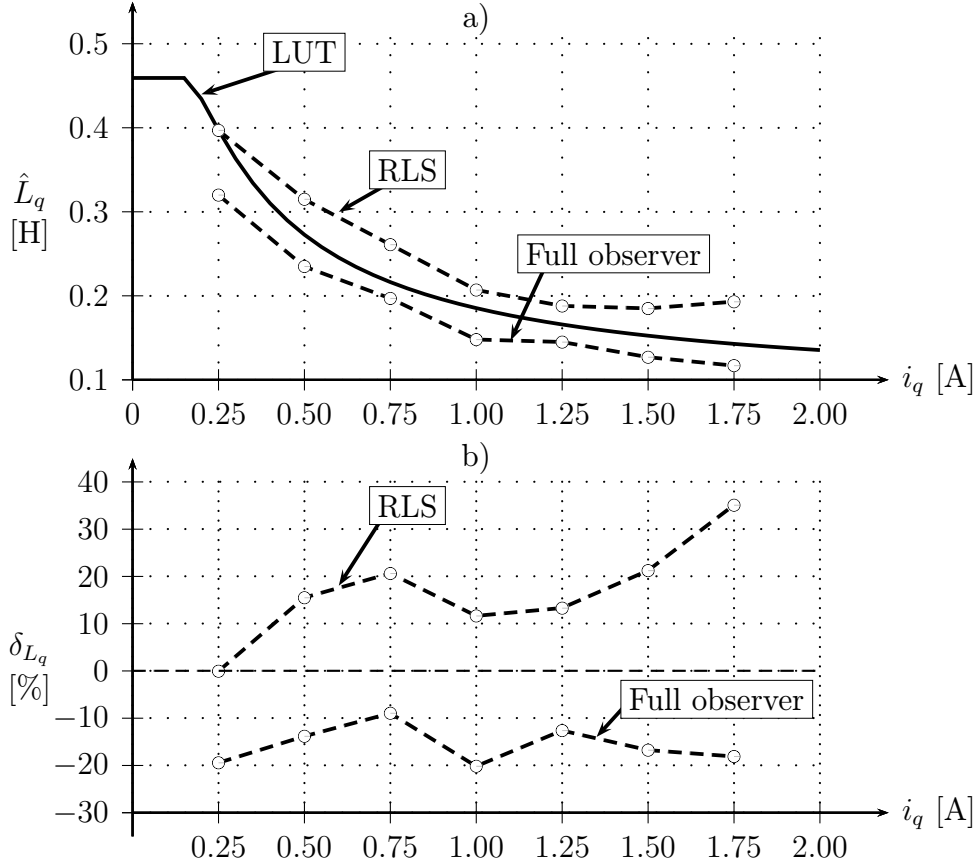
Figure 4.9: Estimated inductance $\hat{L}_q$ in a) absolute and b) relative values

Direct and quadrature inductance estimation results in Figure 4.8 and Figure 4.9 indicate a good performance of the full order observer, however, it takes the benefit of acquiring the non-estimated inductance from the LUT table. A large δ_{L_d} error provided by RLS in Figure 4.8 does not cause a steady-state deterioration of EEMF observer performance, hence it can be neglected. The $\hat{L}_q$ in Figure 4.8 and especially the $\hat{R}_s$ estimate in Figure 4.10, however, reach errors in tens of percent. A similar performance can be seen in the original EEMF and RLS publication [ITDO06].

It is understood, that accuracy of parameter estimators is affected by many phenomenons and higher accuracy can be achieved. The above-stated results show, however, that a high parameter estimation accuracy, which would safely ensure a small position estimation error $\hat{\theta}_e^{\text{err}}$, is not a trivial matter and requires special consideration. This is true even for relatively complex algorithms like the RLS, which also requires a signal injection.
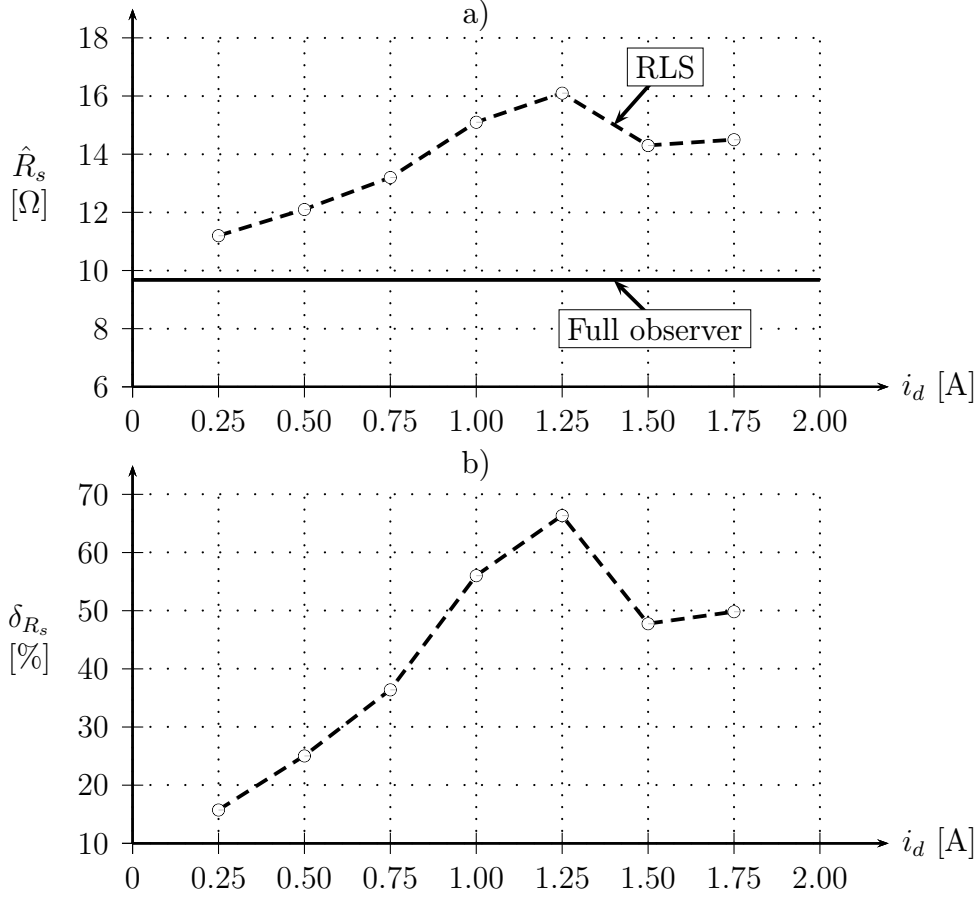
Figure 4.10: Estimated resistance $\hat{R}_s$ in a) absolute and b) relative values

4.3. Goals of the Thesis

Based on the discussion in previous sections, it was determined that a rotor position and motor parameter estimator, which would support the operation of the LMC power-optimization algorithm should be pursued within this thesis. The desired algorithm placed within the FOC block diagram is shown in Figure 4.11. As a summary, the following traits should be achieved:

1. The steady-state position estimate error θ_e^{err} should be below 7.5 degrees, but as small as possible in general. This should be achieved in all load and speed regions. It can be expected, that a robust adaptation to the change of the inductances in both axes will be necessary.

2. The machine parameter estimates should be provided to other algorithms within the FOC structure. This regards especially the stator inductances because their acquisition is not a trivial matter. Accuracy within the ± 30 % range is acceptable, provided that position error θ_e^{err} is not affected.

3. The convergence to the optimal θ_I^{opt} operating point should not require signal injection, which would limit the applicability of the algorithm. This is necessary because the injection is the main limitation of SC algorithms, which are otherwise preferable.

4. The algorithm should require no or inexpensive additional hardware.
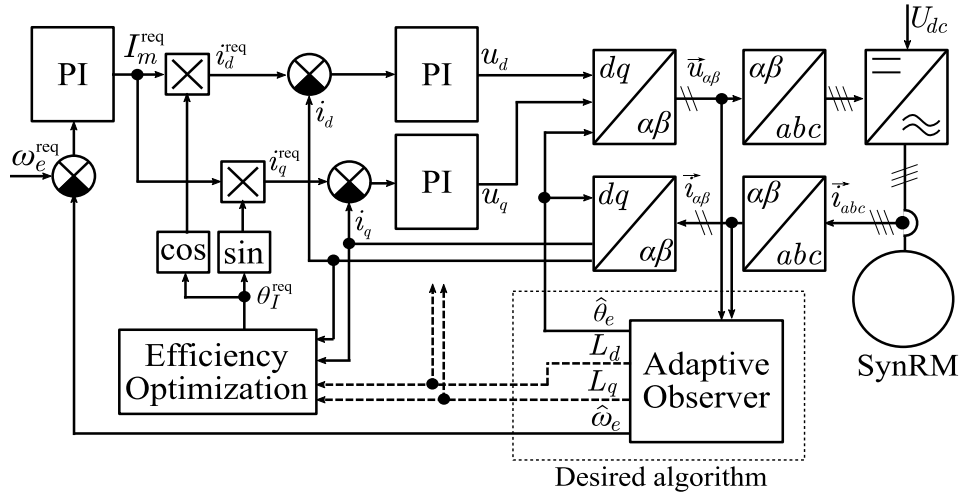
Figure 4.11: Block diagram of desired sensorless estimation algorithm within FOC structure

5. Proposed Sensorless Adaptive Estimation Method

As the discussion in Chapter 4 showed, an accurate rotor position and machine parameter estimation with online adaptation to their change are key features, which could benefit the area of power-optimal sensorless SynRM control. This chapter presents algorithms, which were developed during research for this thesis and should represent an alternative to existing solutions.

As Chapter 2 showed, there are essentially two fundamental physical principles, which could be used to estimate SynRM rotor position; the EEMF model-based estimation and rotor saliency tracking using signal injection. As Section 2.3 showed, there are also hybrid algorithms, which use both principles and achieve operation in a full speed range. The saliency-based algorithms with a fundamental pulse width modulation (PWM) excitation and stator current derivative measurement, like the INFORM method and its modifications in Section 2.2, were found to be promising for further research. This is mainly because it was shown by other authors that it is possible to simultaneously estimate stator inductances, position, and speed [RSW18, RSW19]. The research of this thesis, therefore, focused on the further development of this idea, which yielded several novel improvements, which are described in detail further in this chapter.

The FOC block diagram integrating the proposed algorithms is in Figure 5.1, where the newly added elements are highlighted in grey colour. The remaining portion of the block diagram features the FOC method as described in Section 2, where the motor setpoint is given by the required rotor speed ω_e^{req} and the required current vector angle θ_I^{req}. The efficiency optimization is assumed to be done using unspecified LMC-type algorithm. The newly proposed algorithms are:

- *The current derivative measurement method* (see MC IDC and reluctance measurement blocks in Figure 5.1). Its main benefit is that it requires only a simple hardware, without a need for costly sensors, like is often proposed (e.g. current measurement transformer) [NSS20]. A detailed description of the proposed method itself and a way of obtaining machine reluctances from current derivative measurement is in Section 5.1.

- *The alignment-swap PWM switching scheme.* This algorithm is described in Section 5.2. It was proposed to achieve accurate current derivative measurement on machines with large inductances and to reduce switching losses. While not being essential, it allows accurate measurements up to the upper limit of the PWM duty cycle. The impact of this method on current ripple and overall semiconductor power losses will be discussed as well.

- *The extended Kalman filter utilizing measurement redundancy.* Another important novel idea was to merge measurement of the position-dependent reluctances with machine model (1.18) and stator phase current $\vec{i}_{\alpha\beta}$ measurement as a redundant source of information. The extended Kalman filter theory, which is briefly described in Section 5.3, was used for this purpose as shown

in Section 5.4. Such information redundancy can be exploited in many ways, for example, to estimate additional parameters, improve estimate accuracy, serve as diagnostics within fail-safe systems, or as redundant channel in fail-operational systems. Two variants of the extended Kalman-based algorithm will be presented and analyzed via simulation. Note that not all outputs of EKF block in Figure 5.1 are available for all the variants.

The core of the proposed method was already published [MVB21]. However, this thesis presents a number of modifications, like the inclusion of the stator resistance voltage drop in the reluctance calculation and presenting new variants of the EKF algorithm, bringing lower computational effort or stator resistance $\hat{R}_s$ estimation.

Figure 5.1: Block diagram of vector control using proposed algorithms (newly proposed elements in grey) [MVB21]

5.1. Method of Obtaining Rotor Position from Current Derivative Measurements

As it was shortly discussed in Section 2.2, the SynRM inductances L_a, L_b, and L_c in motor phases $N \in \{a, b, c\}$ are affected by the rotor position θ_e according to equation (2.24). The standard two-state three-phase VSI, as depicted in Figure 2.2, applies six non-zero Space Vector Modulation voltage vectors $\boldsymbol{v}_M = \{\boldsymbol{v}_1, \boldsymbol{v}_2, \boldsymbol{v}_3, \boldsymbol{v}_4, \boldsymbol{v}_5, \boldsymbol{v}_6\}$ for the time durations $\boldsymbol{T}_{vM} = \{T_{v1}, T_{v2}, T_{v3}, T_{v4}, T_{v5}, T_{v6}\}$. The resulting circuits for each non-zero voltage vector are shown in Figure 5.2, including the equivalent RL circuits.

Figure 5.2: Equivalent machine circuits for voltage vectors generated by standard three-phase two-state VSI

For completeness, the equivalent phase resistance R_{ph} is given by relation

$$R_{ph} = R_a + \frac{R_b R_c}{R_b + R_c} = \frac{3}{2} R_s, \tag{5.1}$$

but it does not contain any useful information about rotor position. On the other hand, the equivalent phase inductances $L_{phN} = \{L_{pha}, L_{phb}, L_{phc}\}$ are affected by rotor position and can be expressed using the direct and quadrature inductances as

$$L_{pha} = L_a + \frac{L_b L_c}{L_b + L_c} = \frac{3 L_d L_q}{L_d + L_q - (L_d - L_q) \cos(2\theta_e)}, \tag{5.2}$$

$$L_{phb} = L_b + \frac{L_a L_c}{L_a + L_c} = \frac{3 L_d L_q}{L_d + L_q - (L_d - L_q) \cos\left[2(\theta_e - \frac{2\pi}{3})\right]}, \tag{5.3}$$

$$L_{phc} = L_c + \frac{L_a L_b}{L_a + L_b} = \frac{3 L_d L_q}{L_d + L_q - (L_d - L_q) \cos\left[2(\theta_e + \frac{2\pi}{3})\right]}. \tag{5.4}$$

The example of equivalent phase inductances L_{phN} during one electrical revolution is shown in Figure 5.3a. While the L_{phN} contains rotor position information, it is not a harmonic function and its model involves a division, hence, it will be more

beneficial for later use to work with its inverse. The normalized reluctance $\mathcal{R}'_{phN}$ quantity is, therefore, introduced as

$$\mathcal{R}'_{pha} = \frac{3}{2}\frac{1}{L_{pha}} = \frac{L_d + L_q - (L_d - L_q)\cos(2\theta_e)}{2L_dL_q}, \tag{5.5}$$

$$\mathcal{R}'_{phb} = \frac{3}{2}\frac{1}{L_{phb}} = \frac{L_d + L_q - (L_d - L_q)\cos\left[2(\theta_e - \frac{2\pi}{3})\right]}{2L_dL_q}, \tag{5.6}$$

$$\mathcal{R}'_{phc} = \frac{3}{2}\frac{1}{L_{phc}} = \frac{L_d + L_q - (L_d - L_q)\cos\left[2(\theta_e + \frac{2\pi}{3})\right]}{2L_dL_q}. \tag{5.7}$$

Note that the term *normalized* reluctance is used for two reasons. The first is the fact that the inverse of magnetic reluctance $\mathcal{R} = 1/\mathcal{P} = M^2/L$ is called permeance $\mathcal{P}$ and is proportional to inductance L via the number of coil turns $1/M^2$. However, since the number of turns M is dimensionless number, the $\mathcal{R}'_{phN}$ can be considered to have a character of reluctance. The second reason for the term *normalized* is because of the $\frac{3}{2}$ coefficient in equations (5.2), (5.3), and (5.4). It was added to scale $\mathcal{R}'_{phN}$ as shown in Figure 5.3b, so

$$\min\left(\mathcal{R}'_{phN}\right) = \mathcal{R}'_d = \frac{1}{L_d}, \tag{5.8}$$

$$\max\left(\mathcal{R}'_{phN}\right) = \mathcal{R}'_q = \frac{1}{L_q}, \tag{5.9}$$

where $\mathcal{R}'_d$ and $\mathcal{R}'_q$ are normalized reluctances in direct and quadrature axis. This form is useful for its easy integration into SynRM mathematical model, as will be shown later. The normalized reluctances $\mathcal{R}'_{phN}$ can be also expressed using direct and quadrature axis reluctances as

$$\mathcal{R}'_{pha} = \mathcal{R}'_d \cos^2(\theta_e) + \mathcal{R}'_q \sin^2(\theta_e), \tag{5.10}$$

$$\mathcal{R}'_{phb} = \mathcal{R}'_d \cos^2(\theta_e + \frac{2\pi}{3}) + \mathcal{R}'_q \sin^2(\theta_e - \frac{2\pi}{3}), \tag{5.11}$$

$$\mathcal{R}'_{phc} = \mathcal{R}'_d \cos^2(\theta_e - \frac{2\pi}{3}) + \mathcal{R}'_q \sin^2(\theta_e + \frac{2\pi}{3}). \tag{5.12}$$

Note that for the remainder of this thesis, it is understood that the term reluctance relates to normalized reluctance as defined above, whether the word *normalized* is used or not.
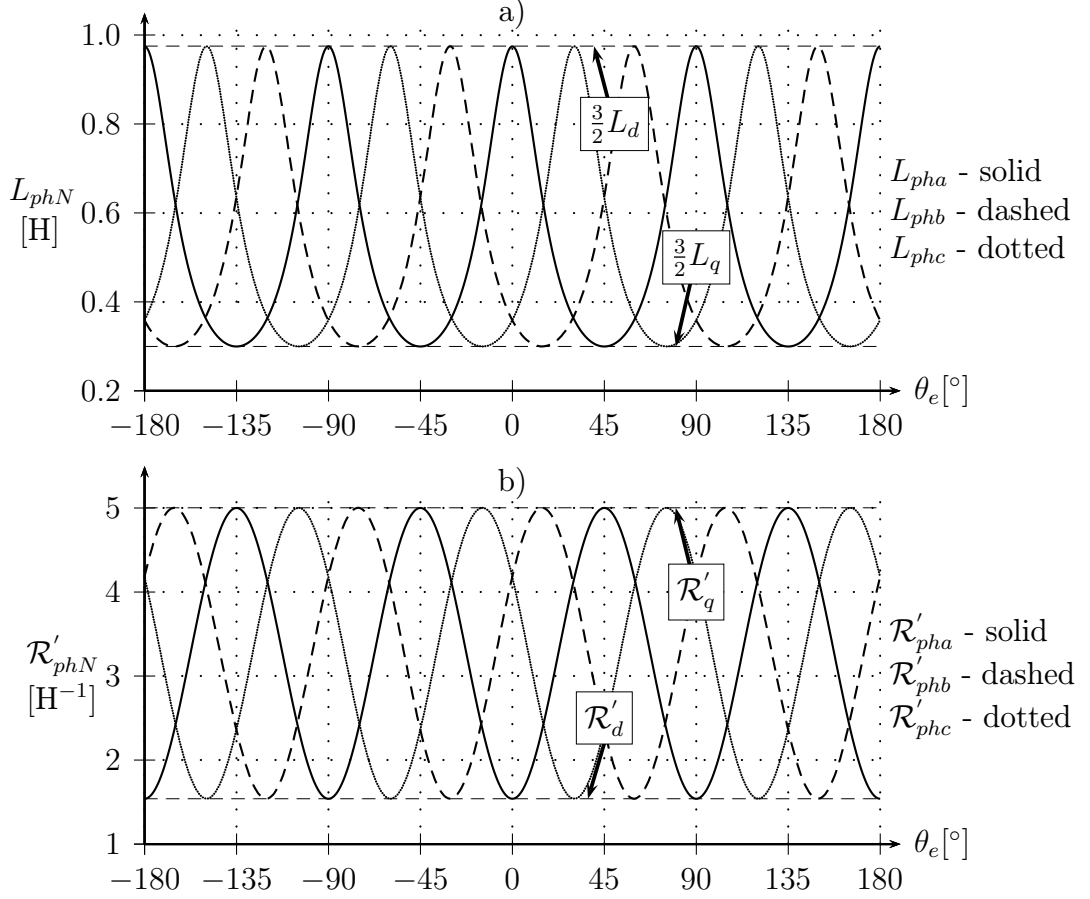
Figure 5.3: Example of rotor position θ_e dependency of a) inductances L_{phN} and b) reluctances $\mathcal{R}'_{phN}$ for $L_d = 0.65$ H and $L_q = 0.2$ H

Looking back at Figure 5.2, the phase reluctances $\mathcal{R}'_{phN}$ can be obtained from the DC-bus current change Δi_{dc} caused by one of the non-zero SVM voltage vectors $\boldsymbol{v}_M$ applied by the inverter for the time duration $\boldsymbol{T}_{vM}$ as

$$\mathcal{R}'_{pha} \cong \left(\frac{\Delta i_{dc}}{T_{v1}}\right) \frac{2}{3} \frac{1}{U_{dc} - R_{ph}i_a} \quad \text{when } \boldsymbol{v}_1 \text{ is applied,} \qquad (5.13)$$

$$\mathcal{R}'_{pha} \cong \left(\frac{\Delta i_{dc}}{T_{v4}}\right) \frac{2}{3} \frac{1}{U_{dc} + R_{ph}i_a} \quad \text{when } \boldsymbol{v}_4 \text{ is applied,} \qquad (5.14)$$

$$\mathcal{R}'_{phb} \cong \left(\frac{\Delta i_{dc}}{T_{v3}}\right) \frac{2}{3} \frac{1}{U_{dc} - R_{ph}i_b} \quad \text{when } \boldsymbol{v}_3 \text{ is applied,} \qquad (5.15)$$

$$\mathcal{R}'_{phb} \cong \left(\frac{\Delta i_{dc}}{T_{v6}}\right) \frac{2}{3} \frac{1}{U_{dc} + R_{ph}i_b} \quad \text{when } \boldsymbol{v}_6 \text{ is applied,} \qquad (5.16)$$

$$\mathcal{R}'_{phc} \cong \left(\frac{\Delta i_{dc}}{T_{v5}}\right) \frac{2}{3} \frac{1}{U_{dc} - R_{ph}i_c} \quad \text{when } \boldsymbol{v}_5 \text{ is applied,} \qquad (5.17)$$

$$\mathcal{R}'_{phc} \cong \left(\frac{\Delta i_{dc}}{T_{v2}}\right) \frac{2}{3} \frac{1}{U_{dc} + R_{ph}i_c} \quad \text{when } \boldsymbol{v}_2 \text{ is applied.} \qquad (5.18)$$

Note that relations (5.13) to (5.18) were improved by considering the resistance voltage drop when compared to the original publication [MVB21]. There is still a

77

simplification by the assumption that the voltage drop on R_{ph} resistance caused by currents $\vec{i}_{abc}$ is constant throughout the T_{PWM} period. This is, however, considered to be acceptable because the stator resistance voltage drop change will usually be very small when compared to the DC-bus voltage U_{dc}.

The measurement of current change Δi_{dc} is, however, not a simple task. The SynRM have usually relatively large stator inductances when compared to different motor topologies of similar power rating. This is a result of a design, which favours large $L_d - L_q$ difference to maximize output torque. At the same time, the standard PWM, as shown in Figure 2.4, generates only short periods $\boldsymbol{T}_{vM}$, during which the Δi_{dc} can be measured. To put things into perspective, for a measurement window corresponding to one of $\boldsymbol{T}_{vM}$ periods with length $T_{PWM}/2 = 50$ μs, inverter DC-bus voltage $U_{dc} = 400$ V, and the SynRM with $\max(L_{phN}) = \frac{3}{2}L_d = 0.975$ H, the minimal current change for measurement would be

$$\min(\Delta i_{dc}) \simeq \frac{T_{PWM}U_{dc}}{2\max(L_{phN})} = \frac{0.0001 \cdot 400}{2 \cdot 0.975} = 20.5 \text{ mA.} \qquad (5.19)$$

The most commonly used method of stator current measurement is current reconstruction from voltage drop measured on bottom shunt resistors R_{sh} using operational amplifiers. This is depicted via the MC IABC block in Figure 5.1. These circuits are set-up for the measurement of complete stator current range $\pm\max(\vec{i}_{abc})$. If we consider an example of a suitable inverter for SynRM described in Section 1.2 with configured current scale $\max(\vec{i}_{abc}) = 3$ A, then we can see that $\min(\Delta i_{dc})$ in (5.19) represents only 0.34 % of measurement scale, which is less than a single LSB of 8-bit ADC measurement. Using MC IABC with such configuration for Δi_{dc} measurement would very likely lead to signal with a high noise content. Existing algorithms, which rely on current derivative measurement, usually employ a specialized current sensor (e.g. current transformer) or compensate for a relatively low ADC measurement resolution, using over-sampling with computation-heavy post-processing (e.g. current slope averaging, Kalman filtering,...) [RSW18, NSS20].

The current derivative measurement method, proposed during research for this thesis, is based on the separate Measurement Circuit of DC-bus current i_{dc} (MC IDC). This circuit amplifies the voltage drop on the common DC-bus shunt resistor R_{shc}, as shown in Figure 5.1. Its basic principle of operation is illustrated in Figure 5.4. Compared to MC IABC, it is configured to have a much higher gain and, as a result, a smaller measurement scale $\max(i_{dc}) \ll \max(\vec{i}_{abc})$. This allows to achieve a much better resolution of the i_{dc} measurement. Such a high gain would normally lead to a quick saturation of the MC IDC output even for a small stator current amplitudes $\vec{i}_{abc}$. To avoid this, the MC IDC measurement window is being actively offset by a DAC-generated signal to be located at the predicted location of i_{dc}. The correct offset value is obtained from the $\vec{i}_{abc}$ measurements from MC IABC and knowledge of upcoming voltage vector $\boldsymbol{v}_M$, which determines the i_{dc} value as shown in Figure 5.2.
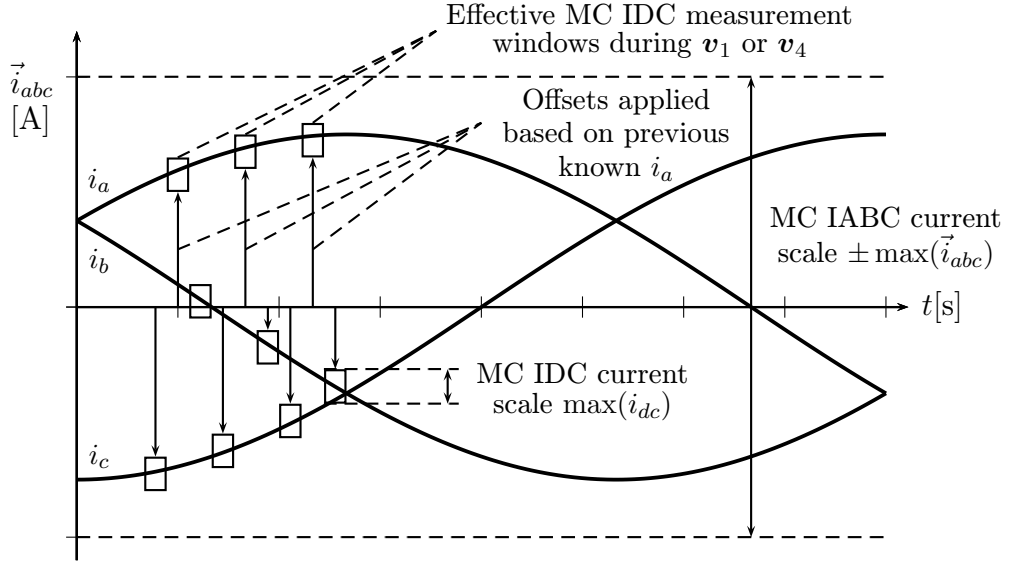
Figure 5.4: Illustration of operation of MC IDC circuit

An example of the schematic diagram of the MC IDC is shown in Figure 5.5. Its output u_{idc} leads to the ADC periphery of MCU and contains amplified information about Δi_{dc}. The u_{DD} is the operational amplifier supply voltage, which ideally limits the MC IDC output to $0\text{ V} < u_{idc} < u_{DD}$ range. The u_{off} is a DAC-generated signal, which, offsets the measured current range to avoid output saturation and fit the predicted i_{dc} location. The circuit functions as a differential amplifier with an analog gain $\max(i_{dc})$ configured as necessary to achieve a good Δi_{dc} resolution while being able to measure maximal expected Δi_{dc}. The output of MC IDC at steady-state can be described as

$$u_{idc} = K_R R_p R_{shc} i_{dc} + K_R R_1' u_{off} - \frac{R_2}{R_n} u_{DD}, \tag{5.20}$$

where

$$K_R = \frac{R_1' R_2 + R_1' R_n + R_2 R_n}{(R_1' + R_p) R_1' R_n} \tag{5.21}$$

and $R_1' = R_1 + R_f$. There are multiple design considerations for the MC IDC circuit. The feedback from u_{DD} supply voltage via resistor R_n offsets the u_{idc} output so for $u_{off} = 0\text{ V}$, even the lowest expected $i_{dc} = -\max(\vec{i}_{abc})$ is measurable. On the other hand, the $0\text{ V} < u_{off} < u_{DD}$ should allow for $i_{dc} = \max(\vec{i}_{abc})$ measurement. As discussed earlier, the u_{off} must also reflect the phase currents $\vec{i}_{abc}$ obtained using the MC IABC. The compensation voltage u_{off} can then be calculated from (5.20) by trying to maintain condition $u_{idc} \simeq \frac{1}{2} u_{DD}$. This leads to the linear function of phase currents

$$u_{off} = \frac{2R_2 + R_n}{2R_n R_1' K_R} u_{DD} - \frac{R_p R_{shc}}{R_1'} i_N, \tag{5.22}$$

where i_N is the last acquired value of the phase current, which is predicted to flow via R_{shc} during i_{dc} measurement (for example $i_N = i_a = i_{dc}$ during T_{v1} and T_{v4}).
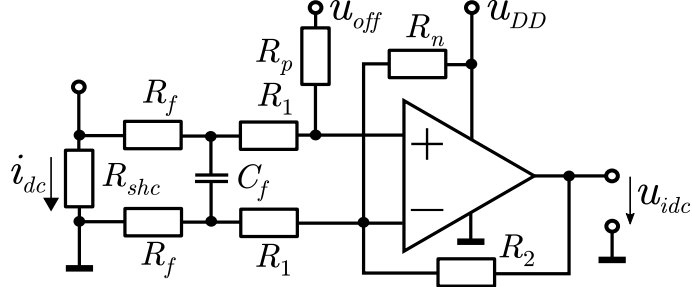
Figure 5.5: Measurement circuit of i_{dc} current MC IDC [MVB21]

Once the MC IDC is properly configured, the u_{idc} can be sampled by ADC to obtain

$$\Delta i_{dc} = \frac{\max(i_{dc})}{u_{DD}\Delta u_{idc}} \tag{5.23}$$

and the u_{off} can be generated by DAC. The exact timing of sampling of both signals is subject to the used PWM switching scheme and availability of active voltage vector period $\boldsymbol{T}_{vM}$. While this measurement method is generally usable together with any switching scheme, like the centre-aligned PWM in Figure 2.4, a specific PWM scheme was proposed during research for this thesis and is described in Section 5.2. More discussion will be had there.

Depending on the desired accuracy and available computation power, the final Δu_{idc} can be obtained from acquired samples using various post-processing methods. The most simple one is a simple calculation of the difference between two ADC samples as

$$\Delta u_{idc} = u_{idc}(t + T_{sidc}) - u_{idc}(t) = u_{idc,k+1} - u_{idc,k}, \tag{5.24}$$

where T_{sidc} is a sampling time between the two samples and k is a discrete sample number. Nowadays MCUs often offer powerful signal processing abilities, like a high ADC sampling rate with DMA data transfer capability. More accurate and noise-suppressing methods can be then employed, utilizing over-sampling, like the well-known offline least square method. For example, the signal u_{idc} can be sampled equidistantly N_{smpl}-times per PWM cycle T_{PWM} with sampling period $T_{sidc} = T_{PWM}/N_{smpl}$. The acquired data can be stored using the DMA to data buffer. A valid sample set of size $N_{vM} \leq N_{smpl}$ within the buffer corresponding to one of active voltage vector periods $\boldsymbol{T}_{vM}$ can then determined using knowledge of the duty cycles $\vec{D}_{abc}$. The measured change Δu_{idc} for a single voltage vector $\boldsymbol{v}_M$ then can be calculated as

$$\Delta u_{idc} = \frac{N_{vM}\left[\sum_{j=1}^{N_{vM}} u_{idc,j}j\right] - \left[\sum_{j=1}^{N_{vM}} j\right]\left[\sum_{j=1}^{N_{vM}} u_{idc,j}\right]}{T_{sidc}\left\{N_{vM}\left[\sum_{j=1}^{N_{vM}} j^2\right] - \left[\sum_{j=1}^{N_{vM}} j\right]^2\right\}}. \tag{5.25}$$

Note that in reality, the selection of valid sample set N_{vM} has to be done carefully, as there could be dynamical events occurring near to the PWM switching events.

Such events are, however, dependent on the exact SynRM and inverter used so their generalization was not considered within this thesis.

An example of the resulting $\mathcal{R}'_{phN}$ measurement versus the rotor position θ_e obtained on a real system is shown in Figure 5.6. It can be seen that the obtained signals correspond to the theoretical model in Figure 5.3 and can be used to extract rotor position θ_e as well as machine reluctances $\mathcal{R}'_d$ and $\mathcal{R}'_q$.
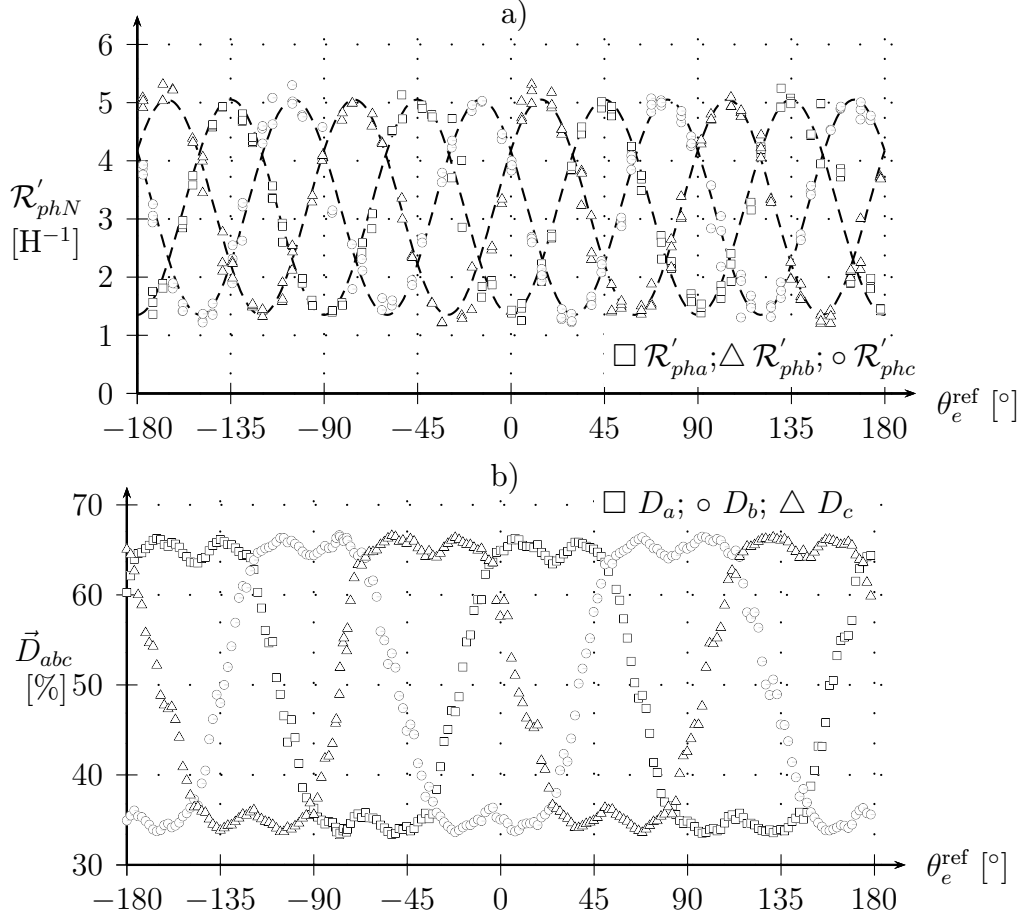
Figure 5.6: Example of a) $\mathcal{R}'_{phN}$ measurement and b) matching duty cycle $\vec{D}_{abc}$ measured on a reference SynRM machine (see Section 1.2)

The fact that the $\hat{\mathcal{R}}'_{pha}$, $\hat{\mathcal{R}}'_{phb}$, and $\hat{\mathcal{R}}'_{phc}$ quantities are obtained as differential measurements from the same sensor limits the likelihood of occurrence of certain types of non-gaussian measurement errors. For example, the bias error $u_{idc} + \Delta_{uidc}$ will not affect the final acquired value Δu_{idc} simply because of the differential nature of (5.25), or

$$\Delta u_{idc} = [u_{idc}(t + T_{sidc}) + \Delta_{uidc}] - [u_{idc}(t) + \Delta_{uidc}] = u_{idc,k+1} - u_{idc,k}. \qquad (5.26)$$

On the other hand, it can be expected that there will be no immunity toward the measurement gain error $\delta_{uidc}u_{idc}$, which can be expressed for (5.25) as

$$\Delta u_{idc} = \delta_{uidc}u_{idc}(t + T_{sidc}) - \delta_{uidc}u_{idc}(t) = \delta_{uidc}[u_{idc,k+1} - u_{idc,k}]. \qquad (5.27)$$

The use of the same sensor input assures that all the phase reluctance measurements will be affected the same way. Such gain error will then directly affect the $\mathcal{R}'_d$ and $\mathcal{R}'_q$ information extracted from the $\delta_{uidc}u_{idc}$ measurement. The root cause of bias and gain errors might, for example, be manufacturing variances or thermal dependencies of parts forming the MC IDC. Depending on the application, it might, therefore, be necessary to address the accuracy and stability of MC IDC measurement gain.

It is possible that non-linear periodic deformations $\mathcal{R}'_{phN} + \Delta_{\mathcal{R}}(\theta_e + \theta_{phN})$ might occur, where θ_{phN} is stator phase offset for actual $\mathcal{R}'_{phN}$ measurement (either $0\,\mathrm{rad}$, $\frac{2\pi}{3}$ rad, or $-\frac{2\pi}{3}$ rad for phase reluctances $\mathcal{R}'_{pha}$, $\mathcal{R}'_{phb}$, and $\mathcal{R}'_{phc}$). This can be a result of dynamic events, which corrupt the u_{idc} sample right after the PWM switching event. There is no general model for these short periodic deformations and care must be taken by the system designer to avoid these errors, for example, by ignoring affected u_{idc} samples. If such errors still occur, then all the phase reluctance measurements will remain periodic, with $120°$ shifts between phases. The extracted position information then might show an error θ_e^{err}, depending on the nature of deformation $\Delta_{\mathcal{R}}(\theta_e + \theta_{phN})$.

5.2. Alignment-Swap PWM Switching Scheme

As discussed in Section 2, there are many PWM switching schemes with various properties. The current derivative Δi_{dc} measurement method presented in the previous section can be generally used with any such scheme, which generates non-zero voltage vectors $\boldsymbol{v}_M$. The Δi_{dc} measurement method, however, benefits from longer uninterrupted non-zero voltage vector periods $\boldsymbol{T}_{vM}$, which allow for the acquisition of higher number or more distant Δi_{dc} samples. When looking at the example of commonly used centre-aligned PWM in Figure 2.4, the $\boldsymbol{T}_{vM}$ periods are divided into halves and, what is more important, zero vectors $\boldsymbol{v}_0$ and $\boldsymbol{v}_7$ can take a significant portion of PWM period T_{PWM}. At duty cycles near to the 50 % minimum or anytime the switching edges are close to each other, there are short or no active vectors, making the Δi_{dc} measurement difficult or impossible. This led to the proposal of the alignment-swap PWM (ASPWM) switching scheme.

The goal of the proposed switching scheme is to maximize the duration of the non-zero voltage vectors $\boldsymbol{T}_{vM}$ so the Δi_{dc} measurement can be taken even for the previously described critical conditions. The principle of the switching scheme is shown in Figure 5.7. The phase PWM signal edge alignment is swapped in every third PWM cycle to the opposite edge consequently in each phase. The non-zero voltage vectors $\boldsymbol{v}_M$ are, thus, going to align to either the beginning or the end of the PWM period once per three PWM cycles. Calculation of phase duty cycles $\vec{D}_{abc}$ remains unchanged compared to the standard SVM method described in Section 2 and the final generated fundamental voltage vector $\vec{u}_{\alpha\beta}$ will be the same as well. This maximizes the length of $\boldsymbol{T}_{vM}$ periods, which serve as Δi_{dc} measurement windows, especially for low and medium duty cycles. In case that duty cycle $\max(\vec{D}_{abc}) \rightarrow$ 100 % and $\min(\vec{D}_{abc}) \rightarrow 0$ %, the voltage vectors near the PWM period edges might become too short for effective Δi_{dc} measurement. In such a case, the Δi_{dc}

information can be extracted from active vectors $\boldsymbol{v}_M$ formed in the centre of the PWM period.
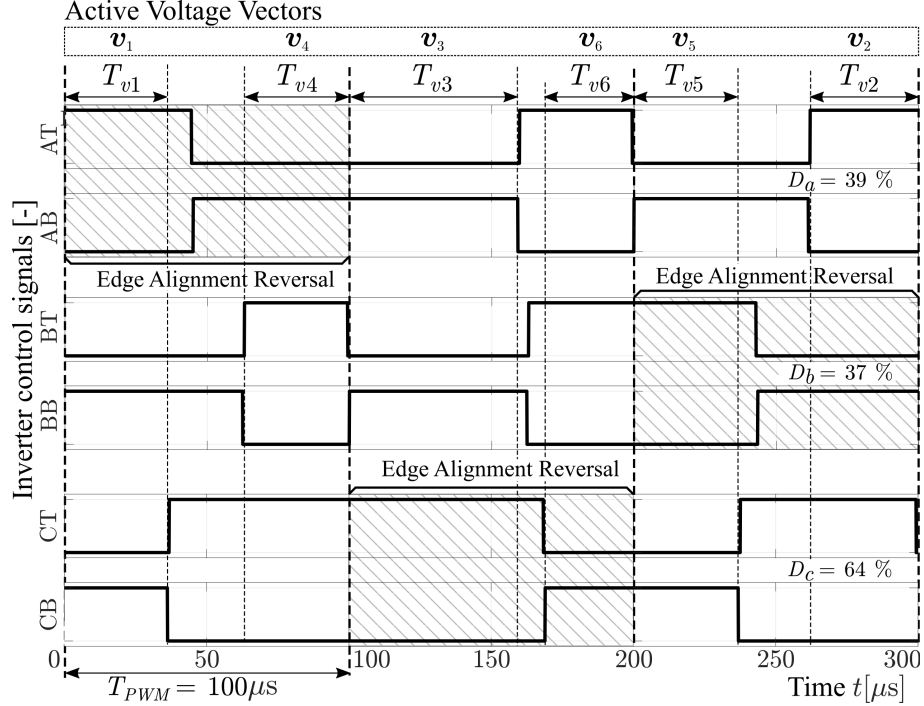
Figure 5.7: Principle of the proposed alignment-swap PWM switching scheme [MVB21]

An example of interaction between the ASPWM scheme and the proposed Δi_{dc} measurement method is shown in Figure 5.8. Signal u_{off} is updated by the DAC at the beginning of the PWM cycle and when the first switching event occurs so the u_{idc} signal does not saturate during the measurement time windows $\boldsymbol{T}_{vM}$ created at the PWM cycle edges. To extract the Δi_{dc} even from centre of the PWM cycle, when one of the duty cycles $\vec{D}_{abc}$ is too low or too high, a different u_{off} signal update sequence could be done to allow measurement during $\boldsymbol{v}_M$ vectors forming at the centre of PWM period.

Besides the Δi_{dc} measurement, the ASPWM switching scheme has to accommodate $\vec{i}_{abc}$ measurement as well by providing a suitable location for phase current sampling by MC IABC circuit. The most commonly used method of phase current reconstruction uses the measurement of voltage drops on phase shunt resistors R_{sh}, as illustrated in Figure 5.1. To reconstruct $\vec{i}_{abc}$, at least two bottom transistors must be conducting so the phase currents are flowing through the shunt resistors R_{sh}. The third phase current then can be calculated according to the first Kirchhoff's law $i_a + i_b + i_c = 0$ A. Such a suitable sampling locations were highlighted in Figure 5.8, near the end of each PWM cycle, where dynamic event from the last switching event settled.

When compared to CAPWM, the proposed ASPWM switching method basically replaces portions of the zero vectors $\boldsymbol{v}_0$ and $\boldsymbol{v}_7$ by a pair of opposite active vectors $\boldsymbol{v}_1$ versus $\boldsymbol{v}_4$, $\boldsymbol{v}_3$ versus $\boldsymbol{v}_6$, or $\boldsymbol{v}_2$ versus $\boldsymbol{v}_5$ in each PWM period. This causes an additional ripple of phase currents $\vec{i}_{abc}$. It improves conditions for the Δi_{dc} measurement, but also causes increased audible noise and, what could be more

83
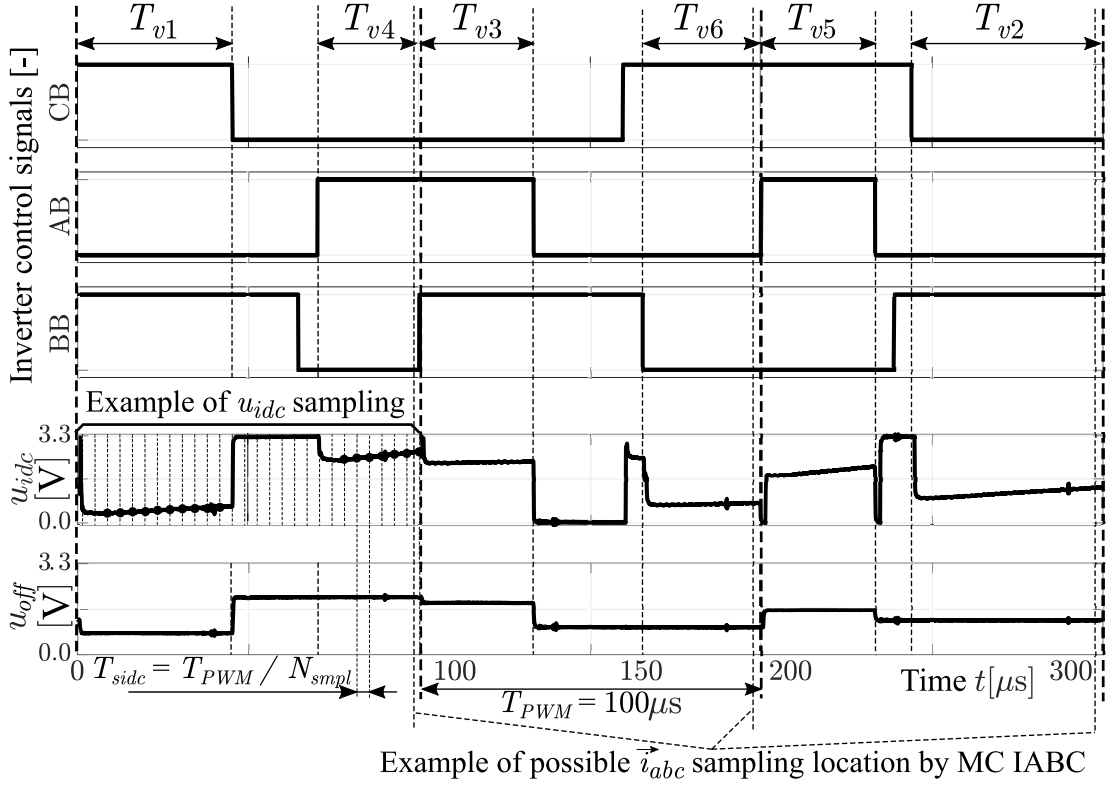
Figure 5.8: Principle of the proposed i_{dc} current slope measurement with ASPWM scheme [MVB21]

important, additional conductive power losses in both the semiconductor and the machine stator.

To evaluate the impact of the additional ripple current component, its RMS and peak-to-peak values were calculated using an analytical approach for both the proposed and the centre-aligned switching scheme [DW12]. The simulation was run for $U_{dc} = 400$ V and the machine stator inductance was chosen $L_{phN} = 0.3$ H, which should correspond to the worst-case scenario when operating the reference SynRM described in Section 1.2. Note that the stator resistance was neglected during the simulation. Also note that for the alignment-swap switching scheme, the resulting RMS value was obtained as an average and the peak-to-peak value as a maximum current ripple amplitude from all phases $N \in \{a, b, c\}$. Results for all stator voltage amplitudes $|\vec{u}_{\alpha\beta}| / \max(|\vec{u}_{\alpha\beta}|)$ and angles $\arg(\vec{u}_{\alpha\beta})$ are shown in Figure 5.9 to Figure 5.12. As expected, both the RMS and peak-to-peak values of the ripple current component are increased for the proposed switching scheme. The audible noise and Total Harmonic Distortion (THD) will be worse when using ASPWM. The main focus of this thesis are, however, the resulting power losses. The ripple RMS value peaks at 10 mA for centre-aligned PWM and 15 mA for ASPWM. It can be seen that the ASPWM generates higher ripples for low stator voltage amplitudes $|\vec{u}_{\alpha\beta}|$, while at the higher amplitudes its performance becomes comparable to centre-aligned PWM. Efficiency at higher speeds and loads will not be, therefore, affected by the ASPWM method as much. When looking at the maximal RMS values of the phase current ripple, the resulting power losses will likely form only a fraction of a Watt, which is significantly less than other power losses, as described

in Section 3. This is, however, mainly because of the relatively high inductances of SynRM machines. The ASPWM method might not be suitable for machines with smaller inductances, because the power losses caused by the resulting increase in phase current ripple would no longer be negligible. It is then a question, however, whether the ASPWM would even be necessary because greater Δi_{dc} changes would be measurable more easily.

When it comes to power efficiency, the ASPWM has actually an advantage over classic centre-aligned PWM. When comparing examples in Figure 2.4 and Figure 5.7, it can be seen that ASPWM generates only eight edges on the AT, AB, BT, BB, CT, and CB signals per PWM period, while the centre-aligned method produces twelve. This will effectively reduce the semiconductor switching losses by a third. For example, as shown in Figure 3.2 this represents several Watts for the reference inverter and fully offsets the power losses caused by the current ripple.
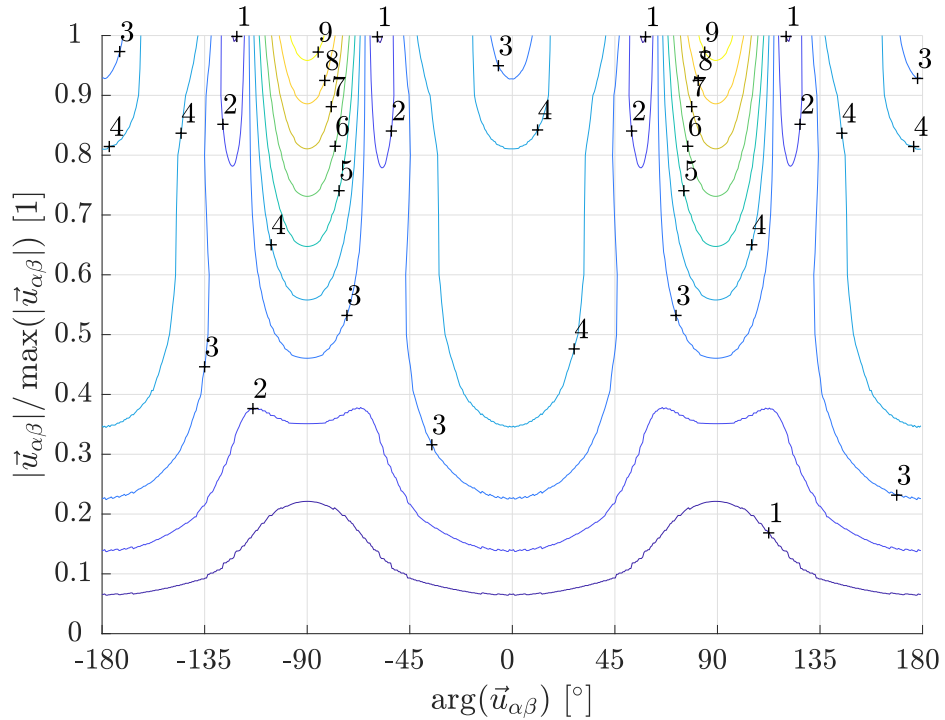
Figure 5.9: Simulated RMS value of phase current ripple component in milliamperes for centre-aligned PWM

Figure 5.10: Simulated peak-to-peak value of phase current ripple component in milliamperes for centre-aligned PWM

Figure 5.11: Simulated RMS value of phase current ripple component in milliamperes for alignment-swap PWM

86
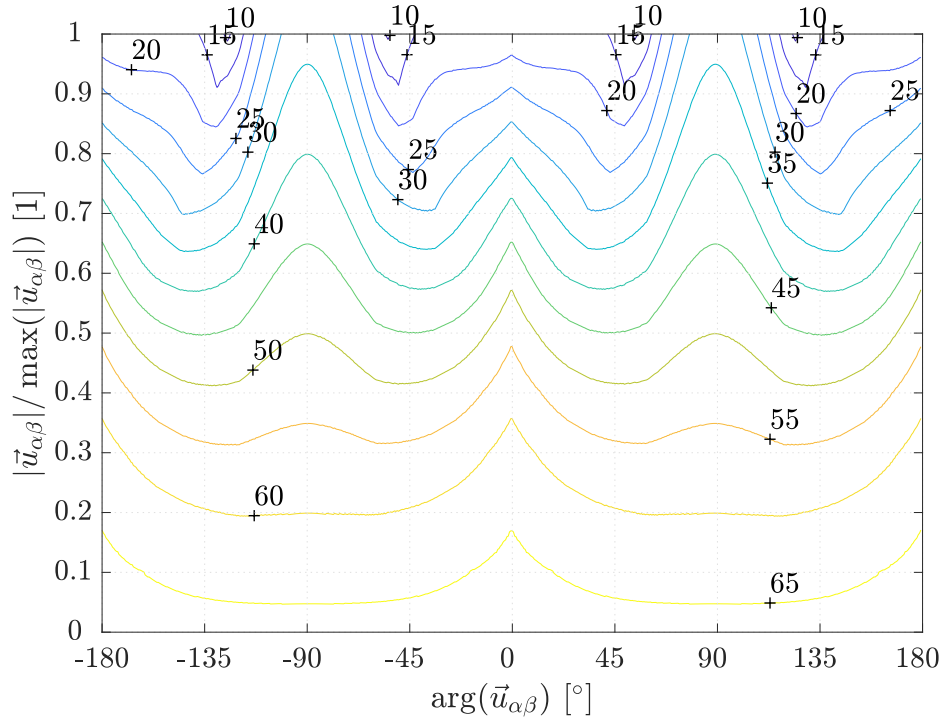
Figure 5.12: Simulated peak-to-peak value of phase current ripple component in milliamperes for alignment-swap PWM

5.3. Kalman Filter

Various methods were proposed for estimation of position, speed, and parameter motor drives, however, the Kalman Filter and its variations are regarded as a high performing and relevant algorithms. This section will first present the theory of the original Kalman Filter (KF) algorithm. It was first proposed by R. E. Kalman in 1960 and it was modified or adapted for many different applications since then. The KF is a recursive algorithm, which minimizes the square of the estimate errors between actual system states $\vec{x}$ and the estimates $\hat{\vec{x}}$. This is done by the alternation of the prediction and correction steps, sometimes also called the time and the measurement updates. The system states are updated based on the known model during the prediction step. The correction step then consists of updating the state estimates based on the measurement [WB06]. To find the true optimal solution, the noise has to have a normal distribution. The probability density for systems with n states can be described as

$$f(\vec{x}) = \frac{1}{(2\pi)^{\frac{n}{2}} |\mathbf{P}|^{\frac{1}{2}}} e^{-\frac{1}{2}(\vec{x}-\hat{\vec{x}})\mathbf{P}^{-1}(\vec{x}-\hat{\vec{x}})^{\mathrm{T}}}, \tag{5.28}$$

where $\mathbf{P}$ is the covariance matrix.

One well-known modification, the Extended Kalman Filter (EKF), will then be described in the second part of this section. The EKF is generally suitable for non-linear systems under influence of Gaussian noise. As will be shown in Section 5.4, this and the ability to near-optimally merge the position and parameter information

from multiple measurements made it suitable for the proposed algorithm. The disadvantages of EKF are, however, relatively high computational demands. Also, the acquisition and description of stochastic properties of measurements and estimated states for both KF and EKF is not always a simple task [LK19, BG10].

5.3.1. Kalman Filter Theory

The KF is considered to be an optimal state estimator for linear systems under influence of white noise. Since the digital implementation of the estimator is expected, we first assume the discrete dynamic system state-space description

$$\vec{x}_{k+1} = \mathbf{A}_k \vec{x}_k + \mathbf{B}_k \vec{u}_k + \vec{w}_k,$$
$$\vec{y}_k = \mathbf{C}_k \vec{x}_k + \vec{v}_k,$$
(5.29)

where $\mathbf{A}$, $\mathbf{B}$, and $\mathbf{C}$ are matrices describing the system dynamic behaviour and relation with system inputs and outputs, $\vec{x}$ is the state vector, $\vec{u}$ is the vector of control variables, $\vec{y}$ is the output vector, and $\vec{w}$ and $\vec{v}$ are the process and measurement noise vectors. The noise vectors are assumed to be white noises with normal distribution $\vec{w} \sim N(0, \mathbf{Q})$ and $\vec{v} \sim N(0, \mathbf{R})$, which means zero first moment and the second moment described by covariance matrices $\mathbf{Q}$ and $\mathbf{R}$. There is also a condition of $\vec{w}$ and $\vec{v}$ not being correlated in time and between each other, or

$$E\{\vec{w}_k, \vec{w}_l\} = E\{\vec{v}_k, \vec{v}_l\} = \mathbf{0} \quad \text{for} \quad k \neq l,$$
$$E\{\vec{w}_k, \vec{w}_k\} = \mathbf{Q}_k,$$
$$E\{\vec{v}_k, \vec{v}_k\} = \mathbf{R}_k,$$
$$E\{\vec{w}_k, \vec{v}_l\} = \mathbf{0},$$
(5.30)

where $E\{\}$ is expected value operator. The KF searches for the optimal solution by minimizing the quadratic error of the estimate $\mathbf{P} = E\{(\vec{x} - \hat{x})(\vec{x} - \hat{x})^{\mathrm{T}}\}$. The matrix $\mathbf{P}$ is called the state error covariance matrix. The values on the main diagonal correspond to state variances and to covariances outside the main diagonal.

As was already mentioned in the previous section, the KF calculation consists of prediction and correction steps. The entire sequence is shown in Figure 5.13. The prediction begins with the calculation of the new state estimate

$$\vec{x}_{k|k-1} = \mathbf{A}\vec{x}_{k-1|k-1} + \mathbf{B}\vec{u}_k,$$
(5.31)

where $k|k-1$ subscript denotes estimate obtained prior to the measurement update and the $k|k$ subscript marks the estimate obtained after the measurement, sometimes also called apriori and aposteriori estimates. Because the estimate $\vec{x}_{k|k-1}$ was obtained only from the system model, the covariance matrix $\mathbf{P}$ should be updated to reflect reduced confidence in the new state estimate. Hence, the apriori update of the covariance matrix is done as

$$\mathbf{P}_{k|k-1} = \mathbf{A}\mathbf{P}_{k-1|k-1}\mathbf{A}^{\mathrm{T}} + \mathbf{Q}.$$
(5.32)

The second step, correction, has a goal to increase confidence in the state estimates using measurements and, as a result, lower the covariance matrix $\mathbf{P}$. This is done

by adding the difference between actual measurements $\vec{y}$ and the estimated system output $\mathbf{C}\vec{x}$ multiplied by the Kalman gain $\mathbf{K}$ to the apriori state estimate. The Kalman gain is obtained as

$$\mathbf{K}_k = \mathbf{P}_{k|k-1}\mathbf{C}^{\mathrm{T}}\left(\mathbf{C}\mathbf{P}_{k|k-1}\mathbf{C}^{\mathrm{T}} + \mathbf{R}\right)^{-1} = \mathbf{P}_{k|k}\mathbf{C}^{\mathrm{T}}\mathbf{R}^{-1}. \qquad (5.33)$$

The higher the uncertainty of the estimate given by covariance matrix $\mathbf{P}$, in relation to the covariance of the measurement $\mathbf{R}$, the higher the $\mathbf{K}$ and resulting correction and vice versa. The aposteriori state estimate can then be calculated as

$$\vec{x}_{k|k} = \vec{x}_{k|k-1} + \mathbf{K}_k(\vec{y}_k - \mathbf{C}\vec{x}_{k|k-1}). \qquad (5.34)$$

Finally, the increased confidence in the corrected estimate $\vec{x}_{k|k}$ should be reflected by the covariance matrix $\mathbf{P}$ aposteriori update. This is done as

$$\begin{aligned}
\mathbf{P}_{k|k} &= (\mathbf{I} - \mathbf{K}_k\mathbf{C})\,\mathbf{P}_{k|k-1}\,(\mathbf{I} - \mathbf{K}_k\mathbf{C})^{\mathrm{T}} + \mathbf{K}_k\mathbf{R}\mathbf{K}_k^{\mathrm{T}} = \\
&= \left(\mathbf{P}_{k|k-1}^{-1} + \mathbf{C}^{\mathrm{T}}\mathbf{R}^{-1}\mathbf{C}\right)^{-1} = (\mathbf{I} - \mathbf{K}_k\mathbf{C})\,\mathbf{P}_{k|k-1},
\end{aligned} \qquad (5.35)$$

where usually only the last expression is used because it assures that the matrix $\mathbf{P}$ will remain positive definite.

To start the recursive Kalman filter algorithm, the initial state estimate $\vec{x}_0$ and state covariance matrix $\mathbf{P}_0$ has to be defined. Based on confidence in the accuracy of $\vec{x}_0$, the $\mathbf{P}_0$ diagonals can be set to higher or lower numbers.

Prediction

1. Estimates states in the next step
$\vec{x}_{k|k-1} = \mathbf{A}\vec{x}_{k-1|k-1} + \mathbf{B}\vec{u}_k$

2. Project the error covariance ahead
$\mathbf{P}_{k|k-1} = \mathbf{A}\mathbf{P}_{k-1|k-1}\mathbf{A}^{\mathrm{T}} + \mathbf{Q}$

Correction

1. Calculate the Kalman gain
$\mathbf{K}_k = \mathbf{P}_{k|k}\mathbf{C}^{\mathrm{T}}\mathbf{R}^{-1}$

2. Update estimate with measurement $\vec{y}_k$
$\vec{x}_{k|k} = \vec{x}_{k|k-1} + \mathbf{K}_k(\vec{y}_k - \mathbf{C}\vec{x}_{k|k-1})$

3. Update the error covariance
$\mathbf{P}_{k|k} = (\mathbf{I} - \mathbf{K}_k\mathbf{C})\,\mathbf{P}_{k|k-1}$

Initial conditions
$\hat{\vec{x}}_0, \mathbf{P}_0$
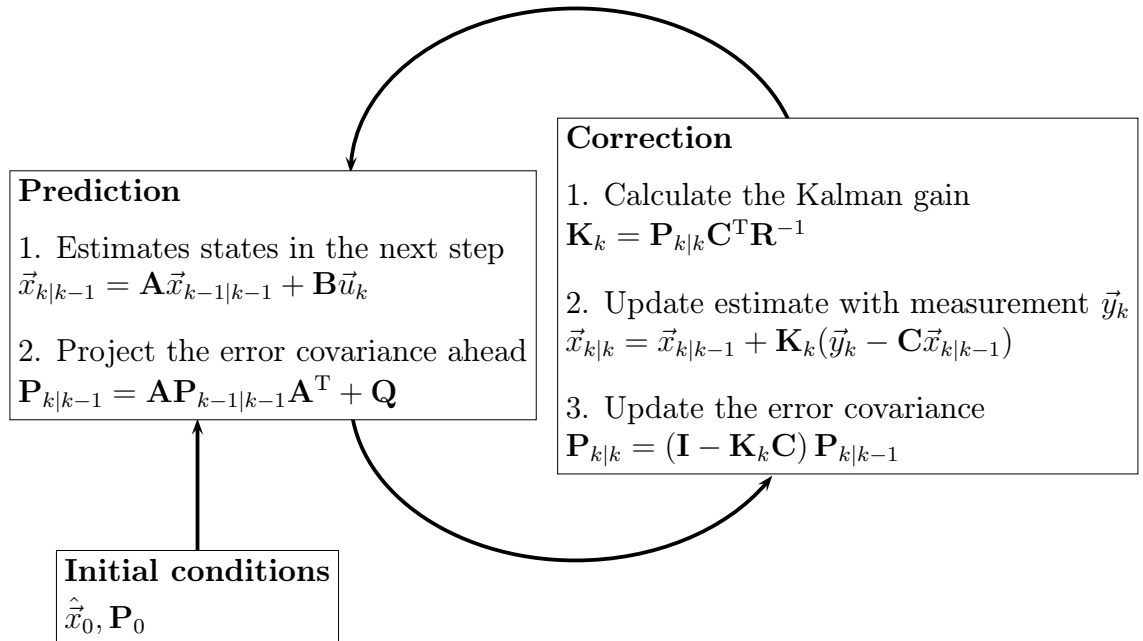
Figure 5.13: Estimation sequence of Kalman filter [WB06]

5.3.2. Extended Kalman Filter Theory

Many real systems, including the SynRM, are non-linear and the standard KF cannot be applied. The EKF was developed for this purpose as a direct extension by applying the KF to the system linearized near the operation point using Taylor expansion [AR15, WB06]. First, we assume a discrete non-linear system state-space description

$$
\begin{aligned}
\vec{x}_{k+1} &= \mathbf{f}\left(\vec{x}_k, \vec{u}_k, \vec{w}_k\right), \\
\vec{y}_k &= \mathbf{h}\left(\vec{x}_k, \vec{v}_k\right),
\end{aligned}
\tag{5.36}
$$

where $\mathbf{f}$ and $\mathbf{h}$ are non-linear time-variant system and output functions and the remaining symbols have the same meaning as in the linear state-space model (5.29). The last state estimate $\hat{\vec{x}}$ will be used as an operation point, around which the system is linearized. Linearization itself is done by taking the first element of Taylor's expansion, which yields Jacobian matrices

$$
\mathbf{F}_k = \left[\frac{\partial \mathbf{f}}{\partial \vec{x}}\right]_{\vec{x}=\hat{\vec{x}}_{k-1|k-1},\vec{u}=\vec{u}_k,\vec{w}=\vec{0}} = \begin{bmatrix} \frac{\partial f_1}{\partial x_1} & \frac{\partial f_1}{\partial x_2} & \frac{\partial f_1}{\partial x_3} & \cdots & \frac{\partial f_1}{\partial x_n} \\ \frac{\partial f_2}{\partial x_1} & \frac{\partial f_2}{\partial x_2} & \frac{\partial f_2}{\partial x_3} & \cdots & \frac{\partial f_2}{\partial x_n} \\ \vdots & \vdots & \vdots & \ddots & \vdots \\ \frac{\partial f_n}{\partial x_1} & \frac{\partial f_n}{\partial x_2} & \frac{\partial f_n}{\partial x_3} & \cdots & \frac{\partial f_n}{\partial x_n} \end{bmatrix},
\tag{5.37}
$$

$$
\mathbf{H}_k = \left[\frac{\partial \mathbf{h}}{\partial \vec{x}}\right]_{\vec{x}=\hat{\vec{x}}_{k|k-1},\vec{v}=\vec{0}},
\tag{5.38}
$$

$$
\mathbf{W}_k = \left[\frac{\partial \mathbf{f}}{\partial \vec{w}}\right]_{\vec{x}=\hat{\vec{x}}_{k|k-1}},
\tag{5.39}
$$

$$
\mathbf{V}_k = \left[\frac{\partial \mathbf{h}}{\partial \vec{v}}\right]_{\vec{x}=\hat{\vec{x}}_{k|k-1}}.
\tag{5.40}
$$

Note that $\vec{w} = \vec{0}$ and $\vec{v} = \vec{0}$ were assumed during linearization because of the zero mean value of the noise signals and the fact that immediate values of $\vec{w}$ and $\vec{v}$ are unknown. We can then reach the linearized error system

$$
\begin{aligned}
\Delta\vec{x}_{k+1} &= \mathbf{F}_k(\Delta\vec{x}_k) + \mathbf{W}_k w_k, \\
\Delta\vec{y}_k &= \mathbf{H}_k(\Delta\vec{x}_k) + \mathbf{V}_k v_k,
\end{aligned}
\tag{5.41}
$$

where $\Delta\vec{x} = \vec{x} - \hat{\vec{x}}$ and $\Delta\vec{y} = \vec{y} - \hat{\vec{y}}$. The error system (5.41) now noticeably resembles the linear state-space model (5.29) so the Kalman filter theory described in Section 5.3.1 can now be applied. Provided that linearization affected the system and measurement covariances as

$$
\tilde{\mathbf{Q}}_k = \mathbf{W}_k \mathbf{Q}_{k-1} \mathbf{W}_k^\mathrm{T},
\tag{5.42}
$$

$$
\tilde{\mathbf{R}}_k = \mathbf{V}_k \mathbf{R}_{k-1} \mathbf{V}_k^\mathrm{T},
\tag{5.43}
$$

we can perform the prediction step as

$$\hat{\vec{x}}_{k|k-1} = \mathbf{f}\left(\hat{\vec{x}}_{k-1|k-1}, \vec{u}_k\right),$$
$$\mathbf{P}_{k|k-1} = \mathbf{F}_k \mathbf{P}_{k-1|k-1} \mathbf{F}_k^{\mathrm{T}} + \tilde{\mathbf{Q}}_k, \tag{5.44}$$

and the correction step as

$$\mathbf{K}_k = \mathbf{P}_{k|k-1} \mathbf{H}_k^{\mathrm{T}} \left(\mathbf{H}_k \mathbf{P}_{k|k-1} \mathbf{H}_k^{\mathrm{T}} + \tilde{\mathbf{R}}_k\right)^{-1},$$
$$\hat{\vec{x}}_{k|k} = \hat{\vec{x}}_{k|k-1} + \mathbf{K}_k \left[\vec{y}_k - \mathbf{h}(\hat{\vec{x}}_{k|k-1}, \vec{0})\right], \tag{5.45}$$
$$\mathbf{P}_{k|k} = \left(\mathbf{I} - \mathbf{K}_k \mathbf{H}_k\right) \mathbf{P}_{k|k-1}.$$

The entire estimation process is illustrated in Figure 5.14. It should be noted that the linearization introduced an error into the estimate $\hat{\vec{x}}$ and the covariance matrix $\mathbf{P}$, making the solution sub-optimal. The more significant non-linearity, the more significant the error. The linearization also has to be performed in each calculation step, which increases the algorithm complexity.
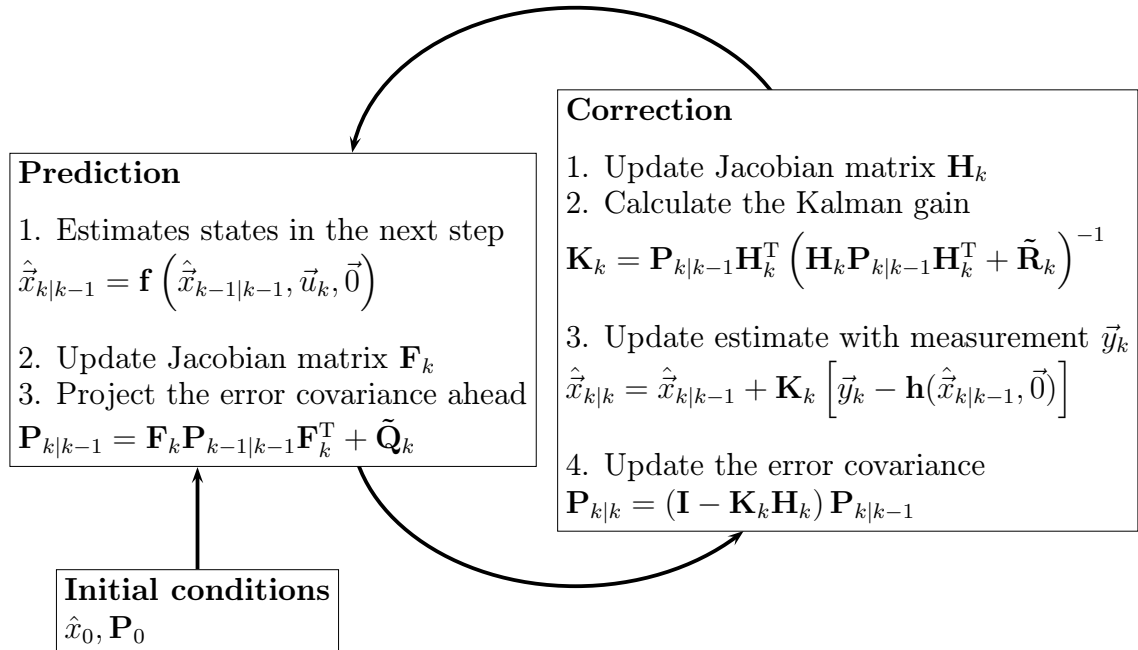
Figure 5.14: Estimation sequence using extended Kalman filter [WB06]

5.4. Proposed EKF-based Estimation Algorithm

The block diagram of the proposed sensorless algorithm in Figure 5.1 shows the proposed EKF-based observer, which provides estimations of rotor electrical position $\hat{\theta}_e$, electrical angular speed $\hat{\omega}_e$, and stator inductances $\hat{L}_d$ and $\hat{L}_q$. Based on the illustration in Figure 5.3, all this information can be extracted from the $\mathcal{R}'_{phN}$ measurement (i.e. its amplitude is inverse to $\hat{L}_d$ and $\hat{L}_q$ and the position is contained in phases

of $\mathcal{R}'_{pha}$, $\mathcal{R}'_{phb}$, and $\mathcal{R}'_{phc}$ harmonic functions). The following Section 5.4.1 will show a basic implementation of the EKF algorithm (further called EKF-BASIC), which can extract mentioned quantities. The main reason for the selection of the EKF was its ability to near-optimally merge the information from multiple sensors with various noise properties. As it was already presented in the literature, the stator current measurements $\vec{i}_{\alpha\beta}$ and knowledge of synchronous machine model can also be used to obtain rotor speed and position information [AR15]. Combining these two models brings a redundancy, which can be exploited in many ways. For example, the previously published version of the proposed EKF-based estimator featured an estimation of core losses [MVB21]. The following Section 5.4.2 will show another example of the implementation of an EKF-based algorithm (called EKF-RS) that provides the stator resistance R_s estimate.

Both the proposed EKF-based algorithm versions (i.e. EKF-BASIC and EKF-RS) were verified using simulation and the results are discussed in the following sections. Simulations were done for the FOC algorithm with an integrated investigated EKF algorithm using the MATLAB Simulink r2018a for the reference SynRM described in Section 1.2. Because the simulation was focused on the EKF-based algorithm, rather than on the $\hat{\mathcal{R}}'_{phN}$ measurement process, the $\hat{\mathcal{R}}'_{phN}$ values were provided directly by the SynRM machine model. This also allowed to simplify the simulation and set the simulation step to $T_s = T_{PWM} = 100~\mu s$.

5.4.1. Proposed Algorithm Variant EKF-BASIC

To extract rotor electrical position $\hat{\theta}_e$, electrical angular speed $\hat{\omega}_e$, and stator inductances $\hat{L}_d$ and $\hat{L}_q$, equations (5.10) to (5.12) are going to be used. If we assume, that $\mathcal{R}'_d$ and $\mathcal{R}'_q$ are slow-changing quantities, we can form the discrete equations

$$
\begin{aligned}
\mathcal{R}'_{pha,k} &= \mathcal{R}'_{d,k} \cos^2(\theta_{e,k}) + \mathcal{R}'_{q,k} \sin^2(\theta_{e,k}), \\
\mathcal{R}'_{phb,k} &= \mathcal{R}'_{d,k} \cos^2(\theta_{e,k} + \tfrac{2\pi}{3}) + \mathcal{R}'_{q,k} \sin^2(\theta_{e,k} - \tfrac{2\pi}{3}), \\
\mathcal{R}'_{phc,k} &= \mathcal{R}'_{d,k} \cos^2(\theta_{e,k} - \tfrac{2\pi}{3}) + \mathcal{R}'_{q,k} \sin^2(\theta_{e,k} + \tfrac{2\pi}{3}),
\end{aligned}
\tag{5.46}
$$

$$
\begin{aligned}
\mathcal{R}'_{d,k+1} &= \mathcal{R}'_{d,k}, \\
\mathcal{R}'_{q,k+1} &= \mathcal{R}'_{q,k}.
\end{aligned}
\tag{5.47}
$$

To obtain the rotor speed $\hat{\omega}_e$, the mechanical model of SynRM can be expressed from (1.19), (1.20), and (1.21) as

$$
\frac{d\omega_e}{dt} = \frac{P_p}{J} \left[\frac{3P_p}{2} \left(\frac{1}{\mathcal{R}'_d} - \frac{1}{\mathcal{R}'_q} \right) i_d i_q - T_l - B_1 \omega_m - \text{sign}(\omega_m) B_2 \omega_m^2 \right],
\tag{5.48}
$$

$$
\frac{d\theta_e}{dt} = \omega_e.
\tag{5.49}
$$

The above dynamical model of rotor speed, however, requires knowledge of the load torque T_l, which is often not available, and the stator current vector $\vec{i}_{dq}$, which is not being considered for the EKF-BASIC algorithm. When further considering that the

above mechanical model will not benefit the steady-state speed estimation accuracy, it was decided to model the rotor speed as constant

$$\frac{\mathrm{d}\omega_e}{\mathrm{d}t} =\sim 0 \; \frac{\mathrm{rad}}{\mathrm{s}^2}. \tag{5.50}$$

Applying the Euler's discretization method to mechanical models (5.49) and (5.50) then leads to the following set of discrete equations

$$\begin{aligned} \omega_{e,k+1} &= \omega_{e,k}, \\ \theta_{e,k+1} &= \theta_{e,k} + T_s\omega_{e,k}, \end{aligned} \tag{5.51}$$

where T_s is sampling period, which is usually set to be equal or multiple of switching period T_{PWM}. The Euler's discretization is a simple but also relatively inaccurate method and, thus, requires sufficiently high sampling frequency. This condition is, however, usually met when controlling SynRM at nominal speed, because its mechanical time constant is usually several orders larger than the PWM switching period T_{PWM}.

The first step to design EKF, as described in Section 5.3.2, is the definition of system state and input vectors. Combining equations (5.47) and (5.51) leads to state vector

$$\hat{\vec{x}} = \begin{bmatrix} \hat{\mathcal{R}}'_d, & \hat{\mathcal{R}}'_q, & \hat{\omega}_e, & \hat{\theta}_e \end{bmatrix}^{\mathrm{T}} \tag{5.52}$$

and the system input vector $\vec{u} = 0$ (i.e. the estimated system is not driven). Note that the $\hat{L}_d$ and $\hat{L}_q$ are assumed to be obtained outside of the EKF-BASIC algorithm using relation (5.8).

As was discussed in Section 5.2, not all the $\mathrm{d}i_a/\mathrm{d}t$, $\mathrm{d}i_b/\mathrm{d}t$, and $\mathrm{d}i_c/\mathrm{d}t$ measurements are available each PWM period, depending on applied active voltage vectors $\boldsymbol{v}_M$. The proposed ASPWM scheme allows to obtain current derivative information for one of the N phases during each T_{PWM}. Hence, only one of equations (5.46), corresponding to the measured phase N, will be used each step k. The available measurement (either $\mathcal{R}'_{pha}$, $\mathcal{R}'_{phb}$, or $\mathcal{R}'_{phc}$) is then going to form the measurement vector

$$\vec{y} = \mathcal{R}'_{phN}. \tag{5.53}$$

The feedback non-linear time-variant system function will then be

$$\mathbf{f}\left(\hat{\vec{x}}_{k-1}, \vec{u}_k, \vec{0}\right) = \begin{bmatrix} \hat{\mathcal{R}}'_{d,k-1} \\ \hat{\mathcal{R}}'_{q,k-1} \\ \hat{\omega}_{e,k-1} \\ \hat{\theta}_{e,k-1} + T_s\hat{\omega}_{e,k-1} \end{bmatrix} \tag{5.54}$$

and the non-linear output function can be assembled from (5.46) as

$$\mathbf{h}\left(\hat{\vec{x}}_k, \vec{0}\right) = \begin{bmatrix} \hat{\mathcal{R}}'_{d,k}\cos^2(\hat{\theta}_{e,k} + \theta_{phN}) + \hat{\mathcal{R}}'_{q,k}\sin^2(\hat{\theta}_{e,k} + \theta_{phN}) \end{bmatrix}, \tag{5.55}$$

where θ_{phN} is stator phase offset matching the phase of actual $\mathcal{R}'_{phN}$ measurement (either $0\,\mathrm{rad}$, $\frac{2\pi}{3}\,\mathrm{rad}$, or $-\frac{2\pi}{3}\,\mathrm{rad}$ for phases $\mathcal{R}'_{pha}$, $\mathcal{R}'_{phb}$, and $\mathcal{R}'_{phc}$).

The Jacobian matrix of output matrix (5.55) is

$$\mathbf{H}_k = \left[\frac{\partial \mathbf{h}}{\partial \vec{x}}\right]_{\vec{x}=\hat{\vec{x}}_{k|k-1},\vec{v}=\vec{0}} = \tag{5.56}$$

$$= \left[\cos^2(\hat{\theta}_e + \theta_{phN}), \quad \sin^2(\hat{\theta}_e + \theta_{phN}), \quad 0, \quad H_{16}\right], \tag{5.57}$$

where

$$H_{16} = \frac{\partial \mathcal{R}'_{phN}}{\partial \theta_e} = 2(\hat{\mathcal{R}}'_q - \hat{\mathcal{R}}'_d)\sin(\hat{\theta}_e + \theta_{phN})\cos(\hat{\theta}_e + \theta_{phN}). \tag{5.58}$$

Discrete-time Jacobian matrix of process matrix (5.54) is

$$\mathbf{F}_k = \left[\frac{\partial \mathbf{f}}{\partial \vec{x}}\right]_{\vec{x}=\hat{\vec{x}}_{k-1|k-1},\vec{u}=\vec{u}_k,\vec{w}=\vec{0}} = \begin{bmatrix} 1 & 0 & 0 & 0 \\ 0 & 1 & 0 & 0 \\ 0 & 0 & 1 & 0 \\ 0 & 0 & T_s & 1 \end{bmatrix}. \tag{5.59}$$

To complete the EKF-based estimator design, the stochastic properties of the state estimates and measurements have to be modelled via covariance matrices $\tilde{\mathbf{Q}}$ and $\tilde{\mathbf{R}}$. In both cases, the matrices can be, for example, obtained using methods like the Expectation-Maximization (EM) algorithm [Moo96]. The EM algorithm fits parameters $\tilde{\mathbf{Q}}$ and $\tilde{\mathbf{R}}$ of Gaussian measurement models to maximize model likelihood by interleaving the expectation and maximization steps over a block of measured data. The expectation step calculates expected values of states and measurements based on the latest obtained $\tilde{\mathbf{Q}}$ and $\tilde{\mathbf{R}}$ parameters using the Kalman smoothing estimator. The maximization step then improves the $\tilde{\mathbf{Q}}$ and $\tilde{\mathbf{R}}$ estimates using previously obtained expected values. These steps continue until a relative steady state of estimates is reached. Such algorithms are, however, relatively computationally intensive, which makes them harder to use in the field. In practice, the matrices $\tilde{\mathbf{Q}}$ and $\tilde{\mathbf{R}}$ are often used as offline design parameters of EKF. This thesis will apply the latter approach and provide a way of calculating the initial configuration of covariance matrices, assuming that additional tuning might be required to improve performance. It is understood that such an approach does not utilize the full potential of the EKF algorithm and only sub-optimal results will be demonstrated. Still, the validity of the proposed algorithms should be proven.

Because there is only a single signal used as a measurement, the noise covariance matrix has a form

$$\tilde{\mathbf{R}} = \sigma^2_{\mathcal{R}_{ph}}, \tag{5.60}$$

where $\sigma_{\mathcal{R}_{ph}}$ is standard deviation of phase reluctance measurements $\mathcal{R}'_{phN}$. The value of $\sigma_{\mathcal{R}_{ph}}$ is difficult to model and in this work it is acquired by offline analysis of recordings of $\mathcal{R}'_{phN}$ measurements from an actual system. An example of such approach will be discussed in Section 6.2.1. Sensitivity to incorrect setup of $\sigma_{\mathcal{R}_{ph}}$

will be analyzed via simulation further in this section. All the states are considered to be uncorrelated, hence, the state noise covariance matrix has a diagonal form

$$\tilde{\mathbf{Q}} = \begin{bmatrix} \sigma_{\mathcal{R}'_d}^2 & 0 & 0 & 0 \\ 0 & \sigma_{\mathcal{R}'_q}^2 & 0 & 0 \\ 0 & 0 & \sigma_{\omega_e}^2 & 0 \\ 0 & 0 & 0 & \sigma_{\theta_e}^2 \end{bmatrix}. \tag{5.61}$$

Based on the dynamic performance required by the application, the states $\hat{\mathcal{R}}'_d$ and $\hat{\mathcal{R}}'_q$ can be considered to be slow-changing parameters. Their standard deviations $\sigma_{\mathcal{R}'_d}$ and $\sigma_{\mathcal{R}'_q}$ can, therefore, be selected close or equal to zero. The speed estimation deviation can be selected as the maximal expected electrical speed change with the moment of inertia J and nominal torque T_{nom} per sampling period T_s, as $\sigma_{\omega_e} = T_s T_{\mathrm{nom}}/J$. Because position θ_e is obtained as a pure integration of ω_e, its deviation will be chosen as $\sigma_{\theta_e} = 0$ rad [BSL$^+$10, AR15].

Finally, the initialization of EKF-BASIC is done through the definition of the initial state vector $\hat{\vec{x}}_0$ and the initial covariance matrix $\mathbf{P}_0$. As discussed in Section 5.3.1, there are multiple approaches. As an example, the state vector can be set

$$\hat{\vec{x}}_0 = \begin{bmatrix} 1/L_{d0}, & 1/L_{q0}, & 0, & 0 \end{bmatrix}, \tag{5.62}$$

where L_{d0} and L_{q0} are rough expected machine inductances. Similarly, the $\mathbf{P}_0$ can be set as a diagonal matrix, usually with sufficiently high variance values on the main diagonal, reflecting the low confidence in vector $\hat{\vec{x}}_0$.

Simulation of EKF-BASIC Variant

To verify behaviour of EKF-BASIC, the estimator was integrated into the SynRM FOC algorithm within the Matlab Simulink simulation environment. Configurations of the state noise matrix $\tilde{\mathbf{Q}}$, measurement noise matrix $\tilde{\mathbf{R}}$, and initial vector $\hat{\vec{x}}_0$ are listed in Table 5.1. The $\mathcal{R}'_{phN}$ measurements were by default distorted with a white noise of parameters matching to the matrix $\tilde{\mathbf{R}}$. The covariance matrix was initialized as

$$\mathbf{P}_0 = \mathrm{diag}\left(0.01\ \mathrm{H}^2, 0.01\ \mathrm{H}^2, 100\ \frac{\mathrm{rad}^2}{\mathrm{s}^2}, 1\ \mathrm{rad}^2 \right). \tag{5.63}$$

Table 5.1: EKF-BASIC setup of vector $\hat{\tilde{x}}_0$ and matrices $\tilde{\mathbf{R}}$ and $\tilde{\mathbf{Q}}$ for simulation

Quantity	Value	Unit
$\sigma_{\mathcal{R}_{ph}}$	0.15	$\frac{1}{H}$
$\sigma_{\mathcal{R}'_d}$	$5 \cdot 10^{-4}$	$\frac{1}{H}$
$\sigma_{\mathcal{R}'_q}$	$5 \cdot 10^{-4}$	$\frac{1}{H}$
σ_{ω_e}	0.096	$\frac{\text{rad}}{\text{s}}$
σ_{θ_e}	0	rad
L_{d0}	0.5	H
L_{q0}	0.5	H
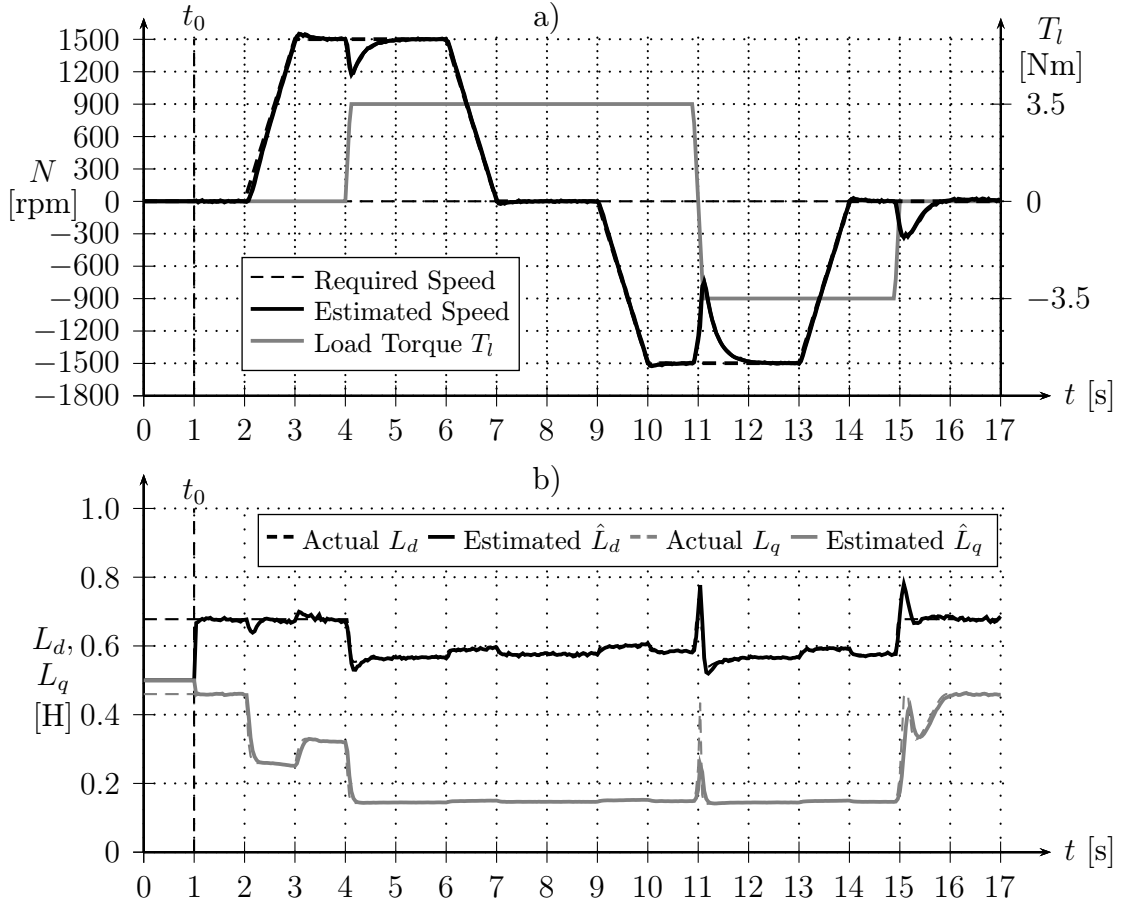
Figure 5.15: EKF-BASIC estimates of a) speed and b) inductances

Figure 5.15 shows estimated states $\hat{\tilde{x}}$ where the estimator was activated at time t_0 and the machine was run in the full speed range with the nominal load steps introduced. Both the speed and inductance estimates showed a very good tracking ability. To better highlight the performance, Figure 5.16 shows errors of the estimated states $\hat{\tilde{x}}$ for the same scenario as in Figure 5.15. With exception of dynamic events, where the inductance estimate relative errors δ_{L_d} and δ_{L_q} peaked to tens of percent and position error θ_e^{err} reached up to eight degrees, the steady-state performance showed estimation errors well below thresholds discussed in Section 4.3.
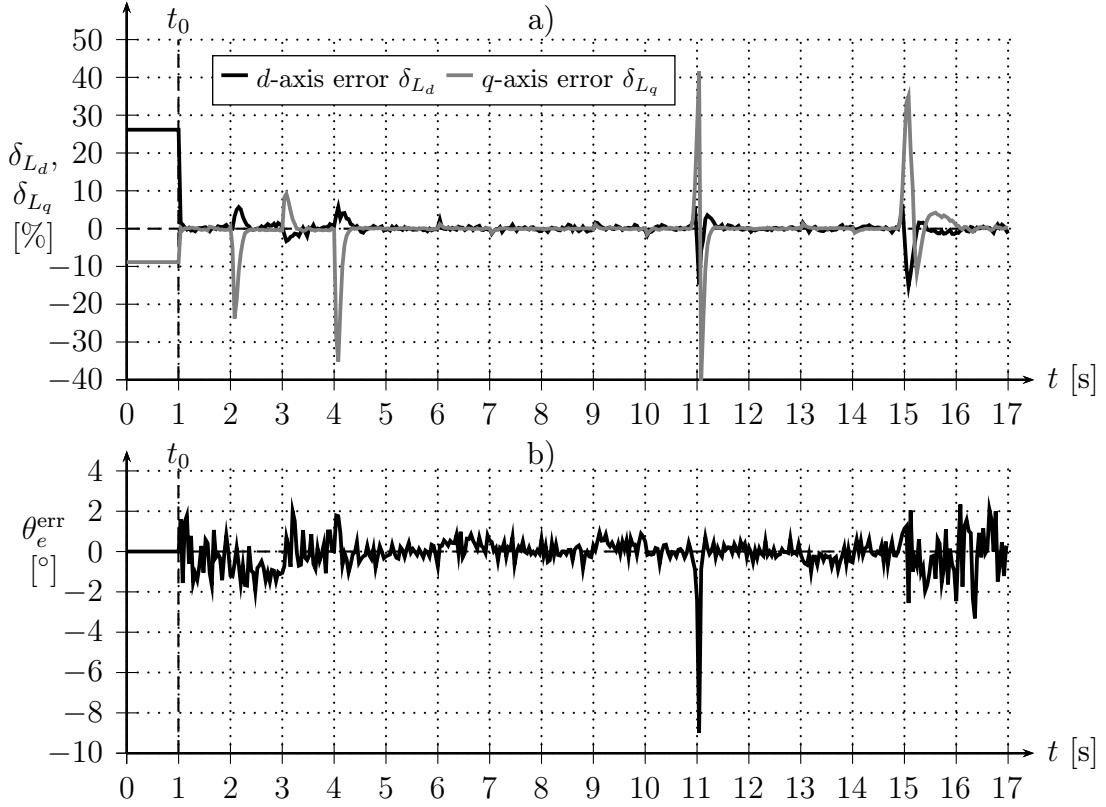
Figure 5.16: EKF-BASIC estimation errors of a) inductance and b) position

The $\hat{\mathcal{R}}'_{phN}$ is the only measurement being taken, hence, the accuracy of all the estimates will depend on its errors. Possible deterministic error models were discussed in Section 5.1. The only measurement error, which can be modelled, is the measurement gain error $\delta_{\mathcal{R}}\hat{\mathcal{R}}'_{phN}$, which is directly related to MC IDC gain measurement error δ_{uidc}. The simulated sensitivity of state estimates to sweep of $\delta_{\mathcal{R}}$ is shown in Figure 5.17. As expected, the $\hat{\mathcal{R}}'_d$ and $\hat{\mathcal{R}}'_q$ are affected directly, while there is no impact to position $\hat{\theta}_e$ and speed $\hat{\omega}_e$ estimation. This highlights the importance of careful determination of the MC IDC measurement gain for accuracy of inductance estimation.
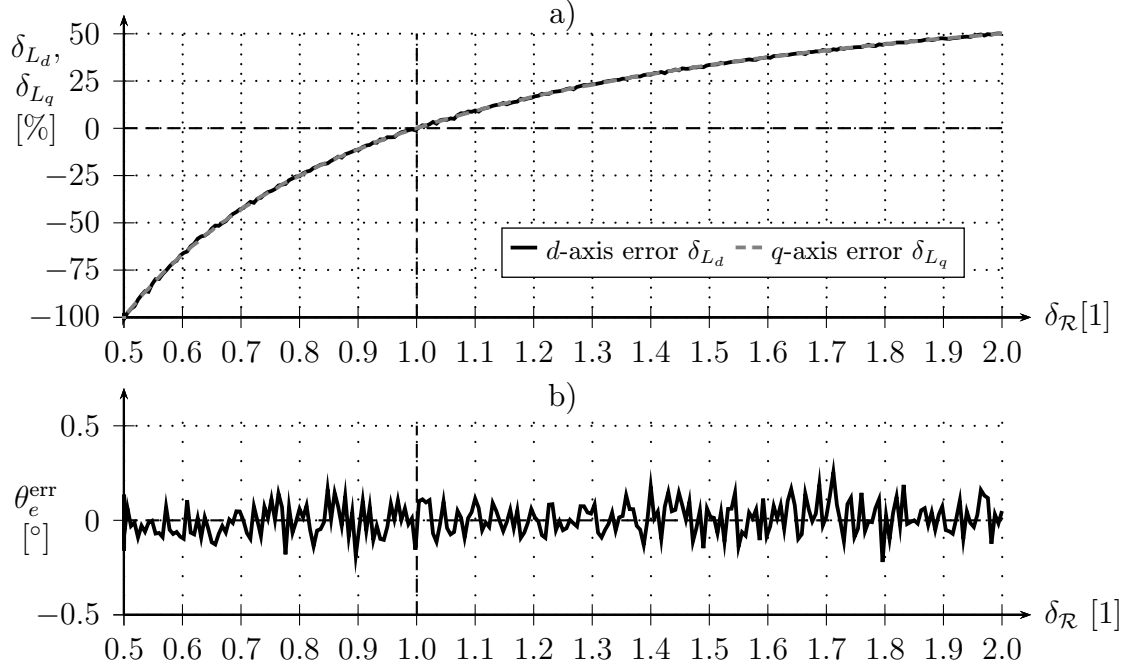
Figure 5.17: Sensitivity of EKF-BASIC a) inductance and b) position estimates to MC IDC measurement gain relative error $\delta_{\mathcal{R}}$ sweep

The stochastic $\hat{\mathcal{R}}'_{phN}$ measurement error can occur by assuming an incorrect value of standard deviance $\sigma_{\mathcal{R}_{ph}}$ in matrix $\tilde{\mathbf{R}}$. The sensitivity of state estimates to sweep of this relative error $\delta_{\sigma_{\mathcal{R}_{ph}}}$ is shown in Figure 5.18. The position estimate is quite insensitive but the inductance estimates show increased noise for underestimated $\sigma_{\mathcal{R}_{ph}}$ value. The key observation is that no steady-state estimate error or instability appeared. It should, however, be noted that the configuration of matrix $\tilde{\mathbf{Q}}$ in relation to matrix $\tilde{\mathbf{R}}$ can affect the results. Both Figure 5.17 and Figure 5.18 were obtained from 100-second recording for machine running at nominal speed and under nominal load, during which the modelled error parameter was swept.
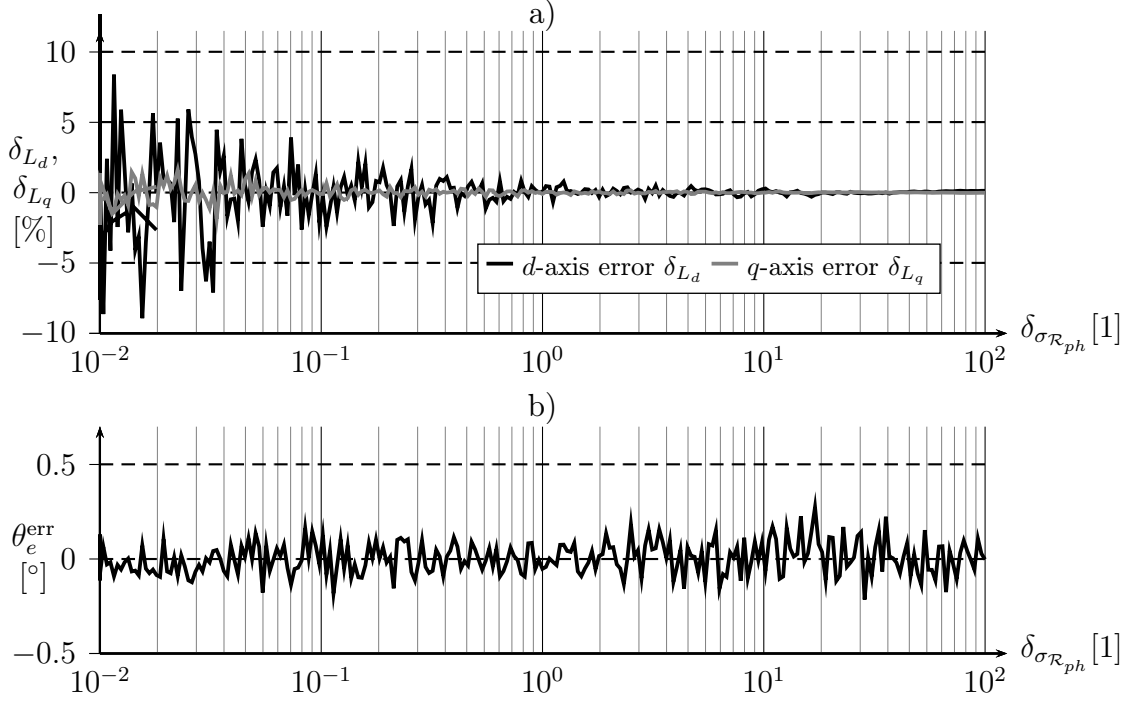
Figure 5.18: Sensitivity of EKF-BASIC a) inductance and b) position estimates to relative error $\delta_{\sigma_{\mathcal{R}_{ph}}}$ of standard deviance $\sigma_{\mathcal{R}_{ph}}$ setting in matrix $\tilde{\mathbf{R}}$

5.4.2. Variant with Stator Resistance Measurement EKF-RS

The EKF-BASIC algorithm already provided the most critical estimates of rotor electrical position $\hat{\theta}_e$, electrical angular speed $\hat{\omega}_e$, and stator inductances $\hat{L}_d$ and $\hat{L}_q$. This section will present the EKF-RS algorithm variant, which takes into account stator current $\vec{i}_{\alpha\beta}$ measurement and knowledge of the machine model to provide estimate of the stator resistance R_s as well.

First, the stator current model (1.18) with neglected core losses and dynamic inductance is assumed. Using the direct and quadrature axis reluctance $\mathcal{R}'_d$ and $\mathcal{R}'_q$ we can obtain SynRM stator current model

$$\begin{bmatrix} \frac{\mathrm{d}i_d}{\mathrm{d}t} \\ \frac{\mathrm{d}i_q}{\mathrm{d}t} \end{bmatrix} = \begin{bmatrix} \mathcal{R}'_d & 0 \\ 0 & \mathcal{R}'_q \end{bmatrix} \left\{ \begin{bmatrix} u_d \\ u_q \end{bmatrix} - \begin{bmatrix} R_s & -\omega_e/\mathcal{R}'_q \\ \omega_e/\mathcal{R}'_d & R_s \end{bmatrix} \begin{bmatrix} i_d \\ i_q \end{bmatrix} \right\}. \tag{5.64}$$

Although the stator current vector $\vec{i}_{\alpha\beta}$ is now considered to be available within the algorithm, the load torque T_l in the model (5.48) is still unknown. Hence, the mechanical models (5.49) and (5.50) are going to be used just like for the EKF-BASIC version. Applying Euler's discretization method to SynRM electrical and mechanical models (5.49), (5.50), and (5.64) leads to

$$\begin{aligned} i_{d,k} &= i_{d,k-1} + T_s \mathcal{R}'_{d,k-1} \left\{ u_{d,k} - R_s i_{d,k-1} + \omega_{e,k-1} i_{q,k-1}/\mathcal{R}'_{q,k-1} \right\}, \\ i_{q,k} &= i_{q,k-1} + T_s \mathcal{R}'_{q,k-1} \left\{ u_{q,k} - R_s i_{q,k-1} - \omega_{e,k-1} i_{d,k-1}/\mathcal{R}'_{d,k-1} \right\}, \\ \omega_{e,k} &= \omega_{e,k-1}, \\ \theta_{e,k} &= \theta_{e,k-1} + T_s \omega_{e,k-1}, \end{aligned} \tag{5.65}$$

99

where T_s is discrete sampling period. The argument of applicability of Euler's discretization method is the same as for the EKF-BASIC implementation, where the electrical and mechanical time constants of SynRM are considered to be longer than switching period T_{PWM} by at least an order.

The above-defined electrical and mechanical models (5.65) would alone be sufficient to design an EKF-based estimator, which could provide position $\hat{\theta}_e$ and speed $\hat{\omega}_e$ estimates [AR15,SKUU03]. However, to get the stator resistance $\hat{R}_s$ information, the EKF-RS will utilize (5.65) as well as (5.46) and (5.47). This leads to state vector

$$\hat{\vec{x}} = \begin{bmatrix} \hat{\mathcal{R}}'_d, & \hat{\mathcal{R}}'_q, & \hat{i}_d, & \hat{i}_q, & \hat{\omega}_e, & \hat{\theta}_e, & \hat{R}_s \end{bmatrix}^{\mathrm{T}}, \tag{5.66}$$

and system input vector

$$\vec{u} = \begin{bmatrix} u_d, & u_q \end{bmatrix}^{\mathrm{T}}. \tag{5.67}$$

The available measurements are stator currents $\vec{i}_{\alpha\beta}$ and phase reluctances $\mathcal{R}'_{pha}$, $\mathcal{R}'_{phb}$, or $\mathcal{R}'_{phc}$, which form the measurement vector

$$\vec{y} = \begin{bmatrix} \mathcal{R}'_{phN}, & i_\alpha, & i_\beta \end{bmatrix}^{\mathrm{T}}. \tag{5.68}$$

The feedback non-linear time-variant system function will then be

$$\mathbf{f}\left(\hat{\vec{x}}_{k-1}, \vec{u}_k, \vec{0}\right) = \begin{bmatrix} \hat{\mathcal{R}}'_{d,k-1} \\ \hat{\mathcal{R}}'_{q,k-1} \\ \hat{i}_{d,k-1} + T_s\hat{\mathcal{R}}'_{d,k-1}\left\{u_{d,k} - \hat{R}_{s,k-1}\hat{i}_{d,k-1} + \hat{\omega}_{e,k-1}\hat{i}_{q,k-1}/\hat{\mathcal{R}}'_{q,k-1}\right\} \\ \hat{i}_{q,k-1} + T_s\hat{\mathcal{R}}'_{q,k-1}\left\{u_{q,k} - \hat{R}_{s,k-1}\hat{i}_{q,k-1} - \hat{\omega}_{e,k-1}\hat{i}_{d,k-1}/\hat{\mathcal{R}}'_{d,k-1}\right\} \\ \hat{\omega}_{e,k-1} \\ \hat{\theta}_{e,k-1} + T_s\hat{\omega}_{e,k-1} \\ \hat{R}_{s,k-1} \end{bmatrix}. \tag{5.69}$$

And, finally, the non-linear output function can be assembled using Park's transformation matrix (1.3) for stator currents and from (5.46) as

$$\mathbf{h}\left(\hat{\vec{x}}_k, \vec{0}\right) = \begin{bmatrix} \hat{\mathcal{R}}'_{d,k}\cos^2(\hat{\theta}_{e,k} + \theta_{phN}) + \hat{\mathcal{R}}'_{q,k}\sin^2(\hat{\theta}_{e,k} + \theta_{phN}) \\ \cos(\hat{\theta}_{e,k})i_{d,k} - \sin(\hat{\theta}_{e,k})i_{q,k} \\ \sin(\hat{\theta}_{e,k})i_{d,k} + \cos(\hat{\theta}_{e,k})i_{q,k} \end{bmatrix}. \tag{5.70}$$

The Jacobian matrix of output matrix (5.70) is

$$\mathbf{H}_k = \left[\frac{\partial \mathbf{h}}{\partial \vec{x}}\right]_{\vec{x}=\hat{\vec{x}}_{k|k-1},\vec{v}=\vec{0}} = \tag{5.71}$$

$$= \begin{bmatrix} \cos^2(\hat{\theta}_{e,k} + \theta_{phN}) & \sin^2(\hat{\theta}_{e,k} + \theta_{phN}) & 0 & 0 & 0 & H_{16} & 0 \\ 0 & 0 & \cos(\hat{\theta}_{e,k}) & -\sin(\hat{\theta}_{e,k}) & 0 & H_{26} & 0 \\ 0 & 0 & \sin(\hat{\theta}_{e,k}) & \cos(\hat{\theta}_{e,k}) & 0 & H_{36} & 0 \end{bmatrix}, \tag{5.72}$$

where H_{16} is defined in (5.58) and

$$
\begin{aligned}
H_{26} &= \frac{\partial i_\alpha}{\partial \theta_e} = -\sin(\hat{\theta}_{e,k})\hat{i}_{d,k} - \cos(\hat{\theta}_{e,k})\hat{i}_{q,k}, \\
H_{36} &= \frac{\partial i_\beta}{\partial \theta_e} = \cos(\hat{\theta}_{e,k})\hat{i}_{d,k} - \sin(\hat{\theta}_{e,k})\hat{i}_{q,k}.
\end{aligned}
\tag{5.73}
$$

Discrete-time Jacobian matrix of process matrix (5.69) is

$$
\mathbf{F}_k = \left[\frac{\partial \mathbf{f}}{\partial \vec{x}}\right]_{\vec{x}=\hat{\vec{x}}_{k-1|k-1},\vec{u}=\vec{u}_k,\vec{w}=\vec{0}} =
\begin{bmatrix}
1 & 0 & 0 & 0 & 0 & 0 & 0 \\
0 & 1 & 0 & 0 & 0 & 0 & 0 \\
F_{31} & F_{32} & F_{33} & F_{34} & F_{35} & F_{36} & F_{37} \\
F_{41} & F_{42} & F_{43} & F_{44} & F_{45} & F_{46} & F_{47} \\
0 & 0 & 0 & 0 & 1 & 0 & 0 \\
0 & 0 & 0 & 0 & T_s & 1 & 0 \\
0 & 0 & 0 & 0 & 0 & 0 & 1
\end{bmatrix},
\tag{5.74}
$$

where

$$
\begin{aligned}
F_{31} &= \frac{\partial i_d}{\partial \mathcal{R}'_d} = T_s\left\{u_{d,k} - \hat{R}_{s,k-1}\hat{i}_{d,k-1} + \hat{\omega}_{e,k-1}\hat{i}_{q,k-1}/\hat{\mathcal{R}}'_{q,k-1}\right\}, \\
F_{32} &= \frac{\partial i_d}{\partial \mathcal{R}'_q} = -T_s\hat{\mathcal{R}}'_{d,k-1}\hat{\omega}_{e,k-1}\hat{i}_{q,k-1}/\hat{\mathcal{R}}'^2_{q,k-1}, \\
F_{33} &= \frac{\partial i_d}{\partial i_d} = 1 - T_s\hat{R}_{s,k-1}\hat{\mathcal{R}}'_{d,k-1}, \\
F_{34} &= \frac{\partial i_d}{\partial i_q} = T_s\hat{\omega}_{e,k-1}\hat{\mathcal{R}}'_{d,k-1}/\hat{\mathcal{R}}'_{q,k-1}, \\
F_{35} &= \frac{\partial i_d}{\partial \omega_e} = T_s\hat{i}_{q,k-1}\hat{\mathcal{R}}'_{d,k-1}/\hat{\mathcal{R}}'_{q,k-1}, \\
F_{36} &= \frac{\partial i_d}{\partial \theta_e} = T_s\hat{\mathcal{R}}'_{d,k-1}u_{q,k}, \\
F_{37} &= \frac{\partial i_d}{\partial R_s} = -T_s\hat{\mathcal{R}}'_{d,k-1}\hat{i}_{d,k-1},
\end{aligned}
\tag{5.75}
$$

$$
\begin{aligned}
F_{41} &= \frac{\partial i_q}{\partial \mathcal{R}'_d} = T_s\hat{\mathcal{R}}'_{q,k-1}\hat{\omega}_{e,k-1}\hat{i}_{d,k-1}/\hat{\mathcal{R}}'^2_{d,k-1}, \\
F_{42} &= \frac{\partial i_q}{\partial \mathcal{R}'_q} = T_s\left\{u_{q,k} - \hat{R}_{s,k-1}\hat{i}_{q,k-1} - \hat{\omega}_{e,k-1}\hat{i}_{d,k-1}/\hat{\mathcal{R}}'_{q,k-1}\right\}, \\
F_{43} &= \frac{\partial i_q}{\partial i_d} = -T_s\hat{\omega}_{e,k-1}\hat{\mathcal{R}}'_{q,k-1}/\hat{\mathcal{R}}'_{d,k-1}, \\
F_{44} &= \frac{\partial i_q}{\partial i_q} = 1 - T_s\hat{R}_{s,k-1}\hat{\mathcal{R}}'_{q,k-1}, \\
F_{45} &= \frac{\partial i_q}{\partial \omega_e} = -T_s\hat{i}_{d,k-1}\hat{\mathcal{R}}'_{q,k-1}/\hat{\mathcal{R}}'_{d,k-1}, \\
F_{46} &= \frac{\partial i_q}{\partial \theta_e} = -T_s\hat{\mathcal{R}}'_{q,k-1}u_{d,k}, \\
F_{47} &= \frac{\partial i_q}{\partial R_s} = -T_s\hat{\mathcal{R}}'_{q,k-1}\hat{i}_{q,k-1}.
\end{aligned}
\tag{5.76}
$$

Note that F_{36} and F_{46} were obtained by integrating the Park's transformation matrix $\mathbf{T}^{\alpha\beta}_{dq}(\theta_e)$ defined by equation (1.3) into process Jacobian matrix $\mathbf{F}$.

Just like in the case of the EKF-BASIC algorithm, the stochastic properties of the state estimate and measurements will be modelled via manually-set constant covariance matrices $\tilde{\mathbf{Q}}$ and $\tilde{\mathbf{R}}$.

Measurements (5.68) are considered to be uncorrelated, therefore the measurement noise covariance matrix has the form

$$\tilde{\mathbf{R}} = \begin{bmatrix} \sigma^2_{\mathcal{R}_{ph}} & 0 & 0 \\ 0 & \frac{2}{3}\sigma^2_i & 0 \\ 0 & 0 & \frac{2}{3}\sigma^2_i \end{bmatrix}, \tag{5.77}$$

where $\sigma_{\mathcal{R}_{ph}}$ and σ_i are standard deviations of phase reluctance $\mathcal{R}'_{phN}$ and $\vec{i}_{\alpha\beta}$ current measurements. The value of $\sigma_{\mathcal{R}_{ph}}$ is assumed to be selected just like for the EKF-BASIC algorithm. Variance σ^2_i can be modelled as the ADC discretization error and the noise introduced by measurement circuit MC IABC, which leads to

$$\sigma^2_i = \left(\frac{\max(\vec{i}_{abc})}{\sqrt{12} \cdot 2^{N_{ADC}}}\right)^2 + \mathrm{EIN}^2\left(\frac{\max(\vec{i}_{abc})}{u_{DD}} + \frac{1}{R_{sh}}\right)^2, \tag{5.78}$$

where $\max(\vec{i}_{abc})$ is the phase current measurement scale, N_{ADC} is the number of ADC bits, R_{sh} is the shunt resistance, u_{DD} is the maximal voltage measurable by ADC, and EIN is the equivalent input noise of the operational amplifier [BSL+10, AR15, CM18]. The resulting current variance in the two-phase stator $\alpha\beta$ reference frame can be calculated by taking into account Clarke's transformation as

$$\mathrm{var}\{i_\alpha\} = \mathrm{var}\left\{\frac{2}{3}i_a - \frac{1}{3}i_b - \frac{1}{3}i_c\right\} = \frac{4}{9}\sigma^2_i + \frac{1}{9}\sigma^2_i + \frac{1}{9}\sigma^2_i = \frac{2}{3}\sigma^2_i, \tag{5.79}$$

$$\mathrm{var}\{i_\beta\} = \mathrm{var}\left\{\frac{1}{\sqrt{3}}i_b - \frac{1}{\sqrt{3}}i_c\right\} = \frac{1}{3}\sigma^2_i + \frac{1}{3}\sigma^2_i = \frac{2}{3}\sigma^2_i. \tag{5.80}$$

The states will be considered to be uncorrelated, hence, the state noise covariance matrix is also diagonal, and has the form

$$\tilde{\mathbf{Q}} = \begin{bmatrix} \sigma^2_{\mathcal{R}'_d} & 0 & 0 & 0 & 0 & 0 & 0 \\ 0 & \sigma^2_{\mathcal{R}'_d} & 0 & 0 & 0 & 0 & 0 \\ 0 & 0 & \frac{2}{3}\sigma^2_i & 0 & 0 & 0 & 0 \\ 0 & 0 & 0 & \frac{2}{3}\sigma^2_i & 0 & 0 & 0 \\ 0 & 0 & 0 & 0 & \sigma^2_{\omega_e} & 0 & 0 \\ 0 & 0 & 0 & 0 & 0 & \sigma^2_{\theta_e} & 0 \\ 0 & 0 & 0 & 0 & 0 & 0 & \sigma^2_{R_s} \end{bmatrix}. \tag{5.81}$$

Setup of $\sigma_{\mathcal{R}'_d}$, $\sigma_{\mathcal{R}'_q}$, σ_{ω_e}, and σ_{θ_e} was already discussed in Section 5.4.1. The stator resistance estimate deviation σ_{R_s} should be chosen as a small or zero value because the stator resistance estimate will be a slow-changing quantity. The variance of the stator currents in the rotating dq reference frame can be estimated by taking into account the Park's transformation as

$$\mathrm{var}\{i_d\} = \mathrm{var}\{i_\alpha \cos(\hat{\theta}_e) + i_\beta \sin(\hat{\theta}_e)\} \simeq \cos^2(\hat{\theta}_e)\frac{2}{3}\sigma^2_i + \sin^2(\hat{\theta}_e)\frac{2}{3}\sigma^2_i = \frac{2}{3}\sigma^2_i, \tag{5.82}$$

$$\mathrm{var}\{i_q\} = \mathrm{var}\{-i_\alpha \sin(\hat{\theta}_e) + i_\beta \cos(\hat{\theta}_e)\} \simeq \sin^2(\hat{\theta}_e)\frac{2}{3}\sigma^2_i + \cos^2(\hat{\theta}_e)\frac{2}{3}\sigma^2_i = \frac{2}{3}\sigma^2_i. \tag{5.83}$$

Note that the above expression was simplified by considering zero rotor position variance σ_{θ_e} and should be treated as a rough setup.

The initialization of EKF-RS will be analogous to the EKF-BASIC variant as well. The initial state vector $\hat{\vec{x}}_0$ can be set as

$$\hat{\vec{x}}_0 = \begin{bmatrix} 1/L_{d0}, & 1/L_{q0}, & 0, & 0, & 0, & 0, & R_{s0} \end{bmatrix}, \tag{5.84}$$

where L_{d0}, L_{q0}, and R_{s0} are rough expected machine parameters. Similarly, the $\mathbf{P}_0$ can be set as a diagonal matrix, usually with sufficiently high variance values for currents $\hat{\vec{i}}_{dq}$, speed $\hat{\omega}_e$, and position $\hat{\theta}_e$ because the confidence in the initial value is low.

Simulation of EKF-RS Variant

To analyze the properties of EKF-RS, the algorithm was again integrated into the SynRM FOC algorithm within MATLAB Simulink simulation environment. The setups of the state noise matrix $\tilde{\mathbf{Q}}$, measurement noise matrix $\tilde{\mathbf{R}}$, and initial vector $\hat{\vec{x}}_0$ are listed in Table 5.2. The $\mathcal{R}'_{phN}$ and $\vec{i}_{\alpha\beta}$ measurements were by default distorted with a white noise of parameters matching to the matrix $\tilde{\mathbf{R}}$. The initial state vector $\hat{\vec{x}}_0$ was intentionally set to inaccurate values to highlight the ability of the algorithm to startup and converge with unknown initial system state. The covariance matrix was initialized as

$$\mathbf{P}_0 = \mathrm{diag}\left(0.01 \ \mathrm{H}^2, 0.01 \ \mathrm{H}^2, 1 \ \mathrm{A}^2, 1 \ \mathrm{A}^2, 100 \ \frac{\mathrm{rad}^2}{\mathrm{s}^2}, 1 \ \mathrm{rad}^2, 0.01 \ \Omega^2 \right). \tag{5.85}$$

Table 5.2: EKF-RS setup of vector $\hat{\vec{x}}_0$ and matrices $\tilde{\mathbf{R}}$ and $\tilde{\mathbf{Q}}$ for simulation

Quantity	Value	Unit
$\sigma_{\mathcal{R}_{ph}}$	0.15	$\frac{1}{\mathrm{H}}$
σ_i	15.8	mA
$\sigma_{\mathcal{R}'_d}$	$5 \cdot 10^{-4}$	$\frac{1}{\mathrm{H}}$
$\sigma_{\mathcal{R}'_q}$	$5 \cdot 10^{-4}$	$\frac{1}{\mathrm{H}}$
σ_{ω_e}	0.096	$\frac{\mathrm{rad}}{\mathrm{s}}$
σ_{θ_e}	0	rad
σ_{R_s}	$5 \cdot 10^{-3}$	Ω
L_{d0}	0.5	H
L_{q0}	0.5	H
R_{s0}	5	Ω

Figure 5.19 shows estimated states $\hat{\vec{x}}$ for full speed range, where the estimator was activated at time t_0 and nominal load T_l steps were introduced during the speed profile. Figure 5.20 shows errors of the estimated states $\tilde{\vec{x}}$ for the same scenario as in Figure 5.19. Both the inductance and position estimates have comparable accuracy as in the case of the EKF-BASIC algorithm and the steady-state performance shows estimation errors well below thresholds discussed in Section 4.3. The stator resistance $\hat{R}_s$ also shows steady-state estimation error below the desired threshold,

but, is generally much higher than in the case of other states. It should also be noted, that convergence of $\hat{R}_s$ relies on sufficient EMF voltage, or in other words, sufficient speed $\hat{\omega}_e$ and stator current $\hat{\vec{i}}_{dq}$. This can be seen in Figure 5.20c, where the estimate error δ_{R_s} drops when the nominal load is introduced. To avoid divergence of $\hat{R}_s$ estimate, and potential numerical instability of EKF-RS, a simple σ_{R_s} runtime adaptation mechanism can be used, where $\sigma_{R_s} = 0 \ \Omega$ is set when absolute value of speed $|\hat{\omega}_e|$ is under the selected speed threshold $|\omega_{e\sigma R_s}|$. Comparison of $\hat{R}_s$ resistance-related variance from the main diagonal of matrix $\mathbf{P}$ (further referenced as $\text{var}(\hat{R}_s)$) with and without such adaptation mechanism is shown in Figure 5.21.
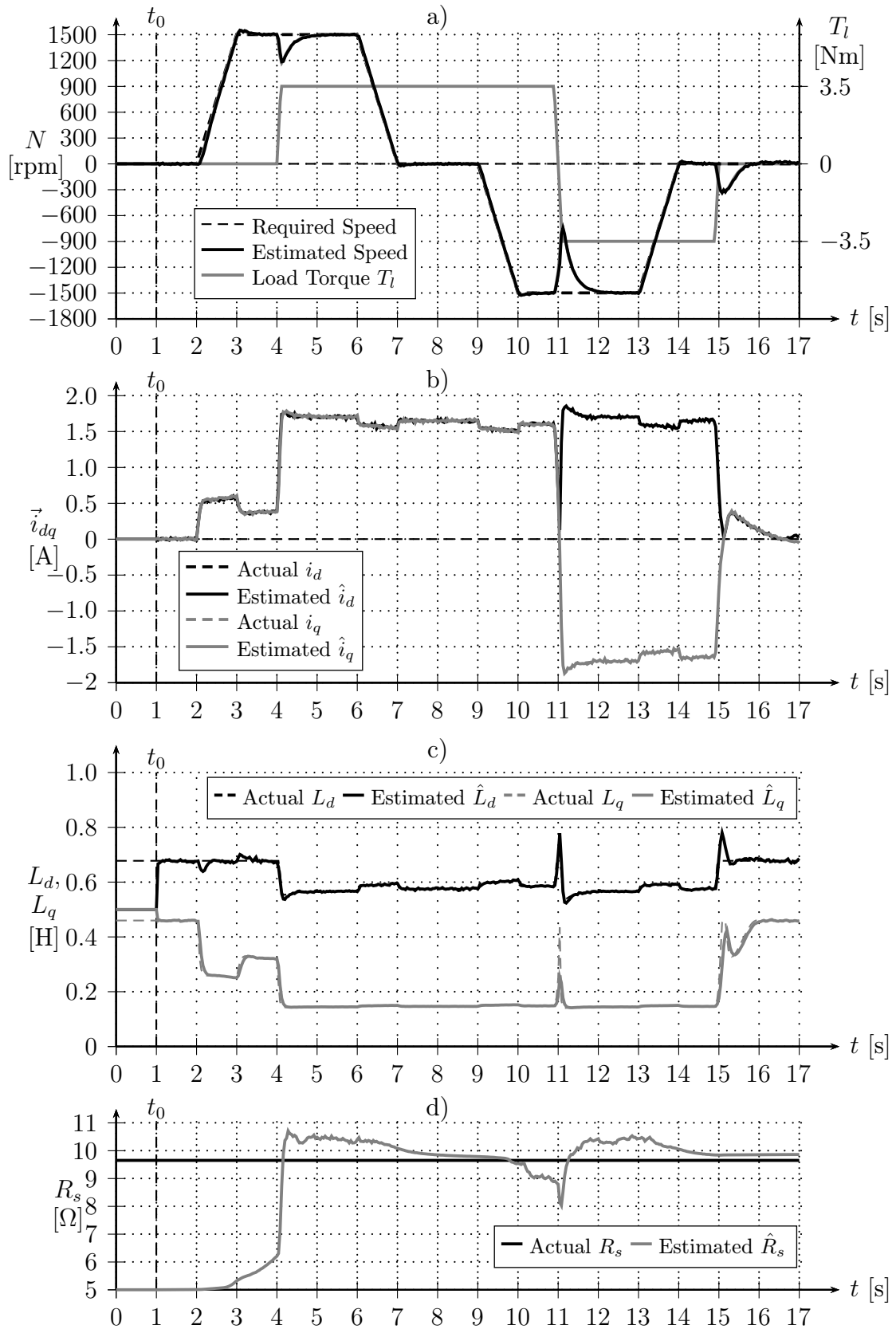
Figure 5.19: EKF-RS convergence of a) speed, b) current, c) inductance, and d) resistance estimates
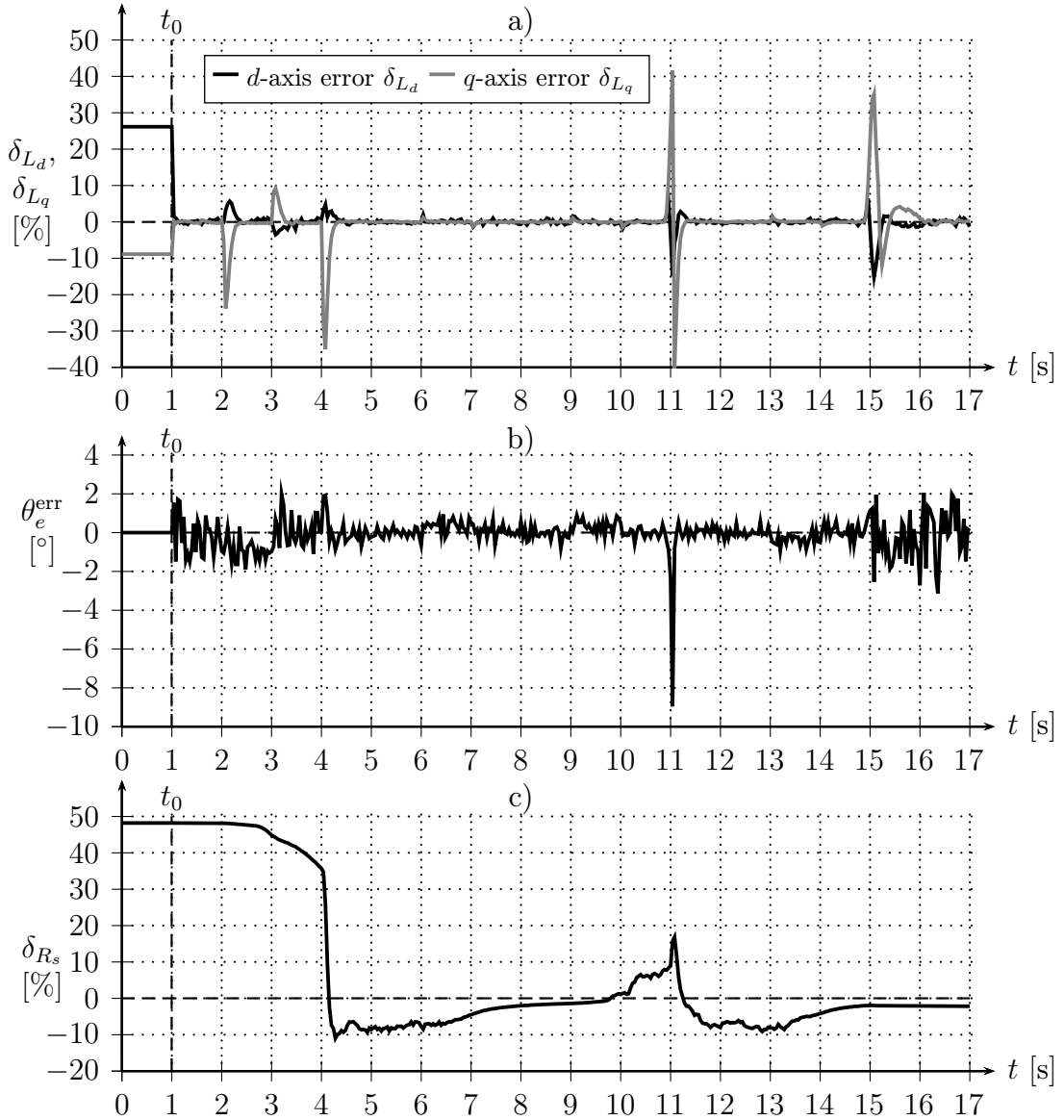
Figure 5.20: EKF-RS estimation errors of a) inductance, b) position, and c) resistance
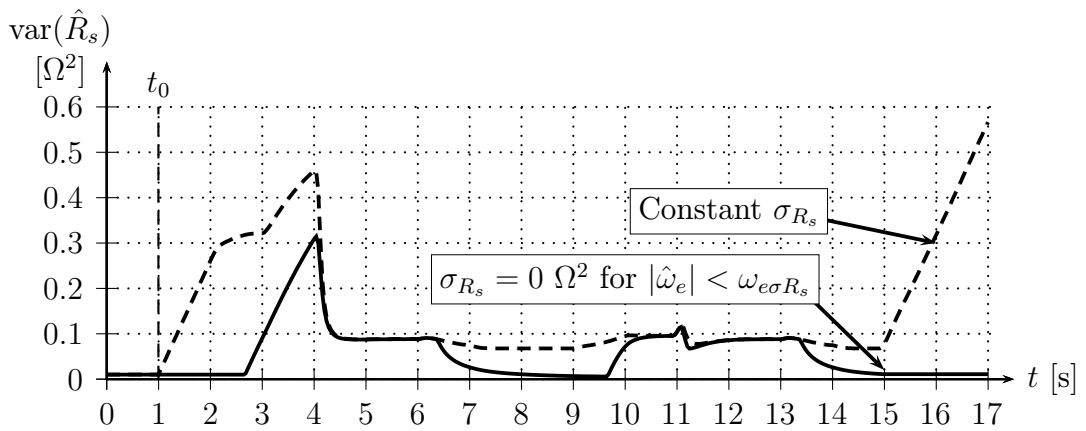
Figure 5.21: Covariance of $\hat{R}_s$ estimate at low speeds and currents with and without the σ_{R_s} state covariance adaptation mechanism

Similarly to EKF-BASIC, the effect of the measurement gain error $\delta_{\mathcal{R}}\hat{\mathcal{R}}'_{phN}$ was analysed. The response to $\delta_{\mathcal{R}}$ sweep in Figure 5.22 shows that the $\hat{\mathcal{R}}'_d$ and $\hat{\mathcal{R}}'_q$ are affected directly again. It is, however, noticeable that $\hat{R}_s$ estimate is greatly affected too. It is, therefore, up to the system designer if he considers the $\mathcal{R}'_{phN}$ measurement to be sufficiently accurate and whether the desired stator resistance estimation accuracy can be reached. Data for Figure 5.22 were measured over a 100-second period for the machine running at nominal speed and under nominal load. The non-gaussian errors in $\vec{i}_{\alpha\beta}$ measurements are considered to be out of the scope of this thesis.
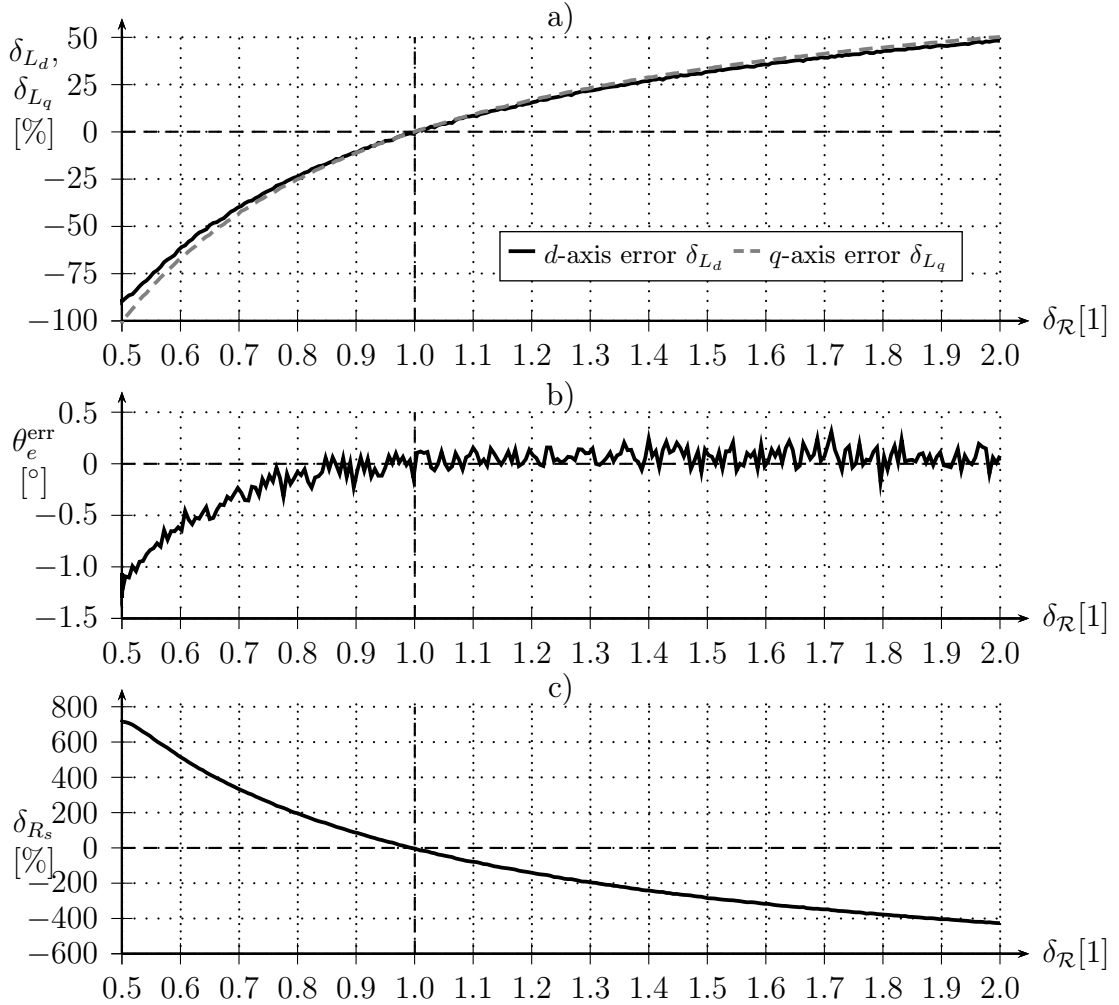
Figure 5.22: Sensitivity of EKF-RS a) inductance, b) position, and c) resistance estimates to measurement gain error $\delta_{\mathcal{R}}$

The error in standard deviance $\sigma_{\mathcal{R}_{ph}}$ value in matrix $\tilde{\mathbf{R}}$ was analyzed as well. Sensitivity of state estimates to sweep of error $\delta_{\sigma_{\mathcal{R}_{ph}}}$ is shown in Figure 5.23. Unlike in the case of EKF-BASIC, a greatly overestimated $\sigma_{\mathcal{R}_{ph}}$ setup can lead to steady-state estimation errors as well. It should be noted that this is only a superficial analysis done to highlight possible dependencies and configuration of other parameters (e.g. matrix $\tilde{\mathbf{Q}}$ in relation to matrix $\tilde{\mathbf{R}}$ can affect the results as well). Figure 5.23 was obtained from a 100-second recording of the machine running at nominal speed and under nominal load, during which the modelled error parameter $\delta_{\sigma_{\mathcal{R}_{ph}}}$ was swept.
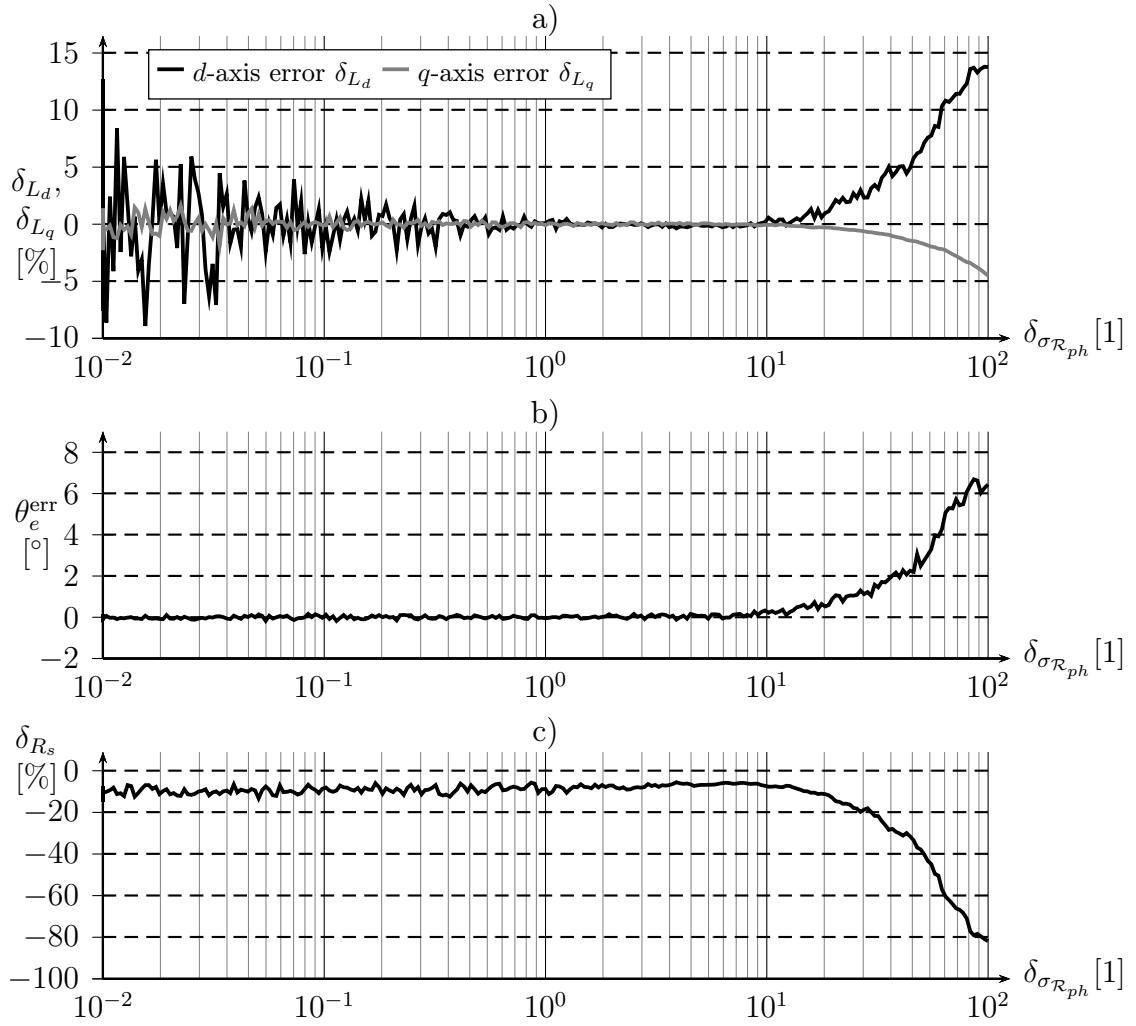
Figure 5.23: Sensitivity of EKF-RS a) inductance, b) position, and c) resistance estimates to relative error $\delta_{\sigma_{\mathcal{R}_{ph}}}$ of standard deviance $\sigma_{\mathcal{R}_{ph}}$ setting in matrix $\tilde{\mathbf{R}}$

6. Experimental Analysis

The goal of this chapter is to compare the performance of the SynRM control algorithms proposed in Section 5 on a real system with other, commonly used, state-of-the-art sensorless estimation algorithms listed in Section 2, as well as the sensor-based control. The first part of this chapter will focus on a description of the experimental hardware setup, which was used for all the measurements, and how the key performance indicators were obtained. The second part then describes the implementation and tuning details for all implemented algorithms. Finally, the acquired results are presented and discussed. The main focus is the evaluation of the achievement of goals set in Section 4.3.

6.1. The Measurement Setup

All measurements were done on reference 550 W machine from KSB manufacturer, which parameters were already presented in Section 1.2. This SynRM machine was integrated into testbench, which high-level block diagram is in Figure 6.2 and photography of the setup is in Figure 6.1. The shaft of the SynRM motor was connected to the 3.5 kW PMSM motor Allan Bradley F-4030-Q-H00AX to act as a loading generator. A benefit of this machine is its integrated 12-bit encoder, which, thanks to the co-axial motor-to-load setup, was used to get reference rotor position θ_e of both the SynRM motor and the load PMSM generator. Both the motor and generator inverter shared the same DC-bus rail so the generated power was used to immediately cover a part of the input power of the SynRM motor.
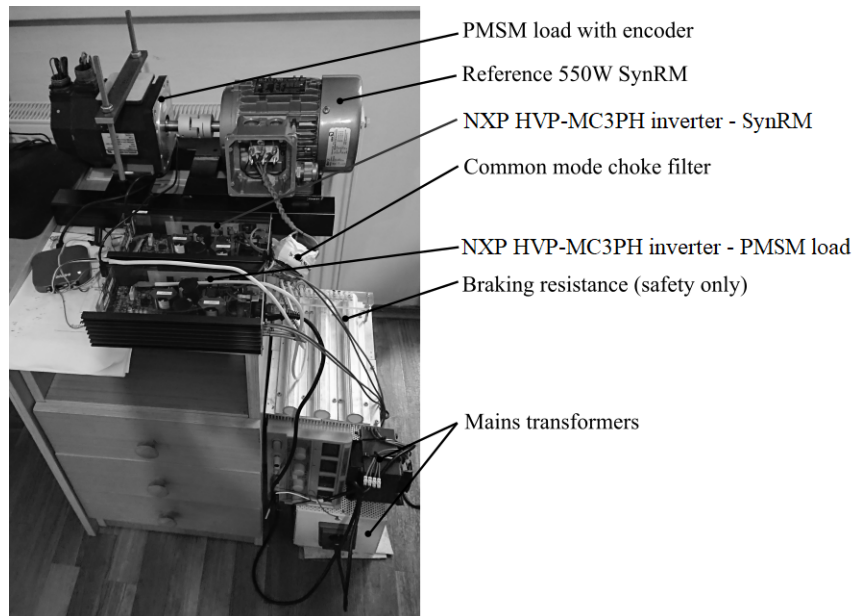
Figure 6.1: Photography of the experimental testbench setup
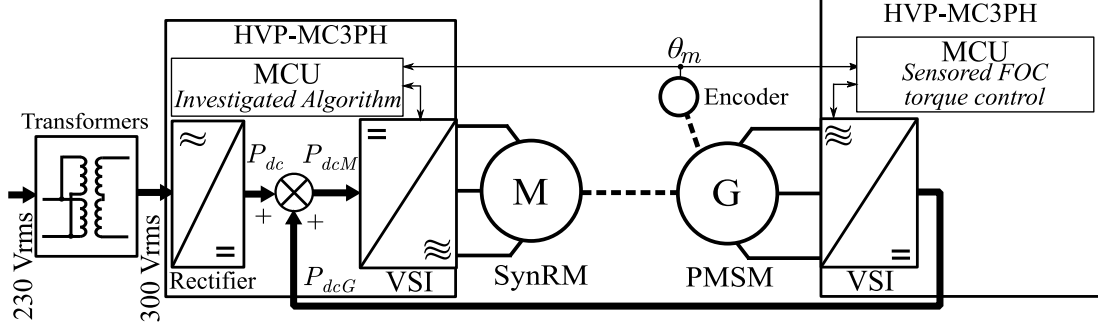
Figure 6.2: High-level block diagram of the experimental set-up

The power diagram of the experimental testbench is in Figure 6.3. Power quantities defined in the diagram are:

- P_{dc}: Rectified electrical power supplied to the testbench.

- $P_{dcM} = U_{dc}I_{dcM} = P_{dc} + P_{dcG}$: Input power of the SynRM motor VSI.

- $P_{inv} = P_{con} + P_{sw}$: Sum of the motor inverter conductive P_{con} and switching power losses P_{con}.

- $P_{in} = P_{dcM} - P_{invM}$: AC electrical power drawn by the SynRM motor.

- P_{Cu}: Joule power losses of the SynRM motor.

- P_{Fe}: Core power losses of the SynRM motor.

- P_{ω}: Mechanical and ventilator power losses of the SynRM motor.

- $P_m = P_{in} - P_{Cu} - P_{Fe} - P_{\omega}$: Mechanical power at the shaft produced by the SynRM motor.

- $P_{\omega G}$: Mechanical power losses of the PMSM generator.

- P_{CuG}: Joule power losses of the PMSM generator.

- $P_{invG} = P_{conG} + P_{swG}$: Sum of the generator inverter conductive P_{conG} and switching power losses P_{swG}.

- $P_{dcG} = U_{dc}I_{dcG} = P_m - P_{\omega G} - P_{CuG} - P_{invG}$: Rectified electrical power delivered by the generator inverter back to the DC rail.

Mathematical modelling of Joule losses P_{Cu}, core losses P_{Fe}, mechanical losses P_{ω}, and shaft mechanical power P_m was discussed in Section 3. The power model of the PMSM generator is relatively similar to SynRM, with the exception of torque calculation. The mechanical power at the common shaft P_m can be estimated from rotor speed ω_m and quadrature axis current of generator I_{qG} as

$$P_m = T_l\omega_m - P_{\omega G} = k_t I_{qG}\omega_m - P_{\omega G} = \frac{3}{2}P_{pG}\Psi_{PM}I_{qG}\omega_m - P_{\omega G}, \qquad (6.1)$$

where P_{pG} is the number of PMSM generator pole-pairs, T_l is braking torque applied to the shaft by generator, k_t is PMSM machine torque constant, and Ψ_{PM} magnetic flux of permanent magnet of the generator. The used PMSM load does not have its own ventilator, hence its mechanical losses can be simply modelled as

$$P_{\omega G} = B_{1G}\omega_m^2, \tag{6.2}$$

where B_{1G} is mechanical loss coefficients. The remaining significant PMSM electrical power losses are the stator winding Joule losses, which can be modelled as

$$P_{CuG} = R_{sG}I_{qG}^2, \tag{6.3}$$

where R_{sG} is the resistance of generator stator winding and I_{qG} is the quadrature axis stator current. The direct axis current is assumed to be controlled to zero setpoint because the selected PMSM does not have significant rotor saliency and there is no need for field weakening.
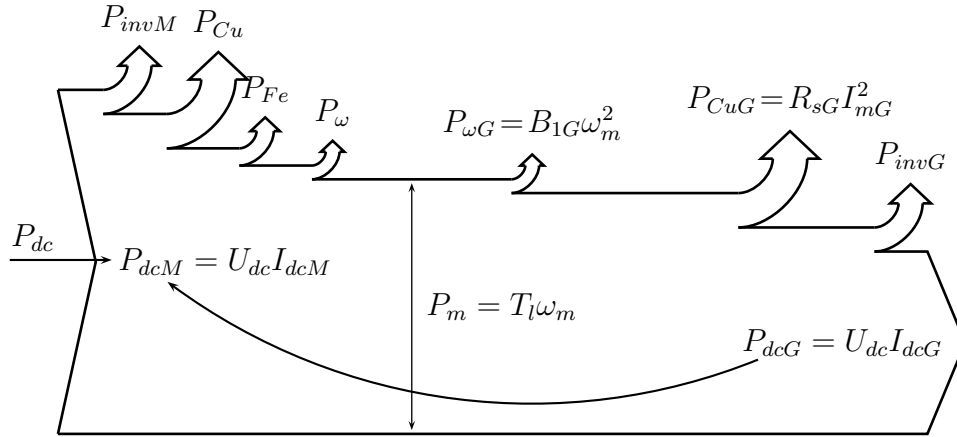
Figure 6.3: A power diagram of the experimental testbench

This thesis is mainly focused on the power efficiency aspect of the SynRM sensorless control, therefore, the experimental testbench was mainly used to obtain stead-state input power and state estimate comparison between the proposed and the reference state-of-the-art algorithms for the same loading conditions. Therefore, for the most of the experiments, the PMSM generator load was used to maintain constant torque T_l on the common shaft using the sensor-based torque vector control method. Accuracy of estimated resistance $\hat{R}_s$ and inductances $\hat{L}_d$ and $\hat{L}_q$ was determined based on comparison with off-line measured values presented in Section 1.2. The estimation accuracy of position $\hat{\theta}_e$ and speed $\hat{\omega}_e$ was measured using encoder sensor. The experiments involving measurement of power efficiency determined the output power P_m from equation (6.1). As for the input power, both the proposed and the reference sensorless SynRM control algorithms involved various injections and PWM schemes, hence, the investigated input power quantity was selected to include all motor inverter power losses P_{invM}. Although this input power P_{dcM} could be calculated or measured in many ways, it was decided to use independent instrument capable of sensing average DC-bus current I_{dcM}, leading to the

input power relation $P_{dcM} = I_{dcM}U_{dc}$. The DC-bus current i_{dc} is highly dynamic quantity, hence, the integrating voltage-to-frequency converter (VFC) with a high sampling frequency was used, so it could provide steady-state information with a good resolution. Diagram of this measurement instrument is shown in Figure 6.4.
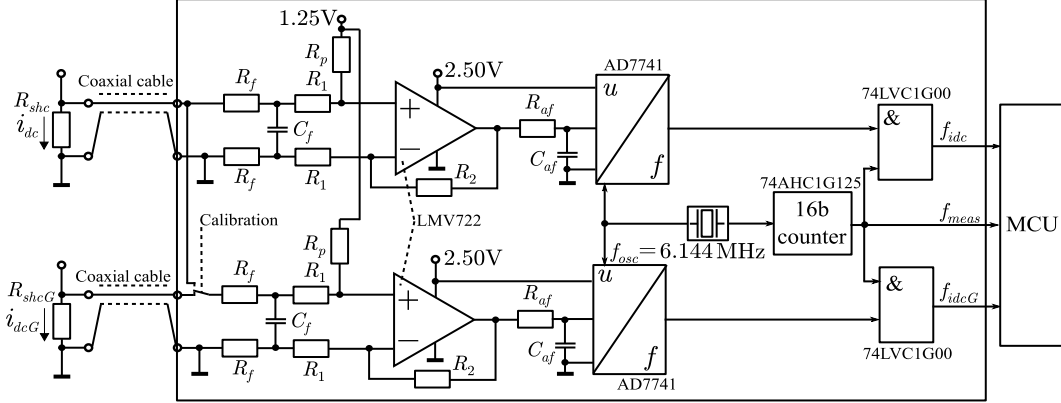
Figure 6.4: Voltage-to-frequency converter measurement instrument

A more detailed control block diagram of the testbench with implemented EKF-based algorithm is in Figure 6.5. The FOC algorithm on the SynRM side of this block diagram might differ based on specifics of the investigated algorithm. See Section 6.2 for more details. Both the motor and the load were driven using NXP HVP-MC3PH high-voltage inverters, which can provide roughly up to one kW of three-phase AC power. The motor-side inverter was modified to feature the MC IDC circuit, which, as described in Section 5.1, was used to acquire necessary i_{dc} current derivative measurements to support the proposed algorithms.

The motor-side inverter was controlled from HVP-KV58F220M daughter card, which is based on the NXP MKV58F1M0 micro-controller, which features a 240 MHz Cortex-M7 core with single-precision floating-point unit, high-speed 12-bit ADC, and high-resolution PWM peripherals. The motor-side FOC algorithm was designed to control the rotor shaft speed $N_m = \frac{2\pi}{60P_p}\omega_e$, where the source of rotor position θ_e and speed ω_e information was the investigated algorithm. The exact details of the motor-side control algorithm block diagram as well as configurations of the investigated estimators are described in Section 6.2.1, Section 6.2.2, and Section 6.2.3. Note that the core of the EKF algorithm, as described in Section 5.3.2, was implemented in floating point arithmetics, using the freely-available C source code of TinyEKF project [Lev]. Also, some basic algorithms (e.g. Clarke's and Park's transformations, PI controllers,…) were used from the NXP Real Time Control Embedded Software Motor Control and Power Conversion Library (RTCESL) software [Semb]. No current angle θ_I optimization algorithm was implemented and its setpoint value was controlled manually. Any optimal MTPA or ME trajectories were obtained offline from measurements corresponding to a range of current angles θ_I^{req}. The PWM frequency $1/T_{PWM}$, phase current sampling frequency $1/T_s$, and the current control loop frequency were set identically to 10 kHz. The speed control loop sampling frequency was set to 1 kHz. The current control loops were tuned to 40 Hz bandwidth and the speed control loop to bandwidth of 3 Hz. Stator voltages $\vec{u}_{\alpha\beta}$ were corrected for inverter non-linearities using LUT-based dead-time compensation

algorithm. The SVM was used to obtain duty cycles $\vec{D}_{abc}$ in all investigated FOC modifications, but the PWM switching scheme was either the ASPWM proposed in Section 5.2, or the centre-aligned PWM as shown in Figure 2.4. The motor-side MCU also collected all measured data and provided them to PC through UART into FreeMASTER online monitoring and debugging utility [Sema]. The measurement collection software assured that the acquired data were obtained and filtered for the same measurement window. The mean DC-bus currents I_{dcM} and I_{dcG} were obtained from the VFC unit using a timer periphery. The control setpoints θ_I^{req} and ω_e^{req} were set using the FreeMASTER utility as well.

The MC IABC circuit current measurement scale was configured to $\pm \max(\vec{i}_{abc}) = \pm 8$ A and the MC UDC measurement scale to $\max(U_{dc}) = 433$ V. Part values for the MC IDC circuit (see diagram in Figure 5.5) were selected as $R_{shc} = 0.1\ \Omega$, $R_f = 220\ \Omega$, $C_f = 47$ pF, $R_1 = 1600\ \Omega$, $R_2 = 82$ kΩ, $R_p = 10$ kΩ, and $R_n = 22$ kΩ. When considering offset voltage range $u_{off} \in \langle 0; 3.3 \rangle$ V and equation (5.20), this allows to measure DC-bus current range $i_{dc} \in \langle -3.05; 3.75 \rangle$ A, which is more than enough for expected maximal phase current for the reference SynRM. The i_{dc} current itself was amplified to voltage u_{idc} by a gain $K_R R_p R_{shc} = 4.21$ V/A. For comparison, if the MC IABC circuit was used to measure Δi_{dc}, it would offer a 20-times lower resolution and, similarly, if MC IABC was configured to measure with such high resolution, its scale $\max(\vec{i}_{abc})$ would drop from 8 A roughly to 395 mA. This highlights the Δi_{dc} measurement resolution improvement provided by MC IDC circuit.

The load-side inverter control daughter card NXP HVP-MKV46F150M is based on the NXP MKV46F256 micro-controller with 168 MHz Cortex-M4 core, single-precision floating-point unit and high-performance ADC and PWM peripherals. The inverter side FOC algorithm was designed for torque control and to always utilize the encoder for position θ_m and speed ω_m information. The load torque T_l polarity was always set to be inverse to the shaft speed ω_m to act as a break. The torque reference T_l^{req} was set from PC via the FreeMASTER utility. The PWM frequency, phase current sampling frequency, and the current control loop frequency were set identically to 10 kHz. The current control loops were configured to 40 Hz bandwidth. The combination of SVM and centre-aligned PWM was used for all experiments.

Figure 6.5: Experimental set-up control block diagram

The HVP-MC3PH inverter was designed to be powered using voltage from a single mains phase. The SynRM machine, as shown by its label in Figure 1.8, has a nominal stator voltage of 350 V_{rms}, which means that it was designed for inverters that can be powered from three-phase mains. This is a common property of commercially available low-power SynRM machines, likely because the high-voltage operation improves efficiency and mitigates impact of low power factor of SynRM. A

serial connection of outputs of two transformers was used to increase mains voltage so the common DC-bus voltage would reach a maximum safe value of $U_{dc} = 420$ V, knowing that 450 V is a limitation of inverter components like the DC-bus capacitors. Even with this modification, the nominal power of selected SynRM could not be reached at nominal speed, hence, all the high-torque experiments were limited to 900 rpm. However, this limitation does not reduce validity of acquired measurements in terms of evaluation of the performance of the proposed algorithm.

6.2. Implementation of Investigated Estimators

Details about the implementation and configuration of the proposed EKF-based algorithms EKF-BASIC and EKF-RS for the experimental analysis are listed in the following Section 6.2.1. To allow a relative comparison of its performance, other position and speed sources with various properties were implemented as well:

- *Encoder measurement* - A conventionally true position and speed was obtained using 12-bit encoder sensor. Both the ASPWM and the centre-aligned PWM switching schemes were implemented to allow investigation of impact of using ASPWM scheme. See more details in Section 6.3.3.

- *High-frequency injection algorithm* - The saliency-based algorithm was used as a reference for low-speed range. Its principle was described in Section 2.2 and details about its implementation are in Section 6.2.2.

- *EEMF observer* - The EEMF-based algorithm was used as a reference at medium and higher speeds. Its principle was described in Section 2.1 and details about its implementation are in Section 6.2.3. The basic EEMF algorithm is not naturally adaptive like the proposed method. Hence, several different variations were implemented:

  - *EEMF observer with constant model parameters* - A basic algorithm version with constant $\hat{R}_s$ and $\hat{L}_q$ values. Considered to evaluate the impact of using non-adaptive algorithms, which neglect saturation. This is a valuable reference because this approach is often chosen in low-performance practical applications [HKS99, KSG$^+$14].

  - *EEMF observer with LUT* - The algorithm version with constant $\hat{R}_s$ value and inductances $\hat{L}_d'$ and $\hat{L}_q$ provided by the LUT table. This modification was included in the analysis to evaluate what performance can be achieved with accurate parameters obtained offline. The algorithm might not be considered to be truly adaptive because the LUT may not reflect the change of inductances due to temperature change, which could be a factor in some applications.

  - *EEMF observer with RLS* - The algorithm version with $\hat{R}_s$, $\hat{L}_d'$, and $\hat{L}_q$ parameters provided online by Recursive Least Square estimation algorithm described in Section 2.4.

6.2.1. Implementation of Proposed EKF Algorithms

The theory of the proposed estimation algorithms EKF-BASIC and EKF-RS, approach to their configuration, as well as simulation results, were described in Section 5.4.1 and Section 5.4.2. The block diagram in Figure 6.5 is valid for all versions of the proposed algorithm, with the following notes:

- EKF-BASIC does not provide the $\vec{i}_{dq}$ current vector on its output so the Park's transformation from $\vec{i}_{\alpha\beta}$ current must be done outside the estimator.

- EKF-BASIC does not take $\vec{i}_{\alpha\beta}$ current and $\vec{u}_{\alpha\beta}$ voltage vectors as inputs.

- EKF-BASIC does not provide $\hat{R}_s$ estimate.

- Only the ASPWM switching scheme is considered for EKF-BASIC and EKF-RS algorithms.

First, the measurement variances had to be determined in order to configure matrix $\tilde{\mathbf{R}}$ for all EKF versions. Variances of normalized phase reluctances were obtained from offline analysis of actual $\mathcal{R}'_{phN}$ measurement recordings for several speed and load operation points. The measurement noise components shown in Figure 6.6, Figure 6.8, and Figure 6.7 were obtained by subtracting the expected harmonic value $\bar{\mathcal{R}}'_{phN}$, which was obtained from (5.10), (5.11), and (5.12). It can be seen that, besides the high frequency noise component, small periodic deformations $\Delta_{\mathcal{R}}(\theta_e + \theta_{phN})$ still occur. These were likely caused by i_{dc} signal deformations after the PWM switching events and were dependent on applied duty cycle $\vec{D}_{abc}$ and stator current $\vec{i}_{abc}$ (i.e. machine rotor speed and load). For the purpose of this thesis, these deformations will not be further addressed by additional measures and considered part of the noise component. As shown by simulation in Figure 5.18 and Figure 5.23, the $\sigma_{\mathcal{R}_{ph}}$ should be set within one order range from the real value to avoid undesired estimation errors. A rough average observed standard deviation of the $\mathcal{R}'_{phN}$ measurement, which was used in the matrix $\tilde{\mathbf{R}}$, was finally determined as

$$\sigma_{\mathcal{R}_{ph}} = 0.15 \text{ H}^{-1}. \tag{6.4}$$
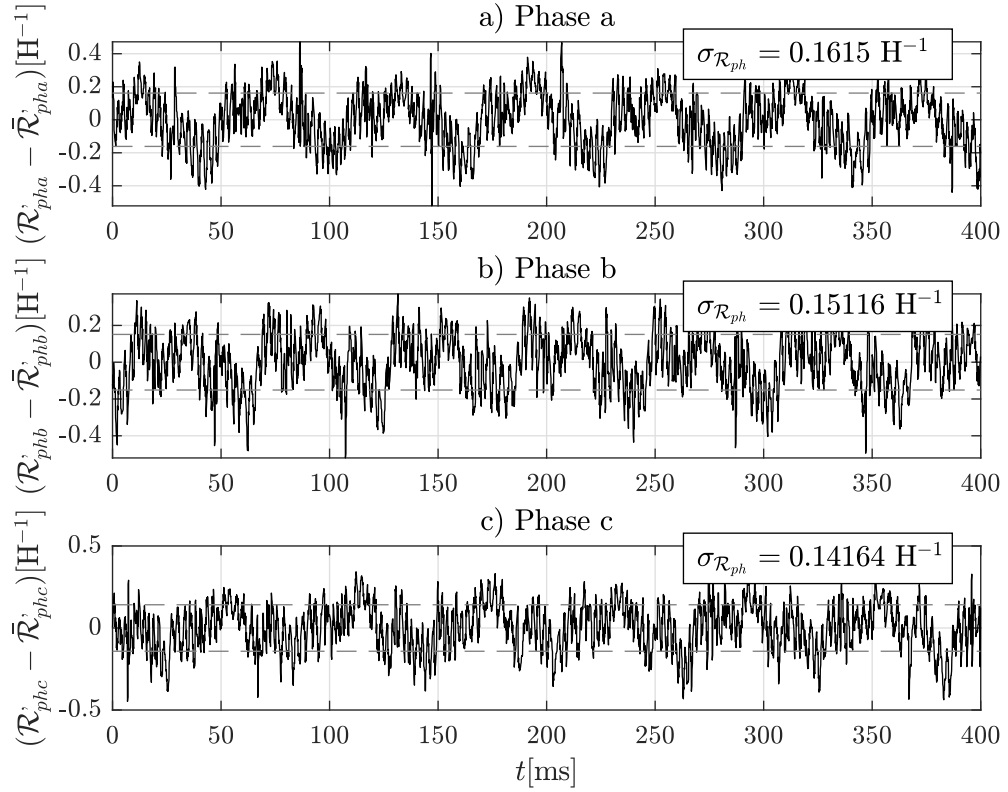
Figure 6.6: Example of experimentally obtained phase reluctance measurement noise $\mathcal{R}_{phN} - \bar{\mathcal{R}}_{phN}$ for $N_m = 500$ rpm and $T_l = 0$ Nm
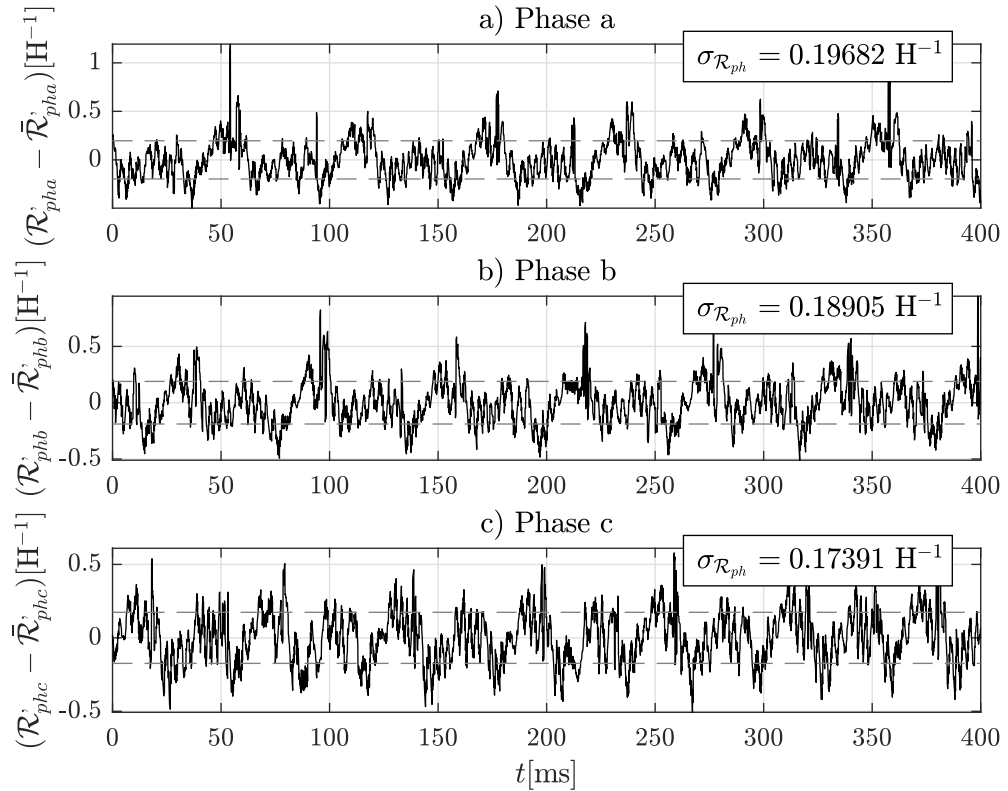
Figure 6.7: Example of experimentally obtained phase reluctance measurement noise $\mathcal{R}_{phN} - \bar{\mathcal{R}}_{phN}$ for $N_m = -500$ rpm and $T_l = 0$ Nm
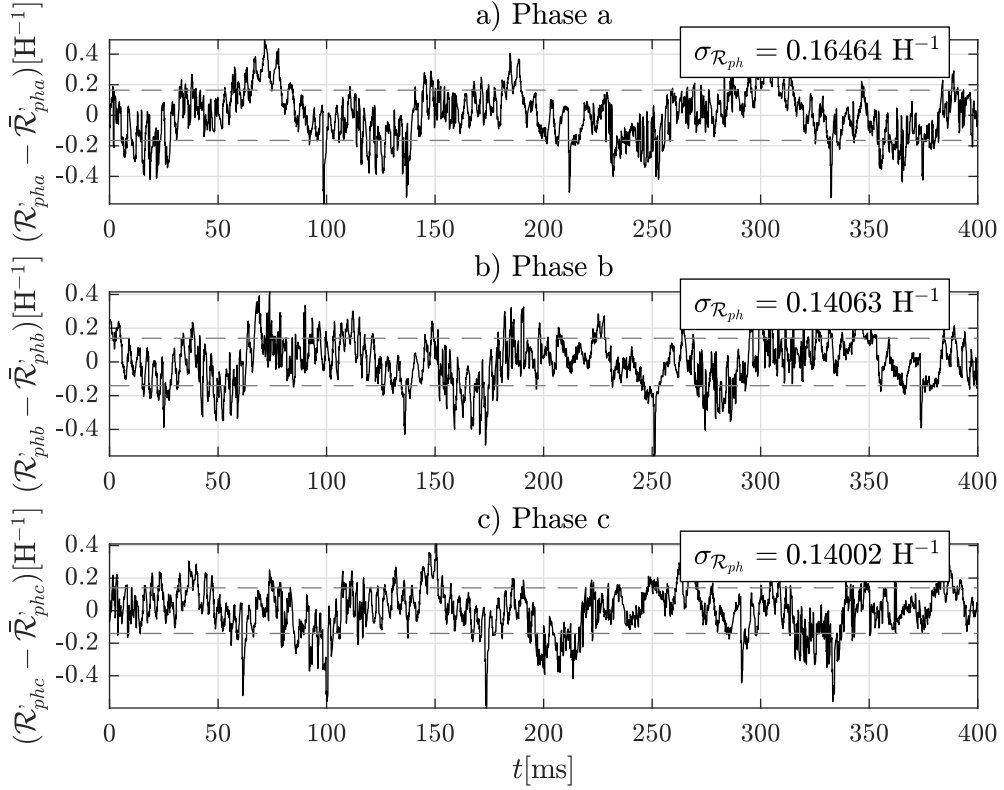
Figure 6.8: Example of experimentally obtained phase reluctance measurement noise $\mathcal{R}_{phN} - \bar{\mathcal{R}}_{phN}$ for $N_m = 250$ rpm and $T_l = 3.5$ Nm

The measurement noise covariance matrix (5.77) for the EKF-RS algorithm also requires knowledge of the phase current measurement noise σ_i. It was obtained from (5.78) as

$$\sigma_i = \sqrt{\left(\frac{\max(\vec{i}_{abc})}{\sqrt{12} \cdot 2^{N_{ADC}}}\right)^2 + \text{EIN}^2 \left(\frac{\max(\vec{i}_{abc})}{u_{DD}} + \frac{1}{R_{sh}}\right)^2} = \tag{6.5}$$

$$= \sqrt{\left(\frac{8}{\sqrt{12} \cdot 2^{12}}\right)^2 + 0.0007^2 \left(\frac{8}{3.3} + \frac{1}{0.05}\right)^2} = 15.8 \text{ mA}, \tag{6.6}$$

where $\max(\vec{i}_{abc})$ is the phase current measurement scale, N_{ADC} is effective resolution of ADC in the number of bits, and EIN was obtained from operational amplifier manufacturers datasheet [BSL+10].

The matrix $\tilde{\mathbf{R}}$ was, therefore, configured identically as for simulations in Section 5.4.1 and Section 5.4.2. The same goes for the matrix $\tilde{\mathbf{Q}}$. The standard deviations of the normalized reluctances $\mathcal{R}'_d$ and $\mathcal{R}'_q$ were selected manually to a small value as it was assumed, that these parameters will not change significantly during a single sampling period. This led to the selection of value

$$\sigma_{\mathcal{R}_d} = \sigma_{\mathcal{R}_q} = 0.0005 \, \text{H}^{-1}. \tag{6.7}$$

118

The speed estimation deviation was selected as maximal electrical speed change with nominal torque T_n and moment of inertia J combining both the SynRM and the PMSM load per sampling period T_s as

$$\sigma_{\omega_e} = \frac{T_s T_{\text{nom}}}{J} = \frac{0.0001 \cdot 3.5}{0.00364} = 0.096 \, \text{rad/s}. \tag{6.8}$$

Because the position θ_e is obtained as pure integration of ω_e, its deviation was set as $\sigma_{\theta_e} = 0$ rad. The standard deviation of the stator resistance $\sigma_{\delta_{R_s}}$ was configured identically as in Section 5.4.2.

6.2.2. High-Frequency Injection Algorithm Implementation

The block diagram of the FOC algorithm with implemented high-frequency injection position and speed estimator is in Figure 6.9, which elaborates the SynRM-side of the diagram in Figure 6.5.

BPF   - Band-Pass Filter
HET   - Heterodyne process
LPF   - Low-Pass Filter
MC IABC - Meas. Circuit of phase currents $\vec{i}_{abc}$
MC UDC - Meas. Circuit of DC-bus voltage U_{dc}
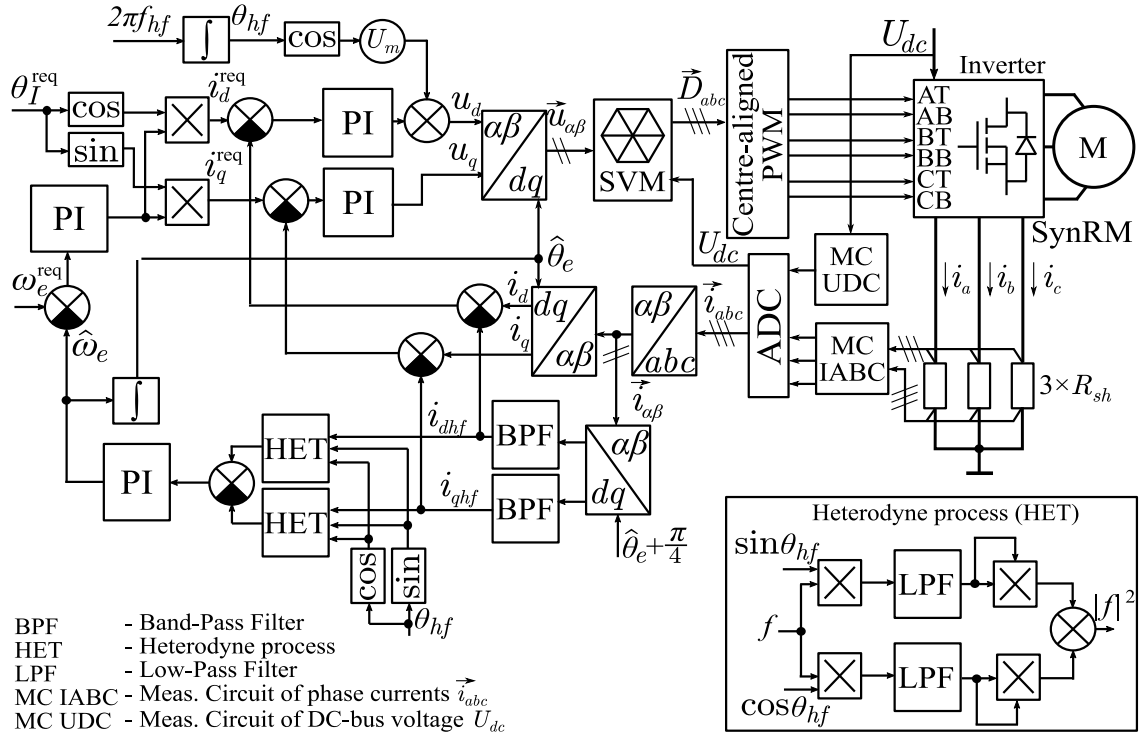
Figure 6.9: Block diagram of FOC with HFI algorithm

A harmonic voltage vector injection into d-axis was used with signal amplitude $U_m = 20$ V and frequency $f_{hf} = 500$ Hz . The current components at injected frequency were filtered using BPF filters with 25 Hz bandwidth for both the direct and quadrature axis shifted by $\frac{\pi}{4}$. This allowed using a version of the heterodyne algorithm, capable of extracting higher error signal ε_{hf} amplitude. Low-pass filters in the heterodyne algorithm were tuned to 500 Hz bandwidth. The speed $\hat{\omega}_e$ tracking was done using the PI controller with proportional and integration gain tuned manually to $K_P = 1 \cdot 10^5$ and $K_I = 100$. The high-frequency components i_{dhf} and i_{qhf} were subtracted from measured current $\vec{i}_{dq}$ to avoid interaction of current PI

controllers with the injected signal. The algorithm was operated with centre-aligned PWM switching scheme only.

6.2.3. Extended EMF Observer Implementation

The block diagram of the FOC algorithm with implemented extended EMF position and speed estimator, which elaborates the SynRM-side of the diagram in Figure 6.5, is in Figure 6.10. The EEMF algorithm cannot be used for low-speed regions and a different algorithm (see LS block in Figure 6.10) must be used to provide estimates $\hat{\omega}_{els}$ and $\hat{\theta}_{els}$ while the machine starts-up to a minimal speed at which EEMF converges. Switching of speed regions is depicted by signal S1. There are many possible implementations of the LS algorithm, ranging from simple open-loop startup algorithm to HFI described in Section 6.2.2. For the purpose of experiments in this thesis, the position was obtained from the encoder sensor. The final rotor position $\hat{\theta}_e$ and speed $\hat{\omega}_e$ were obtained by tracking the voltage vector $\hat{\vec{e}}_{dq}$ using tracking observer (2.13) and integrator (1.21), which formed TO in Figure 6.10. The bandwidth of the tracking observer was set to 5 Hz by configuring gains of the integrated PI controller. As mentioned in Section 6.2, three different approaches to inductance adaptation were implemented:

- *EEMF observer with constant model parameters* - The stator inductances were kept at $\hat{L}_d = L_{d0} = 0.65$ H and $\hat{L}_q = L_{q0} = 0.2$ H throughout the entire EEMF algorithm operation.

- *EEMF observer with LUT* - Inductances were obtained at runtime from LUTs containing offline-measured data shown in Figure 1.11 and Figure 1.12. Cross-saturation effect was considered.

- *EEMF observer with RLS* - The RLS algorithm was implemented using equations (2.30) to (2.39). The forgetting factor was set $\lambda = 0.99$ and the covariance matrix was initialized by setting large values 10^5 in its diagonal. To achieve and maintain convergence at the steady state, the PRBS voltage injection was implemented into both direct and quadrature axis with a different initial seed. The 5-bit PRBS excitation signal with 20 V amplitude and 10 ms sampling period was used. These parameters were selected so the longest step generated by PRBS is several times longer than machine time constant, which is critical for accurate identification.

Selection between adaptation algorithms is depicted by signal S2. The algorithm was operated with a centre-aligned PWM switching scheme only.

EEMF   - Extended EMF observer
LUT   - Look-Up Table
LS   - Low-Speed position and speed estimator/sensor
MC IABC - Meas. Circuit of phase currents $\vec{i}_{abc}$
MC UDC   - Meas. Circuit of DC-bus voltage U_{dc}
PRBS   - Pseudo-Random Binary Sequence generator
RLS   - Recursive Least-Square algorithm
TO   - Tracking Observer algorithm

S1 - Low- to high-speed region switching signal
S2 - Adaptive algorithm selection between
    a) RLS+PRBS
    b) LUT
    c) Constant parameters (no adaptivity)

Figure 6.10: Block diagram of FOC with EEMF algorithm

6.3. Measurement Results

This section presents results of conducted experiments. Section 6.3.1 will focus on the general position and speed estimation capability of EKF-BASIC and EKF-RS. The main analysis, which responds to estimation accuracy goals formulated in Section 4.3, is then available in Section 6.3.2. Finally, Section 6.3.3 will analyze the impact of the ASPWM scheme used by EKF-BASIC and EKF-RS and the impact of signal injections required by HFI and RLS algorithms on power losses and the MTPA and ME trajectories.

6.3.1. Basic Speed and Position Tracking

The basic capability of position and speed tracking in the full speed range of EKF-BASIC and EKF-RS estimators is shown in Figure 6.11 and Figure 6.12. The position error θ_e^{err} spikes up to 25 degrees were recorded during dynamic events in Figure 6.11c and Figure 6.12d, but with the corresponding FOC tuning it did not lead to loss of stability or even significant degradation of performance. The error θ_e^{err} then dropped during stead-state. Deeper analysis of steady-state performance is available in Section 6.3.2.

It is noticeable, that the overall speed and position tracking ability of EKF-BASIC and EKF-RS are very similar. This was expected because the additional machine model integrated within the EKF-RS mainly serves to estimate the stator

resistance $\hat{R}_s$, while the position and speed information is extracted from $\mathcal{R}'_{phN}$ measurement.

The speed reversal during the experiment also shows the ability of both algorithms to run at low-speed or even standstill, which is a considerable benefit when compared to EEMF algorithm.
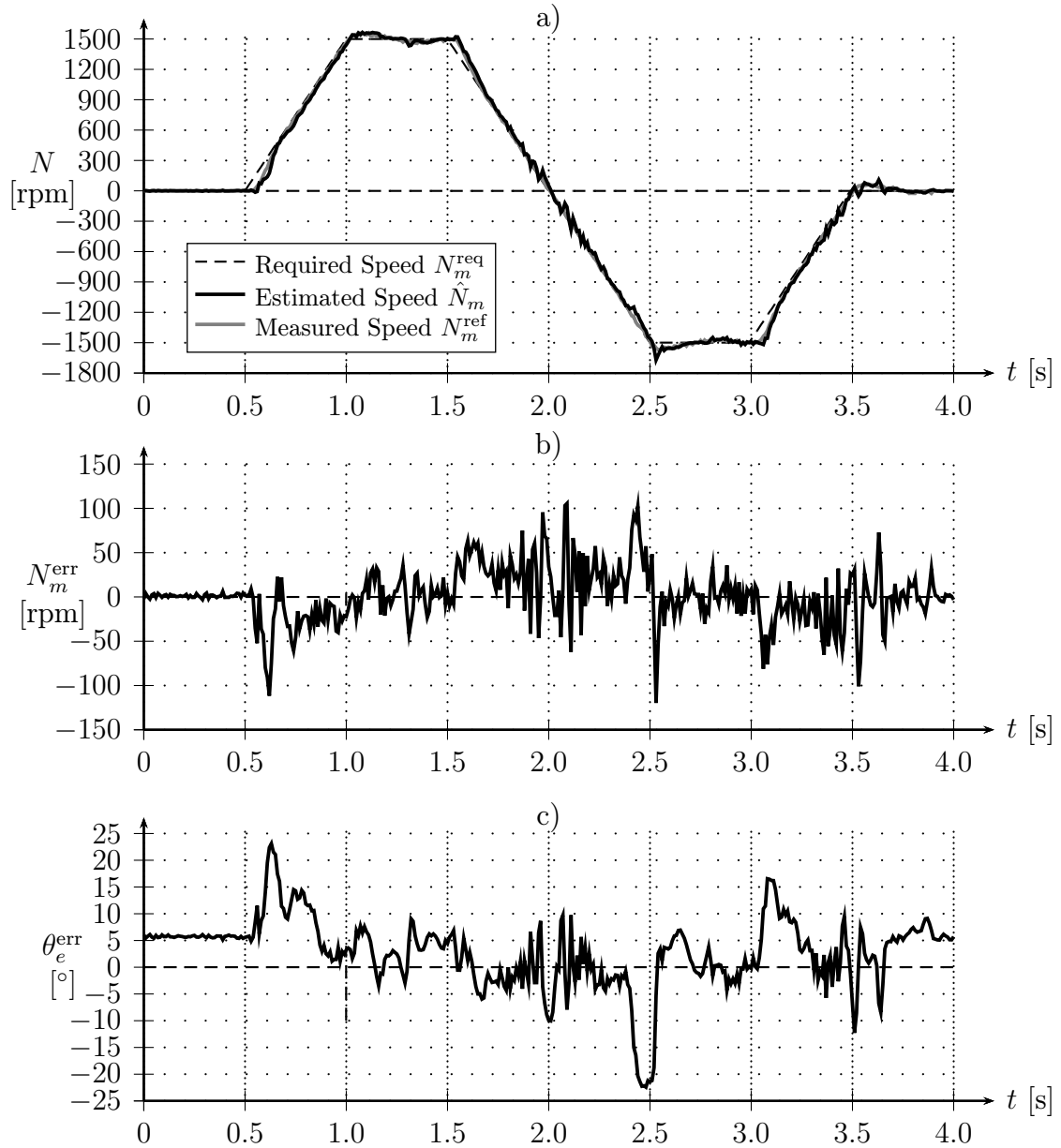

Figure 6.11: EKF-BASIC a) speed estimate and errors of b) speed and c) position estimates in full speed range
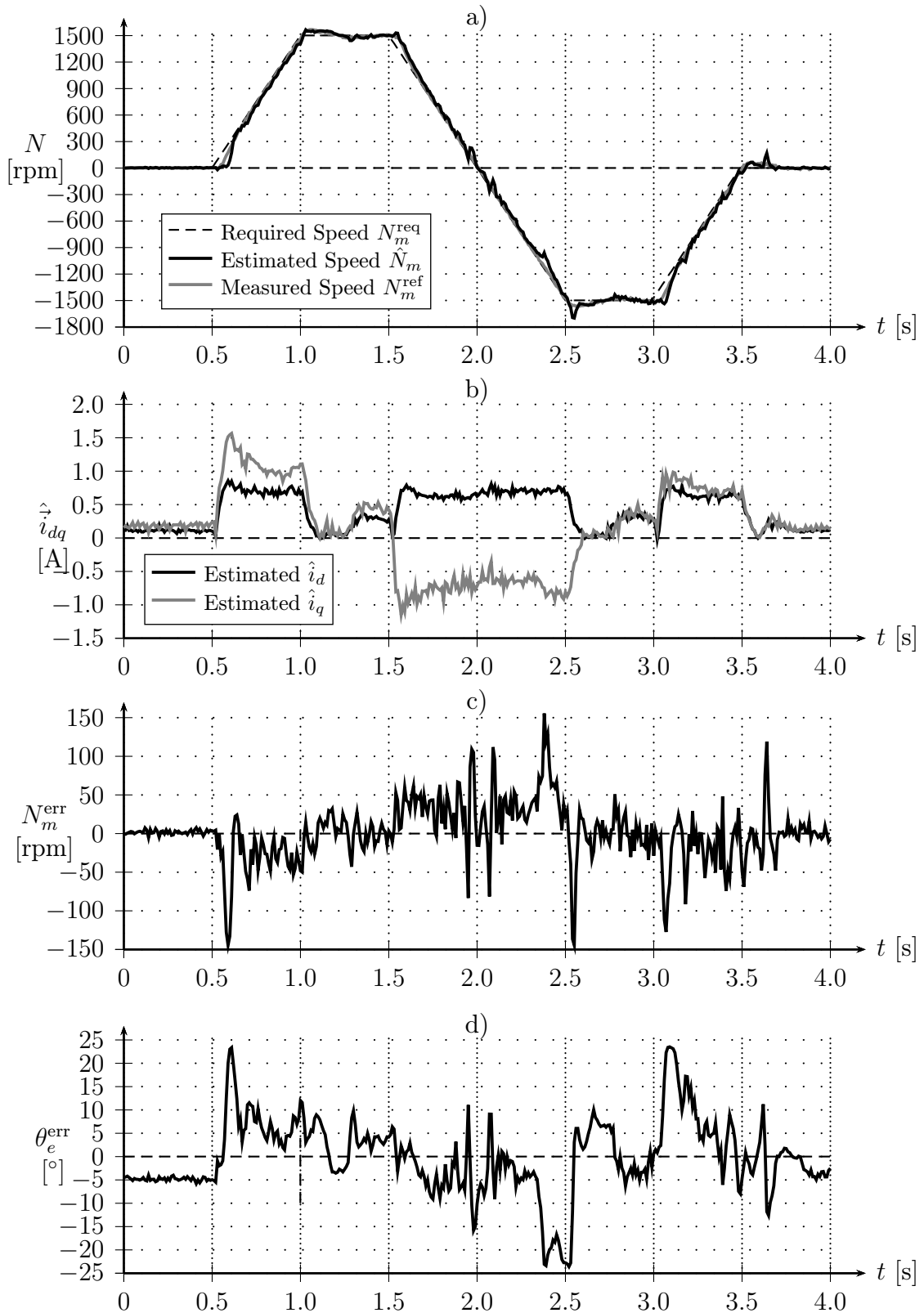
Figure 6.12: EKF-RS a) speed and b) current estimates and errors of c) speed and d) position estimates in full speed range

6.3.2. Steady-State Parameter Estimation Accuracy

To give and idea of investigated algorithm performance from wide speed and load operation range, the data for steady-state estimation accuracy were measured at the following points:

- Speed N_m was set from 100 rpm to 900 rpm with 200 rpm step (i.e. five settings total). The EEMF-based algorithms were tested only at speed 500 rpm and higher, while at the lower speeds the HFI was used. The EKF-BASIC and EKF-RS algorithms were verified at full speed range.

- Load T_l was set from 0.5 Nm to 3.5 Nm with 0.5 Nm step (i.e. seven settings per one speed setup).

- Current angle $\hat{\theta}_I$ was set from 40 degrees to 76 degrees with two-degree steps (i.e. 23 points per each load and speed setup). Note that $\hat{\theta}_I$ was not compensated for θ_e^{err} to avoid inclusion of sensor information into the control loop.

Also note that the machine temperature was maintained roughly 50±5 °C during the measurement of all operating points.

Position Estimation Accuracy

All algorithms listed in Section 6.2 were considered for this analysis. The minimal, average, and maximal values of steady-state position error θ_e^{err} obtained for different current angle $\hat{\theta}_I$ measurements were marked in the following charts. This was done to highlight the robustness of the position estimate as well.

Figure 6.13 shows steady-state position estimation error θ_e^{err} for EKF-BASIC and EKF-RS. Both algorithms showed errors, which generally meet the goals set in Section 4.3. The EKF-RS algorithm position error was sometimes several degrees higher than in the case of EKF-BASIC, but it is not a significant difference and it could be contributed to various factors (e.g. initial encoder position finding).

Figure 6.14 shows measured position error θ_e^{err} values for the HFI algorithm. Generally, its performance is comparable to the proposed algorithms.

Steady-state position errors θ_e^{err} for all EEMF algorithm variants are shown in Figure 6.15. The EEMF with constant parameter setting shows by far the greatest θ_e^{err} error, despite being a popular option in the literature. The RLS implementation achieved low θ_e^{err} error values, but with an increased dependency on the current angle $\hat{\theta}_I$ value (i.e. large variation). The best performance was achieved with accurately identified parameters provided by LUT tables. Although it should be noted, that any discrepancy between such offline-obtained parameters and the actual machine parameters led to significant position error θ_e^{err}. The $\hat{L}_d$ inductance errors $\delta_{L_d} = \pm 25$ % caused position errors close to ten degrees, which is even more than was predicted by simulation in Figure 4.7.
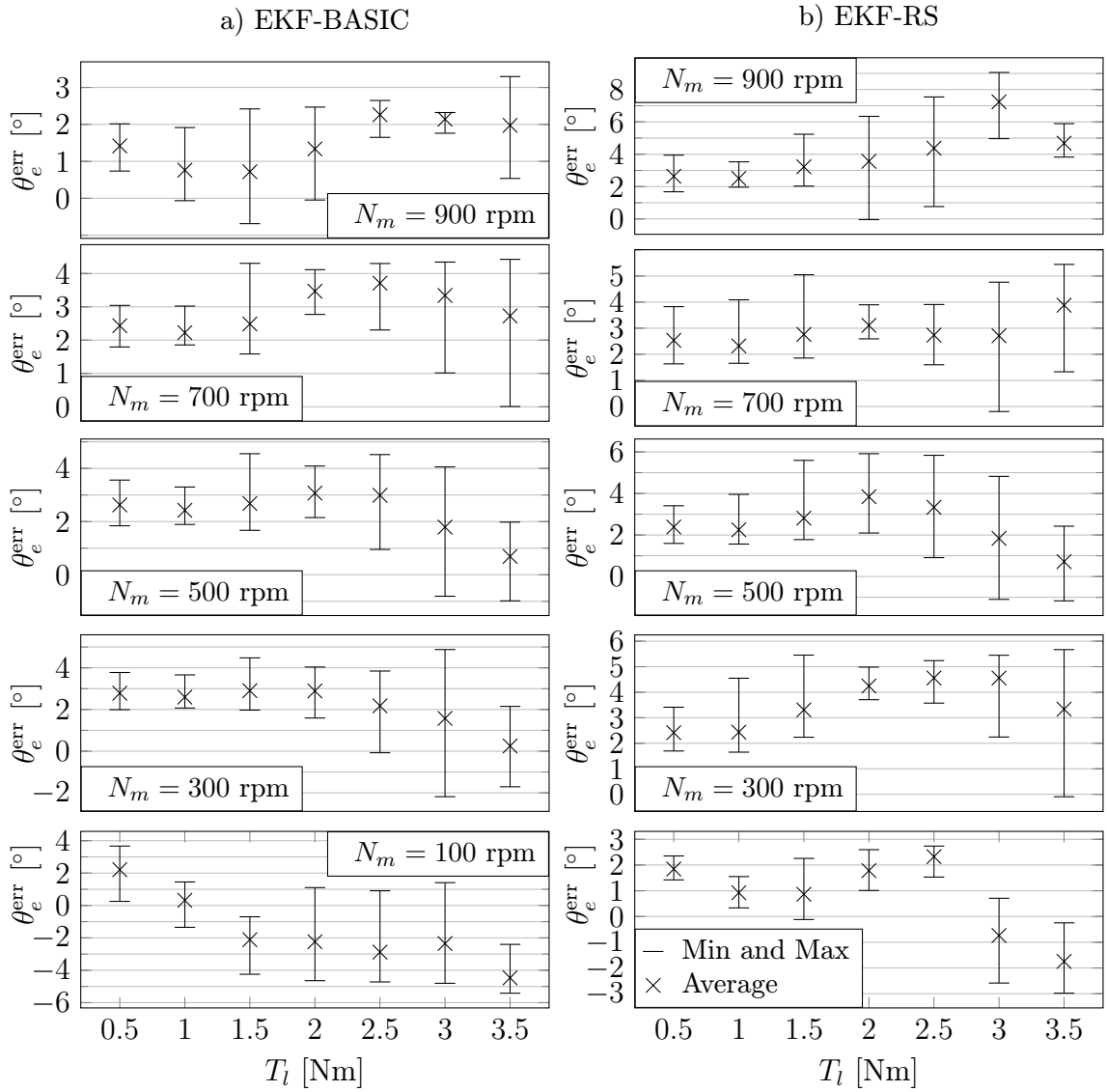
Figure 6.13: Measured steady-state position errors a) EKF-BASIC and b) EKF-RS ('×' marks average and '-' marks min and max values)
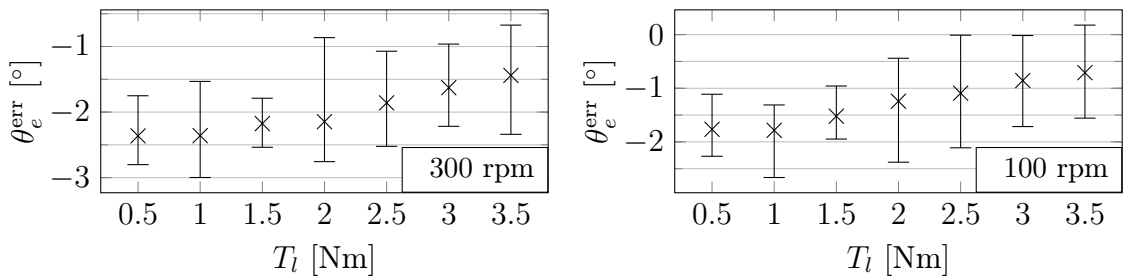
Figure 6.14: Measured HFI observer steady-state position errors ('×' marks average and '-' marks min and max values)
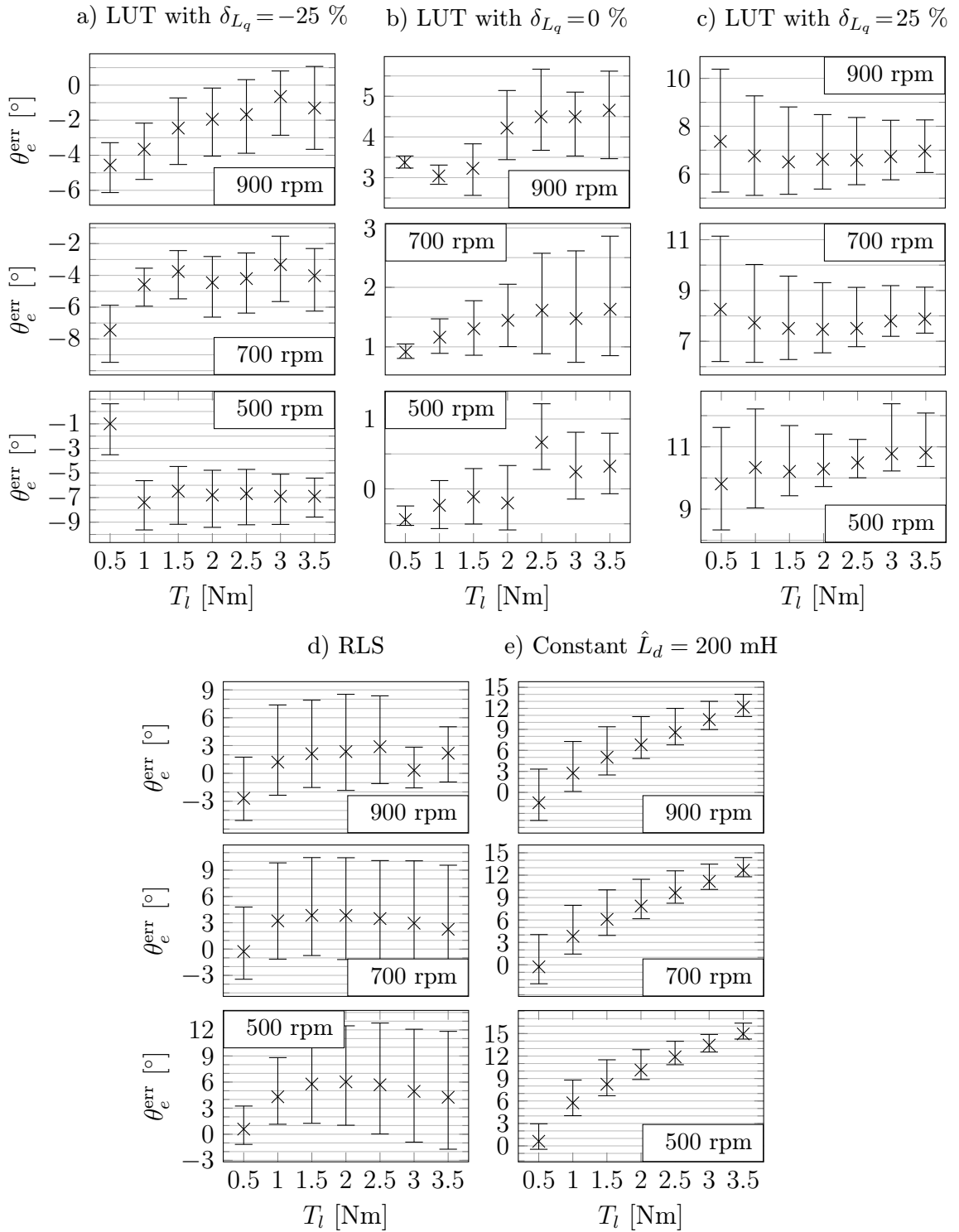
Figure 6.15: Measured EEMF observer steady-state position errors with L_q parameter provided by d) RLS algorithm, e) constant, and LUT with δ_{L_q} error set to a) -25 %, b) 0 %, and c) 25 % ('×' marks average and '-' marks min and max values)

126
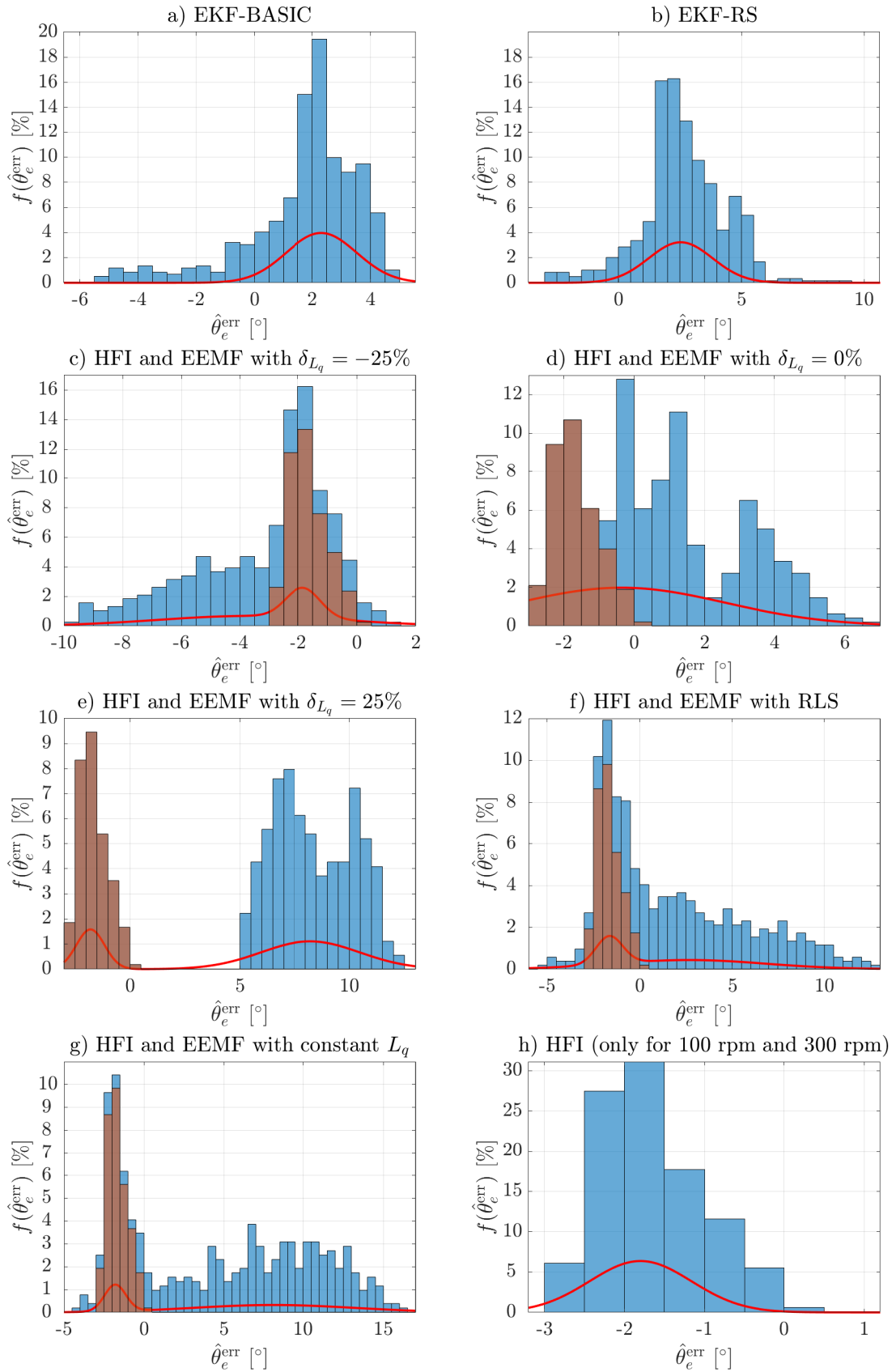
Figure 6.16: Histograms of measured $\hat{\theta}_e^{\mathrm{err}}$ for a) EKF-BASIC, b) EKF-RS, h) HFI only, and HFI with c-e) EEMF+LUT, f) EEMF+RLS, and g) constant EEMF

Another view for all considered combinations of algorithms is available in histogram collection in Figure 6.16. Bin size for all histograms was selected to half of degree. To have a valid comparison of EKF-BASIC and EKF-RS, which can operate in a full-speed range, the HFI was always considered to be used at the low-speed region at 100 rpm and 300 rpm. The contribution of HFI was then marked by orange marked colour bars in Figure 6.16. Overall, the results show that EKF-BASIC and EKF-RS algorithms do not offer better position estimation accuracy, then correctly configured state-of-the-art algorithms. At the same time, however, the proposed algorithms provided acceptable and consistent performance in full measured load and speed range, while not being reliant on precise knowledge of machine parameters.

Inductance and Resistance Estimation Accuracy

This section compares inductance and resistance estimation accuracy of EKF-BASIC, EKF-RS, and RLS algorithms. The relative errors of resistance δ_{R_s}, direct axis inductance δ_{L_d}, and quadrature axis inductance δ_{L_q} estimates were obtained in relation to offline-measured values stated in Section 1.2. Histograms in Figure 6.17, Figure 6.18, and Figure 6.19 show a comparison of the accuracy of estimates over all the measured operation points. Histogram charts used $\delta_{L_d} = \delta_{L_q} = 5\ \%$ or $\delta_{R_s} = 20\ \%$ width of bins.

Both proposed algorithms showed errors, which generally met the goals set in Section 4.3, while the RLS algorithm showed lower performance. Although the original publication with the implemented RLS algorithm showed similar errors, the measurement results should not be interpreted as if better performance could not be reached [ITDO06]. It can, however, be claimed that highly accurate online parameter adaptation is not a trivial task. As for the EKF-BASIC and EKF-RS estimate errors (namely for the stator resistance $\hat{R}_s$), their likely sources are the small periodic deformations $\Delta_{\mathcal{R}}(\theta_e + \theta_{phN})$ in $\mathcal{R}'_{phN}$ measurements as can be seen in Figure 6.6 to Figure 6.8. Especially the $\hat{R}_s$ estimation is sensitive to inductance inaccuracy, as was shown by simulation in Figure 5.22. This highlights the fact that performance of EKF-BASIC and EKF-RS algorithms is closely tied to $\mathcal{R}'_{phN}$ measurements and attention must be paid to MC IDC tuning and to discard any deformed u_{idc} samples.
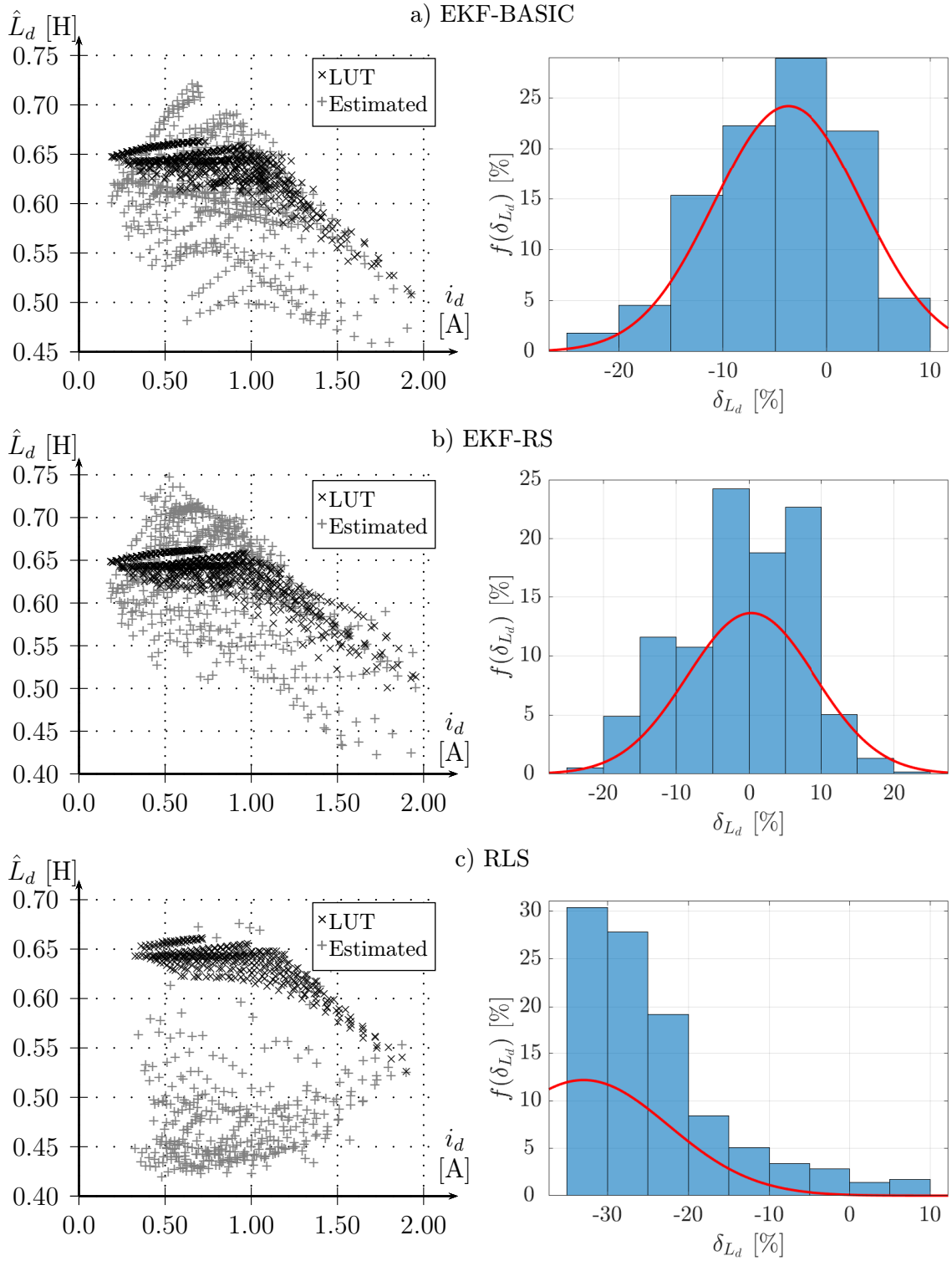
Figure 6.17: Direct axis inductance $\hat{L}_d$ estimates and corresponding histograms of estimate error δ_{L_d} for a) EKF-BASIC, b) EKF-RS, and c) RLS algorithms
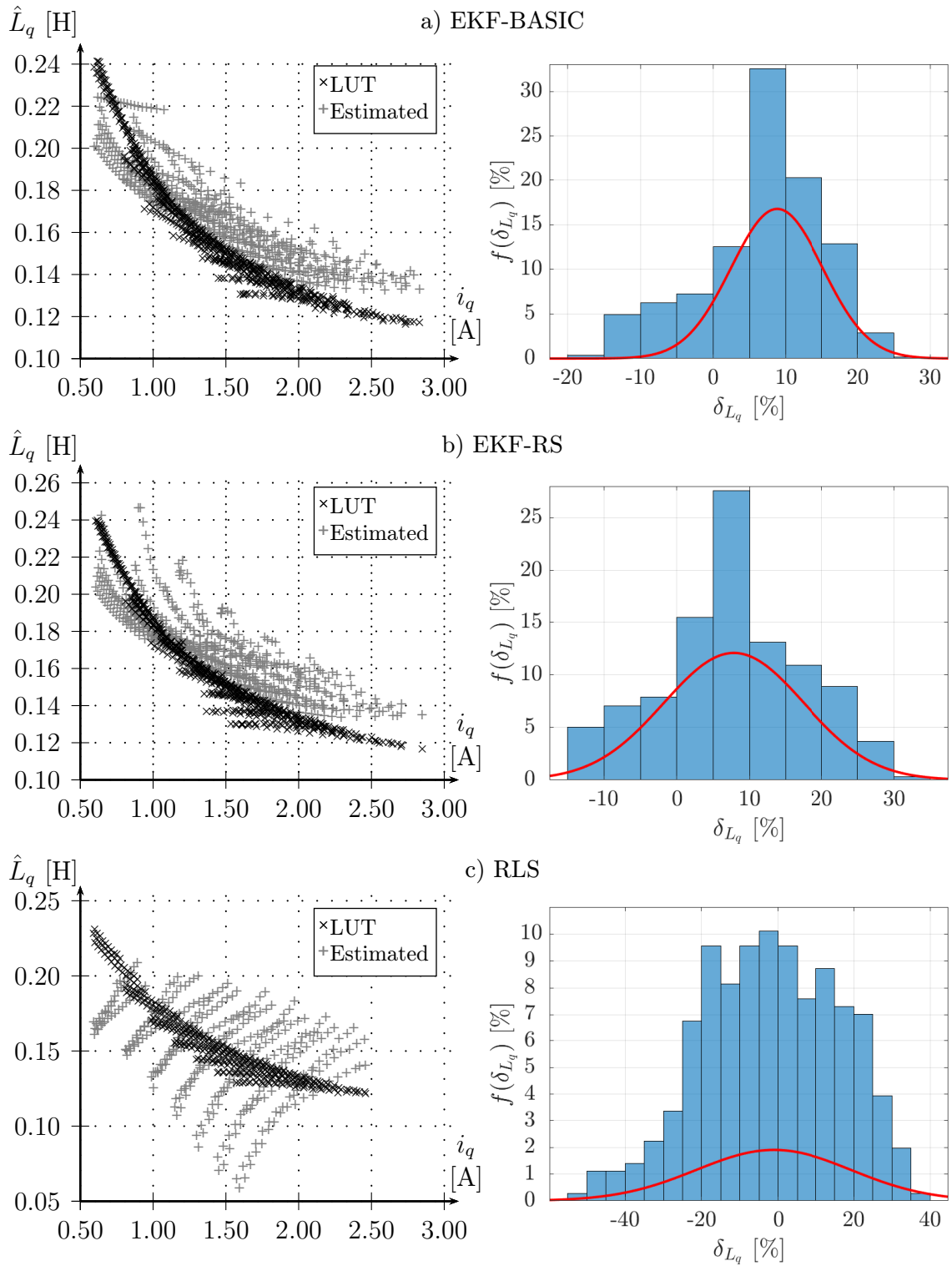
Figure 6.18: Quadrature axis inductance $\hat{L}_q$ estimates and corresponding histograms of estimate error δ_{L_q} for a) EKF-BASIC, b) EKF-RS, and c) RLS algorithms
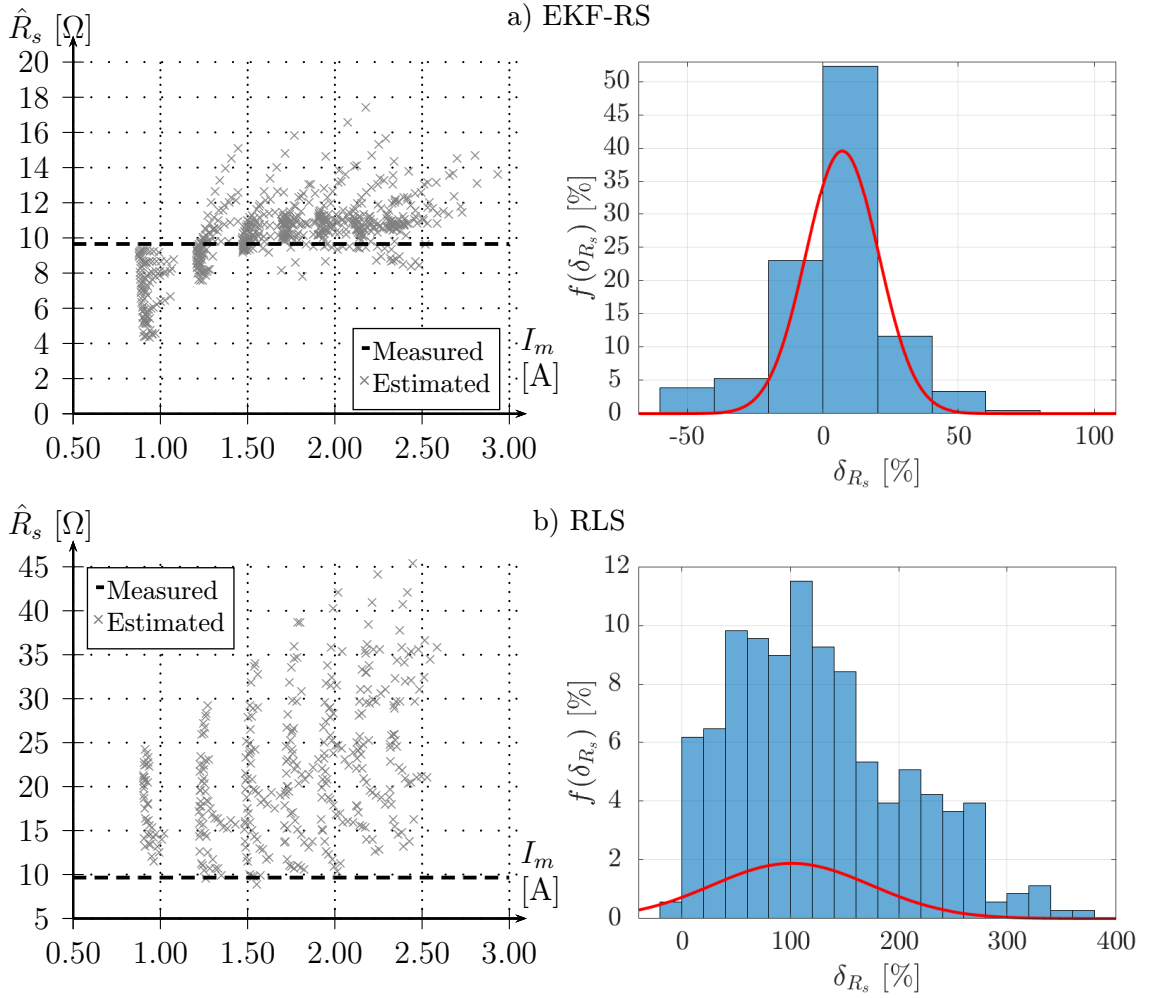
Figure 6.19: Stator resistance $\hat{R}_s$ estimates and corresponding histograms of estimate error δ_{R_s} for a) EKF-RS and b) RLS algorithms

6.3.3. Comparison of Optimal Power Trajectories

This section will analyze data from the same measurements as in Section 6.3.2 in order to determine the impact of signal injections used by HFI and RLS algorithms and the ASPWM switching scheme used by EKF-BASIC and EKF-RS to optimal MTPA and ME trajectory. The centre-aligned PWM switching scheme with no signal injection will be considered as a reference. All optimal MTPA and ME trajectories were obtained from characteristics as shown in the example for $N_m = 700$ rpm in Figure 6.20. Note that in this case the shown current angle θ_I was maintained by the encoder sensor so the characteristics were not skewed by estimator error $\hat{\theta}_e^{\mathrm{err}}$. As can be seen in the example, the MTPA trajectory is always located at lower current angles than the ME trajectory, which corresponds to simulated trajectories in Figure 3.13.
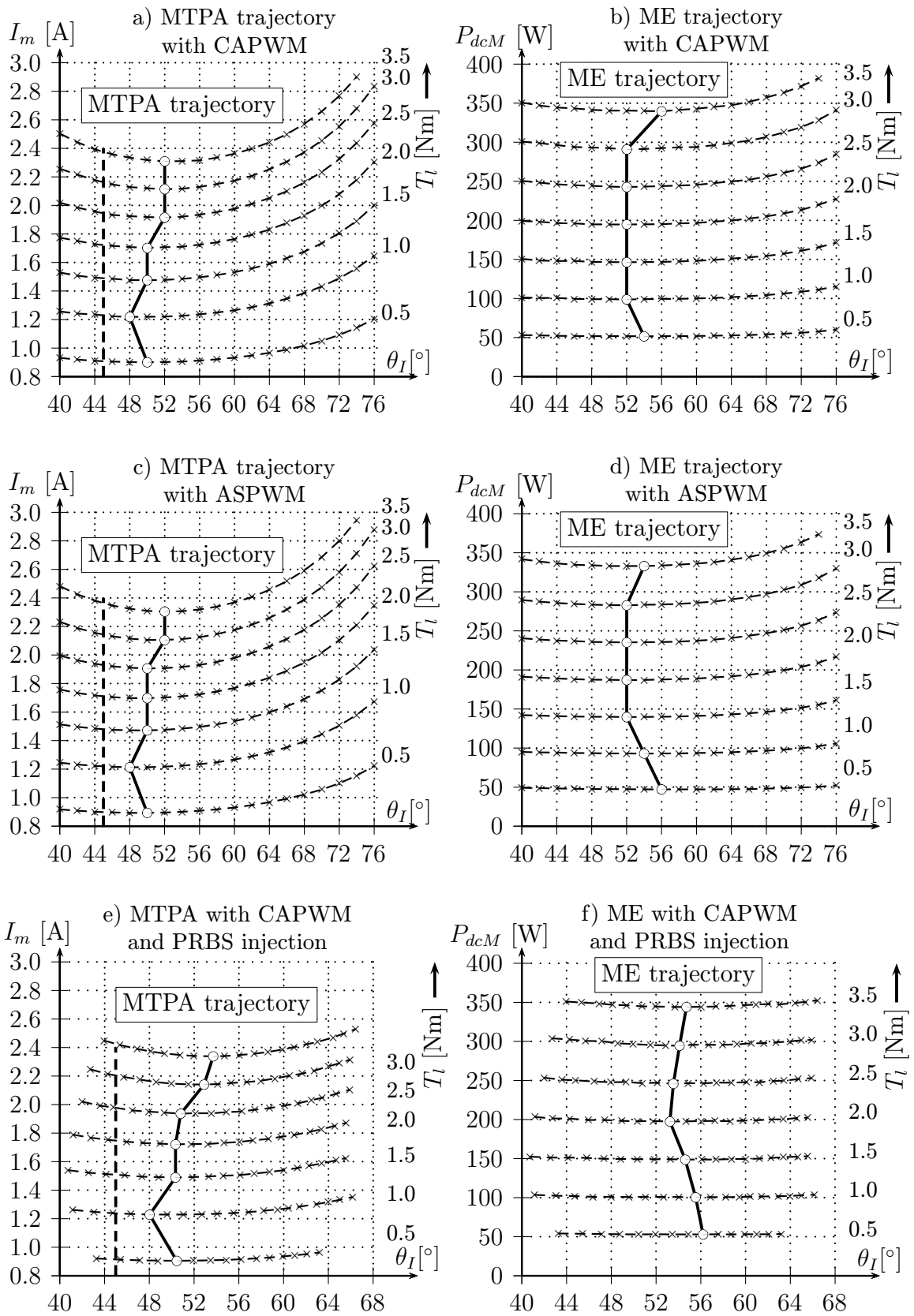
Figure 6.20: Examples for optimal MTPA and ME trajectories obtained at 700 rpm for a-b) centre-aligned PWM, c-d) ASPWM, and e-f) CAPWM with PRBS injection
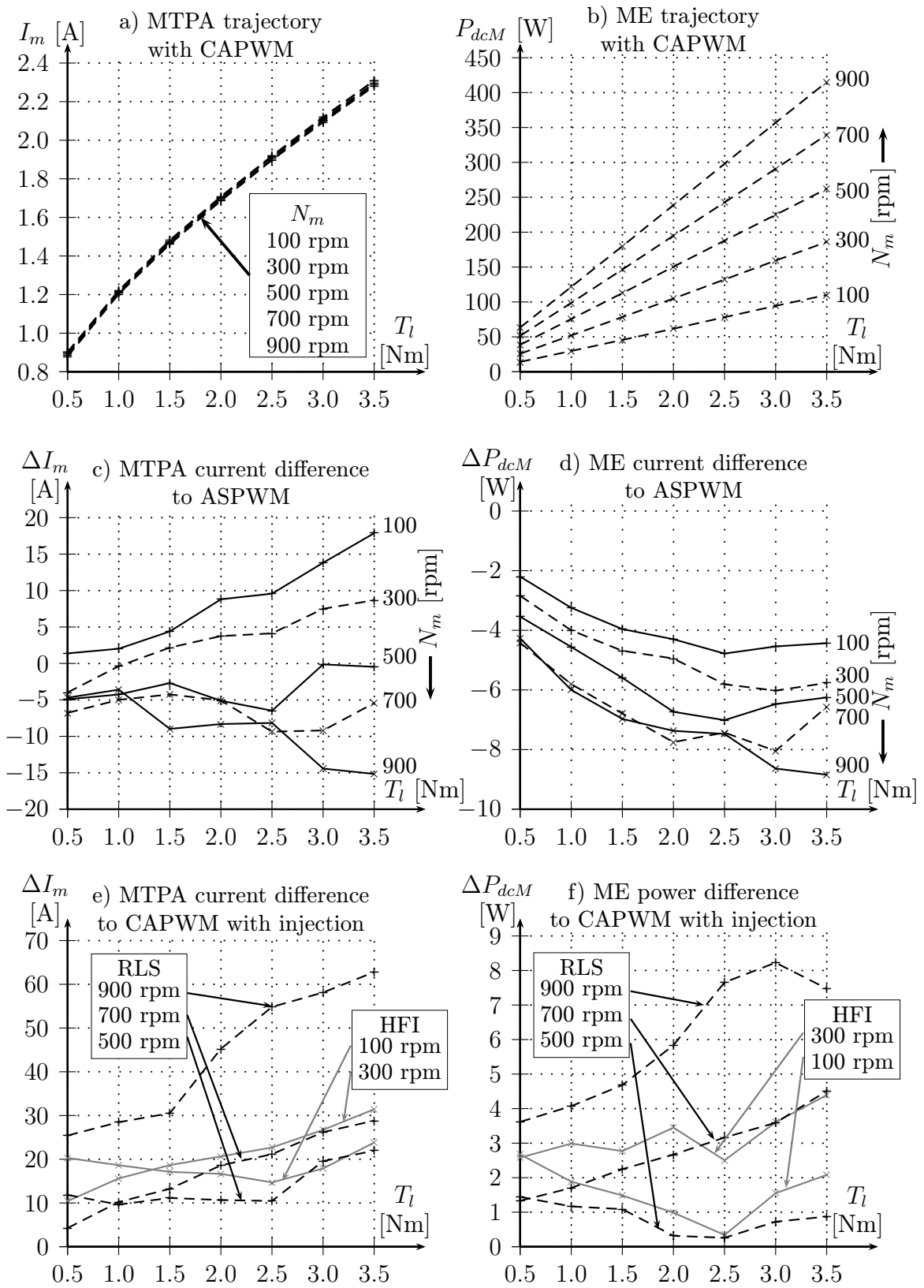
Figure 6.21: Optimal a) MTPA and b) ME trajectories with CAPWM and relative current ΔI_m and input power ΔP_{dcM} differences when using c-d) ASPWM scheme or e-f) signal injections

To evaluate the impact of using ASPWM switching scheme or injections, like the PRBS signal injection used by RLS algorithm and the harmonic signal injection used by HFI, Figure 6.21 shows the stator currents I_m and input powers P_{dcM} corresponding to the optimal MTPA and ME trajectories in comparison to centre-aligned PWM scheme with no injections (i.e. a reference configuration). As expected, the additional PRBS and harmonic injections caused a measurable increase of both the stator current amplitude ΔI_m and input power ΔP_{dcM}. Results in Figure 6.21f show an increase of input power ΔP_{dcM} in units of Watts for both the PRBS and the harmonic injection. The exact increase in a real application would, of course, be a matter of parameters of the injected signal, but it is safe to assume that any injection will always lead to additional power losses. As for the alignment-swap PWM switching scheme used by the EKF-BASIC and the EKF-RS algorithms, it was discussed in Section 5.2 that the method leads to elevated current ripple, but also reduces the switching power losses by factor of one third. Experimental results in Figure 6.21d show a reduction in input power ΔP_{dcM} by units of Watts, which generally confirms this prediction and shows the potential value of the method. This is true especially for drives with high stator inductances, where the increase in THD and audible noise is not as significant.

Conclusions

This thesis focused on the development of SynRM state and parameter estimation algorithms suitable for sensorless power-optimal applications. Chapter 1 of this thesis showed the SynRM machine mathematical model and its significant inductance non-linearity caused by magnetic saturation. Chapter 2 and Chapter 3 then presented the existing SynRM sensorless state and parameter estimation, as well as, power-optimization control algorithms. Evaluation of the SynRM power-optimal sensorless control state-of-the-art was conducted in Chapter 4. The impact of position and inductance estimate errors on the estimated power-optimal current angle θ_I, which directly affects the MTPA and ME power optimality, was simulated on the model of the reference 550 W SynRM machine. The analysis resulted in goals listed in Section 4.3, which were pursued by the algorithms proposed in this thesis. In summary, it was deemed that sensorless position, speed, and inductance estimator is necessary, capable of operating in full-speed range with a good estimation accuracy but without costly hardware and need of significant signal injection.

The proposed method, designed to fit the four defined goals, was presented and verified by simulation in Section 5 and it featured three novel ideas:

- The current derivative measurement method is described in Section 5.1. The simple and low-cost measurement circuit MC IDC allows measuring Δi_{dc} with improved accuracy. As shown by the proposed EKF-BASIC algorithm variant, this measurement alone is enough to obtain machine phase reluctances and consequently estimate the rotor position, speed, as well as actual machine inductances.

- The alignment-swap PWM switching scheme shown in Section 5.2 allows to measure the current derivatives even for small duty cycle values. The method introduces increased stator current ripple at lower duty-cycles but also reduces the inverter switching losses by a third, which might make this approach attractive for suitable power-efficient systems.

- The phase reluctance measurement can be used to extract all the necessary machine states and parameters. Additional measurements and machine models can then be used as redundancy (e.g. to serve as diagnostics for fail safe systems) or to extract further information. The latter was realised in this thesis by integrating the machine model and phase reluctance measurements via the extended Kalman filter. For example, the proposed EKF-RS algorithm variant then allowed to estimate the stator resistance $\hat{R}_s$ and the previously published method provided core losses estimate [MVB21]. It is likely, that many other modifications could be derived to support a wide range of applications.

The use of the ASPWM scheme and the phase reluctance measurement method based on the MC IDC circuit allowed to meet the requirement of low additional cost and ability to operate at low-speed and standstill. To verify the capability of proposed algorithms to meet the position and inductance estimate accuracy goals, Chapter 6 presented results from the experimental verification and comparison with known state-of-the-art algorithms. Carefully designed and tuned existing methods,

like, for example, the EEMF observer with accurate offline-measured inductances in LUT, can generally achieve a great position estimation performance, however, it quickly deteriorates when actual machine parameters differ. On the other hand, the proposed method is highly adaptive, can generally deliver a robust performance, and meets the defined goals when accurate machine parameters are not available or change during runtime (e.g. due to temperature). The impact of using the proposed ASPWM method was compared in terms of achievable MTPA and ME optimal power to the commonly used PWM switching scheme with and without signal injections. The results confirm reduced power losses when using ASPWM and show its potential value for suitable applications.

Overall the presented adaptive sensorless state and parameter estimation method met the goals defined within this thesis. Its parts or as a whole, it might serve as an interesting alternative for SynRM-based high power-efficient applications.

Future research and development may focus on many areas. First, the proposed methods should be tested with a larger sample of SynRM machines, preferably on various real applications to better understand the algorithm suitability for the field. Second, it would be interesting to further investigate the interaction of multiple models and measurements within EKF with accurately obtained state and measurement covariance matrices as it may yield estimate accuracy improvement rather than additional estimated quantities. This could make the algorithm an appealing option for high-performance applications. To make the proposed algorithm more attractive for low-cost applications with limited computational power, its simplification should be investigated. The most complex portion is the EKF calculation, hence, at least a partial replacement should be sought. There are many possibilities worth considering. An example may be a combination of the EKF-BASIC and EEMF using the Model Reference Adaptive System (MRAS) approach to obtain the additional estimates.

Relevant Author's Bibliography

[MVB21] Z. Mynar, P. Vaclavek, and P. Blaha. Synchronous Reluctance Motor Parameter and State Estimation Using Extended Kalman Filter and Current Derivative Measurement. *IEEE Transactions on Industrial Electronics*, 68(3):1972–1981, Mar. 2021. DOI: 10.1109/TIE.2020.2973897.

[MVV16] Z. Mynar, L. Vesely, and P. Vaclavek. PMSM Model Predictive Control With Field-Weakening Implementation. *IEEE Transactions on Industrial Electronics*, 63(8):5156–5166, Apr. 2016. DOI: 10.1109/TIE.2016.2558165.

[Myn15] Z. Mynar. Linear Model Predictive Control of Induction Machine. *Proceedings of the 21th Conference STUDENT EEICT 2015*, pages 465–469, Apr. 2015. ISBN: 978-80-214-5148-3.

[Myn16] Z. Mynar. Power Optimized Control of Synchronous Reluctance machine. *Proceedings of the 22th Conference STUDENT EEICT 2016*, pages 441–445, Apr. 2016. ISBN: 978-80-214-5350-0.

[VM17] L. Vesely and Z. Mynar. Model predictive control of SPMSM based on FPGA and processor. In *2017 IEEE International Conference on Industrial Technology (ICIT)*, pages 324–329, Mar. 2017. DOI: 10.1109/ICIT.2017.7913104.

Bibliography

[AR15]   J. Antons and T. Rösmann. Self-sensing control of a synchronous reluctance machine using an extended Kalman filter. In *2015 IEEE International Conference on Industrial Technology (ICIT)*, pages 831–839, Mar. 2015. DOI: 10.1109/ICIT.2015.7125201.

[ATTM05]   G. Ahmad, H. Tsuyoshi, T. Teruo, and E. Mohamad. A Novel Implementation Method of a Programmable Cascaded Low Pass Filters for a Low Speed Sensorless Control of Synchronous Reluctance Motors. In *2005 International Conference on Power Electronics and Drives Systems*, volume 1, pages 360–365, Nov. 2005. DOI: 10.1109/PEDS.2005.1619713.

[BCP16]   N. Bedetti, S. Calligaro, and R. Petrella. Stand-Still Self-Identification of Flux Characteristics for Synchronous Reluctance Machines Using Novel Saturation Approximating Function and Multiple Linear Regression. *IEEE Transactions on Industry Applications*, 52(4):3083–3092, Jul. 2016. DOI: 10.1109/TIA.2016.2535413.

[BG10]   O. Benjak and D. Gerling. Review of position estimation methods for IPMSM drives without a position sensor part II: Adaptive methods. In *The XIX International Conference on Electrical Machines - ICEM 2010*, pages 1–6, Sep. 2010. DOI: 10.1109/ICELMACH.2010.5607980.

[BP08]   A. Boglietti and M. Pastorelli. Induction and synchronous reluctance motors comparison. In *2008 34th Annual Conference of IEEE Industrial Electronics*, pages 2041–2044, Nov. 2008. DOI: 10.1109/IECON.2008.4758270.

[BPPS10]   S. Bolognani, R. Petrella, A. Prearo, and L. Sgarbossa. On-line tracking of the MTPA trajectory in IPM motors via active power measurement. In *The XIX International Conference on Electrical Machines - ICEM 2010*, pages 1–7, Sep. 2010. DOI: 10.1109/ICELMACH.2010.5607843.

[BSL+10]   S. Beineke, J. Schirmer, J. Lutz, H. Wertz, A. Bähr, and J. Kiel. Implementation and applications of sensorless control for synchronous machines in industrial inverters. In *2010 First Symposium on Sensorless Control for Electrical Drives*, pages 64–71, Jul. 2010. DOI: 10.1109/SLED.2010.5542802.

[CČerný10] Z. Caha and M. Černý. *Elektrické pohony*. SNTL, Praha, 2010.

[CM18]   B. Carter and R. Mancini. *Op Amps for Everyone*. Newnes, 5 edition, 2018. DOI: 10.1016/B978-0-12-811648-7.15003-4.

[CPST02]   D. Casadei, F. Profumo, G. Serra, and A. Tani. FOC and DTC: two viable schemes for induction motors torque control. *IEEE Transactions on Power Electronics*, 17(5):779–787, Sep. 2002. DOI: 10.1109/TPEL.2002.802183.

[DTCB22]   A. Dianov, F. Tinazzi, S. Calligaro, and S. Bolognani. Review and Classification of MTPA Control Algorithms for Synchronous Motors. *IEEE Transactions on Power Electronics*, 37(4):3990–4007, Apr. 2022. DOI: 10.1109/TPEL.2021.3123062.

[DW12]   J. Dong and F. Wang. Study of analytical current ripple of three-phase PWM converter. In *2012 Twenty-Seventh Annual IEEE Applied Power Electronics Conference and Exposition (APEC)*, pages 1568–1575, Feb. 2012. DOI: 10.1109/APEC.2012.6166029.

[FSM+22]   L. Faa-Jeng, C. Shih-Gang, H. Ming-Shi, L. Chia-Hui, and L. Chen-Hao. Adaptive Complementary Sliding Mode Control for Synchronous Reluctance Motor With Direct-Axis Current Control. *IEEE Transactions on Industrial Electronics*, 69(1):141–150, Jan. 2022. DOI: 10.1109/TIE.2021.3050373.

[FZYJ20]   G. Fengtao, Y. Zhonggang, Z. Yanping, and L. Jing. High Efficiency Sensorless Control of SynRM with Inductance Identification Based on Adaptive Alternate EKF. In *IECON 2020 The 46th Annual Conference of the IEEE Industrial Electronics Society*, pages 997–1002, Oct. 2020. DOI: 10.1109/IECON43393.2020.9254901.

[HKS99]   J. Ha, S. Kang, and S. Sul. Position-controlled synchronous reluctance motor without rotational transducer. *IEEE Transactions on Industry Applications*, 35(6):1393–1398, Nov. 1999. DOI: 10.1109/28.806054.

[HNS17]   M. Hofer, M. Nikowitz, and M. Schroedl. Sensorless control of a reluctance synchronous machine in the whole speed range without voltage pulse injections. In *2017 IEEE 3rd International Future Energy Electronics Conference and ECCE Asia (IFEEC 2017 - ECCE Asia)*, pages 1194–1198, Jun. 2017. DOI: 10.1109/IFEEC.2017.7992211.

[IKK+09]   J. Im, W. Kim, K. Kim, C. Jin, J. Choi, and J. Lee. Inductance Calculation Method of Synchronous Reluctance Motor Including Iron Loss and Cross Magnetic Saturation. *IEEE Transactions on Magnetics*, 45(6):2803–2806, Jun. 2009. DOI: 10.1109/TMAG.2009.2018663.

[ITDO06]   S. Ichikawa, M. Tomita, S. Doki, and S. Okuma. Sensorless Control of Synchronous Reluctance Motors Based on Extended EMF Models Considering Magnetic Saturation With Online Parameter Identification. *IEEE Transactions on Industry Applications*, 42(5):1264–1274, Sep. 2006. DOI: 10.1109/TIA.2006.880848.

[JSH+02]   J. Jang, S. Sul, J. Ha, K. Ide, and M. Sawamura. Sensorless drive of SMPM motor by high frequency signal injection. In *APEC. Seventeenth Annual IEEE Applied Power Electronics Conference and Exposition (Cat. No.02CH37335)*, volume 1, pages 279–285, Mar. 2002. DOI: 10.1109/APEC.2002.989259.

[JZL+19]   S. Jia, P. Zhang, D. Liang, M. Dai, and J. Liu. Design and Comparison of Three Different Types of IE4 Efficiency Machines. In *2019 22nd International Conference on Electrical Machines and Systems (ICEMS)*, pages 1–4, Aug. 2019. DOI: 10.1109/ICEMS.2019.8921786.

[KC17]   A. Kumar and D. Chatterjee. A survey on space vector pulse width modulation technique for a two-level inverter. In *2017 National Power Electronics Conference (NPEC)*, pages 78–83, Dec. 2017. DOI: 10.1109/NPEC.2017.8310438.

[Kol10]   J. Kolehmainen. Synchronous Reluctance Motor With Form Blocked Rotor. *IEEE Transactions on Energy Conversion*, 25(2):450–456, Jun. 2010. DOI: 10.1109/TEC.2009.2038579.

[Kos23]   J. K. Kostko. Polyphase reaction synchronous motors. *Journal of the American Institute of Electrical Engineers*, 42(11):1162–1168, Nov. 1923. DOI: 10.1109/JoAIEE.1923.6591529.

[KS96a]   S. Kang and S. Sul. Efficiency optimized vector control of synchronous reluctance motor. In *IAS '96. Conference Record of the 1996 IEEE Industry Applications Conference Thirty-First IAS Annual Meeting*, volume 1, pages 117–121, Oct. 1996. DOI: 10.1109/IAS.1996.557005.

[KS96b]   S. Kang and S. Sul. Highly dynamic torque control of synchronous reluctance motor. In *PESC Record. 27th Annual IEEE Power Electronics Specialists Conference*, volume 2, pages 1793–1797, Jun. 1996. DOI: 10.1109/PESC.1996.548824.

[KSG+14]   S. Kondo, Y. Sato, T. Goto, M. Tomita, M. Hasegawa, S. Doki, and S. Kato. Position and velocity sensorless control for synchronous reluctance motor at low speeds and under loaded conditions using high-frequency extended EMF observer and heterodyne detection. In *2014 International Conference on Electrical Machines (ICEM)*, pages 857–863, Sep. 2014. DOI: 10.1109/ICELMACH.2014.6960281.

[KSIM10]   S. Kim, S. Sul, K. Ide, and S. Morimoto. Maximum efficiency operation of Synchronous Reluctance Machine using signal injection. In *The 2010 International Power Electronics Conference - ECCE ASIA*, pages 2000–2004, Jun. 2010. DOI: 10.1109/IPEC.2010.5543558.

[LBM94]   R. Lagerquist, I. Boldea, and T. J. E. Miller. Sensorless-control of the synchronous reluctance motor. *IEEE Transactions on Industry Applications*, 30(3):673–682, May 1994. DOI: 10.1109/28.293716.

[Lev]   S. Levy. GitHub - simondlevy/TinyEKF: Lightweight C/C++ Extended Kalman Filter with Python for prototyping. <https://github.com/simondlevy/TinyEKF>. Accessed: 2022-08-30.

[LK97]   D. Leggate and R. J. Kerkman. Pulse-based dead-time compensator for
            PWM voltage inverters. *IEEE Transactions on Industrial Electronics*,
            44(2):191–197, Apr. 1997. DOI: 10.1109/41.564157.

[LK19]   X. Li and R. Kennel. Comparison of state-of-the-art estimators for
            electrical parameter identification of PMSM. In *2019 IEEE Interna-
            tional Symposium on Predictive Control of Electrical Drives and Power
            Electronics (PRECEDE)*, pages 1–6, May 2019. DOI: 10.1109/PRE-
            CEDE.2019.8753197.

[Mad03]   C. Mademlis. Compensation of magnetic saturation in maximum torque
            to current vector controlled synchronous reluctance motor drives. *IEEE
            Transactions on Energy Conversion*, 18(3):379–385, Sep. 2003. DOI:
            10.1109/TEC.2003.815827.

[MDD+22]   M. Murataliyev, M. Degano, M. Di Nardo, N. Bianchi, and C. Ger-
            ada. Synchronous Reluctance Machines: A Comprehensive Review and
            Technology Comparison. *Proceedings of the IEEE*, 110(3):382–399, Jan.
            2022. DOI: 10.1109/JPROC.2022.3145662.

[Moo96]   T. K. Moon. The expectation-maximization algorithm. *IEEE Signal
            Processing Magazine*, 13(6):47–60, 1996. DOI: 10.1109/79.543975.

[NSS20]   M. Nikowitz, R. Spiessberger, and M. Schroedl. Influence of the cur-
            rent sensor characteristics on the INFORM-method. In *PCIM Europe
            digital days 2020; International Exhibition and Conference for Power
            Electronics, Intelligent Motion, Renewable Energy and Energy Manage-
            ment*, 2020. ISBN: 978-3-8007-5245-4.

[ODM15]   C. Oprea, A. Dziechciarz, and C. Martis. Comparative analy-
            sis of different synchronous reluctance motor topologies. In *2015
            IEEE 15th International Conference on Environment and Electri-
            cal Engineering (EEEIC)*, pages 1904–1909, Jun. 2015. DOI:
            10.1109/EEEIC.2015.7165463.

[PSLK11]   D. Paulus, J. Stumper, P. Landsmann, and R. Kennel. Encoderless
            field-oriented control of a synchronous reluctance machine with posi-
            tion and inductance estimators. In *8th International Conference on
            Power Electronics - ECCE Asia*, pages 1153–1160, May 2011. DOI:
            10.1109/ICPE.2011.5944694.

[QH13]   Z. Qu and M. Hinkkanen. Loss-minimizing control of synchronous
            reluctance motors - A review. In *2013 IEEE International Confer-
            ence on Industrial Technology (ICIT)*, pages 350–355, Feb. 2013. DOI:
            10.1109/ICIT.2013.6505697.

[RFC10]   M. Rajabi, M. Freddy, and S. Chandur. Theoretical and Exper-
            imental Reevaluation of Synchronous Reluctance Machine. *IEEE
            Transactions on Industrial Electronics*, 57(1):6–13, Jan. 2010. DOI:
            10.1109/TIE.2009.2025286.

[RK20]   P. Resutik and S. Kascak. Estimation of power losses and temperature distribution in three-phase inverter. In *2020 ELEKTRO*, pages 1–5, 2020. DOI: 10.1109/ELEKTRO49696.2020.9130255.

[RSW18]   R. Raja, T. Sebastian, and M. Wang. Practical Implementation of Current Derivative Measurement for Sensorless Control of Permanent Magnet Machines. In *2018 IEEE Transportation Electrification Conference and Expo (ITEC)*, pages 1–6, Jun. 2018. DOI: 10.1109/ITEC.2018.8450148.

[RSW19]   R. Raja, T. Sebastian, and M. Wang. Online stator inductance estimation for permanent magnet motors using PWM excitation. *IEEE Transactions on Transportation Electrification*, 5(1):107–117, Mar. 2019. DOI: 10.1109/TTE.2019.2891047.

[Sema]   NXP Semiconductors. FreeMASTER Run-Time Debugging Tool. `<https://nxp.com/freemaster>`. Accessed: 2022-08-30.

[Semb]   NXP Semiconductors. Real Time Control Embedded Software Motor Control and Power Conversion Libraries. `<https://nxp.com/rtcesl>`. Accessed: 2022-08-30.

[Sem12]   ON Semiconductor. AN-9070 Smart Power Module Motion SPM® Products in SPM45H Packages. `<https://www.onsemi.com/pub/Collateral/AN-9070.pdf>`, Aug. 2012. Accessed: 2022-08-30.

[Sem14]   ON Semiconductor. FNB41560/FNB41560B2 Motion SPM 45 Series Datasheet. `<https://www.onsemi.com/pdf/datasheet/fnb41560b2-d.pdf>`, Jan. 2014. Accessed: 2022-08-30.

[SKUU03]   T. Senjyu, K. Kinjo, N. Urasaki, and K. Uezato. High efficiency control of synchronous reluctance motors using extended Kalman filter. *IEEE Transactions on Industrial Electronics*, 50(4):726–732, Aug. 2003. DOI: 10.1109/TIE.2003.814998.

[TH14]   T. Tuovinen and M. Hinkkanen. Adaptive Full-Order Observer With High-Frequency Signal Injection for Synchronous Reluctance Motor Drives. *IEEE Journal of Emerging and Selected Topics in Power Electronics*, 2(2):181–189, Jun. 2014. DOI: 10.1109/JESTPE.2013.2294359.

[THHL10]   T. Tuovinen, M. Hinkkanen, L. Harnefors, and J. Luomi. A reduced-order position observer with stator-resistance adaptation for synchronous reluctance motor drives. In *Proceedings of 14th International Power Electronics and Motion Control Conference EPE-PEMC 2010*, pages 174–179, Sep. 2010. DOI: 10.1109/EPEPEMC.2010.5606645.

[Tuo14]   T. Tuovinen. *Model-Based Position Estimation for Synchronous Reluctance Motor Drives*. School of Electrical Engineering, Helsinki, 2014. ISBN: 978-952-60-5727-9.

[VPF96]   A. Vagati, M. Pastorelli, and G. Franceschini. High performance control of synchronous reluctance motor. In *IAS '96. Conference Record of the 1996 IEEE Industry Applications Conference Thirty-First IAS Annual Meeting*, volume 1, pages 295–303, Oct. 1996. DOI: 10.1109/IAS.1996.557035.

[WB06]   G. Welch and G. Bishop. *An Introduction to the Kalman Filter*. University of North Carolina at Chapel Hill, Chapel Hill, NC, USA, Jul. 2006.

[WD15]   S. Wiedemann and A. Dziechciarz. Comparative evaluation of DTC strategies for the Synchronous Reluctance machine. In *2015 Tenth International Conference on Ecological Vehicles and Renewable Energies (EVER)*, pages 1–5, Mar. 2015. DOI: 10.1109/EVER.2015.7112972.

[WJPK22]   L. Wonhee, K. Jaehong, J. Pooreum, and N. Kwanghee. On-Line MTPA Control Method for Synchronous Reluctance Motor. *IEEE Transactions on Industry Applications*, 58(1):356–364, Nov. 2022. DOI: 10.1109/TIA.2021.3128468.

[WL00]   L. Wang and R. D. Lorenz. Rotor position estimation for permanent magnet synchronous motor using saliency-tracking self-sensing method. In *Conference Record of the 2000 IEEE Industry Applications Conference. Thirty-Fifth IAS Annual Meeting and World Conference on Industrial Applications of Electrical Energy (Cat. No.00CH37129)*, volume 1, pages 445–450, Oct. 2000. DOI: 10.1109/IAS.2000.881148.

[XXLN91]   L. Xu, X. Xu, T. A. Lipo, and D. W. Novotny. Vector control of a synchronous reluctance motor including saturation and iron loss. *IEEE Transactions on Industry Applications*, 27(5):977–985, Sep. 1991. DOI: 10.1109/28.90356.

[YAA09]   S. Yamamoto, J. B. Adawey, and T. Ara. Maximum efficiency drives of synchronous reluctance motors by a novel loss minimization controller considering cross-magnetic saturation. In *2009 IEEE Energy Conversion Congress and Exposition*, pages 288–293, Sep. 2009. DOI: 10.1109/ECCE.2009.5316379.

[YTA05]   S. Yamamoto, K. Tomishige, and T. Ara. A method to calculate transient characteristics of synchronous reluctance motors considering iron loss and cross-magnetic saturation. In *Fourtieth IAS Annual Meeting. Conference Record of the 2005 Industry Applications Conference*, volume 3, pages 1754–1761, Oct. 2005. DOI: 10.1109/IAS.2005.1518684.